Aerosol Direct Radiative Effect: Contributors, Variability, and Observational Impacts

Qiurun Yu

余秋润

Department of Atmospheric and Oceanic Sciences

McGill University

Montreal, Canada

October 2024

A thesis submitted to McGill University in partial fulfillment of the requirements of the degree of

DOCTOR OF PHILOSOPHY

Dedication

To my mom, Yonggui Zhang, and my dad, Zongming Yu, for their unconditional love and full support.

Table of Contents

Abstract

Aerosols significantly influence Earth's energy budget by scattering and absorbing radiation, which is known as the aerosol direct radiative effect (ADRE). This thesis delves into the fundamental physics of ADRE and its significant impacts on climate variability, model accuracy, and atmospheric monitoring. It integrates findings from four comprehensive studies to elucidate the multifaceted nature of ADRE, its drivers from the surface to the stratosphere, and its impacts on satellite observations.

First, a comprehensive analysis of ADRE and its spatiotemporal variabilities was conducted. A multivariable regression model was developed to reproduce these variabilities based on global reanalysis data. Using this analytical framework, the contributions of aerosol-related and environmental factors to the spatial distributions and trends of ADRE, as well as the poleward energy transport driven by it, were separated. About 70% of the ADRE inhomogeneity is attributed to aerosol optical depth (AOD), with the remainder influenced by environmental factors such as surface albedo and cloud radiative effects. The findings highlight the importance of surface albedo trends, which drive the enhanced ADRE cooling in the Arctic.

Using the analytical ADRE model, the considerable variability of ADRE among global climate models (GCMs) in the Sixth Coupled Model Intercomparison Project (CMIP6) was investigated. Differences in state variables and radiative sensitivity explain 67% and 17% of the global ADRE inter-model spread, respectively. Key factors driving these anomalies, such as AOD, were identified in specific models. The findings suggest that constraining key state variables (AOD, surface albedo, and cloud radiative effect) and ADRE sensitivity to aerosol-related processes (aerosol-only scattering, aerosol-surface interaction) could reduce inter-model discrepancies in ADRE among CMIP6 models.

The research then shifted focus to the stratosphere. A global dataset of spectrally decomposed and broadband ADRE kernels was developed using radiative transfer calculations to quantify the stratospheric ADRE. Using the regression method, physically-sorted aerosol kernels which are independent of geophysical locations were also developed. These kernels can accurately quantify stratospheric ADRE from wildfire and volcanic eruption events with relative errors within 10%, providing an efficient and versatile tool for stratospheric ADRE assessment.

Lastly, the impact of aerosol-radiation interaction on satellite-based atmospheric methane (CH_4) measurements, GHGSat, was investigated. Neglecting aerosols results in biases from -3.0% to 6.3% in retrieved GHGSat CH_4 concentrations, with the bias shifting from negative to positive as surface albedo increases. By integrating angle-dependent scattering information in GHGSat observations, simultaneous retrievals of CH_4 and AOD were conducted and CH_4 retrieval accuracy was significantly improved. The findings provide guidance for incorporating ADRE in satellite-based greenhouse gas monitoring.

Collectively, these studies advance the understanding of ADRE, highlighting its variability, its representation in climate models, and its impact on satellite-based atmospheric measurements. The findings underscore the importance of accurately representing ADRE in climate models and remote sensing to improve climate predictions and atmospheric monitoring.

Résumé

Les aérosols exercent une influence significative sur le budget énergétique de la Terre en diffusant et en absorbant le rayonnement, ce qui est connu sous le nom d'effet radiatif direct des aérosols (ADRE). Cette thèse explore la physique fondamentale de l'ADRE et ses impacts importants sur la variabilité climatique, la précision des modèles et la surveillance atmosphérique. Elle intègre les résultats de quatre études complètes pour élucider la nature multifacette de l'ADRE, ses conducteurs de la surface à la stratosphère et ses impacts sur les observations satellitaires.

D'abord, une analyse complète de l'ADRE et de ses variabilités spatiotemporelles a été menée. Un modèle de régression multivariable a été développé pour reproduire ces variabilités à partir de données de réanalyse globale. Ce cadre analytique a permis de distinguer les contributions des facteurs liés aux aérosols mais aussi des facteurs environnementaux aux distributions spatiales et aux tendances de l'ADRE, ainsi qu'au transport d'énergie polaire qu'il entraîne. Environ 70 % de l'inhomogénéité de l'ADRE est attribuée à la profondeur optique des aérosols (AOD), le reste étant influencé par des facteurs environnementaux tels que l'albédo de surface et les effets radiatifs des nuages. Les résultats soulignent l'importance des tendances de l'albédo de surface, qui entraînent un refroidissement accru de l'ADRE dans l'Arctique.

Utilisant le modèle ADRE analytique, la variabilité considérable de l'ADRE parmi les modèles climatiques globaux (GCMs) dans le cadre du Sixième Projet d'Intercomparaison de Modèles Couplés (CMIP6) a été étudiée. Les différences dans les variables d'état et la sensibilité radiative expliquent respectivement 67 % et 17 % de l'écart inter-modèles de l'ADRE global. Les facteurs clés de ces anomalies, tels que l'AOD, ont été identifiés dans dans certains de ces modèles. Les résultats suggèrent que contraindre les variables d'état clés (AOD, albédo de surface, et effet radiatif des nuages) et la sensibilité de l'ADRE aux processus liés aux aérosols (dispersion

uniquement par les aérosols, interaction aérosol-surface) pourrait aider à réduire les divergences inter-modèles de l'ADRE parmi les modèles CMIP6.

La recherche s'est ensuite déplacée vers la stratosphère. Un ensemble de données global de noyaux ADRE, décomposés spectralement et à bande large, a été développé en utilisant des calculs de transfert radiatif pour quantifier l'ADRE stratosphérique. En utilisant la méthode de régression, un ensemble de noyaux d'aérosols physiquement triés et indépendants des emplacements géophysiques a également été développé. Ces noyaux peuvent quantifier avec précision l'ADRE stratosphérique provenant d'événements tels que l'éruption volcanique de Hunga en 2022 et les incendies de forêt en Australie en 2020, les résultats étant en grande concordance avec les calculs du modèle de transfert radiatif.

Enfin, l'impact de l'interaction aerosol-radiation sur les mesures atmosphériques de méthane (CH4) basées sur un satellites GHGSat, a été étudié. Négliger les aérosols entraîne des biais allant de -3,0 % à 6,3 % dans les concentrations de méthane CH4 mesurées par le satellite GHGSat, le biais passant du négatif au positif à mesure que l'albédo de surface augmente. En intégrant des informations de dispersion dépendantes de l'angle dans les observations GHGSat, des prélèvements simultanés de CH4 et AOD ont été effectués et la précision des récupérations de CH4 a été considérablement améliorée. Les résultats fournissent des orientations pour intégrer l'ADRE dans la surveillance des gaz à effet de serre basée sur les satellites.

Collectivement, ces études améliorent la compréhension de l'ADRE, mettant en évidence sa variabilité, sa représentation dans les modèles climatiques, et son impact sur les mesures atmosphériques basées sur les satellites. Les résultats soulignent l'importance de représenter précisément l'ADRE dans les modèles climatiques et les applications de télédétection pour améliorer les prédictions climatiques et la surveillance atmosphérique.

Acknowledgements

I am profoundly fortunate and deeply grateful to have had the opportunity to study under the guidance of Professor Yi Huang. His consistent kindness, gentleness, patience, support, and encouragement have been a beacon of encouragement throughout my academic journey. In his presence, I've learned to approach interactions with others with a warmth and ease akin to a spring breeze, and to extend generosity while upholding strict self-discipline. Professor Huang's steadfast mentoring and the opportunities he has provided for me to engage with the broader scientific community have significantly boosted my confidence, enhanced my skills, and facilitated my consistent progress as a researcher. With heartfelt appreciation, I extend my deepest gratitude to him for his guidance, for his belief in my potential, and for his immeasurable impact on my personal and professional growth.

I am grateful to the professors in the Department of Atmospheric and Oceanic Sciences. My PhD committee members, Professor Andreas Zuend and Professor Ivy Tan, have consistently provided invaluable advice throughout my doctoral studies. I also appreciate the advice from Professor Djordje Romanic, Professor David Straub, and Professor Bruno Tremblay at various stages of my PhD. I am deeply grateful to Jiangnan Li from the Canadian Centre for Climate Modelling and Analysis, whose wisdom and expertise have guided me in navigating my academic career path.

Special thanks to Dylan Jervis from GHGSat Inc. Although the pandemic prevented us from working together in person, the extensive virtual discussions and guidance he provided on the Mitacs project were instrumental in helping me develop problem-solving skills and grow as a researcher.

I would like to extend my gratitude to all past and present members of our group with whom I've had the pleasure of collaborating. I am especially grateful to Aliia Shakirova, Benjamin Riot, Diana Laura Diaz Garcia, Jing Feng, Lei Liu, Ruogu He, Xun Wang, Yan-ting Chen and Ziling Liang for their friendship, support, and the valuable time we spent together.

I am grateful to friends in Canada. Thanks to Carole Durand and Dalrin Ampritta Amaladhasan for supporting me and making me feel being cherished as a family member. Thanks to Yang Jiao, Chang Su, Chengwei Song, whose friendship helped me go through the isolation of studying abroad during COVID. Thanks to friends at ENSO yoga, especially Sarah Miller-Dorrance, whose laughter and kindness brighten my daily PhD life. Thanks to past and current friends in AOS, specially Mohammad Hadavi, Arya Toghraei, Meng-Tze Lee, Mattie Hibbs, Juliann Wray, Ying Hang and Shanhe Liu, who add color and vibrancy to our days in Burnside Hall.

Finally, I want to extend my deepest thanks to my mother Yonggui Zhang and father Zongming Yu, without whom I would never be able to accomplish my PhD journey. Thank you for being the world’s best parents.

Statement of Originality

This thesis presents original research and offers significant contributions to the understanding of aerosol-radiation interactions and their implications in climate change, atmospheric modeling, and remote sensing.

Trends and distributions of aerosol direct radiative effect (Chapter 2).

Our first objective was to assess the impact of aerosol-related and environmental variables on the global patterns and trends of the Aerosol Direct Radiative Effect (ADRE). To achieve this, we constructed a multivariate regression model capable of predicting global clear-sky and all-sky ADREs along with their trends. Through this model, we successfully pinpointed the critical variables influencing ADRE, evaluated their respective impacts, and determined their sensitivities. This research has laid a foundation for understanding the contributors to ADRE on a global scale. The regression framework we designed for studying ADRE has been rigorously validated and applied not only in our subsequent research projects but also in other researchers' studies.

Model discrepencies of aerosol direct radiative effect (Chapter 3).

We analyzed the discrepancies in ADRE among the Sixth Coupled Model Intercomparison Projects (CMIP6) models by dissecting ADRE anomalies into differences in aerosol and atmospheric states and their sensitivities to aerosol-related radiative processes. Our regression model, developed in Chapter 2, effectively captures the spatial distributions of ADRE anomalies and their inter-model standard deviations. We determined that differences in state variables and radiative sensitivity account for 67% and 17%, respectively, of the global ADRE anomaly. By constraining key state variables (e.g., aerosol optical depth (AOD), surface albedo, cloud radiative

effect) and fine-tuning ADRE sensitivity to aerosol-related processes (such as aerosol-only scattering and aerosol-surface interactions), we can significantly reduce ADRE uncertainties. The diagnostic method we proposed can identify the major factors responsible for ADRE anomalies in each model and the regions where they are most influential, offering insights that can improve ADRE simulations and reduce their uncertainties.

Radiative kernels for stratospheric aerosol direct radiative effect (Chapter 4).

We developed, for the first time, a comprehensive set of radiative kernels specifically designed for quantifying stratospheric ADRE. We introduced both broadband and band-specific kernels to address the spatial, temporal, and spectral variability of stratospheric aerosols. Building on the multivariate regression framework established in Chapter 2, we also developed an analytical set of aerosol kernels by incorporating key controlling variables. These kernels were successfully applied to assess the impact of significant events like the 2022 Hunga volcanic eruption and the 2020 Australia wildfire, with the results agree well with radiative transfer model calculations. Our development offers a versatile and efficient tool for accurately quantifying stratospheric ADRE.

Impact of aerosol-radiation interactions on GHGSat methane retrievals (Chapter 5).

The latest generation of space-borne spectrometers designed for greenhouse gas retrieval demands exceptional accuracy. One significant challenge is the inaccurate understanding of photon path-length distribution, heavily influenced by atmospheric scatterers, particularly aerosols. Our research quantified, for the first time, the errors that arise from ignoring aerosol-radiation interactions in GHGSat methane retrieval. We explored the variations in bias under different conditions of aerosol optical properties, surface albedo, and satellite zenith angles, and performed simultaneous retrievals of AOD and methane. This study provides crucial insights into

the impact of aerosols on GHGSat and offers recommendations for enhancing the accuracy of future GHGSat-like instruments by using the multi-angle viewing method.

Contributions of Authors

This article-based thesis contains six chapters: an introduction (Chapter 1), three articles published in peer-reviewed journals, Chapter 2 in *Journal of Geophysical Research: Atmosphere*, Chapter 3 in *Geophysical Research Letters*, Chapter 5 in *Atmospheric Measurement Techniques*, and one manuscript is under review in *Journal of Geophysical Research: Atmospher*e (Chapter 4), and a concluding (Chapter 6).

I conducted all the research works presented in this dissertation. I wrote all the chapters, co-designed the studies, carried out simulations, analyzed data, developed models, interpreted the results, and created the figures, all under the guidance of Professor Yi Huang.

Professor Yi Huang played a pivotal role in co-designing the studies, offered continuous guidance, support, and critical feedback throughout the research process, contributed to the interpretation of results and discussions, provided experimental insights, and reviewed all articles included in this thesis.

Dylan Jervis, a Senior Scientist at GHGSat Inc., co-authored Chapter 5 of this thesis. Dylan contributed to designing the Observing System Simulation Experiments, provided the GHGSat instrument model, offered scientific insights, and reviewed the manuscript.

The articles used in this thesis reflect the suggestions and constructive comments from all co-authors and several disclosed and anonymous reviewers during the peer-reviewing process.

List of Figures

List of Tables

Lists of Acronyms and Symbols

Acronyms

AAOD	Absorbing Aerosol Optical Depth
ADRE	Aerosol Direct Radiative Effect
ADRF	Aerosol Direct Radiative Forcing
AERONET	Aerosol Robotic Network
AOD	Aerosol Optical Depth
AVIRIS-NG	Airborne Visible/Infrared Imaging Spectrometer Next Generation
BC	Black Carbon
CALIOP	Cloud-Aerosol Lidar with Orthogonal Polarization
CCN	Cloud Condensation Nuclei
COD	Cloud Optical Depth
CRE	Cloud Radiative Effect
CMIP6	the Sixth Coupled Model Intercomparison Projects
DDA	Discrete Dipole Approximation
DISORT	DIScreet Ordinate Radiative Transfer

DMS	Dimethyl Sulfide
EC	Elemental Carbon
ERF	Effective Radiative Forcing
GCM	General Circulation Models
GOSAT	Greenhouse gases Observing SATellite
LBLRTM	Line-By-Line Radiative-Transfer Model
LFM	Linearized Forward Model
LWP	Liquid Water Path
MERRA-2	Modern-Era Retrospective analysis for Research and Applications, Version 2
MISR	Multi-angle Imaging SpectroRadiometer
OC	Organic Carbon
OCO-2	Orbiting Carbon Observatory 2
PRP	Partial Radiative Perturbation
PyroCb	Pyrocumulonimbus
RRTMG	Rapid Radiation Transfer Model for GCM

SAOD	Scattering Aerosol Optical Depth
SCIAMACHY	Scanning Imaging Absorption Spectrometer for Atmospheric Chartography
SOA	Secondary Organic Aerosols
SSA	Single Scattering Albedo
SWIR	Shortwave Infrared
TISR	TOA Incoming Solar Radiation

Symbols

β	backscattering ratio
θ	solar zenith angle
ω	aerosol single scattering albedo
τ	aerosol optical depth
alb	surface albedo
g	asymmetry parameter
ΔP	planetary albedo change
T_{at}	atmospheric transmittance

R_{as}	reflectance of the combined aerosol and atmospheric layer
R_s	tropopause reflectance
R	TOA reflectance
S	solar insolation

Chapter 1 Introduction

1.1. Sources and Components of Aerosols

Aerosols are tiny particles, both microscopic and submicroscopic, suspended in the air (Boucher, O., & Boucher, O., 2015). These particles can exist in solid, liquid, or mixed-phase forms (Hinds & Zhu, 2022). They originate from either natural sources or human activities. Natural sources include sandstorms, volcanic eruptions, wildfires, sea spray, and biogenic emissions (Christensen et al., 2022; H. Yu et al., 2006). Human activities that generate aerosols encompass a wide range of processes, such as fossil fuel combustion, industrial production, agriculture, cooking, and heating (H. Yu et al., 2006; Hinds & Zhu, 2022; Christensen et al., 2022).

Aerosols can be classified based on their formation mechanisms. Primary aerosols are directly emitted into the atmosphere from mechanical processes or natural sources (Kremser et al., 2016; Christensen et al., 2022; J. Li et al., 2022). In contrast, secondary aerosols are formed in the atmosphere from gaseous precursors through chemical or physical reactions, undergoing a gas-to-particle transformation (Tomasi & Lupi, 2017; Hinds & Zhu, 2022).

Once in the atmosphere, aerosols undergo various microphysical transformations such as coagulation and condensation, as well as chemical reactions like oxidation (Yau & Rogers, 1996). These particles are then transported by atmospheric circulations. Depending on the atmospheric conditions, tropospheric aerosols remain in the atmosphere for days to weeks (Kristiansen et al., 2016), while stratospheric aerosols can persist for weeks to months (Willis et al., 2018). These relatively short lifetimes, especially when compared to greenhouse gases, are due to efficient removal processes. Aerosols are either directly deposed to the surface (e.g., sedimentation, precipitation, or turbulence) or scavenged by and into cloud droplets and ice crystals, followed by precipitation (Bellouin et al., 2020; Kremser et al., 2016).

The combination of these physical and chemical processes, along with the spatially heterogeneous distribution of aerosol sources and atmospheric conditions, makes it challenging to model aerosol properties accurately and to assess their impact on air quality, Earth's radiative budget, and climate (Bellouin et al., 2020; J. Li et al., 2022; Kremser et al., 2016; H. Yu et al., 2006; J. Haywood & Boucher, 2000).

1.1.1. Tropospheric Aerosols

Tropospheric aerosols are highly spatial-temporal heterogenous. They are concentrated in and downwind of source regions such as deserts and industrialized regions, with a mean residence time of approximately 5 days and typical transport distances of about 2000 km (Bellouin et al., 2020). Tropospheric aerosols originate from a wide variety of sources. Classifying aerosols based on their composition or source can be somewhat arbitrary, as particles often undergo different processes, such as internal mixing in the atmosphere, leading to inevitable overlaps between groups (Pósfai & Buseck, 2010). In this context, we distinguish among carbonaceous, sulfate, sea-salt, mineral dust, and nitrate aerosols. The estimated annual emissions and atmospheric burdens of these aerosol groups are summarized in Table 1.1.

Table 1.1 Estimated emissions and atmospheric burdens of the major aerosol types for the year 2000. Data are obtained from Andreae & Rosenfeld (2008)

	Mass emission (Tg/year)	**Mass burden (Tg)**
Carbonaceous aerosols		
Primary organic (0–2 μm)	95	1.2
Black carbon (0–2 μm)	10	0.1
Secondary organic	28	0.8

Sulfates	200	2.8
Biogenic	57	1.2
Volcanic	21	0.2
Anthropogenic	122	1.4
Nitrates	18	0.49
Sea Salt	10,130	15
Mineral dust	1,600	18

Table 1.1 suggests that natural aerosols, such as mineral dust, dominate the aerosol mass burden in the atmosphere. Dust mainly originates from wind erosion in the dust belt, a chain of arid regions including the Sahara Desert, deserts in the Middle East, and the Gobi and Taklamakan Deserts (Mahowald et al., 2014). Dried lakebeds and other formerly wet areas are also significant sources of dust as the dust emissions depend on soil moisture, surface wind speed, soil texture, and soil surface conditions (Tegen & Lacis, 1996). Dust mobilization is influenced by surface conditions such as moisture, roughness elements, geological characteristics, as well as atmospheric conditions like low rainfall and high windspeeds (Duce, 1995; Tegen & Lacis, 1996; Mahowald et al., 2014). Desert dust can be the dominant particle type even thousands of kilometers from the source area. Mineral dust is important to human health, air quality, weather, climate, and biogeochemistry, as shown in Figure 1.1 from Mahowald et al. (2014).

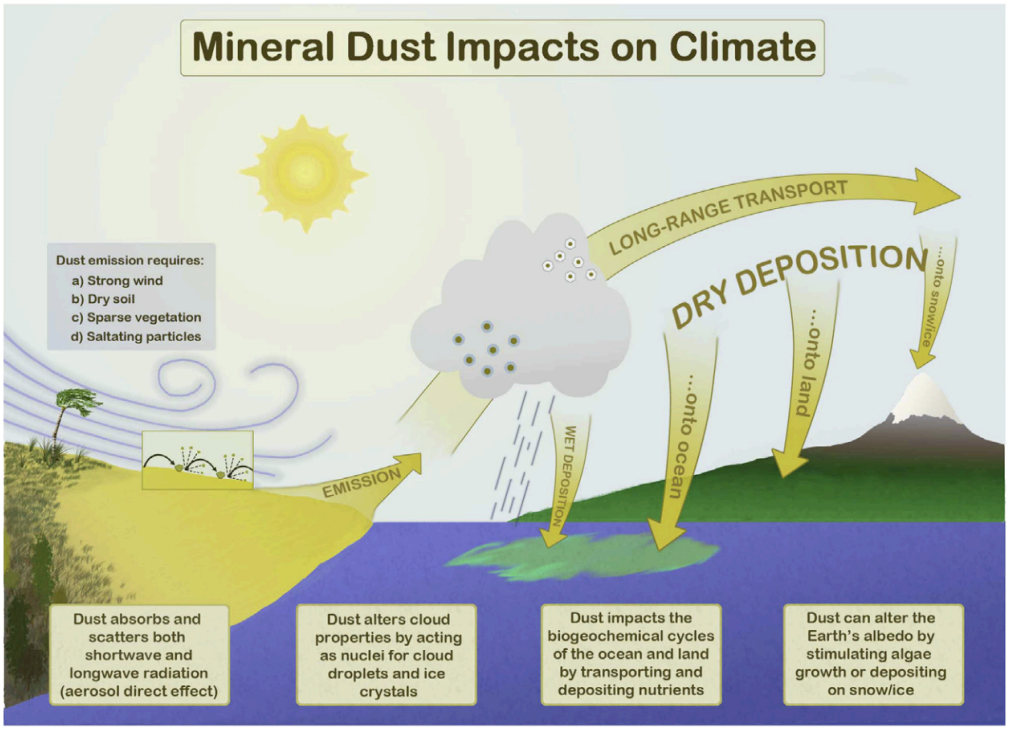

Figure 1.1 Diagram of interactions between dust and climate and biogeochemistry from Mahowald et al. (2014).

Sea-salt aerosols account for the largest mass emission flux in the troposphere (Andreae & Rosenfeld, 2008). They are produced through physical processes such as the bursting of entrained bubbles at the sea surface and the tearing of droplets from wave crests over wind-swept saline water bodies (Grythe et al., 2014; Lewis & Schwartz, 2004). Similar to dust, the emissions of sea-salt aerosols are highly dependent on the surface wind (Andreae & Rosenfeld, 2008; Lewis & Schwartz, 2004). Sea-salt aerosols contain around 10% organic matter, as the ocean surface is enriched with microorganisms, viruses, and extracellular biogenic material (Aller et al., 2005). These aerosols have important radiative effects on the climate: they are responsible for the aerosol-scattered light and comprise a significant fraction of the inferred cloud condensation nuclei (CCN) due to their hygroscopic properties (Murphy et al., 1998).

Sulfate aerosols are a significant component of atmospheric particulates, derived from both natural and anthropogenic sources (Andreae & Rosenfeld, 2008; Pósfai & Buseck, 2010). Naturally, they are produced from the oxidation of sulfur-containing gases emitted by volcanic eruptions and the oxidation of dimethyl sulfide (DMS) from marine phytoplankton (Charlson et al., 1987). Anthropogenic sources include the combustion of fossil fuels and industrial processes, which release sulfur dioxide (SO_2) into the atmosphere. This SO_2 subsequently undergoes chemical reactions to form sulfate aerosols (X. Liu et al., 2005). Sulfate aerosols are typically found in the fine particle ($PM_{2.5}$) mode and are associated with various environmental and health issues, such as acid rain and air pollutions, posing risks to human health (Seinfeld & Pandis, 2016). Due to their ability to scatter solar radiation, sulfate aerosols exert a cooling effect on the Earth's climate, counteracting some of the warming caused by greenhouse gases (Charlson et al., 1992). Additionally, they serve as CCN, influencing cloud properties and albedo, which further impacts the Earth's radiative balance (Twomey, 1977).

Carbonaceous aerosols arise from the combustion of fossil fuels (e.g., transportation and energy production), domestic burning (cooking and heating), the burning of vegetation (such as savannah and deforestation fires), and agricultural waste. These aerosols consist of elemental carbon (EC) and organic carbon (OC) (Rauber et al., 2023).

OC aerosols can originate from biogenic and anthropogenic precursors. Biogenic aerosols cover a wide range of particle sizes due to the variety of particle types (Pósfai & Buseck, 2010). These include (in size sequence) microbial particles such as living and dead viruses, bacterial cells, spores, pollen, algae, and biogenic debris such as marine colloids and plant fragments (Andreae & Rosenfeld, 2008). The sources and evolutionary mechanisms of these aerosols are diverse and remain poorly characterized (Jimenez et al., 2009; Kanakidou et al., 2005). Emissions of organic

carbon from anthropogenic sources are 5 to 10 times lower than those from biogenic sources (excluding methane) (Kanakidou et al., 2005). Between 10% to 40% of the organic aerosols are secondary organic aerosols (SOA), which originate from the condensation of organic vapors in the atmosphere (Volkamer et al., 2006). The precursors of SOA may be biogenic (e.g., terpenes, isoprene) or anthropogenic (e.g., petroleum, combustion) (Volkamer et al., 2006; Kanakidou et al., 2005). Estimates of the global contributions of various SOA sources vary widely (Andreae & Rosenfeld 2008), reflecting the need for more detailed studies on this class of particles. The direct radiative effect of organic aerosols is typically a weak cooling effect, influenced by the treatment of water uptake and consideration of internal mixing of aerosols (Kanakidou et al., 2005). As effective CCN, organic aerosols play a crucial role in regulating cloud properties across both polluted and remote parts of the atmosphere (Andreae & Rosenfeld, 2008).

Combustion-derived carbonaceous soot particles, commonly referred to as black carbon (BC), predominantly arise from the incomplete combustion of fossil fuels, residential biofuel, and biomass (Bond et al., 2013). As one of the key components of fine particulate matter (PM2.5), black carbon is noteworthy not only for its health impacts but also for its significant role in atmospheric and climate science (Choomanee et al., 2024). The atmospheric science community commonly uses the term BC for the strongly absorbing component of the aerosol, which makes them unique among other aerosol species that typically scatter light. This absorption leads to the warming of the atmosphere and, when deposited on snow and ice, can accelerate melting by reducing the surface albedo, thereby further influencing global climate dynamics (Bond et al., 2013). Furthermore, BC influences cloud formation processes by acting as CCN, although its effects are complex and vary based on the atmospheric conditions (McConnell et al., 2007). The climate effects of BC are shown in Figure 1.2 by Bond et al. (2013). Beyond its climatic effects,

BC is linked to serious health issues, as it can penetrate deeply into the lungs and bloodstream (J. Yang et al., 2021). Despite having a shorter atmospheric lifetime, typically lasting from several days to weeks, BC has a potent and immediate effect on the climate system. Controlling the emissions of BC is therefore crucial for both climate mitigation and air quality improvement in the short term (Bond et al., 2013; Ramanathan & Carmichael, 2008).

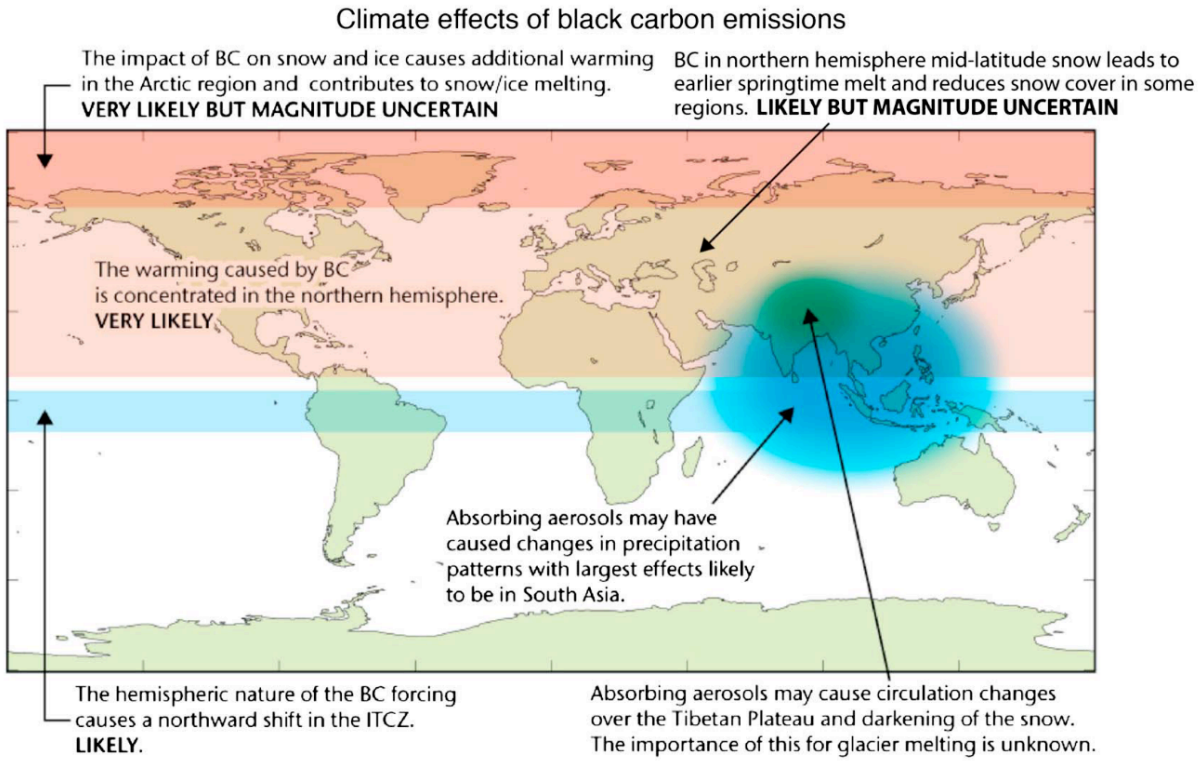

Figure 1.2 Diagram of climate effects of black carbon emissions from Bond et al. (2013)

1.1.2. Stratospheric Aerosols

The primary factor controlling stratospheric aerosol variability is episodic but powerful volcanic eruptions, which inject sulfur directly into the lower stratosphere (Kremser et al., 2016). They reside in the atmosphere for several months to a few years because of slow particle sedimentation velocities and secondary aerosol production (Bellouin et al., 2020). These particles

scatter sunlight and cause a lasting cooling effect on the climate after a major eruption (Solomon et al., 2011; Kremser et al., 2016; Christensen et al., 2022; Schoeberl et al., 2023). Additionally, these aerosols provide surfaces for heterogeneous chemical reactions, enhance the depletion of stratospheric ozone, and change the chemical balance of the atmosphere (Molina et al., 1987). During passive degassing and weakly explosive or effusive eruptions, the relatively low volcanic emissions can also produce a cooling effect by increasing the cloud brightness and cloud droplet numbers (Schmidt et al., 2012).

There are also non-sulfate stratospheric aerosols including volcanic ash, organic carbon, smoke particles from biomass burning, and other species (e.g., meteoric ablation, space debris, rocket emissions) (Kremser et al., 2016). Among them, increasing attention has been paid to pyrocumulonimbus (PyroCb) clouds, which are formed when intense heat from wildfires generates powerful updrafts that can penetrate the tropopause and enter the stratosphere (Fromm et al., 2022; P. Yu et al., 2019; Fromm et al., 2010). The sensible heat released from the fire, the strong vertical velocity, and the lack of precipitation and scavenging act together to effectively transport smoke and other aerosols from large wildfires directly into the stratosphere (Fromm et al., 2010; Kremser et al., 2016). Moreover, buoyancy changes owing to solar heating of black carbon can cause subsequent self-lofting of upper tropospheric aerosols (Ohneiser et al., 2023). Smoke aerosols, consisting of varying fractions of organics, soot, and inorganic carbon, absorb incoming solar radiation and lead to a warming effect in the shortwave (Christian et al., 2019; Damany-Pearce et al., 2022). In response to the heating, the temperature-adjusted stratosphere emits longwave radiation back to space (C.-C. Liu et al., 2022; P. Yu et al., 2023). Overall, the effect radiative forcing of wildfire tends to be negative (C.-C. Liu et al., 2022; P. Yu et al., 2023). With more

intense and frequent wildfires due to climate change, it is important to consider the climate impact of stratospheric wildfire smoke in future climate projections (Friberg et al., 2023).

The impact of stratospheric aerosols on the global climate system, their role in ozone chemistry, and their potential for future geoengineering efforts to offset global warming highlight the importance of studying these particles (Kremser et al., 2016; Visioni et al., 2020; P. Yu et al., 2023). With the help of new measurement systems and techniques such as High altitude Aerosols, Water vapor and Clouds (HAWC) system (Bourassa et al., 2020), there will be an increased understanding of their sources, properties, and behaviors to help accurately model their impacts and predicting future changes in Earth's atmospheric dynamics.

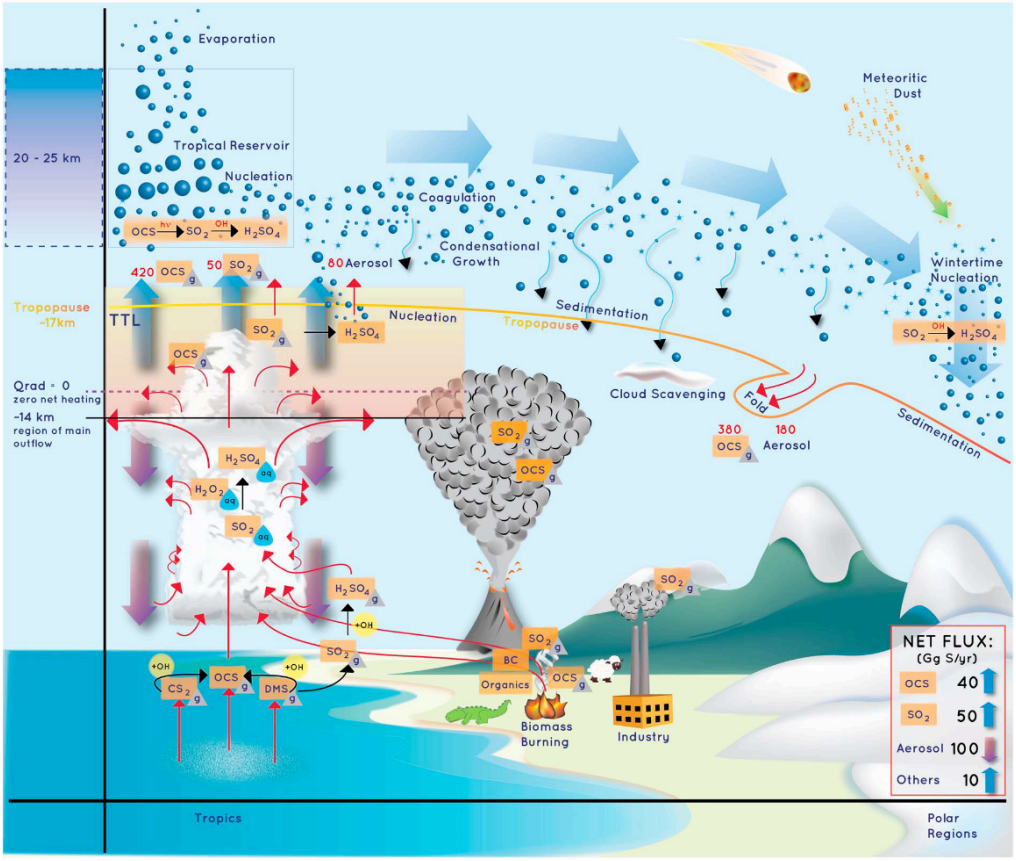

Figure 1.3 Schematic of the relevant processes that determine the life cycle and distribution of stratospheric aerosols. Large-scale atmospheric circulation is represented by large blue arrows, transport processes by red arrows, and chemical transformations between compounds by black arrows. Gas-phase components are shown as grey triangles, and aqueous-phase components as blue drops. The downward movement of aerosols from the stratosphere to the troposphere is indicated by thin blue arrows. This figure is adapted from Kremser et al. (2016).

1.2. Aerosol Distributions

1.2.1 Aerosol Size Distributions

According to diameter, aerosols can be classified into four modes: nuclear mode ($D_p < 0.01\ \mu m$), Aitken mode ($0.01\ \mu m < D_p < 0.1\ \mu m$), accumulation mode ($0.1\ \mu m < D_p < 1\ \mu m$), and coarse mode ($D_p > 1\ \mu m$) (Raes et al., 2000). In reality, aerosol size distributions are complex (e.g., mono-, bi-, tri-, and quad-modal), and they vary a lot according to the seasons, emission types, meteorological conditions, and measurement locations (Kinne, 2019; Q.-R. Yu et al., 2019; Raes et al., 2000).

To simplify the representation of aerosol size in modeling, two main approaches are used: the discrete and continuous approximations. The discrete approximation, also known as the bin method, divides the aerosol size spectrum into discrete intervals and calculates concentrations in each size bin (Mahowald et al., 2014; Q.-R. Yu et al., 2019). Within each bin, however, the size distribution remains constant, implying a fixed relationship between the mass in the bin and the number of particles (Mahowald et al., 2014). The number of bins is usually reduced in general circulation models (GCM) to enhance computation efficiency (Mahowald et al., 2014). For the continuous approximation, a bi-model lognormal size distribution is generally assumed in most aerosol retrieval models, with peak concentrations located at fine and coarse modes, respectively

(Mahowald et al., 2014; Q.-R. Yu et al., 2019). Although both the mass median diameter and number concentration are allowed to change within each mode with fixed geometric standard deviation and effective radius, the potential discrepancies and inaccuracies in parameterizing aerosol size distributions among GCMs can still lead to potential biases when assessing the climate effects of aerosols (Goto et al., 2024; J. Li et al., 2022; Q.-R. Yu et al., 2019).

1.2.2. Aerosol Height Distributions

Aerosols exhibit complex vertical distributions influenced by their sources, atmospheric dynamics, and physical and chemical characteristics (Koffi et al., 2016). These distributions can be analyzed using satellite instruments, ground-based lidars, and measurements from balloons and aircraft (J. Li et al., 2022). Specifically, the Cloud-Aerosol Lidar with Orthogonal Polarization (CALIOP) on space-borne lidar platforms provides reliable global aerosol vertical profiles, although its geographical coverage is limited (Winker et al., 2009). Figure 1.4 illustrates the normalized mean global annual aerosol extinction profiles from CALIOP (2007–2009), compared with model simulations from Koffi et al. (2016). There is significant variability among models and discrepancies between simulated and observed aerosol height distributions. These inconsistencies stem from multiple factors, including uncertainties in emission sources and heights, the complexities of convective transport processes and secondary aerosol formation, and the limited availability of in-situ observations to refine these models (Koffi et al., 2016).

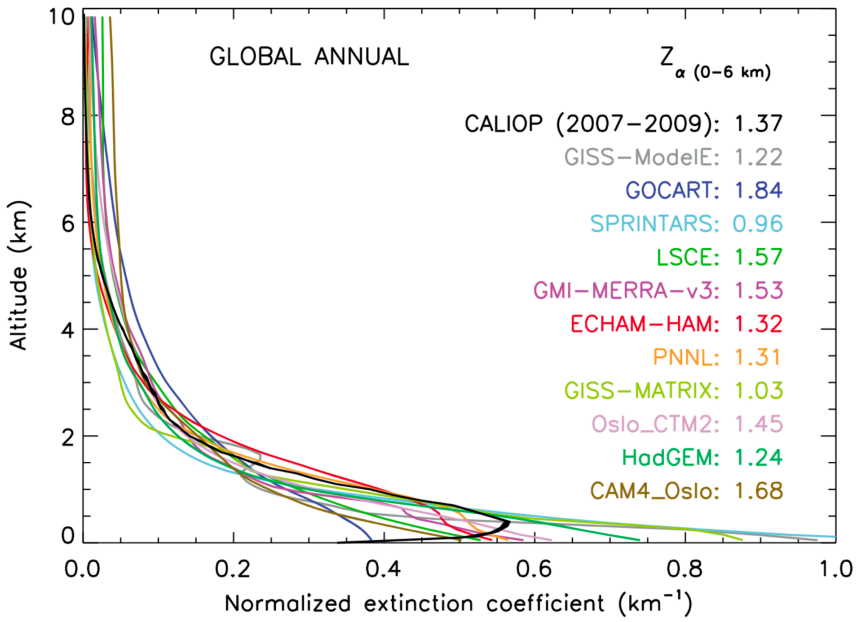

Figure 1.4 "Normalized" extinction coefficient profiles (km^{-1}) at 550 nm for models in the year of 2006 and at 532 nm for CALIOP data from 2007 to 2009. The range for CALIOP data is depicted in black. The profiles are normalized to a common AOD (AOD=1) over the 0-10 km altitude range from Koffi et al. (2016)

The vertical distribution of aerosols plays a crucial role in solar radiative transfer, particularly through their relative altitude compared to clouds, which is especially significant for absorbing aerosols. When clouds are situated above aerosols, they can mask the aerosols' radiative effects (Q. Yu & Huang, 2023b). When aerosols are located near cloud altitude, their radiative effect can be enhanced due to the increase in AOD due to hygroscopic growth effect near clouds (C. K. Yang et al., 2022). The transition regions between cloudy and clear skies, referred to as twilight zone, contain a mix of liquid droplets and aerosols ranging from humidified to dry (Jahani et al., 2022; Koren et al., 2007). This zone is characterized by complex processes such as cloud dissipation and formation, aerosol hydration and dehydration, shearing of cloud fragments, and

clouds becoming undetectable (Jahani et al., 2022). The complexity of characterizing these regions could lead to an underestimation of the aerosol direct effect, since aerosol optical depth (AOD) measurements from current satellite retrievals are typically biased towards cloud-free environments (Koren et al., 2007). Furthermore, when aerosols are positioned above clouds, their absorption is intensified due to the increased brightness of the underlying surface (Q. Yu & Huang, 2023b).

1.2.3. Aerosol Spatial Distributions

The spatial distribution of aerosols varies significantly across the globe, with concentrations typically highest near their sources. High concentrations of sulfate aerosols are predominantly found over East and South Asia, regions known for intense industrial activity and significant anthropogenic emissions (Koch et al., 2007). Both BC and OC are prevalent in South America, Southern Africa, and Southeast Asia. These regions experience extensive biomass burning associated with agricultural practices and land clearing (Koch et al., 2007). Dust aerosols originate predominantly from arid areas such as North Africa, the Middle East, and Central Asia. With strong wind lift and transportation, these particles can travel vast distances, affecting areas far from their desert sources (Schepanski, 2018). Sea-salt aerosols are concentrated primarily over the oceans.

1.3. Radiative Characteristics of Aerosols

1.3.1. Scattering Aerosols

The aerosol complex refractive index (m = n - ki) is a crucial optical parameter that governs how light interacts with aerosols. The real part of the refractive index (n) is associated with particle scattering, while the imaginary part (k) relates to absorption (Sokolik et al., 1993). Globally, the scattering of solar radiation, which enhances the planetary albedo and cools the climate, dominates

the aerosol direct radiative effect (H. Yu et al., 2006; Bellouin et al., 2020; Q. Yu & Huang, 2023b). The scattering aerosols such as sulfate and sea salt, known for their purely scattering properties, are often modeled as spherical particles due to their hygroscopic nature. Using Mie theory, their optical properties, such as the mass extinction coefficient, single scattering albedo (SSA), and asymmetry factor, are calculated based on predefined reflective indices and aerosol size distributions (Q.-R. Yu et al., 2019). For non-spherical particles, some numerical techniques for optical propertie calculations include the T-matrix method and the Discrete Dipole Approximation (DDA) (Draine et al., 1994 and Mishchenko et al., 1996).

Scattering by aerosols is directionally dependent. The angular distribution of aerosol scattering is described by the phase function ($\mathrm{P}(\Theta)$). The first moment of the phase function, defined as the asymmetry parameter (g), can represent the degree of forward scattering (Toublanc, 1996).

$$g = \frac{1}{2}\int_0^{\pi} \cos\Theta \mathrm{P}(\Theta) \sin(\Theta)\, \mathrm{d}\Theta \tag{1.1}$$

A value of g = -1 indicates complete backward scattering, whereas g = +1 signifies complete forward scattering. The global mean value of g is approximately 0.7, indicating primarily forward scattering (Ayash et al., 2008). By taking measurements at multi-angle geometry, satellites can distinguish different types of clouds, aerosol particles, and surfaces (e.g., multi-angle Imaging Spectro Radiometer (MISR)) (Diner et al., 1998).

The radiative effects of scattering aerosols are displayed in Figure 1.5 from Li et al. (2022). Scattering aerosols can cool the climate both by directly scattering sunlight and by increasing the number of cloud droplets, thereby enhancing the cloud reflectance.

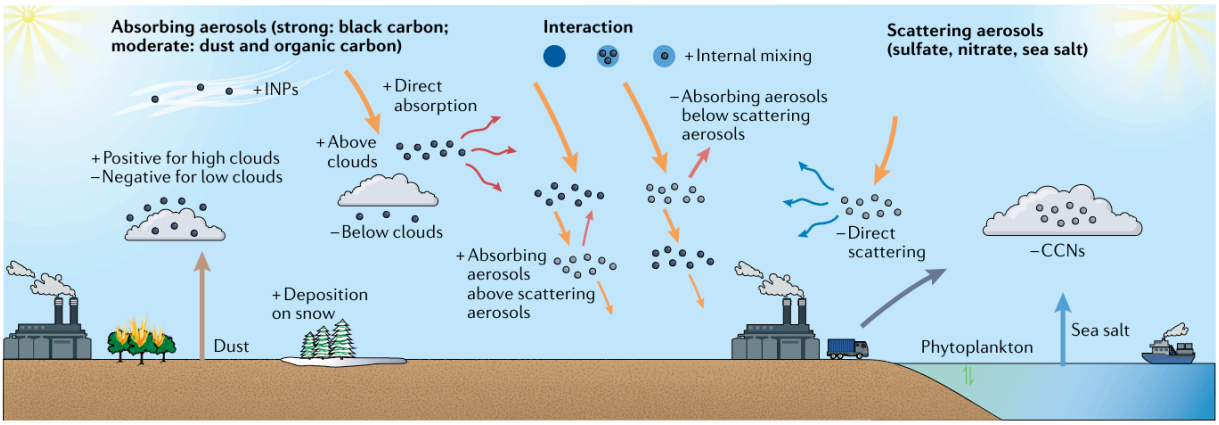

Figure 1.5 Schematic of the radiative effects of scattering and absorbing aerosols, and their interactions from Li et al. (2022)

1.3.2. Absorbing Aerosols

Some aerosols possess the ability to absorb solar radiation, thereby exerting a notable warming effect on the climate system almost instantaneously. Among these, black carbon stands out as a particularly strong absorber, while dust and organic carbon exhibit moderate absorption capabilities (Kanakidou et al., 2005; McConnell et al., 2007; J. Li et al., 2022). This absorption of solar energy by aerosols can lead to atmospheric heating, which, in turn, may cool the surface (C. Wang, 2013; J. Li et al., 2022). This dynamic interplay between heating and cooling significantly influences atmospheric processes on multiple scales, potentially increasing atmospheric stability, and altering patterns of cloud formation and precipitation (C. Wang, 2013). The effectiveness of these absorbing aerosols is contingent upon the brightness of the surface below them. Absorption is markedly enhanced when aerosols are positioned above highly reflective surfaces such as clouds or deserts. Additionally, when absorbing aerosols like black carbon settle on snow and ice, they can reduce the surface albedo, leading to increased solar absorption and accelerated melting.

The radiative effects of absorbing aerosols are depicted in Figure 1.5 from Li et al. (2022). The radiative effect of absorbing aerosols is complex, depending on the relative location of aerosols.

1.4. Climate Effects of Aerosols

1.4.1. Direct Effects

The Aerosol Direct Radiative Effect (ADRE) quantifies changes in radiative flux caused by the direct absorption and scattering of solar radiation by both natural and anthropogenic aerosols (Bellouin et al., 2020; Lei et al., 2020; Q. Yu & Huang, 2023b). ADRE can be measured at different atmospheric levels—namely, the top of the atmosphere (TOA) and the surface—and under varying sky conditions, such as clear-sky or all-sky scenarios (McComiskey et al., 2008; Q.-R. Yu et al., 2019). This effect significantly influences the planetary albedo, leading to either cooling or warming impacts, which crucially affects the Earth's energy balance. It's important to distinguish ADRE from aerosol direct radiative forcing (ADRF), which specifically addresses changes due to anthropogenic aerosols (Thorsen et al., 2021).

Aerosols continue to be the largest uncertainty in determining the radiative forcing of climate and understanding ADRE is the most elementary step (J. Li et al., 2022). The influence of ADRE on global climate is intricate and depends on factors like aerosol properties (size, composition, concentration) and environmental conditions (presence of clouds, angle of solar insolation, and the characteristics of the underlying surface) (Thorsen et al., 2020; Q. Yu & Huang, 2023a, 2023b). Moreover, the interactions between aerosols and these environmental factors add layers of complexity (Q. Yu & Huang, 2023b). Despite its straightforward definition, many critical questions about ADRE remain unsolved, such as what factors predominantly affect ADRE, trends in ADRE in recent years, discrepancies in GCMs, differences in stratospheric versus tropospheric

ADRE sensitivities, efficient quantification of ADRE, and its impact on atmospheric monitoring of greenhouse gases in the shortwave spectrum (Q. Yu et al., 2024; Q. Yu & Huang, 2023b; Q.-R. Yu et al., 2019). Therefore, this thesis focuses on studies related to ADRE, exploring both its theoretical foundations and practical implications in climate.

1.4.2. Indirect and Semi-direct Effects

Aerosols can indirectly influence the climate by altering cloud microphysical properties. These microphysical changes can subsequently lead to alterations in macroscopic properties like cloud albedo, cloud optical thickness, and cloud lifetime (Johnson et al., 2004; Storelvmo, 2017). Aerosols impact liquid clouds by acting as CCNs. Effective CCNs include water-soluble aerosols such as sulfate, nitrate, sea salt, and secondary organic aerosols (Yau & Rogers, 1996). An increase in these particles can increase the number concentration of cloud droplets, reduce their effective radius, and enhance cloud reflectance, resulting in a cooling effect on the climate (Bellouin et al., 2020; J. Haywood & Boucher, 2000). However, the rapid adjustments in aerosol-cloud interactions can vary based on cloud dynamics and environmental conditions. Smaller cloud droplets are less likely to precipitate, which can intensify the cooling effect by increasing cloud lifetime or cloud fraction (Johnson et al., 2004; J. Li et al., 2022; Storelvmo, 2017). Conversely, smaller droplets evaporate more rapidly, and changes in droplet size distribution can potentially leading to a warming effect due to a reduced liquid water path (LWP) (J. Haywood & Boucher, 2000; Johnson et al., 2004; J. Li et al., 2022). Although some studies suggested that aerosols can affect the efficiency of radiatively driven entrainment in the boundary layer. The aerosol-entrainment coupling is still poorly understood (Su et al., 2022; Chylik et al., 2023).

Aerosols also interact with ice and mixed-phase clouds by serving as ice nucleation particles (INPs), particularly in the case of dust and organic aerosols (J. Haywood & Boucher,

2000; J. Li et al., 2022). INPs can increase the heterogeneous ice nucleation rate and suppress homogeneous nucleation (Storelvmo, 2017). When heterogeneous nucleation dominates ice cloud formation, an increase in INPs can elevate the number of ice crystals, increasing cloud optical depth and leading to a warming effect. The opposite is true if homogeneous nucleation dominates. In mixed-phase clouds, an increase in INPs can accelerate cloud glaciation (through diffusional growth or riming), decrease cloud optical depth, and enhance precipitation. Meanwhile, when aerosol precursor gases increase, their ice-nucleating ability may be temporarily or permanently deactivated, reducing cloud glaciation (J. Haywood & Boucher, 2000; Storelvmo, 2017; J. Li et al., 2022).

Lastly, absorbing aerosols can decrease low-cloud cover and LWP by heating the air and reducing relative humidity, contributing to a warming effect on the climate system. This effect is often referred to as the aerosol semi-direct effect (Johnson et al., 2004).

1.5. Key Factors Influencing Aerosol Direct Radiative Effect

1.5.1. Aerosol Microphysical Properties

Aerosol microphysical properties, which include factors such as chemical composition, shape, mixing states, hygroscopicity, and particle size distribution, determine their optical properties (J. Li et al., 2022; X. Liu et al., 2005; H. Yu et al., 2006; Q. Yu & Huang, 2023b). These optical properties, in turn, significantly influence the ADRE (McComiskey et al., 2008; Thorsen et al., 2020).

The chemical composition of aerosols determines their scattering and absorbing ability (Ayash et al., 2008). The shape of aerosol particles can vary from spherical droplets to irregularly shaped dust particles (C. Liu et al., 2017; Mishchenko, 2009). Non-spherical particles interact with light differently from spherical particles, influencing both the magnitude and directionality of

ADRE (Mishchenko, 2009). The aerosol mixing state and aerosol chemical component and morphology are highly correlated. For example, when black carbon is internally mixed with other substances, it can absorb more light, increasing its warming potential by 1.5 to 2.5 times compared to when it is externally mixed (C. Liu et al., 2017). The ability of aerosols to absorb water from the atmosphere, known as hygroscopicity, affects their size and optical properties (Grythe et al., 2014). Given the complexity and variability of these microphysical properties, accurately representing them in climate models remains a significant challenge (Bellouin et al., 2020; J. Li et al., 2022; Q.-R. Yu et al., 2019).

1.5.2. Surface Albedo

ADRE will change when the surface albedo changes even with no change in aerosols (McComiskey et al., 2008; Thorsen et al., 2020; Q. Yu & Huang, 2023b). The efficiency of aerosol scattering decreases over surfaces with high albedo, such as snow and deserts, while it increases over darker surfaces, like the ocean (Q. Yu & Huang, 2023b; J. Li et al., 2022). In contrast, the efficiency of absorbing aerosols behaves oppositely, being more pronounced over high-albedo surfaces and less effective over dark surfaces (Bellouin et al., 2020; Q. Yu & Huang, 2023b). Over a reflective surface, multiple reflections between aerosols and the surface serve to increase surface absorption by enhancing the surface downward flux (Stephens et al., 2015). Moreover, atmospheric absorption (e.g., from atmospheric water vapor) is also enhanced during the multiple-reflection process (Bellouin et al., 2020). The concept of critical surface albedo, which refers to the threshold albedo at which ADRE shifts from negative to positive, is important for both theoretical understanding of ADRE and aerosol satellite retrieval (Bellouin et al., 2020; Seidel & Popp, 2012; J. Haywood & Boucher, 2000).

1.5.3. Clouds

Clouds can impact the ADRE depending on their relative location with respect to aerosols (Bellouin et al., 2020; Myhre et al., 2020). Most anthropogenic aerosols are located in the boundary layer, where the solar radiation they receive is often obscured by clouds above. Therefore, the magnitude of all-sky ADRE is generally smaller than that of clear-sky ADRE (Myhre et al., 2020; Q. Yu & Huang, 2023b). However, in regions where absorbing aerosols are located above clouds (e.g., smoke aerosols above marine stratocumulus decks), the aerosol absorption is enhanced and can lead to a regional warming effect (Adebiyi & Zuidema, 2018; Redemann et al., 2021). Nevertheless, these situations only contribute to a small portion of ADRE on a global scale (Bellouin et al., 2020).

The complex interactions between aerosol properties, such as SSA, and environmental factors like clouds complicate the determination of their individual contributions to the ADRE, making it challenging to quantify the specific impacts of each factor on ADRE (Q. Yu & Huang, 2023b).

1.6. Impacts of ADRE

1.6.1 Regional and Global Climate Impacts of ADRE

Aerosols influence local climates by inducing cooling or warming, affecting temperature gradients and consequently impacting broader climate dynamics through dynamical processes like convection and precipitation and feedback mechanisms such as surface albedo feedback (Adebiyi & Zuidema, 2018; Z. Li et al., 2016; Schmale et al., 2021; Willis et al., 2018). This localized impact can ripple out to affect global climate systems in significant ways (Z. Li et al., 2016; Lei et al., 2020).

For example, in Asia, aerosols can modulate the amplitude, frequency, intensity, and phase of the Asia monsoon via many mechanisms such as increasing atmospheric stability, reducing the land-ocean thermal contrast, and inducing dynamical feedback processes (Z. Li et al., 2016). Aerosol also contributes to solar dimming over both South and East Asia, profoundly affecting the energy radiation budget, atmospheric circulations, precipitation patterns, and agriculture (Z. Li et al., 2016; Wild, 2009).

Similarly, the impact of the ADRE over the Arctic is complex but not well-constrained due to unique environmental conditions (Willis et al., 2018; Schmale et al., 2021). The Arctic experiences no sunlight for half the year, has surfaces that are often covered by sea ice and snow, and features low-level clouds that are frequently mixed-phase with pollution plumes transported into the area (McConnell et al., 2007; Schmale et al., 2021). These unique characteristics make the ADRE in this region particularly challenging to observe, understand, and represent in models (Willis et al., 2018). Absorbing aerosols in the Arctic free troposphere cool the surface while absorbing aerosol particles within the planetary boundary layer warm the surface (Schmale et al., 2021). Furthermore, mineral dust (and to some extent black carbon) deposited on a surface covered by snow and ice may substantially modify the surface albedo (J. Li et al., 2022). The surface albedo feedback triggered by ADRE can in turn impact aerosol emissions. For example, the retreating snow and sea ice can free soil and dusty regions, leading to more open ocean, allowing more socioeconomic activities, which in return allow more sea-salt, dust, and anthropogenic aerosol production (Schmale et al., 2021).

ADRE can change atmospheric circulation and induce surface temperature responses on a hemispheric scale (Yoshimori & Broccoli, 2008; H. Wang, Xie, Tokinaga, et al., 2016; Diao et al., 2021). The inhomogeneity of ADRE, including interhemispheric asymmetry (northern versus

southern hemisphere), latitudinal difference (tropical versus extratropical), and meridional differences (eastern versus western hemisphere), have led to energy transport and associated large-scale circulation changes (e.g., jet stream and Intertropical Convergence Zone shifts) (Yoshimori & Broccoli, 2008; H. Wang, Xie, Tokinaga, et al., 2016; Diao et al., 2021; J. Li et al., 2022). Volcanic and anthropogenic aerosols also play a role in the recent slowdown of global surface warming (D. M. Smith et al., 2016; J. Li et al., 2022).

The aerosol-radiation interactions can cause different feedbacks depending on aerosol types and locations. For example, there is a positive feedback between absorbing aerosols and the boundary layer (Li et al., 2017). As aerosols absorb heat, the surface cools while the atmosphere warms. This reduces the lapse rate and increases the likelihood of temperature inversions, which hinder the dispersion of pollutants, further stabilizing the atmosphere. This increased stability leads to greater aerosol accumulation, thereby amplifying the initial ADRE. Additionally, other feedbacks exist, such as enhanced warming caused by absorbing aerosols (dust, black carbon), which heat the middle troposphere over the Himalayan-Gangetic region and the Himalayan foothills. This intensifies the warming associated with the elevated heat pump effect, promoting a positive dynamical feedback (Lau et al., 2006).

1.6.2. Impact on Trace Gas Atmospheric Monitoring

To combat climate change, it is important to reduce greenhouse gas emissions, especially those from anthropogenic source sectors. Methane is a powerful greenhouse gas that has increased from 720 to 1800 ppb and has contributed 0.6 °C of global warming since pre-industrial times (Stocker et al., 2014). Satellites have the ability to identify strong point sources and quantify atmospheric methane concentrations on a regional and global scale. However, most satellites retrieve atmospheric methane using spectrally resolved backscattered solar radiation in the

shortwave near-infrared band (Jacob et al., 2016; Parker et al., 2020). The methane retrieval in the SWIR spectral range requires accurate knowledge of the lightpath through the Earth's atmosphere and the aerosol-radiation interaction can introduce biases during these processes (Aben et al., 2007; Y. Huang et al., 2020; Sanghavi et al., 2020).

Aerosol-radiation interactions, through direct scattering or absorption of insolation, can either lengthen or shorten the optical path relative to conditions without aerosols (Q. Yu et al., 2024; Y. Huang et al., 2020; Frankenberg et al., 2012). The net effect of neglecting aerosols in gas retrieval depends on various factors including aerosol optical characteristics, vertical distribution of aerosols, surface albedo, and solar and viewing angles (Aben et al., 2007; Frankenberg et al., 2012; Jacob et al., 2016).

GHGSat is a Canadian company that provides a precise, scalable, and economical method of measuring greenhouse gas (GHG) emissions from industrial facilities worldwide (Jervis et al., 2021). GHGSat operates a constellation of satellites with high spatial and spectral resolution. The FabryPérot (F–P) imaging spectrometer onboard GHGSat satellite can resolve methane absorption lines at around 1.65 μm (Jervis et al., 2021). The details of the GHGSat satellite parameters are listed in Table 1.2. To date, their CH4 retrievals have not included the effect of aerosol (Jervis et al., 2021; Q. Yu et al., 2024). Therefore, it is crucial to estimate and understand the errors induced by aerosol-radiation interactions in GHGSat's CH_4 retrievals under varying atmospheric conditions to help future generations of GHGSat-like instruments.

Table 1.2 Satellite parameters for GHGSat-D from Jervis et al. (2021)

Parameter	Value
Satellite mass	15 kg
Satellite dimensions	$20 \times 30 \times 40\,cm^3$
Payload dimensions	$12 \times 12 \times 25\,cm^3$
Launch date	21 June 2016
Orbit type	Polar, sun-synchronous
Local time at descending node	09:30
Altitude	514 km

1.7. ADRE Uncertainties

1.7. ADRE Uncertainties

Aerosols remain the largest source of uncertainty in determining the radiative forcing of the climate (Intergovernmental Panel on Climate Change, 2014). This uncertainty arises from various factors, including the inaccurate quantification of aerosol optical properties (AOD, SSA, and g) and environmental factors (such as surface albedo and cloud optical depth), incomplete knowledge of the spectral dependencies of aerosol scattering properties, oversimplifications of the aerosol vertical profile, and inaccurate estimations of the anthropogenic fraction of aerosols (Intergovernmental Panel on Climate Change, 2014; Stier et al., 2013; Thorsen et al., 2021; Q. Yu & Huang, 2023a). Sensitivity experiments indicate that SSA and the vertical distribution of absorbing aerosols are the major contributors to ADRE uncertainty (Intergovernmental Panel on Climate Change, 2014; Stier et al., 2013; Thorsen et al., 2021; Yu & Huang, 2023a). Discrepancies not only exist between model simulations and observations, but also between the ADRE calculations in different GCMs (Halthore et al., 2005; Randles et al., 2013; Stier et al., 2013; Q. Yu & Huang, 2023a). Despite significant advancements in global aerosol modeling, climate

models still report at least a 30% uncertainty in ADRE (Thorsen et al., 2021; Q. Yu & Huang, 2023a). This multi-model uncertainty depends on various factors: aerosol emissions and transport, assumed aerosol microphysical properties, aerosol radiative properties, representations of surface albedo and clouds, and the treatment of radiative transfer, including spectral resolution and molecular scattering (Randles et al., 2013; Thorsen et al., 2021; Q. Yu & Huang, 2023a). It is, therefore, crucial to dissect and identify the contributors to the inter-model spread in ADRE, which will help improve the models' ability to accurately constrain ADRE.

1.8. ADRE Quantifications

1.8.1. Tropospheric ADRE Quantifications

The classical single aerosol layer model (Charlson et al., 1991; Chlek & Coakley Jr, 1974; J. Haywood & Boucher, 2000) quantified ADRE using a straightforward formula. ADRE is expressed as a function of insolation, solar zenith angle, AOD, SSA, aerosol backscattering ratio, surface albedo, and cloud fraction (Charlson et al., 1991; J. Haywood & Boucher, 2000; Q. Yu & Huang, 2023b). This analytical relationship provides fundamental insights into the physical mechanisms behind ADRE and the nonlinear interactions between aerosol-related and environmental variables. However, this analytical approach overlooks the wavelength dependency of AOD, assumes a thin layer of aerosol concentration near the surface, and does not account for multiple scattering processes (Charlson et al., 1991; J. Haywood & Boucher, 2000; Bellouin et al., 2020).

To calculate ADRE accurately, a comprehensive set of aerosol optical properties is required, along with detailed radiative transfer calculations (H. Yu et al., 2006; Q.-R. Yu et al., 2019). Model settings such as plane-parallel radiative transfer, the number of streams, and spectral resolution, along with assumptions about aerosol mixing and the Henyey-Greenstein phase

function, can introduce uncertainties into ADRE calculations (Jacobson, 2001; Toublanc, 1996; Wiscombe & Grams, 1976). Even with accurate ADRE calculated, the impact of individual contributors and their sensitivity to those contributors still remains unclear, especially on a global scale (Thorsen et al., 2020; Q. Yu & Huang, 2023b).

1.8.2. Stratospheric ADRE Quantifications

Quantifying Stratospheric ADRE can be challenging due to the limited sampling of aerosols in the stratosphere, the difficulty in accurately identifying the tropopause, and the complexity associated with various aerosol species (Andersson et al., 2015; Friberg et al., 2023; Kremser et al., 2016; Ohneiser et al., 2023). To address these issues, many studies simplify the calculation by assuming a linear relationship between stratospheric ADRE and stratospheric Aerosol Optical Depth (AOD), typically applying a fixed scaling factor (Hansen et al., 2005; Schoeberl et al., 2023, 2024a; P. Yu et al., 2023). This approach, while reducing computational complexity, overlooks the nuances of aerosol interactions.

As mentioned before, ADRE is influenced not just by aerosol properties but also by environmental conditions (Q. Yu & Huang, 2023a). Neglecting these factors can introduce potential biases, even in the case of stratospheric ADRE. Clouds, for example, can modify the solar radiation pathway, affecting both the scattering and absorption processes of aerosols above them, and thus altering the net radiative effect (Andersson et al., 2015; Kremser et al., 2016; Ohneiser et al., 2023). These interactions can vary significantly depending on the geographic location, season, and current climatic conditions, suggesting that a one-size-fits-all approach might not be sufficient.

1.9. Outstanding Questions

The modeling of aerosol optical properties is challenging due to their diverse sizes, concentrations, shapes, compositions, and the chemical and physical processes they undergo. Additionally, the interactions between aerosol physical properties (e.g., aerosol optical properties and vertical distributions) and the surrounding environment (e.g., clouds) make it difficult to disentangle the characteristics, the dominant factors, and the uncertainties in ADRE. As climate change progresses, understanding the ADRE trend and its associated climate impact becomes crucial for future climate projections and policymaking. Moreover, ADRE uncertainty (e.g., inter-model spread) needs to be reduced for better analysis of climate forcing and feedback. With increased wildfire and discussion about stratospheric geoengineering, more attention should be paid to stratospheric ADRE. Furthermore, to improve monitoring of greenhouse gas emissions, particularly from super emitters like heavily polluted industrial sites, it is essential to account for aerosol-radiation interactions.

Thus, this thesis begins with an exploration of the fundamental physics behind ADRE and then extends this knowledge to practical applications. The research presented in this thesis is guided by four pivotal yet unresolved questions:

1. How do aerosol and environmental variables contribute to the distribution and trends in ADRE, and what is the extent of their individual contributions?

2. What causes the discrepancies in ADRE across different GCMs as observed in the Coupled Model Intercomparison Project CMIP6?

3. How can stratospheric ADRE be quantified both efficiently and accurately?

4. How do aerosol-radiation interactions affect methane monitoring by GHGSat, and how can their impacts be mitigated?

1.10. Dissertation Outline

Following the questions above, this thesis is organized into six chapters as follows:

Chapter 2 discusses the distributions and trends of the ADRE from 2000 to 2020. A regression model is proposed to quantify the clear-sky and all-sky ADREs and to separate the contributions of aerosol-related and environment-related factors to the spatial distributions and trends for the ADRE and the poleward energy transport driven by it. This regression framework has been validated against radiative transfer calculations and will continue to be carried out in Chapters 3 and 4 for ADRE representations. This chapter has been published in the Journal of Geophysical Research: Atmosphere (Q. Yu & Huang, 2023b).

Chapter 3 analyzes the inter-model spread of ADRE among the GCMs of CMIP6 using the regression method. Contributions from the differences in state variables and the radiative sensitivity are separately quantified and compared. This chapter has been published in Geophysical Research Letters (Q. Yu & Huang, 2023a).

Chapter 4 provides a comprehensive set of radiative kernels for stratospheric ADRE for the first time. Kernels developed here include both broadband and spectral band-by-band TOA flux kernels provided on conventional latitude-longitude-month grids, as well as physically sorted broadband kernels whose values are determined from regression models. The developed aerosol radiative kernels are validated as effective in assessing the stratospheric ADRE of different aerosol types. This chapter is under review in the Journal of Geophysical Research: Atmosphere.

Chapter 5 investigates the impacts of aerosol-radiative interaction on GHGSat methane retrieval and conducts simultaneously AOD and methane retrieval using the multi-angle viewing method under different aerosol optical properties, surface albedo, and satellite zenith angle conditions. This chapter has been published in Atmospheric Measurement Techniques (Q. Yu et al., 2024).

Chapter 6 summarizes the main conclusions of this dissertation and discusses the future research plan.

Chapter 2 Distributions and Trends of the Aerosol Direct Radiative Effect in the 21st Century: Aerosol and Environmental Contributions

This Chapter is a reprint of the published article in Journal of Geophysical Research: Atmospheres.

Yu, Q., & Huang, Y. (2023). Distributions and trends of the aerosol direct radiative effect in the 21st century: Aerosol and environmental contributions. *Journal of Geophysical Research: Atmospheres*, 128, e2022JD037716.

DOI: https://doi.org/10.1029/2022JD037716

The thesis author is the lead author and principal investigator for this paper.

Distributions and Trends of the Aerosol Direct Radiative Effect in the 21st Century: Aerosol and Environmental Contributions

Qiurun Yu[1], Yi Huang[1]

[1] Department of Atmospheric and Oceanic Sciences, McGill University, Montreal, Quebec, Canada.

Corresponding author: Qiurun Yu (qiurun.yu@mail.mcgill.ca)

Key Points:

- Nonaerosol factors contribute significantly to the spatial inhomogeneity of the aerosol direct radiative effect (ADRE) and its trends in recent decades
- The hemispheric difference in scattering aerosols drives northward cross-equator energy transport, which shows a declining trend
- Changes in the surface albedo due to sea ice melt strongly influence the ADRE trends in, and the energy transport to, the Arctic

Abstract

The aerosol direct radiative effect (ADRE) is controlled by both aerosol distributions and environmental factors, making it interesting and important to quantitatively assess their effects on the ADRE inhomogeneity and climate trends. By analyzing the ADRE in the 21st century from a global reanalysis data set, we find that the spatial variability of the ADRE and its trends can be well explained by a linear regression model. In this model, scattering and absorbing aerosol optical depths (AODs) are used, along with critical environmental variables such as surface albedo and cloud radiative effect, as predictors. Based on this model, we find that approximately 70% of the ADRE inhomogeneity is due to the AOD distributions and the remainder is attributable to environmental factors. This study also shows that a stronger cooling effect of the scattering aerosols in the Northern Hemisphere drives northward cross-equator meridional energy transport, although this transport exhibits a declining trend over the last two decades. The changes in surface albedo and cloud radiative effect strongly influence the trends in the regional ADRE and the meridional energy transport driven by them. In particular, the reduction of surface albedo (sea ice) is primarily responsible for the enhancement of the cooling ADRE, as well as an associated trend in meridional energy transport, in the Arctic.

Plain Language Summary

Aerosols are particles produced by natural events such as volcanic eruptions and anthropogenic emissions such as fossil fuel combustion. They can scatter and absorb incoming solar radiation, leading to a strong local cooling or warming effect on the Earth's climate. The impact of aerosols on the Earth's radiative balance is known as the aerosol direct radiative effect (ADRE). Factors that can affect ADRE include the types and amounts of aerosols and the environmental conditions such as surface albedo and clouds. This study proposed a regression

model to predict the distributions and trends of global ADRE. According to the results, 70% of the ADRE variability is contributed by aerosols, while the rest is influenced by surface albedo and clouds. The high aerosol concentrations in the Northern Hemisphere require energy to be transported from the South Hemisphere to the North. However, this demand has decreased over the past two decades. Changes in surface albedo and clouds have a significant impact on the ADRE trend. In particular, the retreating sea ice plays a major role in the ADRE trend in the Arctic.

2.1 Introduction

The Aerosol Direct Radiative Effect (ADRE) affects the planet's energy balance and hence the average temperature of Earth's climate. The effect is caused by aerosols, which are microscopic particles suspended in the atmosphere that are chemically highly variable. These particles are emitted both by natural events such as sea spray, volcanic eruptions, wildfires, and dust storms and by anthropogenic sources such as fossil fuel combustion and agricultural activities. Aerosols can scatter and absorb solar (shortwave) radiation, leading to a strong cooling or warming effect on the radiation energy budget (Q.-R. Yu et al., 2019). This effect is known as the ADRE, as it does not involve atmospheric adjustments. To determine the ADRE, radiative transfer models require aerosol optical properties obtained from ground-based measurements, satellite observations, or model simulations (Bellouin et al., 2020; Thorsen et al., 2020; Loeb et al., 2021; X. Wu et al., 2021). The quantification of the ADRE has improved significantly over the past decades (H. Yu et al., 2006; McComiskey et al., 2008; Peters et al., 2011; Willis et al., 2018; Bellouin et al., 2020; Loeb et al., 2021), although it still remains a contributor to the uncertainty in climate forcing (Pörtner et al., 2022).

The sign and strength of the ADRE depend on aerosol and environmental state variables such as aerosol optical depth (AOD), relative humidity, surface albedo, and the solar zenith angle.

Yu et al. (2006) investigated the distribution of the clear-sky global ADRE for March–May, finding a correlation between the patterns of the ADRE and AOD. For example, AOD as high as 0.8 in East Asia results in a top-of-atmosphere (TOA) cooling of more than -10 Wm^{-2}, and this cooling can extend as far as the northern Pacific. Besides aerosol emissions, atmospheric relative humidity can affect the ADRE by changing the microphysical structures of aerosols and thus their optical properties. Zhang et al. (2008) found that soot particles coated with sulfuric acid acquire large hygroscopic size and mass growth at subsaturated conditions (<90% relative humidity), causing a tenfold increase in their scattering and a twofold increase in their absorbing effect. Unlike relative humidity, surface albedo affects the ADRE without changing the aerosol chemical compositions and microphysical structures. Many studies have shown that the ADRE changes nonlinearly with surface albedo. For example, McComiskey et al. (2008) studied the ADRE uncertainty due to measurement uncertainties in aerosol optical properties, surface albedo, and solar geometry. In their study, the ADRE varies linearly with AOD but nonlinearly with surface albedo. Based on the Aerosol Robotic Network (AERONET) observations, Yoon et al. (2019) empirically determined how the ADRE varies with surface albedo. According to their study, the radiative forcing efficiency of biomass-burning aerosols can switch from negative to positive depending on the surface type. These results are consistent with the "critical single scattering albedo" concept, which describes how the ADRE switches from net cooling to net warming at a certain value of single scattering albedo (SSA), depending on surface albedo (Chlek & Coakley Jr, 1974; Lenoble et al., 1982). The solar zenith angle is another important environmental state variable that determines the ADRE. Yu et al. (2019) mentioned that the ADRE first decreases and then increases with the increase in the solar zenith angle due to a competition between the increased light path and the decreased solar energy. The above studies have demonstrated that the clear-sky

ADRE depends not only on aerosol distributions but also on environmental variables including relative humidity, surface albedo, and the solar zenith angle.

In addition to the environmental variables mentioned above, clouds have been found to have a significant impact on the ADRE. The ADRE is generally less negative (cooling) in all-sky conditions than in clear-sky conditions, since the amount of solar radiation aerosols interact with is reduced by reflective clouds (Bellouin et al., 2020). In some studies, the all-sky ADRE is approximated by scaling the clear-sky ADRE with the clear-sky fraction ($ADRE_{all} = ADRE_{clr}$ (1 - f), where f is the cloud fraction; (Quaas et al., 2008; Su et al., 2013). Cloud cover, however, is not the only factor determining the all-sky ADRE. Aerosol absorption and their vertical location relative to clouds are also important. The absorption of aerosols above clouds may result in a strong positive ADRE (Chand et al., 2009), while the ADRE is considerably weaker when aerosols are located below clouds (Takemura et al., 2002). Some observations and model simulations have focused on the Southeastern Atlantic where absorbing biomass-burning aerosols often lie above bright marine stratocumulus clouds, causing net warming of the regional climate (Peters et al., 2011; Adebiyi & Zuidema, 2018; Redemann et al., 2021). Cloud optical depth (COD) is another environmental state variable that affects the all-sky ADRE. Thorsen et al. (2020) calculated the ADRE radiative kernels for aerosol optical properties, surface albedo, and cloud fraction. Their results show that the all-sky ADRE kernels are more sensitive to AOD, asymmetry factor, and surface albedo in the case of thin cloud ($COD < 2$) than thick cloud ($COD \geq 2$). Myhre et al. (2020) found the interaction of aerosols with clouds is important for determining the strength of the all-sky shortwave ADRE. These studies indicate that a variety of factors can impact the effect of clouds on the ADRE, making it important to determine the global extent of this influence and whether it can be predicted based on cloud properties.

This study aims to develop an analytical model that can explain the global distributions and variations of the ADRE under both clear- and all-sky conditions and to elucidate how aerosols and environmental state variables are tied together to influence the ADRE. Previous theoretical work has established a quantitative relationship between the ADRE and aerosol properties. For example, Charlson et al. (1991) developed a global model to estimate the TOA ADRE for sulfate. The analytical model is, however, limited to simplified assumptions such as optically thin sulfate aerosol layers and no regional variations in surface albedo and atmospheric transmittance. There are also conceptual models built based on the regional ADRE. Using satellite observation data, Quaas et al. (2008) divided the 60 S–60 N region into 14 regions and linked the planetary albedo change (ΔP) due to the ADRE to log(AOD), although it was unclear whether this logarithmic relationship applies to the high latitudes. Chen et al. (2022) fitted satellite-retrieved radiative fluxes to an exponential function of AOD over the 20–40 N region according to the Beer-Lambert law, but this is also a regional ADRE study and does not apply to cloudy sky conditions. With the development of the global aerosol data sets (H. Yu et al., 2006; Myhre et al., 2013; Gueymard & Yang, 2020), it is important to quantify the degree to which aerosol and environmental variables contribute to the distribution and variation of the ADRE worldwide.

An analytical model of the global ADRE can also facilitate the analyses of aerosol-induced poleward energy transport (PET) and circulation changes. As the atmospheric circulations are fundamentally driven by the uneven distribution of radiation energy, aerosols, as well as greenhouse gases (GHGs), strongly influence the circulation by modulating the radiation distribution pattern (e.g., Huang and Zhang 2014; Merlis 2015). Many studies have indicated that aerosols can induce regional climate responses. Using a slab ocean model, Yoshimori and Broccoli (2008) demonstrated that sulfate aerosols and black carbon can cause shifts in the Intertropical

Convergence Zone (ITCZ). Based on CMIP5 models, Wang, Xie, and Liu (2016) identified the climate response patterns of aerosol radiative forcing versus the change in GHG emissions. Their findings indicate that aerosol-induced negative radiative forcing in the Northern Hemisphere requires a cross-equatorial Hadley circulation to compensate for interhemispheric energy imbalances. Wang, Xie, Tokinaga, et al. (2016) detected a robust change in the zonal mean cross-equatorial wind over the twentieth century, and they considered this wind change as a fingerprint of anthropogenic aerosol forcing. By separating the fossil-fuel-related aerosol forcing in different Hemispheres, Diao et al. (2021) concluded that the aerosol forcing in Western Hemisphere, located in the extratropics, drives a northward shift of the Hadley cell, while the aerosol forcing in Eastern Hemisphere, located near the tropics, drives an equatorward shift of the Northern Hemisphere jet stream. The extensive research on this subject emphasizes the importance of ascertaining what physical factors govern the inhomogeneity of the ADRE and thus the resulting changes in atmospheric circulations.

Besides identifying the key variables that influence the ADRE distributions globally, this study also aims to understand how changes in these variables, including those related to the environment, influence the trend in ADRE patterns and the atmospheric circulation driven by the radiation inhomogeneity. Although no significant trend in the global mean ADRE was detected since 2002 (Loeb et al., 2021), there are significant regional trends. For example, the ADRE has become less strong (negative) over China, the United States, South America, and Europe, but stronger over India. Apart from the impact of the AOD and solar radiation trends (Boers et al., 2017; Streets et al., 2006), few studies have addressed the impact of environmental changes (e.g., surface albedo change) on the ADRE trend. The sea ice loss and land use changes (e.g., Amazonian deforestation) have led to significant changes in surface albedo (Pistone et al., 2014; Lejeune et

al., 2015). Meanwhile, the regional cloud cover also changes in response to global warming (Sfîcă et al., 2021; Zhong et al., 2021). Given the importance of these environmental variables for the ADRE, it is important to understand how the changes in these variables affect the ADRE trend.

This study aims to connect the distribution and trends in the ADRE to those in the aerosol and environmental variables on a global scale. A regression model is proposed to quantify the clear-sky and all-sky ADREs and to determine their sensitivity to key aerosol and environmental variables that govern the inhomogeneous ADRE spatial patterns. This conceptual model affords a straightforward means for determining how the changes of these key variables would change the ADRE. It can also help infer the energy transport and circulation changes due to the ADRE. Furthermore, this study separates the contributions of aerosol and environmental variables to aerosol-induced poleward energy transport and its trend in the 21st century. The data and method used to estimate the ADRE and its trend are described in Section 2.2. Section 2.3 examines the relative contributions of key variables to the distribution of global ADRE, as well as the ADRE sensitivities to these variables. Aerosol-induced PET is decomposed into different physical processes in Section 2.4. Section 2.5 discusses how the trends in the ADRE are related to the trends in the key variables over the 21st century. In Section 2.6, a summary of the findings is provided.

2.2 Data and Method

2.2.1 Aerosol and Meteorological Data Sets

This analysis is built on the aerosol and radiation diagnostics and meteorological fields from the Modern-Era Retrospective analysis for Research and Applications, Version 2 (MERRA-2) data set. The MERRA-2 aerosol simulation is performed by the Goddard Chemistry, Aerosol, Radiation, and Transport model (Chin et al., 2002). The assimilated AOD products include observations from ground-based (AERONET) and satellite (MODIS, MISR, and AVHRR)

measurements (Randles et al., 2017). The MERRA-2 diagnostics total aerosol products include major aerosol types of sulfate, dust, black carbon, organic carbon, and sea salt. The hygroscopic growth process is parameterized as a function of ambient relative humidity (Chin et al., 2002, 2004). Many studies have shown that MERRA-2 aerosol products are consistent with aircraft, in situ, and satellite observations (Buchard et al., 2017; Gueymard & Yang, 2020).

The analysis is conducted for the period from 2000 to 2021 to avoid the perturbations in aerosol concentrations caused by the volcanic eruptions in the 1980s and 1990s as well as the changes in the MERRA-2 observing system. Previous studies have shown that MERRA-2 aerosol data become more reliable and consistent after 2000, when Earth Observation System data (e.g., MODIS on Terra and Aqua, and MISR) are assimilated (Korras-Carraca et al., 2021). The spatial resolution of the data used is 2.5° × 2.5°, while the temporal resolution is 1 hour.

The ADRE is the difference in radiative fluxes with and without aerosols. The TOA net fluxes from MERRA-2 are available in all-sky conditions, including clear-sky no aerosol, clear-sky, all-sky no aerosol, and all-sky conditions. Therefore, the instantaneous clear-sky and all-sky ADREs can be calculated from these fluxes:

$$\mathrm{ADRE_{clr}(hour)} = \mathrm{F_{clr}^{net}(hour)} - \mathrm{F_{clr,cln}^{net}(hour)} \tag{2.1}$$

$$\mathrm{ADRE_{all}(hour)} = \mathrm{F_{all}^{net}(hour)} - \mathrm{F_{all,cln}^{net}(hour)}, \tag{2.2}$$

where F is the net shortwave flux (downward positive) at the TOA, $\mathrm{F_{clr}^{net}}$ and $\mathrm{F_{all}^{net}}$ are for clear- and all-skies with aerosols, and $\mathrm{F_{clr,cln}^{net}}$ and $\mathrm{F_{all,cln}^{net}}$ are for clear and all skies without aerosols. Subscript cln denotes clean conditions, and hour indicates the hourly average data at a given time. Since the ADRE does not exist during the night, the climatological mean ADRE can be calculated as follows:

$$\mathrm{ADRE} = \frac{1}{\mathrm{days}} \sum_{\mathrm{days}} \frac{1}{24\mathrm{hours}} \int_{\mathrm{sunrise}}^{\mathrm{sunset}} \mathrm{ADRE}(\mathrm{hour})\mathrm{d}(\mathrm{hour}) \quad (2.3)$$

Note that the ADRE values analyzed here are averaged over a full diurnal cycle, as opposed to only during daytime.

2.2.2 The Selection of Predictors

A conceptual model of aerosol-radiation interaction is built based on Charlson et al. (1991). Assuming an optically thin reflective aerosol layer in the boundary layer, they proposed the TOA $\mathrm{ADRE_{clr}}$ as follows:

$$\mathrm{ADRE_{clr}} = -\mathrm{TISR} \cdot \Delta \mathrm{P} = -\mathrm{TISR} \cdot \mathrm{T_{at}^2} \, (\mathrm{R_{as}} - \mathrm{alb}), \quad (2.4)$$

where TISR is the TOA incoming solar radiation, ΔP is the planetary albedo change caused by aerosols, $\mathrm{T_{at}}$ is the atmospheric transmittance, $\mathrm{R_{as}}$ is the combined reflectance of the aerosol layer and the Earth's surface, and alb is the surface albedo. Following Haywood and Boucher (2000), the ADRE can be further expressed as follows:

$$\mathrm{ADRE_{clr}} = -\mathrm{TISR} \cdot \mathrm{T_{at}^2} \cdot \beta \cdot \mathrm{SSA} \cdot \mathrm{AOD} \cdot \sec\theta \frac{(1-\mathrm{alb})^2 - \frac{\mathrm{alb}(1-\mathrm{SSA})}{\beta}\left[\frac{2-\mathrm{AOD}\cdot\sec\theta}{\mathrm{SSA}} - \mathrm{AOD}\cdot\sec\theta(2\beta-1)\right]}{1-\mathrm{alb}\cdot\mathrm{AOD}\cdot\sec\theta\cdot\beta\cdot\mathrm{SSA}} \quad (2.5)$$

In the equation above, several parameters are considered to influence the ADRE. Among them, the aerosol-related parameters are AOD, SSA, and the backscattering ratio (β). The backscattering ratio is the ratio of the radiation energy reflected to space to the energy scattered in all directions. It is important to note that β is not only affected by the aerosol but also affected by the solar geometry (Wiscombe & Grams, 1976). The environment-related parameters are the solar zenith angle (θ), TISR, $\mathrm{T_{at}}$, and alb. Although the above expression was derived based on a simplified representation of radiative transfer, it suggests that it is possible to select a few key

parameters to represent the aerosol–radiation interaction processes and to quantify the ADRE accordingly.

Selecting the predictive variables is an essential step in building a multivariate linear regression model that captures the variations in the ADRE. The selection criterion needs to balance between maximizing explained ADRE variance and minimizing the number of predictors (principle of parsimony). Predictors are chosen based on the conceptual model of Equation 2.5. First, to disentangle covariabilities between the ADRE and incident solar radiation, the regression model is formulated to predict the planetary albedo change due to aerosols ($\frac{\mathrm{ADRE}}{\mathrm{TISR}}$). To measure the reflection of the aerosol layer, SAOD is included as a predictor. To account for the multiple scattering between the aerosol layer and the underlying surface, $\mathrm{SAOD} \cdot \mathrm{alb}$ is selected as a predictor. The solar zenith angle affects not only the length of the path that light travels in the atmosphere but also the aerosol backscattering ratio, so it is also considered. Furthermore, because aerosols absorb radiation and this effect is highly sensitive to the surface albedo, the aerosol absorption effect is represented by $\mathrm{AAOD} \cdot \mathrm{alb}$.

Considering the complexity of the cloud-induced ADRE, this paper examines clear-sky and all-sky ADREs separately. Shortwave cloud radiative effect (CRE) is used for all-sky situations based on the findings of other studies showing that CRE is a good predictor of both shortwave and longwave radiative forcing (Y. Huang et al., 2016; Myhre et al., 2020; Balmes & Fu, 2021). This predictor is expressed as $\mathrm{SAOD} \cdot \frac{\mathrm{CRE}}{\mathrm{TISR}}$ to better represent the aerosol-cloud radiative interactions. These predictor variables are chosen despite their correlations because the form of the prediction model reflects physical laws governing the ADRE, which varies nonlinearly with these key aerosol and environmental variables.

To abide by the principle of parsimony, many other factors that influence the ADRE to a lesser extent or are not independent from the above-selected predictors are omitted. For example, the relative humidity is important for hydrophilic aerosols like sulfate because they absorb water and grow, thereby enhancing their optical properties. This analysis uses the optical properties (e.g., SAOD and AAOD) of five major aerosol species whose values have been simultaneously adjusted based on the appropriate relative humidity conditions in the MERRA-2 data set. Therefore, the effect of relative humidity has already been included in the covarying aerosol optical properties. The effects of SSA are considered by separating SAOD and AAOD, so it is not necessary to include it in the regression model. Despite the known sensitivity of the ADRE to aerosol asymmetry factor (McComiskey et al., 2008; Su et al., 2013), its effect is found to be small in explaining the globe inhomogeneity in the ADRE (less than 0.1% according to our study). The effect of cloud fractions has been included in the CRE term, so this study does not consider it separately. Furthermore, although other environmental variables such as ozone and water vapor have been linked to regional ADREs (e.g., Stubenrauch et al. 2013; Gharibzadeh, Bidokhti, and Alam 2021), they are less representative than the above-selected predictors and the regression model does not improve with their addition. As a result, they are not considered in the regression model. Interested readers can find a summary of various candidate variables we have tested in Tables S2.1–S2.3 in Appendix A.

In summary, the choice of the predictors in our prediction model is guided by a physical model (Equation 2.5) and its prediction ability is statistically evaluated. The following aerosol-related and environment-related predictors are selected: scattering aerosol optical depth (SAOD), scattering aerosol optical depth × surface albedo (SAOD · alb), absorbing aerosol optical depth × surface albedo (AAOD · alb), cosine solar zenith angle ($\cos\theta$), and scattering aerosol optical depth

× cloud shortwave radiative effect (normalized by TISR; $\mathrm{SAOD} \cdot \frac{\mathrm{CRE}}{\mathrm{TISR}}$). The predictands are the TOA ADRE normalized by incoming solar radiation in clear-sky and all-sky conditions ($\frac{\mathrm{ADRE_{clr}}}{\mathrm{TISR}}$ and $\frac{\mathrm{ADRE_{all}}}{\mathrm{TISR}}$), respectively.

2.2.3 The Regression Model

A multivariate regression model for the global ADRE distribution is formulated as follows:

$$\frac{\mathrm{Y(i,j)}-\overline{\mathrm{Y}}}{\overline{\mathrm{Y}}} = \sum_{\mathrm{k=1}}^{\mathrm{n}} \mathrm{A_k} \frac{\mathrm{X_k(i,j)}-\overline{\mathrm{X_k}}}{\overline{\mathrm{X_k}}}, \tag{2.6}$$

where i and j represent latitude and longitude, X are predictors (e.g., SAOD) and n is the number of predictors. A_k is the regression coefficient, which represents the sensitivities of the predictor X_K to Y. Y is the predictand, and it can either be the clear-sky or all-sky ADRE normalized by insolation ($\frac{\mathrm{ADRE}}{\mathrm{TISR}}$). The global mean value is denoted by a bar. To better represent the spatial distribution anomaly, both predictors and predictands are normalized by their global mean values. Therefore, it is a combination of all these anomalies in the predictors that leads to anomalies in the ADRE. Calculating regression coefficients A_k requires finding the weighted least squares solution by minimizing $\sum_{\mathrm{I,j}} \mathrm{W_i} \left(\frac{\mathrm{Y(I,j)}-\overline{\mathrm{Y}}}{\overline{\mathrm{Y}}} - \sum_{\mathrm{n}} \mathrm{A_k} \frac{\mathrm{X_k(I,j)}-\overline{\mathrm{X_k}}}{\overline{\mathrm{X_k}}} \right)^2$, where $\mathrm{W_I}$ is the cosine of the latitude of each sample.

One advantage of this regression model is it can capture the nonlinear radiative interactions between aerosols and the environment (e.g., AOD and surface albedo). The validation of the regression model against the radiative transfer model can be found in Figure A1 in Appendix A. Another advantage of this regression model is that it effectively provides a "recipe" for constructing the global ADRE and enables a comparison of the relative importance of the different predictors. This regression model is also simple to be incorporated in energy balance models,

allowing us to link the variations in the predictors to the changes in the atmospheric circulation in response to the ADRE changes.

One potential disadvantage of the linear regression method is that the radiative sensitivity determined may be subject to inaccuracies caused by the correlated variations (collinearity) of the predictor variables, for example, caused by the coemitted scattering and absorbing aerosols or black carbon depositions on snow. However, through a test with idealized covariations of AAOD and SAOD (Figure A2 in Appendix A) and also by comparing to results obtained from a different regression technique addressing the collinearity impacts (Figure A3 in Appendix C S2), we find the sensitivities of the ADRE to key aerosol-related and environmental-related variables robustly quantified.

This study uses the 22-year climatological mean ADRE data (Equation 2.3) to construct the regression model. The global mean $\overline{X}$ and $\overline{Y}$ values are listed in Table 1. It is worth mentioning that the values of *A* are not sensitive to the chosen study period. As we have tested this regression model over different study periods, the regression coefficients show similar values.

To compare the relative importance of different predictors to the ADRE, a standardized regression coefficient (coef) is calculated by adjusting each regression coefficient according to a ratio of sample standard deviations (Siegel, 2016). Thus, the values of the standardized regression coefficients can be directly compared to determine their relative importance.

$$\mathrm{coef_k} = \mathrm{A_k}\frac{\mathrm{std(X_k \cdot TISR)}}{\mathrm{std(ADRE)}}, \tag{2.7}$$

where $\mathrm{std(X_k \cdot TISR)}$and $\mathrm{std(ADRE)}$ are the standard deviations of predictors and the predictand. The relative contributions of each predictor to the change in the ADRE explained by the regression model are further evaluated using

$$\mathrm{rela}_{\mathrm{contrib}_k} = \frac{(\mathrm{coef}_k)^2}{\sum_{k=1}^{n}(\mathrm{coef}_k)^2} \cdot R^2, \tag{2.8}$$

where the coefficient of determination (R^2) is the percentage of the ADRE variance that the regression model explains.

Table 2.1 Climatological Global Mean Values of the Parameters Used in the Regression Models

$\overline{X}$					$\overline{Y}$	
$\overline{SAOD}$	$\overline{\cos\theta}$	$\overline{SAOD \cdot alb}$	$\overline{AAOD \cdot alb}$	$\overline{SAOD \cdot \frac{CRE}{TISR}}$	$\overline{\frac{ADRE_{clr}}{TISR}}$	$\overline{\frac{ADRE_{all}}{TISR}}$
0.13	0.25	0.02	1.1×10^{-3}	-0.02	-9.86×10^{-3}	-4.36×10^{-3}

Note. The standard units are used: ADRE, TISR, and CRE in Wm^{-2}; SAOD, AAOD, alb, and $\cos\theta_{I,j}$ are dimensionless.

2.2.3.1 The clear-sky ADRE

For the $ADRE_{clr}$, the regression model is constructed as follows:

$$\frac{\frac{ADRE_{i,j}^{clr}}{TISR_{i,j}} + 9.86\times10^{-3}}{-9.86\times10^{-3}} = A_1 \frac{SAOD_{i,j} - 0.13}{0.13} + A_2 \frac{\cos\theta_{i,j} - 0.25}{0.25} + A_3 \frac{(SAOD\cdot alb)_{i,j} - 0.02}{0.02} + A_4 \frac{(AAOD\cdot alb)_{i,j} - 1.1\times10^{-3}}{1.1\times10^{-3}} \tag{2.9}$$

when regressed with the climatological mean values of all the predictor variables in their standard units (ADRE and TISR in Wm^{-2}; SAOD, AAOD, alb, and $\cos\theta_{I,j}$ are dimensionless), the regression coefficients A_1 to A_4 take the values of 1.40, -0.94, -0.27 and -0.20, respectively.

The four predictor terms on the right-hand side of Equation 2.9 represent the key physical processes that control the sign and strength of the $ADRE_{clr}$ over the globe. The SAOD term is a proxy for the aerosol single scattering effect, which measures the solar radiation directly scattered to space by the aerosol layers. Positive A_1 indicates that an increase in SAOD leads to an increase in the strength of the negative ADRE, resulting in a stronger cooling effect (more negative ADRE) on the planet. The $AAOD \cdot alb$ term provides a measure for aerosol absorption. Negative A_4 indicates the aerosol absorption process tends to reduce the photons reflected over a bright surface, thereby reducing the negative ADRE (a warming effect). The $SAOD \cdot alb$ term is a proxy for aerosol-surface multiple scattering effects, which also increase energy loss due to surface or atmospheric absorption. Hence, negative A_3 indicates an increase in $SAOD \cdot alb$ making the ADRE less negative. As for the $\cos\theta$ term, it determines the effective AOD encountered by incident radiation in different solar geometry conditions and also affects the aerosol backscattering ratio β. The smaller the $\cos\theta$ (the higher the latitude), the longer the light path and the more photons are scattered back to space at a smaller scattering angle (as aerosol particles tend to scatter more to the "forward" direction), leading to a more negative ADRE.

2.2.3.2 The all-sky ADRE

Apart from the four predictors mentioned above, $SAOD \cdot \frac{CRE}{TISR}$ term is added to represent the effect of clouds through the aerosol-cloud radiative interactions. Therefore, the regression model for the $ADRE_{all}$ becomes:

$$\frac{\frac{ADRE_{i,j}^{all}}{TISR_{i,j}}+4.36\times10^{-3}}{-4.36\times10^{-3}} = A_1\frac{SAOD_{i,j}-0.13}{0.13} + A_2\frac{\cos\theta_{i,j}-0.25}{0.25} + A_3\frac{(SAOD\cdot alb)_{i,j}-0.02}{0.02} +$$

$$A_4\frac{\left(SAOD\cdot\frac{CRE}{TISR}\right)_{i,j}+0.02}{-0.02} + A_5\frac{(AAOD\cdot alb)_{i,j}-1.1\times10^{-3}}{1.1\times10^{-3}} \quad (2.10)$$

When regressed with the climatological mean global distributions of the $ADRE_{all}$, A_1-A_5 take these values: 3.08, -0.42, -0.74, -0.98 and -0.29, respectively.

Similar to the clear-sky regression model, Equation 2.10 quantifies the effect of each anomaly term on the spatial inhomogeneity in the normalized ADRE ($\frac{ADRE_{I,j}^{all}}{TISR_{I,j}}$). A thicker cloud or a larger cloud fraction, represented by a larger CRE, tends to reduce the strength of the $ADRE_{all}$. Therefore, the sensitivity of $SAOD \cdot \frac{CRE}{TISR}$ to the all-sky ADRE is negative. The sensitivities of ADRE to other predictors (the regression coefficients) in all-sky conditions have the same sign as that of the clear-sky conditions, but are generally weaker. This is due to the cloud masking effect, which reduces the amount of radiation that interact with aerosols.

2.3 Aerosol Direct Radiative Effects

2.3.1 The Spatial Distribution of Predictors and Predictands

Figures 2.1a and 2.1b show the climatological mean clear-sky and all-sky ADREs from 2000 to 2021 at TOA from the MERRA-2 data set, which vary significantly between regions in both sign and magnitude. Globally, aerosols cool the planet by −3.41 W m^2 in clear-sky conditions and −1.64 W m^2 in all-sky conditions, which are consistent with those of other studies (e.g., Thorsen et al. 2020). This can be attributed to many factors, including the vast differences between aerosol emissions and the prevailing aerosol types. Over heavy aerosol loading regions such as East China, Indo-Gangetic Plain, and their adjacent areas, a strong negative ADRE is caused by the anthropogenic sulfate, carbonaceous, and dust aerosols. In regions affected by seasonal biomass-burning (e.g., central Africa and South America), organic and black carbon aerosols result in a slightly negative ADRE. Additionally, carbonaceous aerosols in central Africa are transported westward to the Southeast Atlantic, resulting in a negative ADRE. Over remote oceanic regions,

the presence of sea salt aerosols is responsible for the negative ADRE values. The climatological AOD for different aerosol species can be found in Figure A4 in Appendix A. Another factor contributing to the strong spatial inhomogeneity in the ADRE is the variance of the underlying surface. When high albedo surfaces are present (e.g., polar and desert regions), the ADRE is positive (warming), because the aerosol absorption effect outweighs the aerosol scattering effect. Except for the polar regions, the $ADRE_{all}$ shows a similar global pattern to the $ADRE_{clr}$, but at a smaller magnitude due to the cloud masking effect. In regions of high surface albedo such as over sea ice, the multiple scattering between clouds and surface enhances atmospheric absorption caused by absorbing aerosols, leading to a positive $ADRE_{all}$. Both $ADRE_{all}$ and $ADRE_{clr}$ distributions suggest that aerosol properties alone are not sufficient to explain the large regional differences in the ADRE patterns. Environmental variables such as surface reflection and clouds significantly influence ADREs. Hence, a proper assessment of the global ADRE distribution needs to measure the effects of both aerosol and environmental factors.

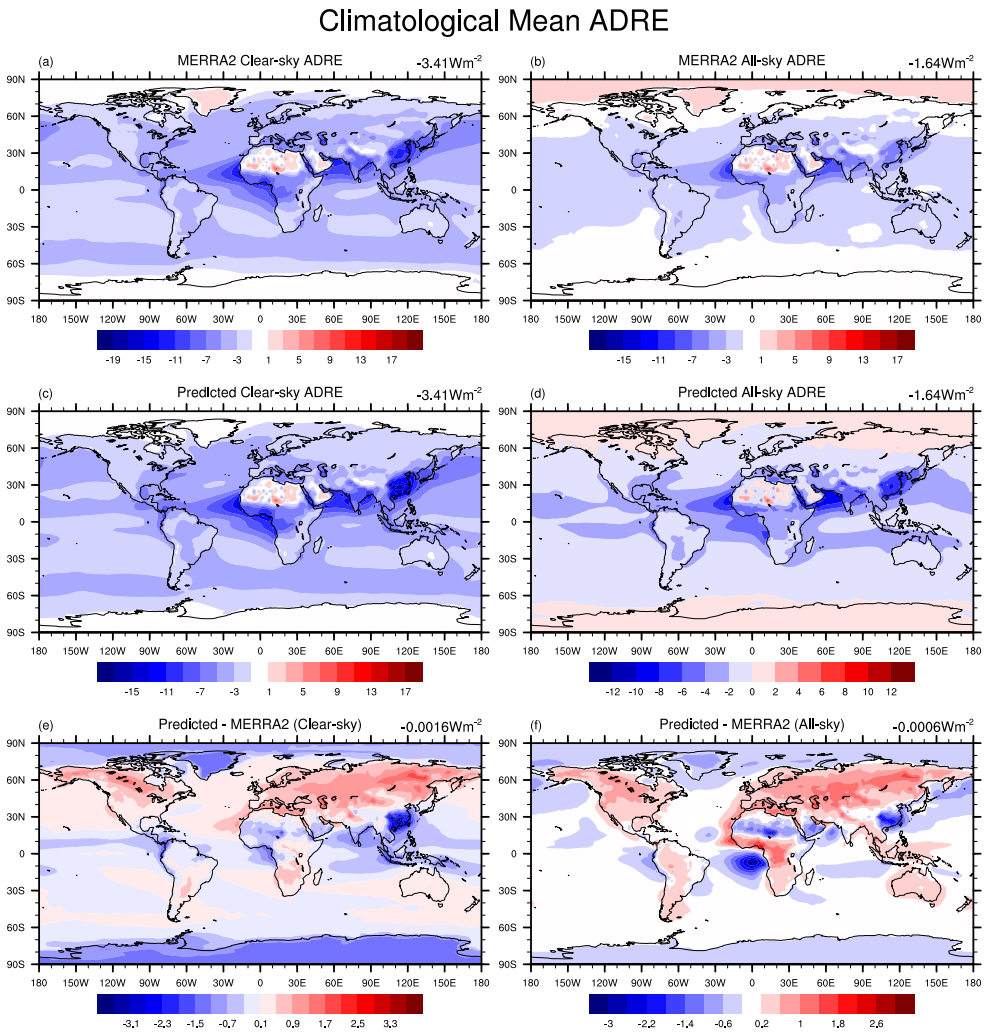

Figure 2.1 The geographic distributions of the climatological mean values of (a) MERRA-2 $ADRE_{clr}$, (b) MERRA-2 $ADRE_{all}$, (c) predicted $ADRE_{clr}$, (d) predicted $ADRE_{all}$, (e) predicted $ADRE_{clr}$ - MERRA-2 $ADRE_{clr}$, and (f) predicted $ADRE_{all}$ - MERRA-2 $ADRE_{all}$. The global mean values are indicated in the top-right corner of each subplot.

2.3.2 The Predicted Clear-sky and All-sky ADREs

Following Equations 2.9 and 2.10, the clear-sky and all-sky ADREs can be obtained by the regression model. In Figure 2.2, we compare the predicted climatological mean ADREs with the benchmark "true" values from MERRA-2. The sample number is 10512 and the color shading

indicates the probability density of the ADRE. Regardless of the sky condition, the predicted ADREs are very close to the true ADREs (following the 1:1 line). The root mean square error (RMSE) is 0.62 W m^{-2} for the $ADRE_{clr}$ and 0.43 W m^{-2} for the $ADRE_{all}$. The R-squared (R^2) values, which show the percentage of the variance in the ADRE explained by the regression models, are 92.96% and 93.13% in clear- and all-sky conditions, respectively. These results indicate general agreements between the predicted and true ADRE values and the reliability of the regression model. In comparison, if using log(AOD) or AOD as the sole predictor for the $ADRE_{clr}$, the R^2 value is only 62.48% and 56.06% (Table A2 in Appendix A.1). This again shows that it is necessary to include environmental variables in the conceptual model to explain the ADRE inhomogeneity.

To further examine how the regression model captures the regional features of the ADRE distributions, the predicted global distribution of the ADRE is compared to that of the benchmark MERRA-2 ADRE in Figure 2.1. Figure 2.1e indicates that the clear-sky regression model well captures the sign of the global $ADRE_{clr}$, while the relative bias of the magnitude is less than 20%. While the regression model effectively captures the most important physical processes influencing the ADRE, it does have some quantitative biases. The regression model underestimates the $ADRE_{clr}$ magnitude over midlatitudes and high latitudes, but overestimates the $ADRE_{clr}$ magnitude over the ITCZ. This is because the atmospheric transmittance differs from region to region, which can influence the ADRE. For example, the abundant tropospheric water vapor in tropical areas can potentially mask the clear-sky ADRE, which is not taken into account in the regression model. In addition, the cooling $ADRE_{clr}$ is generally overestimated in heavily polluted regions such as East Asia and is underestimated over land. These biases are unavoidable when using a linear (regression) model to represent the nonlinear radiative transfer process governing the ADRE.

Despite these biases, the predicted $ADRE_{clr}$ well reproduces the global pattern of the true $ADRE_{clr}$. Similarly, Figure 2.1f shows that the all-sky regression model successfully captures the regional differences in the $ADRE_{all}$ with local biases generally less than 22%. The bias pattern is similar to Figure 2.1e except for the Southeast Atlantic. In this region, biomass-burning aerosols overlie (and sometimes interact with) the relatively bright stratocumulus clouds (e.g., Adebiyi and Zuidema 2018). When clouds are located beneath aerosols, the highly reflected cloud layers can enhance the aerosol warming effect or change the ADRE sign from negative to positive depending on the surface type as well as the aerosol SSA (Redemann et al., 2021). Therefore, the regression model does not adequately capture the $ADRE_{all}$ because nonlinear processes are involved. Moreover, the regression model does not distinguish the relative locations of aerosols and clouds, which can also lead to potential biases. Except for such regions, the regression model makes a reasonably well prediction of the inhomogeneous global distribution of the $ADRE_{all}$.

After validating the accuracy of the regression model, the calculated regression coefficients are applied to Equations 2.7 and 2.8 to quantify the relative importance of each predictor to the global ADRE inhomogeneity. The results are shown in Table 2.2. Of the 92.96% of explained spatial variance in the $ADRE_{clr}$, SAOD (aerosol direct scattering effect) is the primary contributor, accounting for 72.69% of the spatial inhomogeneity. The remaining variance is due to environmental factors. There is a 10.56% contribution from the multiple scattering effects between aerosols and surface (SAOD · alb), and 6.86% and 9.89% contributions from solar geometry ($\cos\theta$) and aerosol absorption (AAOD · alb), respectively. In all-sky conditions, SAOD is still the dominant factor (70.12%). The relative contributions of the aerosol-surface multiple scattering (SAOD·alb) and the aerosol-cloud radiative interactions ($\text{SAOD} \cdot \frac{\text{CRE}}{\text{TISR}}$) to the $ADRE_{all}$ spatial variation are 15.51% and 10.02%, respectively. In terms of the aerosol absorption (AAOD·alb)

and the cosθ term, the contributions are 4.07% and 0.003%, respectively. Overall, Table 2.2 indicates that SAOD is the dominant contributor to the spatial inhomogeneity in the ADRE, while environmental factors contribute the remainder.

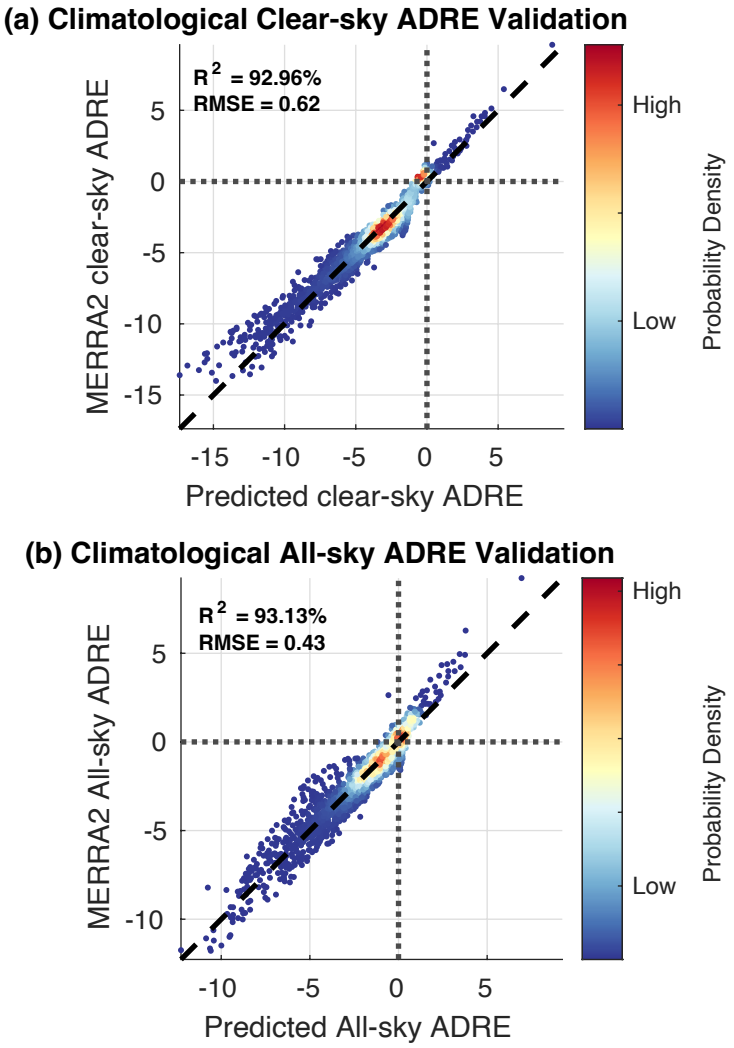

Figure 2.2 Scatterplots of the predicted climatological mean ADRE against MERRA-2 ADRE for (a) clear-sky and (b) all-sky conditions. The color coding indicates the probability density of the ADRE values.

Table 2.2 Relative Contributions From Each Predictor to the Spatial Inhomogeneity in the Global ADRE

	SAOD (%)	cosθ (%)	SAOD · alb (%)	AAOD · alb (%)	SAOD · $\frac{\text{CRE}}{\text{TISR}}$ (%)	Total (%)
ADRE_{clr}	72.69	6.86	10.56	9.89	-	92.96
ADRE_{all}	70.12	0.003	15.51	4.07	10.02	93.13

2.3.3 The Sensitivity of the ADRE

In addition to dissecting the spatial pattern of the ADRE, the regression model can also help quantify the sensitivity of the ADRE to its controlling factors (the aerosol and environmental variables governing the ADRE). Based on the regression Equation 2.9, the following is the ADRE_{clr} sensitivity to SAOD, surface albedo, and AAOD.

$$\frac{\partial \text{ADRE}_{\text{i,j}}^{\text{clr}}}{\partial \text{SAOD}_{\text{i,j}}} = \left(-\frac{1.40}{0.13} + 0.27\ \frac{\text{alb}_{\text{i,j}}}{0.02}\right) \cdot (9.86 \times 10^{-3}) \cdot\ \text{TISR}_{\text{i,j}} \tag{2.11}$$

$$\frac{\partial \text{ADRE}_{\text{i,j}}^{\text{clr}}}{\partial \text{alb}_{\text{i,j}}} = \left(0.27\ \frac{\text{SAOD}_{\text{i,j}}}{0.02} + 0.20\ \frac{\text{AAOD}_{\text{i,j}}}{1.1\times10^{-3}}\right) \cdot (9.86 \times 10^{-3}) \cdot\ \text{TISR}_{\text{i,j}} \tag{2.12}$$

$$\frac{\partial \text{ADRE}_{\text{i,j}}^{\text{clr}}}{\partial \text{AAOD}_{\text{i,j}}} = \left(0.20\ \frac{\text{alb}_{\text{i,j}}}{1.1\times10^{-3}}\right) \cdot (9.86 \times 10^{-3}) \cdot\ \text{TISR}_{\text{i,j}} \tag{2.13}$$

Based on the equations above, Figure 2.3 shows the ADRE_{clr} sensitivities to SAOD, surface albedo, and AAOD. In each subplot, the global mean sensitivities are displayed at the top-right. Sensitivity values are expressed in units of W m^{-2} per unit change in the dependent variable; for example, Figure 2.3a illustrates that if SAOD were increased by 1 globally then the cooling ADRE_{clr} would be strengthened by 29.4 W m^{-2}. Similarly, if the surface albedo and AAOD were

enhanced by one unit globally, the $ADRE_{clr}$ would increase by 10.4 and 93.5 W m^{-2}, respectively (Figures 2.3b and 2.3c).

The $ADRE_{clr}$ sensitivities to SAOD, surface albedo, and AAOD are regionally dependent on aerosol types and surface characteristics. The regional $ADRE_{clr}$ sensitivity to SAOD is typically negative (i.e., an increase in SAOD causes a stronger radiative cooling effect) as shown in Figure 2.3a. The sensitivity to SAOD over the ocean is generally greater than that over land, because the planetary albedo is more sensitive to scatterer changes over a dark surface. The highest sensitivity to SAOD locates in tropical regions because the aerosol direct scattering effect dominates the aerosol-surface multiple scattering effects and it is most sensitive to insolation. The $ADRE_{clr}$ sensitivity to surface albedo is always positive (Figure 2.3b), since brighter surfaces leave less room for aerosols to increase the planetary albedo and cool the planet. Also, it is noted that the surface albedo sensitivity has a larger magnitude in regions with high aerosol loadings, such as East Asia and India where scattering aerosols (sulfate) are abundant and Sahara and Arabian Peninsula where absorbing aerosols (dust) are abundant. In terms of the $ADRE_{clr}$ sensitivity to AAOD (Figure 2.3c), it is also always positive and increases with an increase in surface albedo.

Let us now examine the sensitivity of the $ADRE_{all}$ to SAOD, surface albedo, AAOD, and $\frac{CRE}{TISR}$, which are calculated as follows:

$$\frac{\partial \mathrm{ADRE}_{i,j}^{all}}{\partial \mathrm{SAOD}_{i,j}} = \left(-\frac{3.08}{0.13} + 0.74\frac{\mathrm{alb}_{i,j}}{0.02} - 0.98\ \frac{\frac{\mathrm{CRE}}{\mathrm{TISR}_{i,j}}}{0.02} \right) \cdot (4.36 \times 10^{-3}) \cdot \mathrm{TISR}_{i,j} \tag{2.14}$$

$$\frac{\partial \mathrm{ADRE}_{i,j}^{all}}{\partial \mathrm{alb}_{i,j}} = \left(0.74\frac{\mathrm{SAOD}_{i,j}}{0.02} + 0.29\ \frac{\mathrm{AAOD}_{i,j}}{1.1\times10^{-3}} \right) \cdot (4.36 \times 10^{-3}) \cdot \mathrm{TISR}_{i,j} \tag{2.15}$$

$$\frac{\partial \mathrm{ADRE}_{i,j}^{all}}{\partial \mathrm{AAOD}_{i,j}} = \left(0.29\ \frac{\mathrm{alb}_{i,j}}{1.1\times10^{-3}} \right) \cdot (4.36 \times 10^{-3}) \cdot \mathrm{TISR}_{i,j} \tag{2.16}$$

$$\frac{\partial \mathrm{ADRE}_{\mathrm{i,j}}^{\mathrm{all}}}{\partial\left(\frac{\mathrm{CRE}}{\mathrm{TISR}}\right)_{\mathrm{i,j}}} = \left(-0.98\frac{\mathrm{SAOD}_{\mathrm{i,j}}}{0.02}\right)\cdot(4.36\times10^{-3})\cdot\mathrm{TISR}_{\mathrm{i,j}} \tag{2.17}$$

As a result of the cloud masking effect, the magnitudes of the ADRE sensitivities to SAOD, surface albedo and AAOD tend to be weaker in all-sky conditions (Figure 2.4) than in clear-sky conditions (Figure 2.3). Figure 2.4a shows that if SAOD were to increase by 1 globally then the negative $\mathrm{ADRE}_{\mathrm{all}}$ would strengthen by 15.7 Wm^{-2}. If $\frac{\mathrm{CRE}}{\mathrm{TISR}}$ were to increase by 1, the cooling ADRE would be 8.8 Wm^{-2} weaker. Furthermore, if the surface albedo and AAOD were increased by 1 globally, the $\mathrm{ADRE}_{\mathrm{all}}$ would weaken by 10 Wm^{-2} and 61.5 Wm^{-2}, respectively (Figures 2.4b and 2.4d). Clouds also alter the regional pattern of the ADRE's sensitivity to the key variables. The sensitivity to SAOD (Figure 2.4a) is noticeably damped in very cloudy regions such as the ITCZ. The $\frac{\mathrm{CRE}}{\mathrm{TISR}}$ sensitivity (Figure 2.4c) is always negative because an increase in CRE values means a reduction of the aerosol-cloud radiative interactions, resulting in weaker atmospheric and surface absorption and thus a more negative ADRE. Like the surface albedo sensitivity, the $\frac{\mathrm{CRE}}{\mathrm{TISR}}$ sensitivity is especially pronounced over regions with high aerosol loading.

Despite using a linear regression model with a limited number of predictors, the regression method allows us to physically and quantitatively interpret the sensitivity of the ADRE to the changes in AAOD, SAOD, surface albedo, and $\frac{\mathrm{CRE}}{\mathrm{TISR}}$. The results here are comparable to those of other studies; e.g., the quantification of Thorsen et al. (2020) based on radiative transfer computations (Figure A5 in Appendix A).

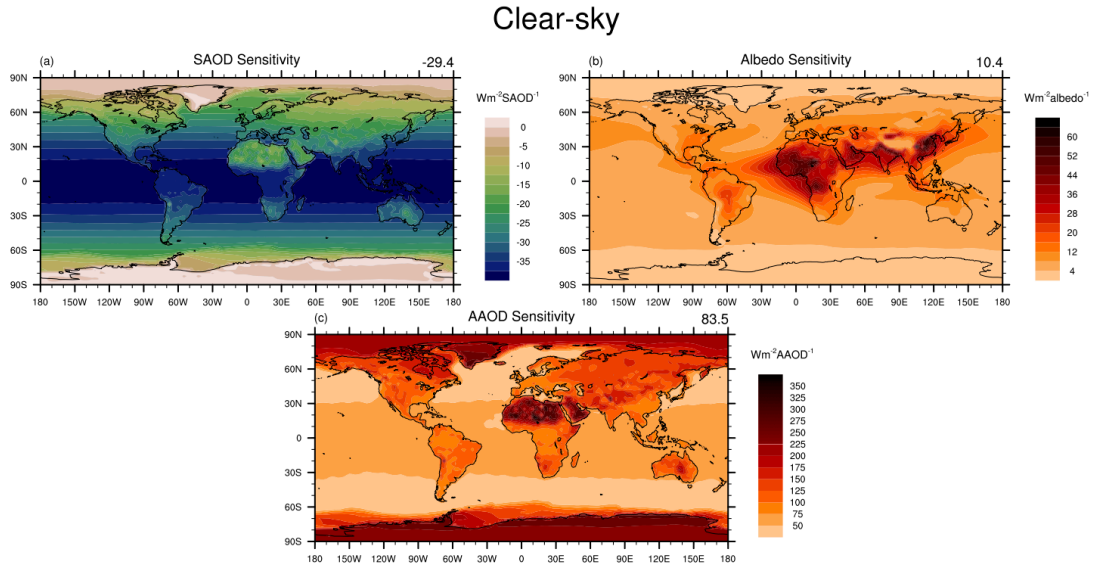

Figure 2.3 The sensitivities of the $ADRE_{clr}$ to (a) scattering aerosol optical depth, (b) surface albedo, and (c) absorbing aerosol optical depth. The global mean values are indicated in the top-right corner of each subplot.

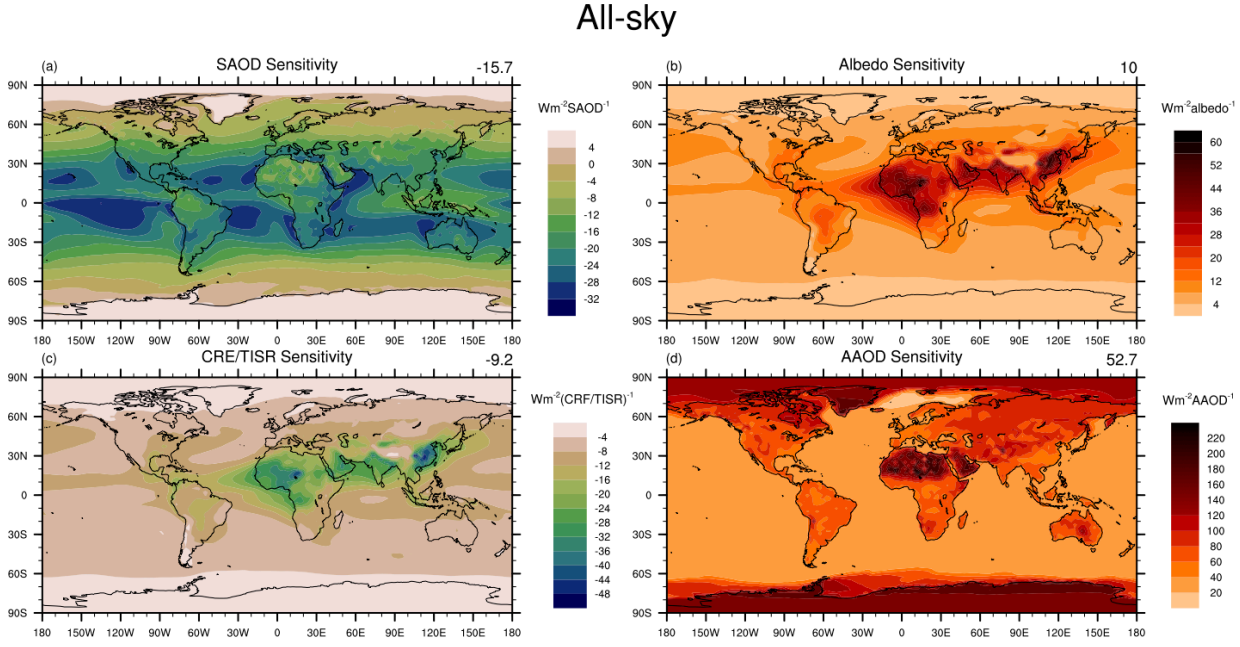

Figure 2.4 The sensitivities of the $ADRE_{all}$ to (a) scattering aerosol optical depth, (b) surface albedo, (c) cloud shortwave radiative effect normalized by insolation, and (d) absorbing aerosol optical depth. The global mean values are indicated in the top-right corner of each subplot.

2.4 The Climatological Zonal Mean ADRE and the Poleward Energy Transport

Based on Equations 2.9 and 2.10, we can calculate the zonal mean clear-sky and all-sky ADREs, which can be used to assess the contribution of aerosol-induced radiation change to poleward energy transport (PET). According to Hartmann (2015), the PET due to the ADRE is calculated as follows:

$$\mathrm{PET(i)} = \int_{-\frac{\pi}{2}}^{\mathrm{i}} \int_{0}^{2\pi} \mathrm{ADRE(i,j)} r^2 \cos(\mathrm{i})\, \mathrm{djdi}, \tag{2.18}$$

where PET is the ADRE-induced northward energy flux, r is the Earth radius, i and j are the latitude and longitude, and ADRE is the TOA clear-sky or all-sky aerosol radiative effect. A positive PET value indicates northward energy transport driven by the ADRE compared to a world without aerosols.

Figures 2.5a and 2.5c compare the predicted zonal mean $ADRE_{clr}$ and the poleward energy transport it induces by using the regression model with the results from MERRA-2. There is a good agreement between these two results. As shown in Figure 2.5a, the $ADRE_{clr}$ show peaks between the 30°S and 60°S due to the sea salt aerosols generated by strong winds over the vast open ocean, and between 0° and 30°N due to the presence of dust aerosols. Due to the more intense anthropogenic activities in the Northern Hemisphere midlatitude regions, the $ADRE_{clr}$ is also strong in these regions. As a result of the absorbing aerosols over bright sea ice surfaces, especially in the Arctic, the MERRA-2 zonal mean $ADRE_{clr}$ exhibits a slight warming effect over the polar regions, which eludes the regression model.

Cross-equator energy transport is a dominant feature of the $ADRE_{clr}$-induced PET (Figure 2.5c). From 90°S to 30°N, the energy transport due to the presence of aerosols is northward and can reach 0.15 PW at 15°S. From 30°N to 90°N, the aerosol-induced energy transport is southward and peaks at 55°N with 0.07 PW. An asymmetric aerosol-induced poleward energy transport leads to northward cross-equatorial energy transport (~0.13 PW) in clear-sky conditions, which may enhance and/or shift the location of the Hadley circulation (Frierson & Hwang, 2012).

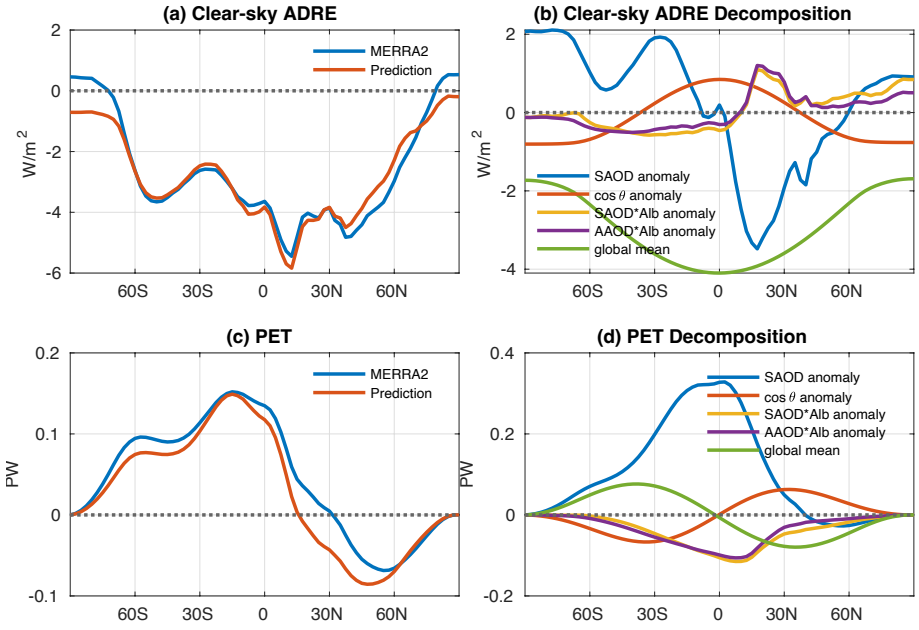

Figure 2.5 The climatological zonal mean clear-sky (a) ADRE, (b) corresponding poleward energy transport (northward positive), (c) ADRE contributed by different predictors, and (d) poleward energy transport contributed by different predictors.

Figures 2.5c and 2.5d illustrate how the regression model decomposes the $ADRE_{clr}$ and the corresponding PET into the contributions from the SAOD anomaly, cosθ anomaly, SAOD · alb anomaly, AAOD · alb anomaly, and global mean terms. If the predictors are global mean values for all locations, the ADRE and its PET, which is only affected by insolation, are symmetric (green line). However, SAOD, cosθ, AAOD, and alb are not uniformly distributed, leading to an inter-

hemispheric asymmetric zonal $ADRE_{clr}$ pattern. Among all the predictors, the SAOD terms caused the energy transport from the Southern Hemisphere to the Northern Hemisphere. This significant interhemispheric transport amounts to as large as 0.4 PW, as shown in Figure 2.5d. In contrast, the SAOD · alb and the AAOD · alb terms act oppositely to the SAOD term, resulting in an offsetting southward energy transport as large as 0.11 PW and 0.10 PW near the equator, respectively. As a result of these offsetting effects, the SAOD-driven cross-equator northward energy transport is reduced by 62.4%.

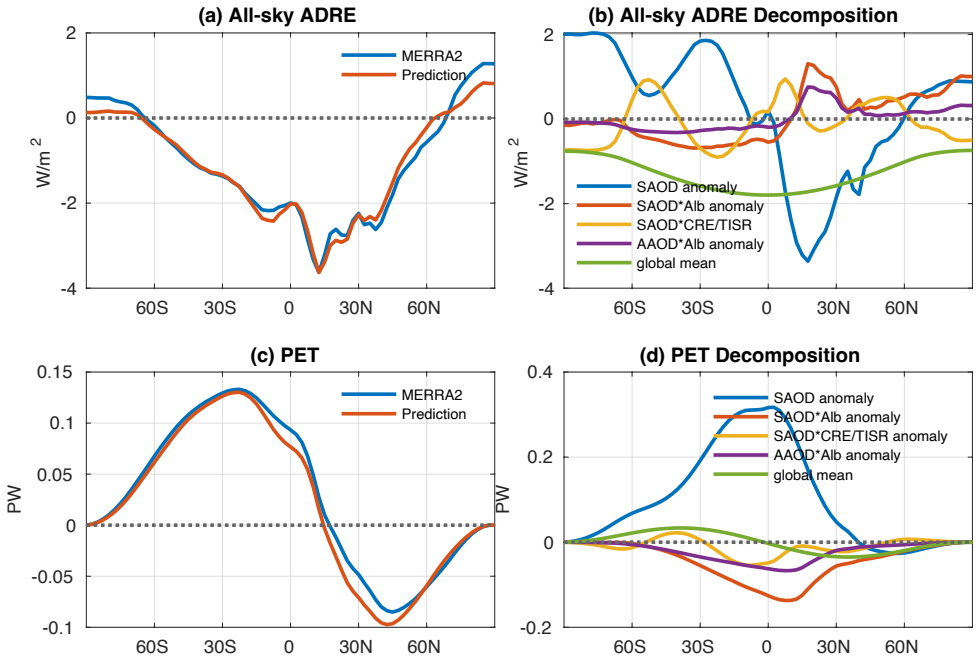

Figure 2.6 The same as Figure 2.5, but for all-sky conditions.

The zonal mean $ADRE_{all}$ and PET patterns are similar to those of clear-sky cases but with a smaller magnitude due to the cloud masking (Figure 2.6). Again, the predictions of the regression model are in good agreement with the truth results of MERRA-2. The SAOD term is still the primary contributor to the cross-equator energy transport in all-sky conditions despite being partly (75.8%) offset by the SAOD · alb, AAOD · alb and SAOD · $\frac{\text{CRE}}{\text{TISR}}$ terms. Due to the cloud masking in

the Southern Hemisphere storm track regions, there is no longer a peak in the $ADRE_{all}$ in the north of 60°S. Instead, the $ADRE_{all}$ mostly peaks at 15°N. The cross-equator energy transport driven by $ADRE_{all}$ is around 0.09 PW as shown in Figure 2.6d.

2.5 The ADRE and PET Trend Analysis

2.5.1 The ADRE Trend Decomposition

The $ADRE_{clr}$ and $ADRE_{all}$ have been changing since 2000, and these changes are associated with changes in aerosol properties (e.g., due to emission control) and environmental variables (e.g., melting sea ice and changing cloud distribution). By using regression models, we can isolate the influence of aerosols and the environmental variables on ADRE trends, and better understand the role that environmental variables played in ADRE trends. According to Equation 2.10, the global $ADRE_{clr}$ is dominated by SAOD, AAOD, alb, and $\cos\theta$. Since there is no trend in $\cos\theta$, trends in $ADRE_{clr}$ can be attributed to trends (noted by $\partial_t(\dots)$ terms below) in SAOD, AAOD, and alb, as shown below:

$$\partial_t \mathrm{ADRE}_{i,j}^{clr} = \frac{\partial \mathrm{ADRE}_{i,j}^{clr}}{\partial \mathrm{SAOD}_{i,j}} \partial_t \mathrm{SAOD} + \frac{\partial \mathrm{ADRE}_{i,j}^{clr}}{\partial \mathrm{AAOD}_{i,j}} \partial_t \mathrm{AAOD} + \frac{\partial \mathrm{ADRE}_{i,j}^{clr}}{\partial \mathrm{alb}_{i,j}} \partial_t \mathrm{alb}, \tag{2.19}$$

where $\frac{\partial \mathrm{ADRE}_{I,j}^{clr}}{\partial(\dots)_{I,j}}$ terms are the $ADRE_{clr}$ sensitivities as Equations 2.11 – 2.13. Similarly, trends in $ADRE_{all}$ result from the joint effect of SAOD, AAOD, alb, and $\frac{\mathrm{CRE}}{\mathrm{TISR}}$ trend.

$$\begin{aligned} &\partial_t \mathrm{ADRE}_{i,j}^{all} \\ &= \frac{\partial \mathrm{ADRE}_{i,j}^{all}}{\partial \mathrm{SAOD}_{i,j}} \partial_t \mathrm{SAOD} + \frac{\partial \mathrm{ADRE}_{i,j}^{all}}{\partial \mathrm{AAOD}_{i,j}} \partial_t \mathrm{AAOD} + \frac{\partial \mathrm{ADRE}_{i,j}^{all}}{\partial \mathrm{alb}_{i,j}} \partial_t \mathrm{alb} + \frac{\partial \mathrm{ADRE}_{i,j}^{all}}{\partial \frac{\mathrm{CRE}}{\mathrm{TISR}_{i,j}}} \partial_t \frac{\mathrm{CRE}}{\mathrm{TISR}}, \end{aligned} \tag{2.20}$$

where $\frac{\partial \mathrm{ADRE}_{I,j}^{all}}{\partial(\dots)_{I,j}}$ terms are the $ADRE_{all}$ sensitivity as Equations 2.14 – 2.17.

The above equations disclose the relationship between ADRE trends and the trends of predictor variables, providing a means for attributing ADRE trends. Note that trend contributions (Equations 19 and 20) quantified this way use the climatological mean values of each sensitivity term determined from the training of the regression model. In other words, this trend decomposition assumes that the ADRE sensitivity to key variables does not vary with time, which could lead to a source of error in the attribution results.

The geographical distribution of the predicted ADRE trends is compared to that of the MERRA-2 ADRE trends in Figure 2.7. All trends in the predictors and MERRA-2 ADRE have passed the Student t test with a significance level of 1%. Globally, the trend in $ADRE_{clr}$ is -0.01 W m^{-2}/decade. In contrast, the global mean $ADRE_{all}$ trend is 0.05 W m^{-2}/decade, which is primarily the result of an increase in the global mean cloud shortwave radiative effect (Figures A7 and A8 in Appendix A). The regional ADRE trend is quite different according to regions. From 2000 to 2021, the enhancement of cooling $ADRE_{all}$ in India could reach -1.8 W m^{-2}/decade, while over Northeastern America, Europe, and East Asia, the decrease of cooling $ADRE_{all}$ could be as high as 0.57, 0.29, and 0.55 W m^{-2}/decade, respectively. For both clear-sky and all-sky conditions, the predicted trends in the ADRE are in good agreement with the MERRA-2 trends. Although the regression models are simple linear models, they can explain 75.88% and 68.87% of the global ADRE trends in the clear-sky and all-sky conditions, respectively, and the RMSE is smaller than 0.11 W m^{-2}/decade (Figure A6 in Appendix A). The regression model overestimated the magnitude of the ADRE trend in certain regions (e.g., East China and Northeast Russia), which could be caused by other factors ignored by our regression model. For example, if the vertical distribution of aerosols becomes closer to the ground, the ADRE magnitude can be more likely

masked by clouds or atmospheric water vapor even though the column concentration of aerosols remains unchanged.

The regression model allows us to further examine how the $ADRE_{clr}$ and $ADRE_{all}$ trends are driven by the trends of SAOD, AAOD, and surface albedo (Figures 2.8 and 2.9). In general, $ADRE_{clr}$ trends over low and midlatitudes are primarily driven by the changes in local aerosol loading, while the $ADRE_{clr}$ trends in the Arctic are dominated by the declining surface albedo trend. As for the regional $ADRE_{clr}$ trends, it is negative (more cooling) in the Indo-Gangetic Plain, Central Africa, Northwestern North America, and Northern South America. This is mainly due to the SAOD trends (Figure 2.8a), with the AAOD trends slightly offsetting them (Figure 2.8b). The $ADRE_{clr}$ in the Southern Ocean is also declining due to the enhanced SAOD trend (Figure A9 in Appendix A). There are regions where the $ADRE_{clr}$ becomes less negative (more warming) such as Southeastern North America and Europe. For Southeastern North America, positive $ADRE_{clr}$ trends are caused by the SAOD trends, whereas in Europe, the positive $ADRE_{clr}$ trends result from the trends of both SAOD and surface albedo. The contributions of the SAOD and AAOD trends to the ADRE trends are generally synchronized; however, the two trends can change separately in some regions. For example, both the SAOD and AAOD trends cause a decreasing $ADRE_{clr}$ (more cooling) in Southeast China, which is caused by the change in aerosol types (more scattering aerosols and less absorbing aerosols). Similarly, the decreasing $ADRE_{clr}$ trends in Southeast America are weakly contributed by the increasing scattering aerosols, while the absorbing aerosols remain unchanged. Figure 2.9 presents the $ADRE_{all}$ trends contributed by SAOD trends, AAOD trends, surface albedo trends, and $\frac{\mathrm{CRE}}{\mathrm{TISR}}$ trends. Due to $\frac{\mathrm{CRE}}{\mathrm{TISR}}$ trends, the negative ADRE trends in central Africa, the midlatitude Southern Hemisphere, and Northern South America in clear-sky conditions have become positive in all-sky conditions.

The ADRE in the Arctic, where sea ice retreat is significant in the 21st century, can be greatly influenced by changes in surface albedo. Figures 2.8c and 2.9c indicate the albedo trend dominates the trends of the $ADRE_{clr}$ and $ADRE_{all}$ near 70°N, while AOD shows little trend. These results allow us to better understand how the interplay between aerosols and the environment would change the ADRE and the PET trend. Interested readers can find the trend of key variables in Figure A8 in Appendix A.

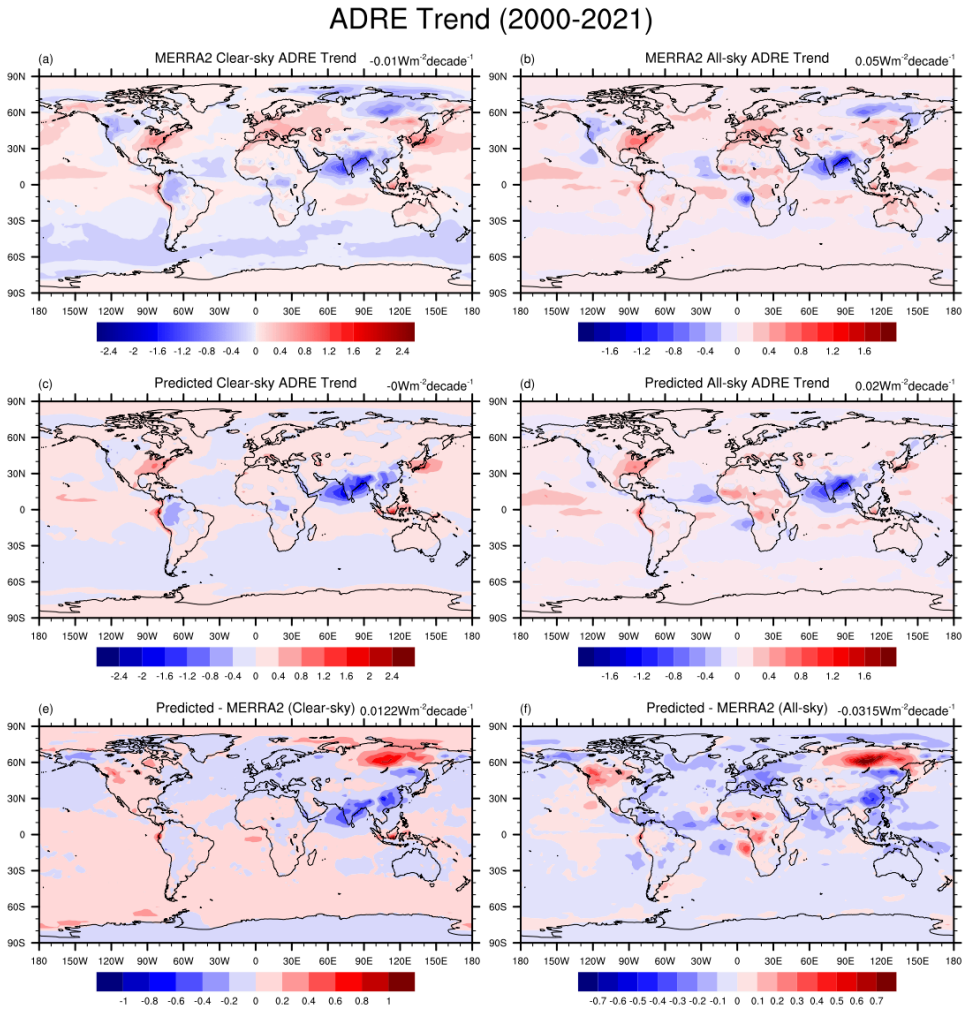

Figure 2.7 The geographic distributions of (a) MERRA-2 $ADRE_{clr}$ trend, (b) MERRA-2 $ADRE_{all}$ trend, (c) predicted $ADRE_{clr}$ trend, (d) predicted $ADRE_{all}$ trend, (e) predicted $ADRE_{clr}$

trend - MERRA-2 $ADRE_{clr}$ trend (f) predicted $ADRE_{all}$ trend - MERRA-2 $ADRE_{all}$ trend. The global mean values are indicated in the top-right corner of each subplot.

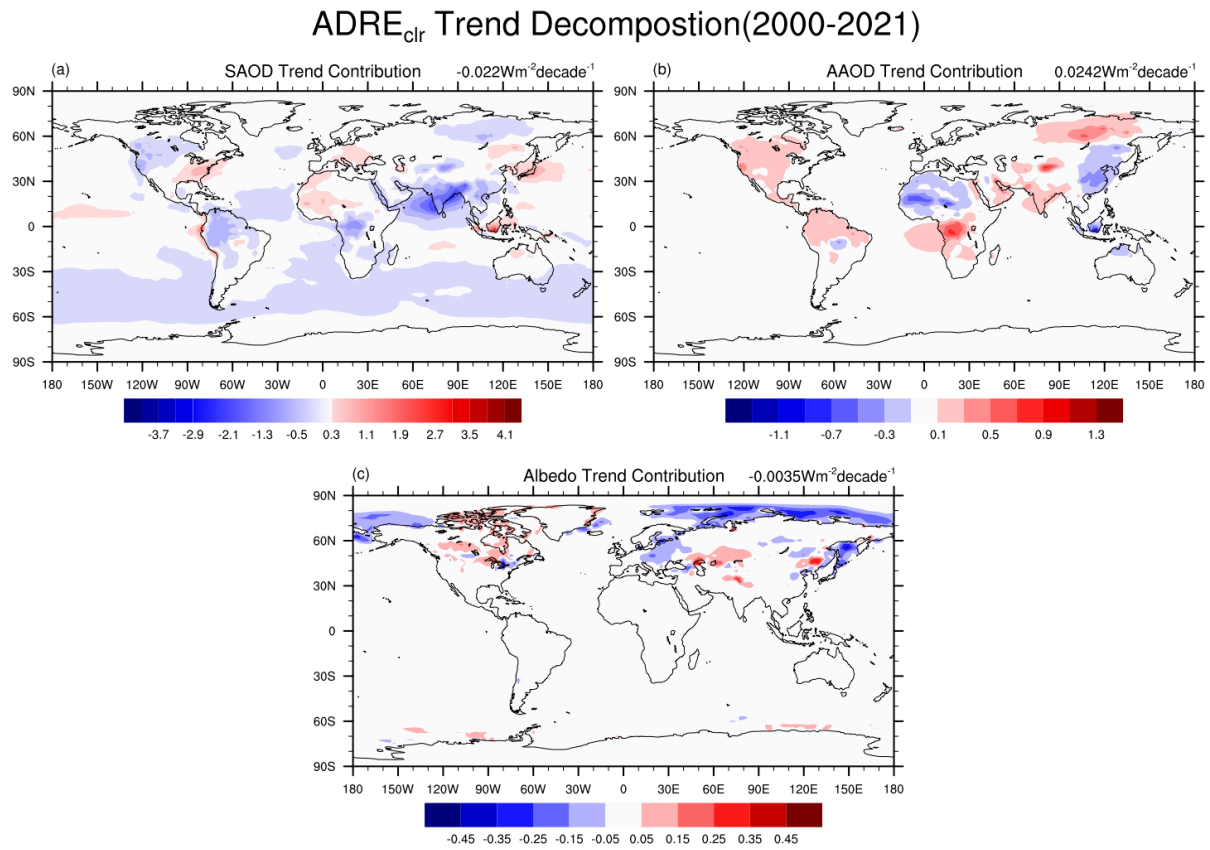

Figure 2.8 The geographic distributions of predicted $ADRE_{clr}$ trends contributed by (a) SAOD trend, (b) AAOD trend and (c) surface albedo trend. The global mean values are indicated in the top-right corner of each subplot.

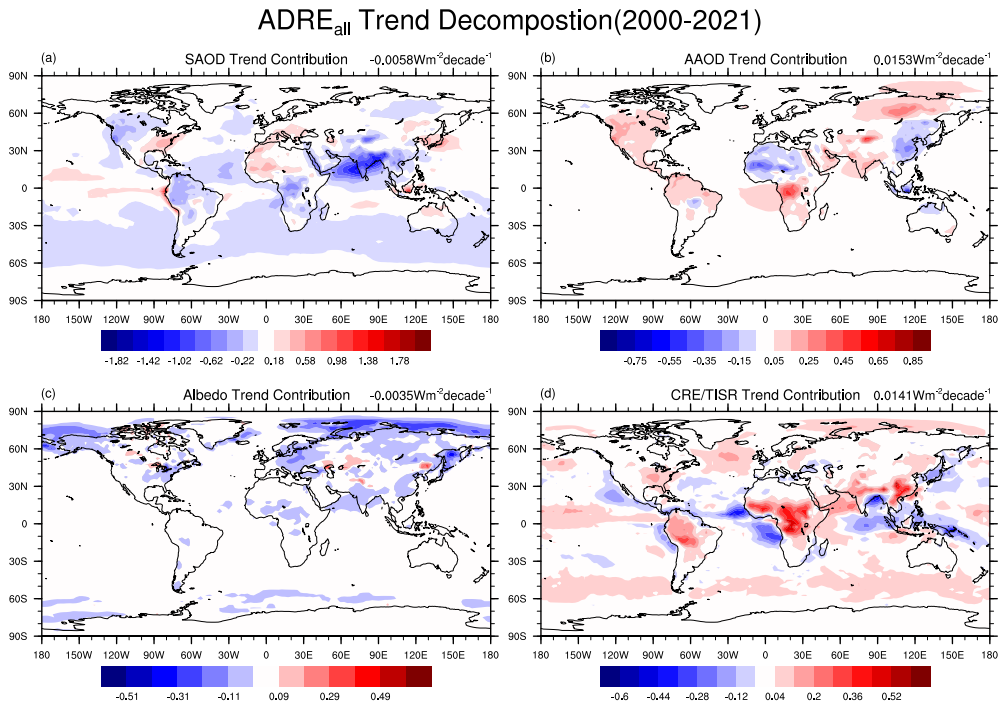

Figure 2.9 The geographic distributions of predicted ADRE$_{all}$ trend contributed by (a) SAOD trend, (b) AAOD trend, (c) surface albedo trend and (d) CRE/TISR trend. The global mean values are indicated in the top-right corner of each subplot.

2.5.2 The PET Trend

The ADRE-induced PET trend is important because it is a direct indicator of how circulation may change in response to aerosol emissions (primarily anthropogenic sources) and environmental conditions. With the ADRE trend known, the PET trend it induced can be calculated as follows:

$$\frac{\partial \mathrm{PET}}{\partial \mathrm{t}}(\mathrm{i}) = \int_{-\frac{\pi}{2}}^{\mathrm{i}} \int_{0}^{2\pi} \frac{\partial \mathrm{ADRE}}{\partial \mathrm{t}}(\mathrm{i},\mathrm{j}) \mathrm{r}^2 \cdot \cos(\mathrm{i})\, \mathrm{djdi} \tag{2.21}$$

Figures 2.10 and 2.11 show the zonal mean ADRE$_{clr}$ and the PET trend driven by it, respectively. The ADRE$_{clr}$ is increasing in 30°S–60°S and 0°–30°N, while it is decreasing in 30°S–

60°S and 30°N–60°N. Based on this $ADRE_{clr}$ trend, a negative PET trend is observed, which weakens the climatological positive PET in Figure 5. During the period from 2000 to 2021, aerosol-induced cross-equator energy transport decreases by 1.26×10^{-2} PW in clear-sky conditions, which is 9.67% of its climatological mean value. Similar to the clear-sky situation, the $ADRE_{all}$ trend results in a negative PET trend (Figures 2.11a and 2.11b), leading to a slight decline in aerosol-induced cross-equator energy transport. It is estimated that northward cross-equator energy transport caused by the ADRE has declined by 1.07×10^{-3} PW over the 22-year period, which is about 1.19% of its climatological mean value. Using the regression model, the zonal mean ADRE and PET trends are decomposed into the contributions from SAOD, surface albedo, AAOD, and $\frac{\mathrm{CRE}}{\mathrm{TISR}}$. As presented in Figure 2.10c, the $ADRE_{clr}$ trend is mainly controlled by the SAOD trend, except for the Arctic regions, where the surface albedo and AAOD trends are strong. For all-sky conditions (Figure 2.11c and 2.11d), the SAOD trend still dominates the lower latitude area and leads to a decreasing PET trend, whereas other variables partly mitigate this effect.

To further quantify the contributions from each factor to the PET trend in the different regions, Figure 2.12 lists the all-sky PET trend contributed from the SAOD, AAOD, surface albedo and $\frac{\mathrm{CRE}}{\mathrm{TISR}}$ trend at 70°N, the equator, and 45°S, respectively. At 70°N, the influence of the decreasing surface albedo contributes a strong positive PET trend, and it is offset by the trend of other variables. As a result, the all-sky southward energy transport in the Arctic is slightly weakened over the past 22 years. At the equator, where the albedo and $\frac{\mathrm{CRE}}{\mathrm{TISR}}$ trends are not significant, the PET trend is dominated by the SAOD trend. Despite the SAOD trend causing a negative $ADRE_{all}$ trend at 45°S, the $\frac{\mathrm{CRE}}{\mathrm{TISR}}$ trend compensates for it, resulting in an insignificant local $ADRE_{all}$ trend in this region.

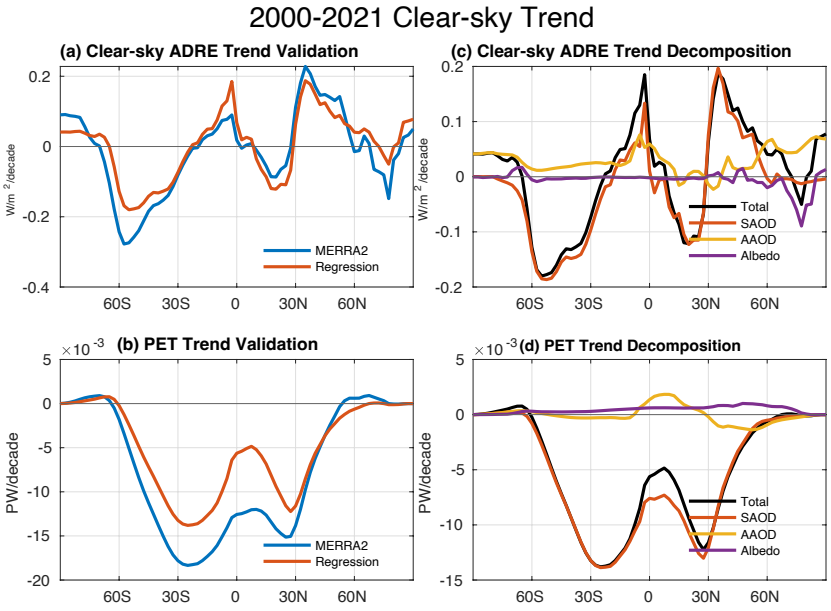

Figure 2.10 The zonal mean clear-sky (a) ADRE trend, (b) corresponding poleward energy transport trend, (c) ADRE trend contributed by key variables, and (d) poleward energy transport trend contributed by key variables.

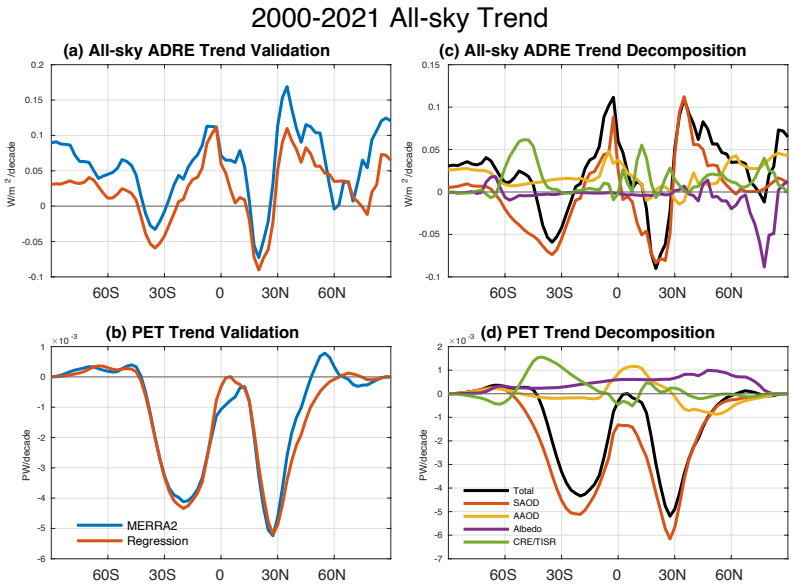

Figure 2.11 Same as Figure 2.10 but for all-sky conditions.

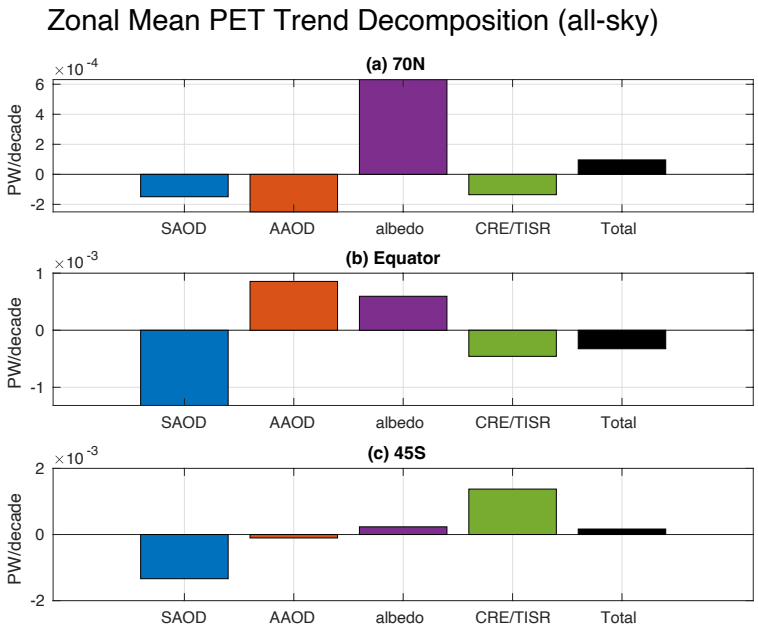

Figure 2.12 The decomposition of the PET trends at 70°N, the equator, and 45°S for all-sky conditions.

2.6 Conclusions

The ADRE plays an important role in modulating the regional energy budgets and shows strong inhomogeneity in its global distribution patterns. This study develops a multivariate regression model for the global clear-sky and all-sky ADREs and separates the contributions of aerosol-related and environment-related factors to the spatial distributions and trends for the ADRE and the poleward energy transport driven by it.

The global distribution of the clear-sky ADRE, $ADRE_{clr}$, is largely explained by the scattering aerosol optical depth, absorbing aerosol optical depth, surface albedo, and the solar zenith angle. Using these predictors, the regression model can explain 92.96% of the spatial inhomogeneity in the $ADRE_{clr}$ (Figure 2.1 and 2.2a). Unlike studies that focus on the correlation between AOD and the $ADRE_{clr}$, this study suggests that AOD alone, which explains only 56.06%

of the spatial variance, is insufficient to account for the geographical variability of the $ADRE_{clr}$, and the remaining variance is caused by environmental factors. The $ADRE_{clr}$ is controlled by four key processes: aerosol direct scattering, aerosol absorption, multiple scattering between surface and aerosols, and solar geometry, which account for 72.69%, 9.89%, 10.56% and 6.86% of the geographical inhomogeneity, respectively. Aside from these four factors, clouds, which are represented by the cloud shortwave radiative effect, also play a role in determining the spatial inhomogeneity in all-sky ADRE distributions. In total, 93.13% of the spatial changes in the global all-sky ADRE, $ADRE_{all}$, can be explained by the five predictor variables (Figures 2.1 and 2.2b). The relative contributions of aerosol direct scattering, aerosol-surface multiple scattering, aerosol–cloud radiative interactions, aerosol absorption, and solar geometry are 70.12%, 15.51%, 10.02%, 4.07%, and 0.003%, respectively.

In addition to global patterns of the ADRE, the regression model also helps understand the sensitivity of the ADRE to its key controlling variables. Increases in scattering aerosols (SAOD) typically result in enhanced ADRE cooling. On the global average, an increase in SAOD by 1 would result in a reduction of 29.4 and 15.7 W m^{-2} in the $ADRE_{clr}$ and $ADRE_{all}$. However, the sensitivity of ADRE can also be affected by other factors. Surface albedo and AAOD are always positively correlated with the ADRE, suggesting that aerosol absorption increases as surface albedo or AAOD increases. The ADRE sensitivity to AAOD peaks at high surface albedo regions, while the ADRE sensitivity to surface albedo increases with aerosol loadings. These sensitivities quantified here suggest that the changes in these factors can potentially lead to nonnegligible changes in ADRE. For example, if surface albedo were decreased by 0.1 due to the sea ice melt in the Arctic, the cooling ADRE there would decrease by 0.5 and 0.4 W m^{-2} in clear-sky and all-sky conditions, respectively.

There is a cross-equator energy transport driven by both the clear-sky and all-sky ADREs (0.13 PW and 0.09 PW, respectively), which can influence the strength of the Hadley circulation and the location of the ITCZ. Most of this northward cross-equator energy transport is due to the hemispheric difference in SAOD, which is mitigated by aerosol absorption, aerosol-surface multiple scattering, and aerosol–cloud radiative interactions (Figures 2.5 and 2.6).

We further apply the regression models to analyze the ADRE and PET trends in the 21st century (2000–2021). The global mean trend for the $ADRE_{clr}$ and $ADRE_{all}$ is −0.01 and 0.05 W m^{-2}/decade, respectively; however, regional trends are significantly higher, given their strong inhomogeneity. For example, the reduction of the cooling $ADRE_{all}$ amounts to over 0.1 W m^{-2}/decade in terms of the zonal mean values at 30°N. In India, the cooling $ADRE_{all}$ is enhanced by −1.8 W m^{-2}/decade, whereas in Northeastern America, Europe, and East Asia, the cooling $ADRE_{all}$ is decreased by 0.57, 0.29, and 0.55 W m^{-2}/decade (Figure 2.7b).

With the regression model, we can reproduce the global ADRE trends by linearly decomposing them into the contributions from the trends in the key controlling variables. The regression model explains 75.88% and 68.87% of the global $ADRE_{clr}$ and $ADRE_{all}$ trends, respectively. During the 22 years, the ADRE-induced northward cross-equator energy transport has decreased by 9.67% and 1.19% in clear-sky and all-sky conditions, respectively (Figures 2.10 and 2.11).

This study also indicates changes in the environment can have a significant impact on the regional ADRE trend. In the Arctic, the decreasing surface albedo in the past 22 years leads to a more negative $ADRE_{clr}$, despite the trends in the scattering and absorbing AODs acting the opposite way (Figure 2.12a). At midlatitudes in the Southern Hemisphere, the changes in CRE can mitigate the effect of the SAOD trend, neutralizing the local $ADRE_{all}$ trends (Figure 2.12c). In

general, the ADRE trend is dominated by the SAOD trend at low and midlatitudes, while at high latitudes it is strongly influenced by the albedo trend.

This study presents a MERRA-2 reanalysis-based dissection of the ADRE and adopts a regression method to quantify the relative contributions of aerosol and environmental variables to the ADRE spatial inhomogeneity. Despite the success of the method in explaining most of the ADRE spatial variance, the simple model does not fully describe the aerosol–radiation interaction, which is a complex nonlinear process, and thus is left with unavoidable quantitative errors in certain regions. Moreover, the results of this study are limited by the accuracy of the MERRA-2 data set, given that there are known uncertainties both in its forecast model and assimilated satellite observations. Nevertheless, the attribution of the global ADRE inhomogeneity and the sensitivities to various controlling factors quantified here provide a reference, which can be verified based on other data sets and attribution methods in future studies.

Data Availability Statement

The Modern-Era Retrospective analysis for Research and Applications, Version 2 (MERRA-2) data used to study the variations and trends in the ADRE are provided by NASA Global Modeling and Assimilation Office (Randles et al., 2017). The radiation and aerosol diagnostics data are available at Global Modeling and Assimilation Office via https://doi.org/10.5067/Q9QMY5PBNV1T and https://doi.org/10.5067/KLICLTZ8EM9D. Our processed climatological mean ADRE and its trend as well as all the other data necessary to reproduce the reported findings in this paper are uploaded to Mendeley Data at https://doi.org/10.17632/8tgk5799k7.3

Chapter 3 A Dissection of the Inter-Model Spread of the Aerosol Direct Radiative Effect in CMIP6 Models

This Chapter is a reprint of the published article in Geophysical Research Letters.

Yu, Q., & Huang, Y. (2023). A dissection of the inter-model spread of the aerosol direct radiative effect in CMIP6 models. Geophysical Research Letters, 50, e2023GL105112.https://doi.org/10.1029/2023GL105112

The thesis author is the lead author and principal investigator for this paper.

A Dissection of the Inter-model Spread of the Aerosol Direct Radiative Effect in CMIP6 Models

Qiurun Yu[1*], Yi Huang[1]

[1]Department of Atmospheric and Oceanic Sciences, McGill University, Montreal, QC, Canada

[*]Corresponding author: Qiurun Yu (qiurun.yu@mail.mcgill.ca)

Key Points:

- A regression model is used to dissect the inter-model spread of the all-sky Aerosol Direct Radiative Effect (ADRE) in Sixth Coupled Model Intercomparison Projects Models
- The model explains 86% of ADRE inter-model spread, with variances in state-variable and radiative sensitivity contributing 67% and 17% each
- Differences in aerosol optical depth and ADRE sensitivity to aerosol-surface interactions drive the spatial variance in global ADRE spread

Abstract

The all-sky Aerosol Direct Radiative Effect (ADRE) varies considerably among global climate models (GCMs), which results from differences in aerosol and atmospheric states and ADRE sensitivity to aerosol-related radiative processes. This study uses a regression method to analyze the inter-model spread of ADRE among the GCMs of the Sixth Coupled Model Intercomparison Projects (CMIP6). The key state variables examined include scattering and absorbing aerosol optical depth, surface albedo, and shortwave cloud radiative effect. We find that differences in state variables and radiative sensitivity explain 67% and 17%, respectively, of the global ADRE anomaly. The ADRE anomaly in different models is dominated by different factors, which sometimes leads to compensating effects. For the global mean ADRE anomaly, aerosol optical depth differences dominate in CNRM-ESM2-1 and GFDL-ESM4 models, while ADRE sensitivity variations to aerosol-only scattering effect dominate in HadGEM3-GC31-LL, MPI-ESM-1-2-HAM, and MRI-ESM2-0 models.

Plain Language Summary

Aerosols scatter and absorb solar radiation, impacting the Earth's climate. Global climate models differ in their quantification of this effect. The differences in quantification arise from different state variables, including the aerosol properties and atmospheric conditions. Additionally, the radiative sensitivity of aerosol effect to aerosol-related physical processes varies with models. In this study, we identify the primary causes of the differences in aerosol radiative effect among climate models and quantify their respective impacts by using a regression method. We find that besides the aerosol optical depth, whose influence on aerosol radiative effect is well recognized, the radiative sensitivity of aerosol and surface interactions significantly contributes to the aerosol radiative effect differences in the latest climate models.

3.1 Introduction

Aerosols affect the Earth's radiative energy budget by scattering or absorbing solar radiation. This effect is termed the Aerosol Direct Radiative Effect (ADRE). The magnitude and spatial distribution of ADRE influence the global surface temperature, the atmospheric circulation, and regional climate patterns (Bellouin et al., 2020; Visioni et al., 2020; Günther et al., 2022; Q.Yu & Huang, 2023b). ADRE is usually quantified using radiative transfer models based on aerosol optical properties from in-situ and satellite observations or model simulations. However, ADRE quantifications exhibit a wide range of values, reflecting significant underlying uncertainties (H. Yu et al., 2006; Bellouin et al., 2020; Thorsen et al., 2021). To better constrain ADRE uncertainty and its impact on climate projection, it is crucial to identify the primary causes of the uncertainty in the global climate models (GCM).

The inter-model spread of ADRE arises from many factors, including aerosol and atmospheric states as well as radiative transfer calculations. The representation of aerosols in CMIP6 models remains discrepant, especially in heavily polluted areas, desert and polar regions (Cherian & Quaas, 2020; Lapere et al., 2023). The discrepancies can result from various factors, including aerosol emissions and deposition, the representation of microphysics (such as size distribution and hygroscopicity) as well as the vertical distribution of aerosols (J. Li et al., 2015; Q.-R. Yu et al., 2019; Guo et al., 2021; Su et al., 2021; Lapere et al., 2023). Many studies have highlighted the uncertainty in aerosol optical properties. For example, Zhang et al. (2022) found that Aerosol Optical Depth (AOD) and Single Scattering Albedo (SSA) each explained 36% of the total ADRE uncertainty in the GCMs of the Coupled Model Intercomparison Project (CMIP6) for external and internal mixing assumptions, respectively.

Apart from aerosol properties, the representation of environmental conditions such as surface albedo and cloud accounts for the ADRE inter-model spread (Thorsen et al., 2021). In regions with poorly constrained cloud and surface albedo (i.e., stratocumulus cloud decks and sea ice), ADRE uncertainty may be especially large. By prescribing identical aerosol radiative properties in AeroCom models, Stier et al. (2013) showed that host model uncertainties, particularly surface albedo, clouds, and radiative transfer, could explain about 36% of the overall sulfate forcing diversity.

Besides the aerosol and environmental parameters, which constitute the inputs to radiative transfer models for the ADRE quantification, uncertainties can result from the structural differences in radiative transfer models (Halthore et al., 2005; Randles et al., 2013; Zanchettin et al., 2022). For example, Randles et al. (2013) showed a large inter-model diversity in aerosol radiative forcing primarily due to the treatment of multiple-scattering; they also demonstrated that global models with two-stream radiation approximation are subject to persistent biases compared to multi-stream models.

On a relevant note, GCMs are complex modeling tools that are often subject to compensating errors in their simulated processes (Cherian & Quaas, 2020; Zhao et al., 2022; H. Huang & Huang, 2023). Zhao et al. (2022) indicated that a seemingly good agreement in cloud radiative effect (CRE) and absorption of solar radiation (ASR) between CMIP6 models and satellite observations may result from the compensating errors between cloud optical depth (COD) and liquid water path (LWP). Similarly, Cherian & Quaas (2020) noted that LWP and cloud fraction (CF) errors may compensate for setting the CRE trend. Recognizing the radiative transfer coupling among aerosols, clouds, and other radiative constituents in GCMs, these studies demonstrate the importance of identifying ADRE uncertainty arising from their coupling effects.

Although many studies have examined ADRE uncertainty, quantitative and comparative assessments of the contributions to ADRE uncertainty from the different factors remain lacking, especially for the latest CMIP6 GCMs. To address this issue, this study uses an analytical model developed by Q.Yu & Huang (2023b) that quantitatively relates the global ADRE to several key aerosol-related and environment-related variables, accounting for their coupled effects. We apply this approach to dissect the ADRE inter-GCM spread and to address the following questions: (a) How well does the analytical model explain the all-sky ADRE inter-model spread in the CMIP6 models? (b) How much do the differences in state variables and ADRE radiative sensitivity respectively contribute to the spread? And (c) what are the dominant factors in each GCM that contribute to its ADRE anomaly? The paper is structured as follows: Section 3.2 describes the analytical model used in this study and the data from CMIP6 models; Section 3.3 documents the contributions to the ADRE spread; Section 3.4 summarizes the answers to these questions.

3.2 Data and Method

3.2.1 CMIP6 data

This study uses five CMIP6 coupled ocean-atmosphere models (listed in Table B1) that provide the necessary variables for our analysis. To reduce sampling bias, only one model is selected from each modeling center. The following variables are extracted from the Earth System Grid Federation platform (Cinquini et al., 2014), for the period running from 2000 to 2014 from the historical experiment. The variable fields used include the ambient aerosol optical thickness at 550 nm (od550aer), ambient aerosol absorption optical thickness at 550 nm (abs550aer), top-of-atmosphere (TOA) outgoing aerosol-free shortwave radiation (rsutaf), TOA outgoing shortwave radiation (rsut), TOA incident shortwave radiation (rsdt), TOA outgoing clear-sky, aerosol-free shortwave radiation (rsutcsaf), surface downwelling clear-sky shortwave radiation (rsdscs), and

surface upwelling clear-sky shortwave radiation (rsuscs). The model outputs are re-gridded to a common 2.5° × 2.5° latitude-longitude grid for comparison. The all-sky ADRE, shortwave cloud radiative effect (CRE), and broad-band shortwave surface albedo (ALB) are derived as:

$$\mathrm{ADRE} = (\mathrm{rsut} - \mathrm{rsdt}) - (\mathrm{rsutaf} - \mathrm{rsdt}) = \mathrm{rsut} - \mathrm{rsutaf} \tag{3.1}$$

$$\mathrm{CRE} = (\mathrm{rsutaf} - \mathrm{rsdt}) - (\mathrm{rsutcsaf} - \mathrm{rsdt}) = \mathrm{rsutaf} - \mathrm{rsutcsaf} \tag{3.2}$$

$$\mathrm{ALB} = \frac{\mathrm{rsuscs}}{\mathrm{rsdscs}} \tag{3.3}$$

Although the sampling size in our study is limited due to data availability, the multi-model mean and standard deviation of key variables such as AOD and ALB from the 5-model subset agree well with the mean from all CMIP6 models, which confirms the representativeness of the multi-model mean ADRE (Figures B1–B3 in Appendix B).

3.2.2 Regression Model

Following Yu & Huang (2023, YH23 in short), we represent the global distribution of the all-sky ADRE with a multivariate regression model:

$$\frac{Y-\overline{Y}}{\overline{Y}} = \sum_{i=1}^{4} \beta_i \cdot \frac{X_i-\overline{X_i}}{\overline{X_i}} \tag{3.4}$$

where Y is the predictand variable and is defined as the ADRE value normalized by the TOA insolation (TISR): $\frac{\mathrm{ADRE}}{\mathrm{TISR}}$; X_I and β_I are the i^{th} predictor and regression coefficient. This regression model includes four predictors: the scattering AOD: SAOD, the product of SAOD and surface albedo: $\mathrm{SAOD} \cdot \mathrm{ALB}$, the product of absorptive AOD and surface albedo: $\mathrm{AAOD} \cdot \mathrm{ALB}$, and the product of SAOD and the TISR-normalized CRE: $\mathrm{SAOD} \cdot \frac{\mathrm{CRE}}{\mathrm{TISR}}$. Both the predictand and predictor variables vary spatially, although this dependency is omitted in the equation for a simpler expression. The global mean values are denoted by an overbar. Note that, as shown by YH23, a main advantage of this regression model is that the analytical form it adopted recognizes the

nonlinear coupling between the aerosol-related and environment-related variables. Consequently, it captures well the spatially varying ADRE sensitivity to these variables (Figure 4 in YH23 and Figures B4 and B5 in Appendix B). For individual GCMs, the model generally explains over 92% of the spatial variance of the ADRE values (Table B1 in Appendix B).

Using the CMIP6 data described above, we train a regression model with the globally distributed multi-model mean values of the predictor and predictand variables and denote the prediction of this model as $\mathrm{ADRE}_0^{\mathrm{p}}$, where the subscript 0 denotes the multi-model mean values. We also train a prediction model with the predictor and predictand values from each GCM; these predictions are denoted as $\mathrm{ADRE}_{\mathrm{j}}^{\mathrm{p}}$, where the subscript j denotes the j^{th} CMIP6 model. The superscript p denotes the predicted ADRE, which distinguishes from the *truth* ADRE value of each model: $\mathrm{ADRE}_{\mathrm{j}}$ and that of the multi-model mean: ADRE_0, both of which are obtained from the CMIP6 archive.

In this way, we decompose the ADRE anomaly of a GCM with respect to the multi-model mean as:

$$\Delta\mathrm{ADRE}_{\mathrm{j}} = \mathrm{ADRE}_{\mathrm{j}} - \mathrm{ADRE}_0 = \Delta\mathrm{ADRE}_{\mathrm{j}}^{\mathrm{p}} + \mathrm{res} \tag{3.5}$$

The first term on the right-hand side represents the ADRE anomaly explained by the regression method:

$$\Delta\mathrm{ADRE}_{\mathrm{j}}^{\mathrm{p}} = \mathrm{ADRE}_{\mathrm{j}}^{\mathrm{p}} - \mathrm{ADRE}_0^{\mathrm{p}} \tag{3.6}$$

The residual term represents the unexplained part and takes the form:

$$\mathrm{res} = \left(\mathrm{ADRE}_{\mathrm{j}} - \mathrm{ADRE}_{\mathrm{j}}^{\mathrm{p}}\right) - \left(\mathrm{ADRE}_0 - \mathrm{ADRE}_0^{\mathrm{p}}\right) \tag{3.7}$$

Based on the expression of the regression model, the explained part can be further decomposed to terms that multiply with $\Delta X_{I,j}$, which is the anomaly of the i^{th} predictor in the j^{th} model compared to the multi-model mean and those that multiply with $\Delta\beta_{I,j}$,

$$\Delta\beta_{i,j} = \frac{\beta_{i,j}}{\overline{X_{i,j}}} - \frac{\beta_{i,0}}{\overline{X_{i,0}}} \tag{3.8}$$

which measures the anomaly in the ADRE sensitivity to the i^{th} predictor in the j^{th} model.

The $\Delta X_{I,j}$ terms measure the contributions to ADRE anomaly in a GCM by the anomaly of the aerosol and environment state variables in this GCM. For instance, if a GCM has anomalously high SAOD values, the term multiplying with $\Delta SAOD_j$ measures how much $\Delta ADRE_j$ anomaly is caused by this factor. The $\Delta\beta_{I,j}$ terms, explained in Table 3.1, measure the contribution from the differences in ADRE sensitivity to aerosol-related radiative processes such as aerosol-only scattering. These ADRE sensitivity variations among models can be attributed to the differences in radiative transfer (such as radiative transfer solvers, spectral resolution, and stream approximation) and other state variables excluded from the selected predictors (such as atmospheric water vapor). For example, due to $\Delta\beta_{SAOD}$ differences, even if two models have identical SAOD values, their ADRE values may differ. See Text B1 in Appendix B for a full decomposition of the ADRE anomaly in our analysis and the definitions of all relevant terms.

3.3 Results and Discussions

3.3.1 ADRE

Figure 3.1a displays the multi-model mean ADRE computed by the GCMs, which discloses several regions with pronounced local ADRE, including strong warming effects in the Sahara and Arabian Deserts as well as strong cooling effects in the Arabian Sea, Bay of Bengal, and the tropical Atlantic Ocean (consistent with the global reanalysis—e.g., Figure 1b in YH23).

In addition, ADRE exhibits positive values in the Arctic and Greenland, while it takes negative values in Antarctica. Figure 1b shows that these regional features are captured very well by the regression model, which explains a total of 95% (measured by the R^2 value) of the spatial variance of the multi-model mean ADRE.

Figures 3.1d and 3.1e show the standard deviation (Std) of the ADRE values in every GCM as simulated by the GCMs and predicted by the regression method, respectively. The regions with large inter-model spread are East Asia and the Sahara, with Std values greater than 3 W/m^2. In the Arctic, although the absolute Std values are small, they are comparable to the magnitude of ADRE values there, indicating considerable discrepancies among the models. Again, the regression method effectively captures these regional features and explains a total of 94% of the Std variance.

In summary, we find that the simple regression model (Equation 3.4) explains very well both the average global distribution of the ADRE in the CMIP6 GCMs and the inter-GCM differences, except for some regions with relatively large prediction bias (the hatched areas in Figure 3.1c). The unexplained residual is likely due to the factors and nonlinearity that are neglected in Equation 3.4, including the absence of vertical distribution information of aerosols and clouds as well as unaccounted nonlinear coupling, which, for example, may make ADRE delicately depend on the underlying surface and cloud (Chlek & Coakley, 1974).

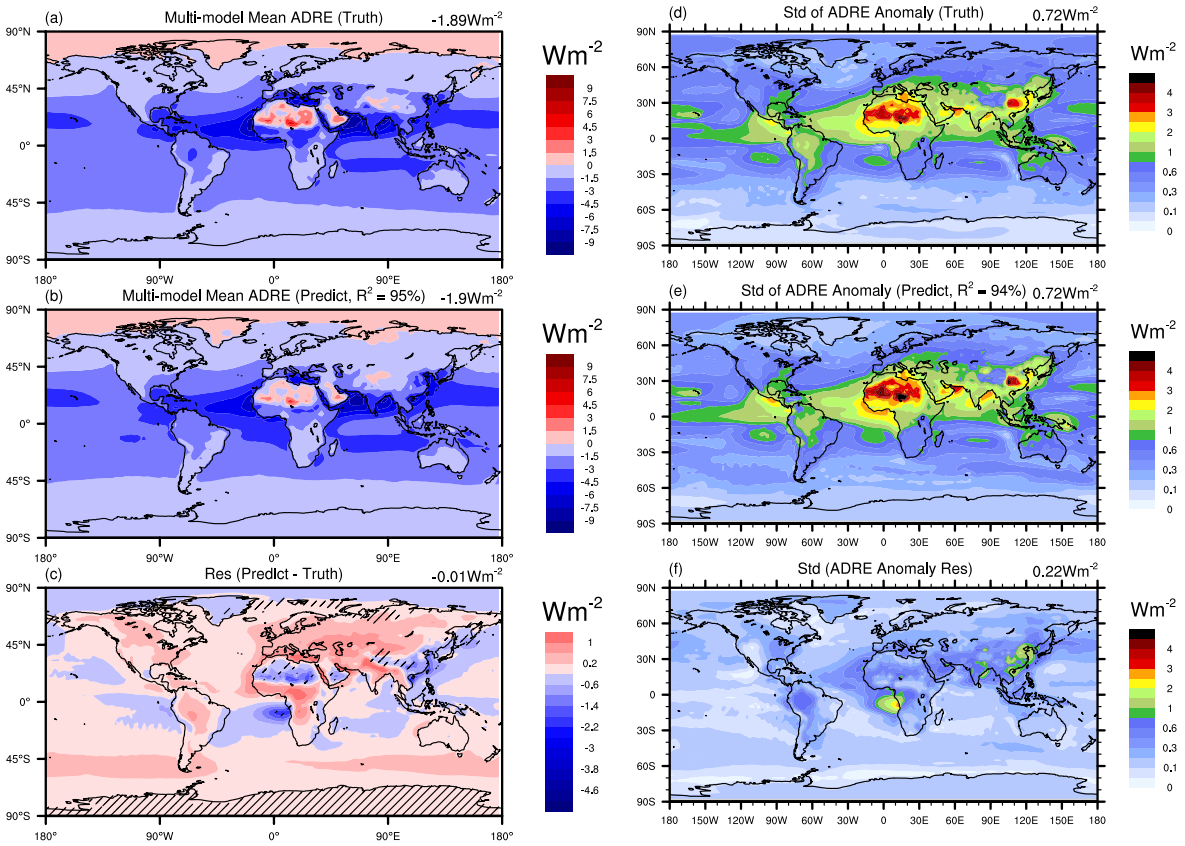

Figure 3.1 *Truth* values of the (a) multi-model mean ADRE ($ADRE_0$) and (d) the standard deviation of ADRE inter-model anomaly ($std(\Delta ADRE_j)$); the regression model predicted (b) multi-model mean ADRE ($ADRE_0^p$) and (e) the standard deviation of ADRE inter-model anomaly ($std(\Delta ADRE_j^p)$); (c,f) corresponding prediction biases. The hatched areas in (c) indicate regions where the magnitude of the bias exceeds that of the truth value. Global mean values are indicated in the top-right corner of each subplot.

Table 3.1 CMIP6 Models Used in This Study and the Spatial Variance in the Global ADRE Anomaly in Each Model Explained by the Regression Method (Bold Values) and Its Component Terms

	Spatial variance explained (R^2)										
	Total	State difference ($\Delta X_{I,j}$ terms)					Radiative sensitivity difference ($\Delta\beta_{I,j}$ terms)				
		Total	ΔSAOD	ΔAOD	ΔALB	ΔCRE	Total	$\Delta\beta_1$	$\Delta\beta_2$	$\Delta\beta_3$	$\Delta\beta_4$
CNRM-ESM2	**87%**	**39%**	7%	0%	1%	27%	**29%**	14%	7%	12%	0%
GFDL-ESM4	**83%**	**77%**	9%	28%	22%	0%	**1%**	11%	42%	32%	5%
HadGEM3	**81%**	**65%**	20%	8%	0%	19%	**48%**	39%	20%	23%	8%
MPI-ESM	**88%**	**75%**	24%	16%	2%	3%	**0%**	1%	5%	7%	9%
MRI-ESM2-0	**89%**	**78%**	46%	0%	1%	13%	**7%**	5%	6%	4%	5%
Avg± Std	**86± 3%**	**67±16%**	21±16%	11±12%	5±10%	12±11%	**17±21%**	14±15%	16±16%	16±12%	5± 3%
ADRE radiative sensitivity to different aerosol-related radiation processes ($\beta_{I,j}$ terms): β_1 or β_{SAOD}: Aerosol-only scattering effect.											

β_2 or $\beta_{SAOD \cdot ALB}$: Scattering aerosols and surface interaction. β_3 or $\beta_{AAOD \cdot ALB}$: Absorptive aerosols and surface interaction. β_4 or $\beta_{SAOD \cdot CRE}$: Cloud masking effect.
Full model names and references The Centre National de Recherches Météorologiques Earth System Model (Séférian et al., 2019): CNRM-ESM2-1 The Geophysical Fluid Dynamics Laboratory Earth System Model (Dunne et al., 2020): GFDL-ESM4 The Hadley Centre Global Environmental Model (Sellar et al., 2020): HadGEM3-GC31-LL The Max Planck Institute Earth System Model (Gutjahr et al., 2019): MPI-ESM-1-2-HAM The Meteorological Research Institute Earth System Model (Yukimoto et al., 2019): MRI-ESM2-0

3.3.2 The ADRE Anomaly

3.3.2.1 Global Mean

Given the success of the regression method in explaining the distributions of the multi-model mean ADRE and Std of the inter-model ADRE anomaly, we then examine the ADRE anomaly in every GCM. A survey of the global mean ADRE in different GCMs and its predictor variables (Text B2 in Appendix B) discloses substantial inter-GCM differences in both ADRE and its controlling factors. Following the formulation in Section 3.2.2, we decompose $\Delta ADRE_j$ into contributions from state and radiative sensitivity differences. Table 3.1 summarizes the spatial variance of the explained ADRE anomaly. On average, the regression model explains 86±3% of

the ADRE anomaly in the GCMs, with state differences contributing 67±16%, and radiative sensitivity differences contributing 17±21%.

Figure 3.2b summarizes the component contributions to the global mean ADRE anomaly in every GCM, which shows that the dominant contributors differ among the models. The ADRE anomaly in the CNRM-ESM2 and GFDL-ESM4 models is primarily caused by the state anomaly of these two models, while the other models exhibit stronger impacts from radiative sensitivity differences.

Figure 2c identifies the main factors contributing to the ADRE anomaly in each model. For example, the CNRM-ESM2 model has an underestimation of SAOD and AAOD compared to the multi-model mean. Despite the compensation of their effects, the SAOD difference dominates the ADRE anomaly in this model. In contrast, in the GFDL model, AAOD is the primary cause for its ADRE anomaly. The contributions from differences in ALB and CRE are relatively small. In the HadGEM3, MPI-ESM, and MRI-ESM2 models, the ADRE sensitivity to aerosol-only scattering effects (the $\Delta\beta_{\mathrm{SAOD}}$ term) is the main driver of the ADRE spread. Overall, the CNRM-ESM2 model appears to be an outlier with large contributions from its differences in both state variables and radiative sensitivity.

On regional scales, the major contributors to the ADRE anomaly differ from the global means. In East Asia (100°E-125°E, 20°N-40°N, Figure B8 in Appendix B), where the ADRE displays the largest inter-model spread (Figure 3.1d), higher AAOD compared to the multi-model mean contributes most to the ADRE anomaly in the GFDL model, while for the MPI-ESM model, reduced CRE (less cooling and masking effect of clouds) is the main driver. For the MRI-ESM2 model, the anomaly in SAOD, ALB, and the ADRE sensitivity to aerosol-only scattering effect contribute nearly equally to its ADRE anomaly. The Arctic is also a region with a large ADRE

discrepancy because the ADRE anomaly surpasses its mean value, and the regression residual is relatively large. Results suggest that over the Arctic (70°N – 90°N, Figure B9 in Appendix B), the anomaly in AAOD contributes the most to the ADRE anomaly in the GFDL and MRI-ESM2 models. In the CNRM-ESM2 and MPI ESM models, the ADRE anomaly is mainly caused by the differences in the evaluation of the scattering aerosol and surface interaction (the $\Delta\beta_{\mathrm{SAOD\cdot ALB}}$ term), which can lead to uncertainty in atmospheric absorption due to changes in photon path-length. The HadGEM3 model shows the largest bias in the regression model's prediction of the ADRE spread, indicating a distinct relationship between the predictors and the ADRE in this model compared to others in the region.

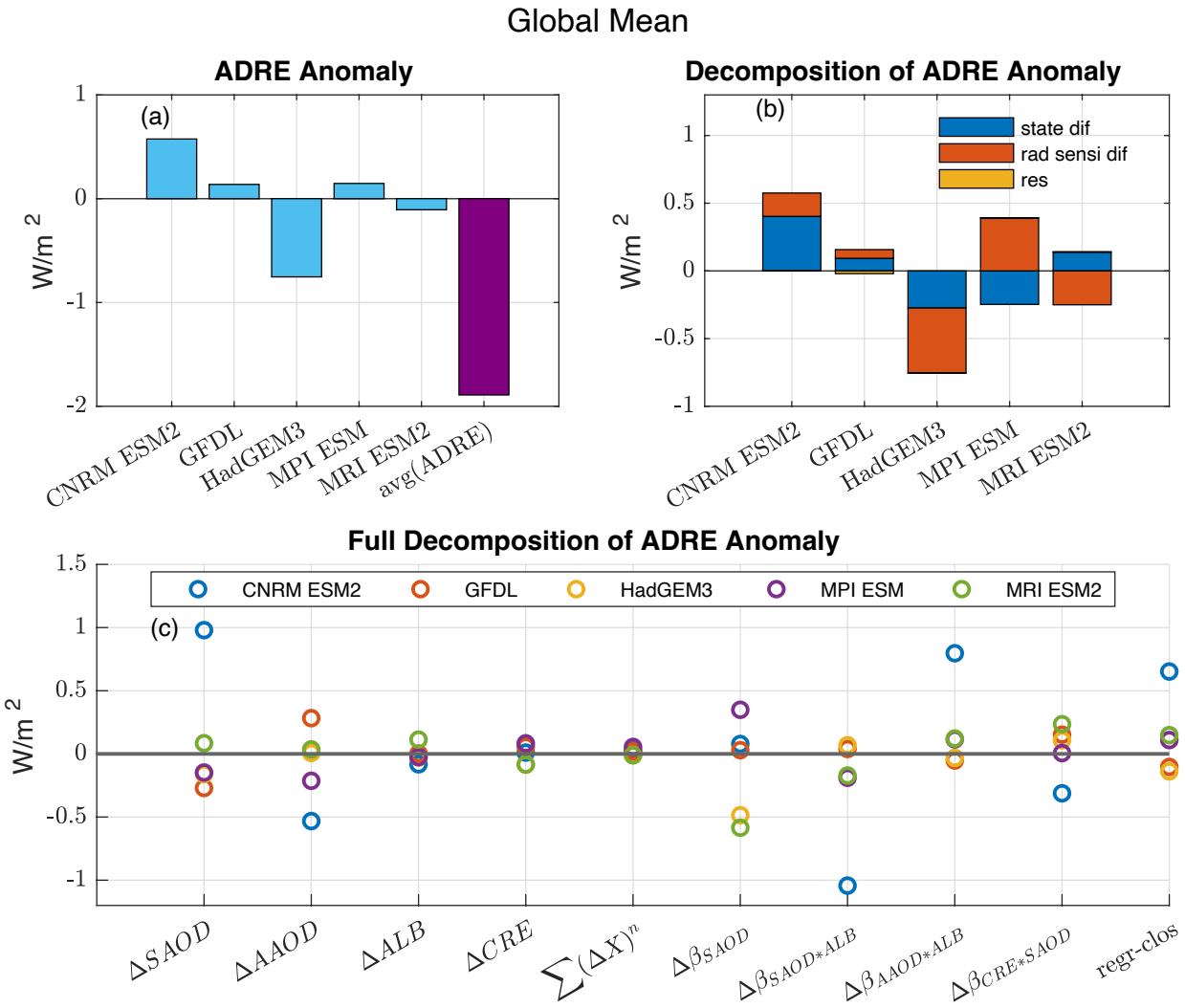

Figure 3.2 Global mean ADRE anomaly in the CMIP6 GCMs. The ADRE anomaly in each GCM (a) compared to the multi-model mean, (b) decomposed to contributions from the state and radiative sensitivity differences and unexplained residual, and (c) fully decomposed to contributions due to the differences in state variables: ΔSAOD, ΔAAOD, ΔALB, ΔCRE, and $\Sigma(\Delta X)^n$ and due to the differences in radiative sensitivities as measured by regression coefficient differences: $\Delta\beta_{SAOD}$, $\Delta\beta_{SAOD\cdot ALB}$, $\Delta\beta_{AAOD\cdot ALB}$, $\Delta\beta_{CRE\cdot SAOD}$, and regr-clos. See Text B1 in Appendix B for the full expressions of the component terms.

3.2.2 Spatial Distributions

Next, we analyze the spatial distribution of the ADRE discrepancies in the GCMs. Figures 3.3a-3.3e show the spatial distribution of the inter-GCM Std of the ADRE anomaly caused by different state variables (i.e., the $\Delta X_{I,j}$ terms, Equation. B9 in Appendix B). The ΔSAOD term prevails in several mid-latitude regions, especially in China, India, and central Africa, which reflects large inter-GCM discrepancies in SAOD values in these regions. The ΔAAOD term is the most noticeable in the desert areas, China, and India. China is an interesting hotspot as both aerosol-related and environment-related state variables (ΔALB and ΔCRE) contribute strongly to inter-model ADRE discrepancies in this region. In other regions, the contributions from ΔALB and ΔCRE terms are generally small. Overall, the inter-model differences in SAOD contribute the most (0.66 W/m^2 globally) to the inter-model differences in ADRE, which is consistent with other studies (Regayre et al., 2018). Scattering aerosols, such as sea salt and sulfate, have a greater impact on the global ADRE uncertainty compared to absorbing aerosols like carbonaceous aerosols. This is because carbonaceous aerosols contribute to ADRE uncertainty primarily during high-emission months, and their effect is more limited to regions proximate to emission sources. These results suggest that it is a priority to constrain the base states in the GCMs to reduce ADRE

uncertainty. Given the significant compensating errors caused by different state variables (Figure B10a in Appendix B), it is important to simultaneously address the GCM biases in SAOD, AAOD, ALB, and CRE.

The dominant contributor to the state variable induced ADRE differences differs in each model: ΔSAOD contributes the most in the CNRM-ESM2 and HadGEM3. ΔAAOD dominates the GFDL and MPI-ESM model. ΔALB has the largest impact in the MRI-ESM2 model.

Apart from the state variables that are prescribed as inputs to radiation models, ADRE quantification is subject to a variety of uncertainties in the radiative transfer calculation, including the representations of the vertical distributions of aerosols and clouds, the parameterizations of spectrally and angularly dependent surface reflection and aerosol scattering, the difference in atmospheric absorbers (e.g., water vapor), and the simplifications in the solvers of the radiative transfer equation (Table B2 in Appendix B). These result in differences in the ADRE sensitivities quantified by the regression method (β_I in Equation B4) and their contribution to ADRE anomaly are represented by the $\Delta\beta_{I,j}$ terms in our decomposition (Equation B20 in Appendix B).

Figures 3.3f - 3.3j presents the Std of the radiative sensitivity-caused ADRE anomaly. The $\Delta\beta_{SAOD}$, $\Delta\beta_{SAOD\cdot ALB}$, $\Delta\beta_{AAOD\cdot ALB}$, and $\Delta\beta_{CRE\cdot SAOD}$ terms represent discrepancies resulting from the ADRE sensitivity to the aerosol-only scattering, scattering aerosol and surface interaction, absorptive aerosol and surface interaction, and cloud masking processes, respectively. We find that, in oceanic regions, the aerosol-only scattering effect dominates the ADRE discrepancies, which may result from the backscattering representation of the sea salt aerosols that are dominant in those regions. In polluted regions such as China, the contribution from the scattering aerosol and surface interaction is strong. In desert regions, absorptive aerosols and surface interaction is important. The contribution from the cloud masking effect is generally smaller. In terms of global

mean values, the scattering aerosol and surface interaction contributes the most (0.4 W/m^2) to the spread of ADRE, which is consistent with other studies (e.g., Randles et al., 2013).

For the dominant contributor to the radiative sensitivity-caused ADRE differences in each model (Figure B10b in Appendix B), the ADRE sensitivity differences to scattering aerosols and surface interaction and cloud masking effect contribute most to the CNRM-ESM2 model and the GFDL model, respectively. The sensitivity to aerosol-only scattering effect dominates the HadGEM3, MPI-ESM, and MRI-ESM2 models.

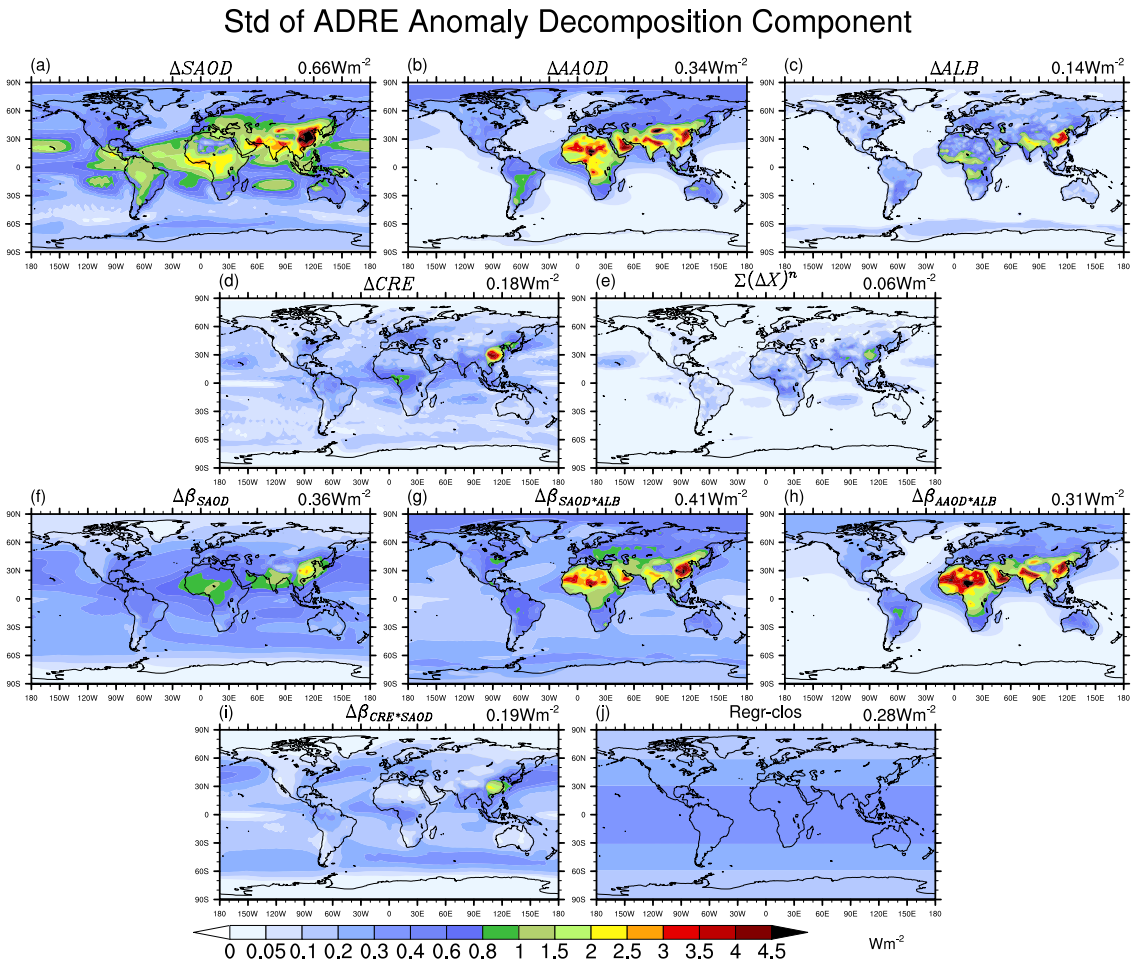

Figure 3.3 Spatial distributions of the standard deviations of decomposed components of ADRE anomaly in the CMIP6 GCMs. (a–e) Contributions from differences in state variables. (f–j) Contributions from differences in radiative sensitivity. Global mean values are indicated in the top-right corner of each subplot.

3.4 Conclusions

This work evaluates the contributions to the ADRE anomaly in CMIP6 models using a novel regression method abiding by the principle of parsimony while accounting for the key nonlinear radiative transfer effects. Contributions from the differences in state variables and the radiative sensitivity are separately quantified and compared. The following questions are addressed.

How well does the analytical (regression) model represent the ADRE inter-model spread $\left(\Delta ADRE_j\right)$ *in the CMIP6?* The regression model effectively captures the spatial distributions and global mean values of the ADRE anomaly (Figure 3.1). For individual GCMs, it explains 86±3% of the spatial variance in the ADRE anomaly; it also captures 94% of the spatial variance in the inter-model standard deviations of the ADRE anomaly. The model almost perfectly constrains the global mean values of the ADRE anomaly and their standard deviation (0.72 Wm^{-2}). The unexplained ADRE anomaly, accounting for 2% of the ADRE standard deviation, is primarily located in China and the Southeast Atlantic likely because the regression model is limited by its linear assumption and the simplified representations of the ADRE.

How much do the differences in state variables and radiative sensitivity contribute to the ADRE discrepancy? On average, the state variable differences explain 67±16% of the model spread in ADRE, while the radiative sensitivity variances explain 17±21% (Table 3.1). Among the state variables assessed, scattering aerosol optical depth (ΔSAOD) contributes most to the standard

deviation of the ADRE anomaly, with the global mean value being 0.66 W/m^2. Other factors, such as cloud and surface albedo (ΔCRE and ΔALB), also manifest regional impacts (Figure 3), for example, contributing significantly over China where the standard deviation of the ADRE spread exceeds 3 W/m^2. The radiative sensitivity differences assessed in this study account for the treatments of aerosol-only scattering, scattering and absorptive aerosol-surface interaction, and cloud masking effects. Over the ocean, the contribution from the aerosol-only scattering effect dominates, while in desert regions and East Asia, the treatment of aerosol and surface interaction is more important.

What are the dominant contributors in each selected CMIP6 model? For global mean values (Figure 3.2), the CNRM-ESM2 and GFDL-ESM4 models are mainly influenced by differences in state variables, while others are more affected by radiative sensitivity variance. The dominant contributor in the CNRM-ESM2 model is the overall underestimation of SAOD, whereas in the GFDL model it is the overestimation of AAOD. For the HadGEM3, MPI-ESM, and MRI-ESM2 models, the ADRE sensitivity to aerosol-only scattering effects is the main contributor. The CNRM-ESM2 model stands out as an outlier, displaying substantial contributions from both state variables and radiative sensitivity in comparison to other models. The dominant contributor to the ADRE anomaly varies across regions. In East Asia, the main contributors in the GFDL and MPI-ESM models are the AAOD and CRE differences, respectively. In the Arctic, the main contributor in the GFDL and MRI-ESM2 models is the AAOD difference. It is also noticeable that the compensations from different contributors can be significant.

These results highlight the need for constraining the inter-model discrepancies in ADRE among the CMIP6 models. In particular, constraining the key state variables (AOD, ALB, and

CRE) and the ADRE sensitivity to aerosol-related processes (aerosol-only scattering, aerosol-surface interaction) could help reduce ADRE uncertainty according to our findings.

While this work provides a simple way of diagnosing the inter-model ADRE spread, the regression method has limits in its accuracy because of the number of predictors included and simplified representation of their interactions (e.g., inability to represent relative vertical positions of aerosol and clouds). Nevertheless, the method identifies the major factors accounting for the ADRE anomaly in each model and the regions where they matter, which warrants, and provides guidance to, future work to improve their ADRE simulations.

Data Availability Statement

The CMIP6 data used for this analysis including the radiation and aerosol optical depth data are available at Earth System Grid Federation (Krasting et al., 2018; Seferian, 2018; Ridley et al., 2019; Neubauer et al., 2019; Yukimoto et al., 2019).

Chapter 4 Quantifying the Direct Radiative Effect of Stratospheric Aerosols Using Radiative Kernels

Chapter 4, in full, is a manuscript submitted to Journal of Geophysical Research: Atmospheres.

Qiurun Yu, Yi Huang. Quantifying the Direct Radiative Effect of Stratospheric Aerosols Using Radiative Kernels. *ESS Open Archive.* August 15, 2024.

DOI: 10.22541/essoar.172374105.56686934/v1

The thesis author is the lead author and principal investigator for this paper.

Quantifying the Direct Radiative Effect of Stratospheric Aerosols Using Radiative Kernels

Qiurun Yu[1*], Yi Huang[1]

[1] Department of Atmospheric and Oceanic Sciences, McGill University, Montreal, Quebec, Canada.

Corresponding author: Qiurun Yu (qiurun.yu@mail.mcgill.ca)

Key Points:

- A global dataset of radiative sensitivity kernels is developed to quantify stratospheric aerosol direct radiative effect (ADRE).
- An analytical model is developed to emulate the kernel values from a handful of predictor variables.
- The stratospheric aerosol kernels capture the spatiotemporally varying ADRE values of volcanic eruptions and wildfire events well.

Abstract

To facilitate the quantification of the stratospheric aerosol radiative effect, this study generates a set of aerosol direct radiative effect (ADRE) kernels based on MERRA-2 reanalysis data. These radiative kernels measure the sensitivities of ADRE to perturbations in scattering and absorbing aerosol optical depth (AOD), respectively. Both broadband and band-by-band radiative kernels are developed to account for the wavelength dependency of ADRE. The broadband kernels are then emulated by a multivariate regression model, which predicts the kernel values from a handful of predictors, including the top-of-atmosphere (TOA) insolation, TOA reflectance, and stratospheric AOD. These kernels offer an efficient and versatile way to assess the ADRE of stratospheric aerosols. The ADREs of the 2022 Hunga volcano eruption and the 2020 Australia wildfire are estimated from the kernels and validated against radiative transfer model-calculated results. The Hunga eruption induced a global mean cooling forcing of -0.46 W/m² throughout 2022, while the Australia wildfire caused a warming forcing of +0.28 W/m² from January to August. The kernel estimation can capture over 90% of the ADRE variance with relative errors within 10%, in these assessments. The results demonstrate the spectral dependencies of stratospheric ADRE and highlight the distinct radiative sensitivity of stratospheric aerosols, which differs significantly from that of tropospheric aerosols.

Plain Language Summary

Stratospheric aerosols influence the Earth's energy balance by scattering and absorbing solar radiation, making it crucial to accurately measure their radiative impact. However, quantifying the aerosol radiative impact is computationally expensive if using radiative transfer models. In this work, we develop a set of aerosol radiative kernels, which can provide a flexible and efficient means for calculating the radiative effects of stratospheric aerosols. The kernels have

been demonstrated to effectively quantify the radiative impacts of stratospheric aerosols resulting from wildfire and volcanic eruption events.

4.1 Introduction

Stratospheric aerosols influence the Earth's radiative energy budget and have profound climate impacts (Kremser et al., 2016). The largest contributor to stratospheric aerosols is volcanic eruptions, which can inject a mixture of sulfur dioxide, sulfuric acid, and water directly into the stratosphere, where they transform into stratospheric aerosols (Martinsson et al., 2019). By increasing the reflection of solar radiation, those volcanic aerosols exert a negative radiative forcing at the top-of-the-atmosphere (TOA), which can lead to pronounced surface cooling and changes in atmospheric circulation and water cycle (Robock, 2000; Grinsted et al., 2007; C.-H. Wu et al., 2023; Günther et al., 2024). Apart from volcanic eruptions, wildfires-induced pyrocumulonimbus (PyroCb) events can also transport a significant amount of carbonaceous aerosols into the lower stratosphere (Fromm et al., 2010; Ohneiser et al., 2020; C.-C. Liu et al., 2022; Damany-Pearce et al., 2022). Observation and model studies suggest that the absorptivity of biomass-burning aerosols can warm the stratosphere, deplete the stratospheric ozone, and modify vertical dynamics and horizontal dispersion (Damany-Pearce et al., 2022; Ohneiser et al., 2020, 2023).

Although the importance of stratospheric aerosols is well recognized, the quantification of their radiative effect has not been an easy task, as it requires the consideration of multiple factors, including aerosol types, height and size distributions, as well as the environmental factors at their locations (Weisenstein et al., 2015; MacMartin et al., 2017; Q.-R. Yu et al., 2019; Visioni et al., 2020; P. Yu et al., 2023; Q. Yu et al., 2024). The straightforward and most accurate way to quantify the aerosol direct radiative effect (ADRE) is the Partial Radiative Perturbation (PRP) method,

which requires running a radiative transfer model and differencing the modeled radiative fluxes with and without aerosol perturbations, although this quantification method is computationally expensive. Many studies used alternative approaches to estimate ADRE, for example, by using an analytical relationship between the aerosol optical depth (AOD) and the radiative effect. Hansen et al. (2005) estimated a radiative sensitivity of -22 W/m^2 per unit AOD change, based on the simulation of the Pinatubo eruption case using a global climate model. P. Yu et al. (2023) reported a similar scaling relation for stratospheric aerosols also based on modeling experiments. (Schoeberl et al., 2023, 2024a) applied the radiative sensitivity kernels of Q. Yu & Huang (2023b) to evaluate the climate impacts of the 2022 Hunga volcano eruption. However, these kernels were derived based on the aerosol perturbations in the whole atmospheric column, which is dominated by tropospheric, as opposed to stratospheric aerosols.

To the best of our knowledge, a global dataset of radiative sensitivity kernels specifically developed for assessing the ADRE of stratospheric aerosols is still lacking. The existing global aerosol kernels, including those of Q. Yu & Huang (2023b) and Thorsen et al. (2020), were developed with a focus on tropospheric aerosols, whose radiative sensitivity, as shown later in this paper, differ markedly from stratospheric aerosols. A recent study by Gao et al. (2023) tested the kernel quantification of the ADRE of tropopause aerosols, although the development was limited to the East Asia region. A global kernel dataset, which can facilitate an efficient yet accurate quantification of the spatiotemporally varying radiative impacts of stratospheric aerosols, is expected to have a broad spectrum of applications. This is especially relevant given the frequent occurrence of wildfires (Damany-Pearce et al., 2022), recent volcanic eruptions (Taha et al., 2022), and the increasing discussions about stratospheric aerosol geoengineering (Visioni et al., 2020).

It is well recognized that the aerosol optical properties, radiative transfer, and the resulting aerosol radiative effects, all have a strong spectral dependence. For example, the spectral dependence of AOD is often approximated using the Angstrom relationship (Ångström, 1929), although the Angstrom exponent (AE) may vary with wavelength (Schuster et al., 2006) and height (Z. Chen et al., 2020). Incorporating spectrally measured aerosol optical properties can reduce uncertainty in the ADRE quantification (Chauvigné et al., 2021). Thorsen et al. (2020) found that distinguishing column-integrated aerosol optical properties in the mid-visible and near-infrared wavelengths can help constrain ADRE, pointing to the potential benefits of developing band-by-band kernels. In addition, spectral kernels may take advantage of the spectral AOD information, which is available from many state-of-the-art climate models as well as satellite and ground-based measurements. Therefore, in addition to a set of broadband stratospheric aerosol kernels, we also aim to produce an accompanying set of spectrally decomposed, band-by-band kernels, to facilitate the use of spectral information in the ADRE quantification.

Observational and modeling studies have shown that ADRE sensitivity is strongly influenced by environmental conditions such as clouds, relative humidity, and surface albedo (McComiskey et al., 2008; Loeb et al., 2019; Schoeberl et al., 2023; Q. Yu & Huang, 2023a, 2023b). However, the primary environmental factors affecting stratospheric ADRE sensitivity and their underlying physics remain to be elucidated. Another objective of our study is to investigate this environmental dependence. Integrating a physical model with statistical analyses, we experiment with sorting the global aerosol kernels, which are conventionally computed on geographic grids (latitude, longitude, and calendar month), based on the geophysical variables that govern the kernel values according to radiative transfer physics. We aim to establish an analytical equation to capture the spatiotemporal variations of the kernel values. Such an analytical relation

can be considered a physical (as opposed to geographical) kernel dataset and can be used for the ADRE quantification under arbitrary situations regardless of the geographic location, which potentially makes the kernels suitable for broader applications.

In summary, in this study, we aim to develop a set of radiative sensitivity kernels that are specifically designed for quantifying the stratospheric ADRE. The kernels developed here include both broadband and spectral band-by-band TOA flux kernels provided on conventional latitude-longitude-month grids, as well as physically sorted broadband kernels whose values are determined from analytical equations. The structure of this paper is as follows. Section 4.2 details the methods used to calculate both broadband and band-by-band kernels. Section 4.3 describes the development of physically sorted kernels. These aerosol kernels constitute a versatile means to quantify the stratospheric ADRE. We demonstrate the use and performance of these kernels by applying them to two cases: the 2022 Hunga volcanic eruption (Bourassa et al., 2023; Kloss et al., 2022; Taha et al., 2022) and the 2020 Australia wildfire (Ohneiser et al., 2020; Damany-Pearce et al., 2022; Sellitto et al., 2022) in Section 4.4. A summary is provided in Section 4.5.

4.2 Data and Methods

4.2.1 Stratospheric Aerosol Direct Radiative Effect

The stratospheric ADRE is calculated as the difference in net radiative fluxes at TOA with and without stratospheric aerosols:

$$\text{Stratos ADRE} = F^{net}(all\ aerosols) - F^{net}(no\ stratos\ aerosols) \quad (4.1)$$

where $F^{net} = F^{\downarrow} - F^{\uparrow}$, with the downward flux $F^{\downarrow}$ being positive.

In this study, we focus on the shortwave stratospheric ADRE at the TOA under all-sky conditions. This is because the longwave ADRE is orders of magnitude smaller (Reddy et al., 2005; Heald et al., 2014; Balmes & Fu, 2021), and aerosol scattering is often neglected in the longwave schemes

of radiative transfer models (Mlawer et al., 1997, 2016), despite stratospheric aerosols being primarily scattering particles. However, the method described here can also be used to calculate aerosol kernels in the longwave spectrum, at the surface, or for atmospheric heating rate. Radiative fluxes are computed using the Rapid Radiative Transfer Model (RRTMG) (Mlawer et al., 1997, 2016). The required inputs for these calculations are obtained from the Modern-Era Retrospective Analysis for Research and Applications, Version 2 (MERRA-2) dataset (Gelaro et al., 2017). We use instantaneous atmospheric and cloud profiles, including air temperature and pressure, surface temperature, surface albedo, water vapor, ozone, specific humidity, cloud fraction, and the mass fraction of cloud liquid and ice water. The tropopause is defined according to the criterion of the World Meteorological Organization (WMO, 1957) as the lowest level where the temperature lapse rate decreases to 2 K/km or less, and the average lapse rate from this level to any level within the next 2 km does not exceed 2 K/km.

Aerosol optical properties are calculated based on the MERRA-2's instantaneous aerosol mixing ratio profiles, which include 72 layers. MERRA-2 provides 15 externally mixed aerosol tracers: hydrophobic and hydrophilic black and organic carbon, sulfate, dust (five size bins), and sea salt (five size bins) (Randles et al., 2017). Aerosol optical properties vary with relative humidity to account for hygroscopic growth. For computational efficiency, the 3-hourly MERRA-2 inputs are resampled into a 2.5° × 2.5° grid box. Our goal is to replicate the aerosol radiative transfer calculations from the MERRA-2 dataset and isolate the impact of stratospheric aerosols to study the stratospheric ADRE. Validations of aerosol optical property inputs and total ADRE calculations against MERRA-2 diagnostic aerosol and radiation products are provided in the Appendix C (Figures C1-C3).

4.2.2 Computation of Stratospheric Aerosol Kernels

Aerosol radiative kernels ($\frac{\partial(ADRE)}{\partial x}$) are the partial derivative of the ADRE to an aerosol-related property x such as AOD and single scattering albedo. These kernels represent how ADRE responds to atmospheric aerosol perturbations. By multiplying the radiative kernels with the changes in x, we can approximate the resulting change in ADRE, which provides a convenient means for estimating the radiative impact of aerosols.

In this study, we develop kernels for both stratospheric scattering aerosol optical depth (AOD_{scat}) and absorbing aerosol optical depth (AOD_{abs}). For each type of kernel, radiative transfer calculations are performed twice: one with background aerosols and one with perturbations in the stratospheric aerosols. The sizes of the perturbation are 0.1 for AOD_{scat} and 0.01 for AOD_{abs} at 550 nm. The perturbation magnitude differs between stratospheric AOD_{scat} and AOD_{abs} due to the smaller background stratospheric AOD_{abs} compared to AOD_{scat}. We use absolute perturbation values instead of relative ones (such as 1%) to minimize noise from numerical errors caused by very small background AOD values. We have verified that the radiative flux changes respond linearly to the AOD perturbations within the typical magnitudes of stratospheric aerosol perturbations (ΔAOD_{scat} ranging from 10^{-3} to 1 and ΔAOD_{abs} ranging from 10^{-4} to 1, respectively). The sum of the AOD_{scat} and AOD_{abs} effects can also be linearly added to determine the total stratospheric ADRE. Sensitivity tests have also been conducted to determine the impacts of perturbation height on the aerosol kernels. Results indicate minimal difference between perturbing a single layer at random altitudes versus the entire stratosphere. Therefore, for our perturbation runs, we assume a conserved vertical profile shape of stratospheric aerosols. Details about sensitivity tests of linear scaling, linear additivity, and height dependency of stratospheric aerosol kernels are provided in the Appendix C (Figures C4-C6).

The perturbation computations produce both broadband and band-by-band stratospheric aerosol kernels. To account for the diurnal cycle, the 3-hourly kernels are averaged into monthly mean values. These aerosol kernels are computed for an El Niño-Southern Oscillation (ENSO) neutral year, 2022. The impact of interannual variability on aerosol kernels is small, as demonstrated by the comparisons of monthly mean kernels between 2020 and 2022. The R-squared values and Root Mean Squared Errors (RMSE) between the monthly mean AOD_{scat} kernels in those two years are 92% and 3.62, respectively, while for the AOD_{abs} kernels, they are 97% and 46.90, respectively. Detailed comparisons are provided in the Appendix C (Figure C7), showing consistency in both spatial distributions and global mean values.

4.2.2.1 Broadband Aerosol Kernels

Given that solar energy peaks in the mid-visible bands and that aerosol optical properties are commonly observed in this range, we use the 550 nm AOD as the perturbation variable. The stratospheric AOD_{scat} and AOD_{abs} kernels are defined as follows:

$$\frac{\partial(ADRE)}{\partial(AOD_{scat})} = \frac{F^{net}(AOD_{scat}+\Delta AOD_{scat},\ AOD_{abs}, \text{SSA', g'}) - F^{net}(AOD_{scat},\ AOD_{abs},\ \text{SSA, g})}{\Delta AOD_{scat}^{550}} \quad (4.2)$$

$$\frac{\partial(ADRE)}{\partial(AOD_{abs})} = \frac{F^{net}(AOD_{sca},\ AOD_{abs}+\Delta AOD_{abs}, \text{SSA', g'}) - F^{net}(AOD_{scat},\ AOD_{abs},\ \text{SSA, g})}{\Delta AOD_{abs}^{550}} \quad (4.3)$$

In the unperturbed runs, the background aerosol profiles of AOD, single scattering albedo (SSA), and asymmetry factor (g) are taken from reconstructed MERRA-2 aerosol optical property profiles. In the perturbation runs, an aerosol layer representing the stratospheric aerosol perturbations is added to the background aerosol profile. This added aerosol layer has the scattering or absorbing AOD values at 550 nm of 0.1 and 0.01, respectively, and the incremental AOD values (ΔAOD_{scat} and ΔAOD_{abs}) at other wavelengths are prescribed according to the Angstrom relationship (with the AE being 1). For the scattering AOD perturbation, the SSA and g values of

this added layer are assumed to be 1 and 0.7. The g value is based on annual and global mean asymmetry factor values reported by Ayash et al. (2008) as well as the background upper troposphere and lower stratosphere aerosol configurations in Sellitto et al. (2022). Weighted averaging is used to calculate the values of these aerosol properties in the perturbation runs. For AOD_{scat} perturbation runs,

$$SSA' = \frac{SSA^{550} \cdot AOD^{550} + 1 \cdot \Delta AOD_{scat}^{550}}{AOD^{550} + \Delta AOD_{scat}^{550}} \tag{4.4}$$

$$g' = \frac{g^{550} \cdot SSA^{550} \cdot AOD^{550} + 0.7 \cdot 1 \cdot \Delta AOD_{scat}^{550}}{SSA^{550} \cdot AOD^{550} + 1 \cdot \Delta AOD_{scat}^{550}} \tag{4.5}$$

For AOD_{abs} perturbation runs, the SSA and g values are

$$SSA' = \frac{SSA^{550} \cdot AOD^{550} + 0 \cdot \Delta AOD_{abs}^{550}}{AOD^{550} + \Delta AOD_{abs}^{550}} \tag{4.6}$$

$$g' = g \tag{4.7}$$

To use the aerosol kernels derived here to calculate ADRE, users simply need to obtain stratospheric ΔAOD_{scat}^{550} and ΔAOD_{abs}^{550} values appropriate to the case of interest, and then multiply these with broadband kernel values.

$$\Delta ADRE = \frac{\partial(ADRE)}{\partial(AOD_{scat})} \cdot \Delta AOD_{scat}^{550} + \frac{\partial(ADRE)}{\partial(AOD_{abs})} \cdot \Delta AOD_{abs}^{550} \tag{4.8}$$

Figure 4.1 shows the global distribution of annual mean stratospheric AOD_{scat} and AOD_{abs} kernels, in the units of W/m^2 per unit change in stratospheric AOD. Both AOD_{scat} and AOD_{abs} kernels exhibit strong atmosphere dependencies. In cloudy regions (e.g., the Intertropical Convergence Zone, tropical eastern Atlantic, northwest Pacific Ocean, and Southern Ocean), the sensitivity of stratospheric ADRE to stratospheric AOD_{scat} is relatively lower due to the presence of underlying clouds, while the sensitivity to AOD_{abs} is relatively higher, compared to other regions. This is because in the case of the scattering effect, clouds already brighten the atmosphere and make the TOA radiation less sensitive to scattering aerosols and in the case of the absorbing effect, clouds

increase the solar radiation reflected into the stratosphere, thereby amplifying the absorption by the stratospheric aerosols. Similar patterns are observed over the polar and desert regions with high surface albedo. Because of their scattering or absorbing nature, AOD_{scat} kernels are always negative, while AOD_{abs} kernels are always positive. In terms of global means, a 0.1 increase in stratospheric AOD_{scat}^{550} results in a -2.65 W/m² cooling, while a 0.1 increase in AOD_{abs}^{550} results in a +41.95 W/m² warming at the TOA. Note that these sensitivity values are larger than those reported by Q. Yu & Huang (2023b), particularly for absorbing aerosols. This is because the kernels developed in this study focus exclusively on stratospheric aerosols. These aerosols interact with a larger proportion of photons that have not been attenuated by clouds or tropospheric absorbers. Additionally, underlying clouds enhance the brightness of the troposphere, which further intensify the sensitivity of stratospheric ADRE to AOD_{abs}.

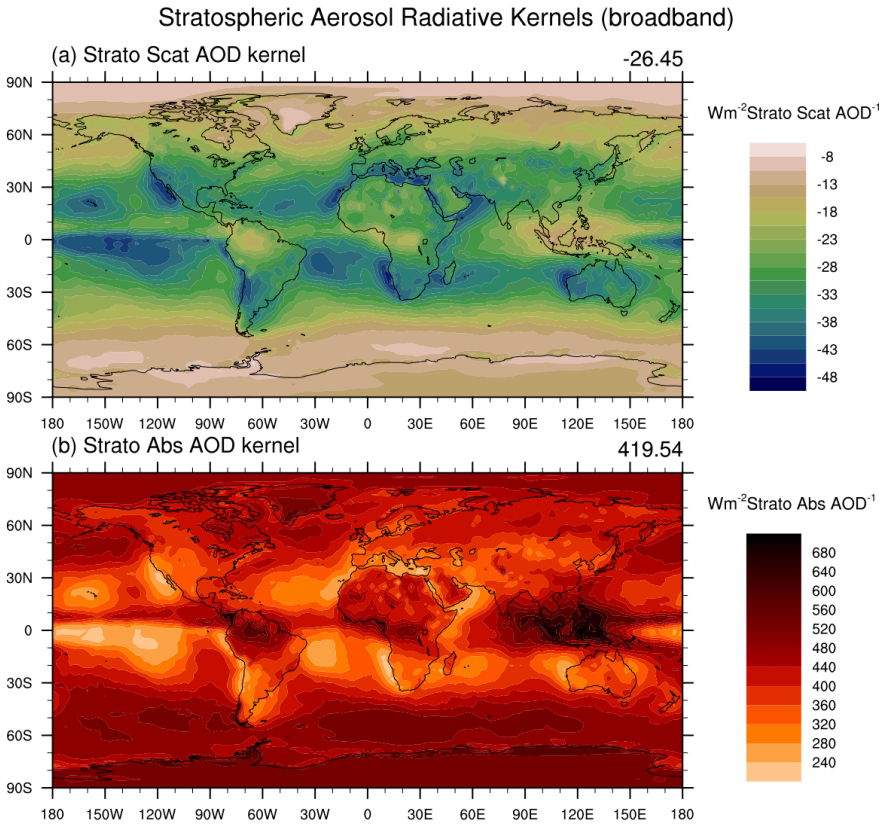

Figure 4.1 Spatial distributions of annual mean broadband aerosol kernels (a) for stratospheric AOD_{scat} and (b) for stratospheric AOD_{abs}. The global mean and annual mean values are indicated in the upper right corner of each subplot. Kernels are shown in units of watts per square meter per unit change in stratospheric AOD at 550 nm.

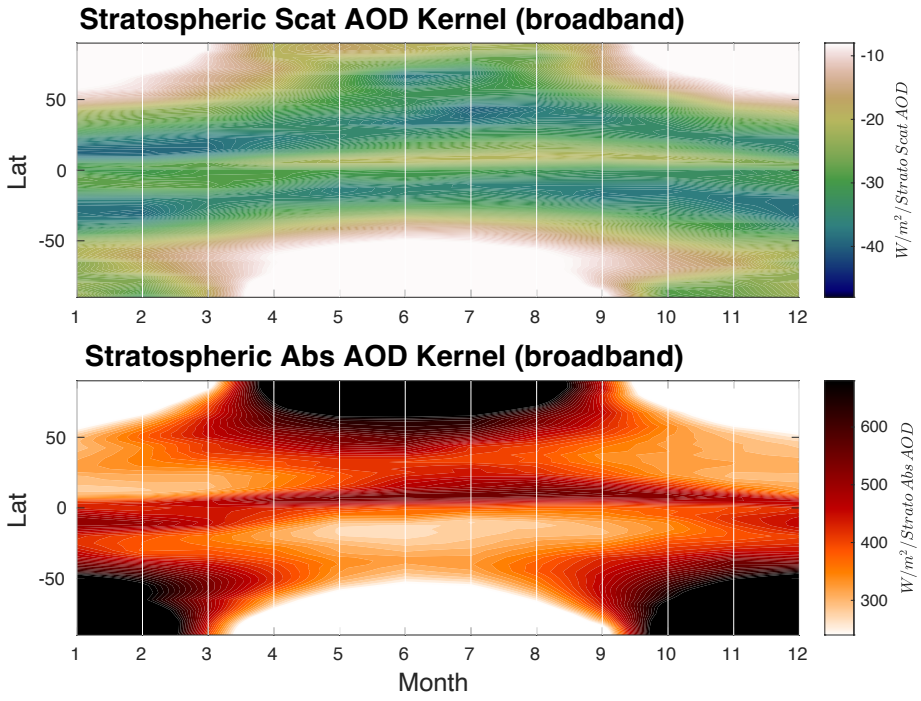

Figure 4.2 Temporal variations of zonal mean broadband stratospheric aerosol kernels (a) for stratospheric AOD_{scat} and (b) for stratospheric AOD_{abs}.

Apart from the spatial inhomogeneity, stratospheric aerosol kernels also display strong temporal variations. Figure 4.2 displays the temporal variations in zonal mean stratospheric broadband AOD_{scat} and AOD_{abs} kernels. The pronounced latitudinal differences in aerosol kernels reflect patterns of solar insolation. In tropical regions, the sensitivity of ADRE to stratospheric aerosols remains high throughout the year, while polar regions show notable seasonal variations.

4.2.2.2 Band-by-band Aerosol Kernels

While broadband aerosol kernels are convenient to use, they rely on assumptions about the wavelength dependency of aerosol optical properties, which may not always be accurate. To facilitate a more flexible and accurate ADRE quantification, we leverage the band configuration of the RRTMG model to calculate a set of band-by-band stratospheric aerosol kernels. The RRTMG shortwave bands, detailed in Table 1, cover a spectrum from 0.2 μm to 12.2 μm across 14 bands.

Table 4.1 RRTMG Shortwave Bands.

SW band	**Wavenumber** $\boldsymbol{v[cm^{-1}]}$	**Wavelength** $\boldsymbol{\lambda\,[nm]}$	**AOD wavelength [nm]**
Band 29	820-2600	12195- 3846	7082.2
Band 16	2600-3250	3846-3077	3444.7
Band 17	3250-4000	3077-2500	2777
Band 18	4000-4650	2500-2151	2320.2
Band 19	4650-5150	2151-1942	2044.2
Band 20	5150-6150	1942-1626	1778.4
Band 21	6150-7700	1626-1299	1455.2
Band 22	7700-8050	1299-1242	1270
Band 23	8050-12850	1242-778	944.3

Band 24	12850-16000	778-625	693.5
Band 25	16000-22650	625-442	527.1
Band 26	22650-29000	442-345	399.8
Band 27	29000-38000	345-263	329.1
Band 28	38000-50000	263-200	229.8

The stratospheric aerosol band-by-band kernels for AOD_{scat} and AOD_{abs} are expressed as:

$$\frac{\partial ADRE^i}{\partial AOD^i_{scat}} = \frac{F^{net}\left(AOD^i_{scat}+\Delta AOD^i_{scat}, AOD^i_{abs}, \text{SSA}', \text{g}'\right)-F^{net}\left(AOD^i_{scat}, AOD^i_{abs}, \text{SSA}^i, \text{g}^i\right)}{\Delta AOD^i_{scat}} \quad (4.9)$$

$$\frac{\partial ADRE^i}{\partial AOD^i_{abs}} = \frac{F^{net}\left(AOD^i_{scat}, AOD^i_{abs}+\Delta AOD^i_{abs}, \text{SSA}', \text{g}'\right)-F^{net}\left(AOD^i_{scat}, AOD^i_{abs}, \text{SSA}', \text{g}'\right)}{\Delta AOD^i_{abs}} \quad (4.10)$$

In the equations above, i represents the i[th] band in RRTMG. ΔAOD^i_{scat} and ΔAOD^i_{abs} are the added AOD perturbation at the i[th] band, which vary with wavelength according to the Angstrom relation in our calculation.

$$\Delta AOD^i_{scat} = 0.1 \cdot \left(\frac{wavelength^i}{550}\right)^{-1} \quad (4.11)$$

$$\Delta AOD^i_{abs} = 0.01 \cdot \left(\frac{wavelength^i}{550}\right)^{-1} \quad (4.12)$$

Note that for each band, perturbed AOD is calculated at the central wavelength following RRTMG configuration as listed in Table 4.1. The SSA and g calculations in the perturbation runs are similar to those in the broadband kernel calculation.

To use the band-by-band kernels, users need to obtain the ΔAOD^i_{scat} and ΔAOD^i_{abs} for each band, multiply them by band-by-band kernels, and sum over the 14 bands.

$$\Delta\text{ADRE} = \sum_{i=16}^{29}\left(\frac{\partial ADRE^i}{\partial AOD^i_{scat}} \cdot \Delta AOD^i_{scat}\right) + \sum_{i=16}^{29}\left(\frac{\partial ADRE^i}{\partial AOD^i_{abs}} \cdot \Delta AOD^i_{abs}\right) \quad (4.13)$$

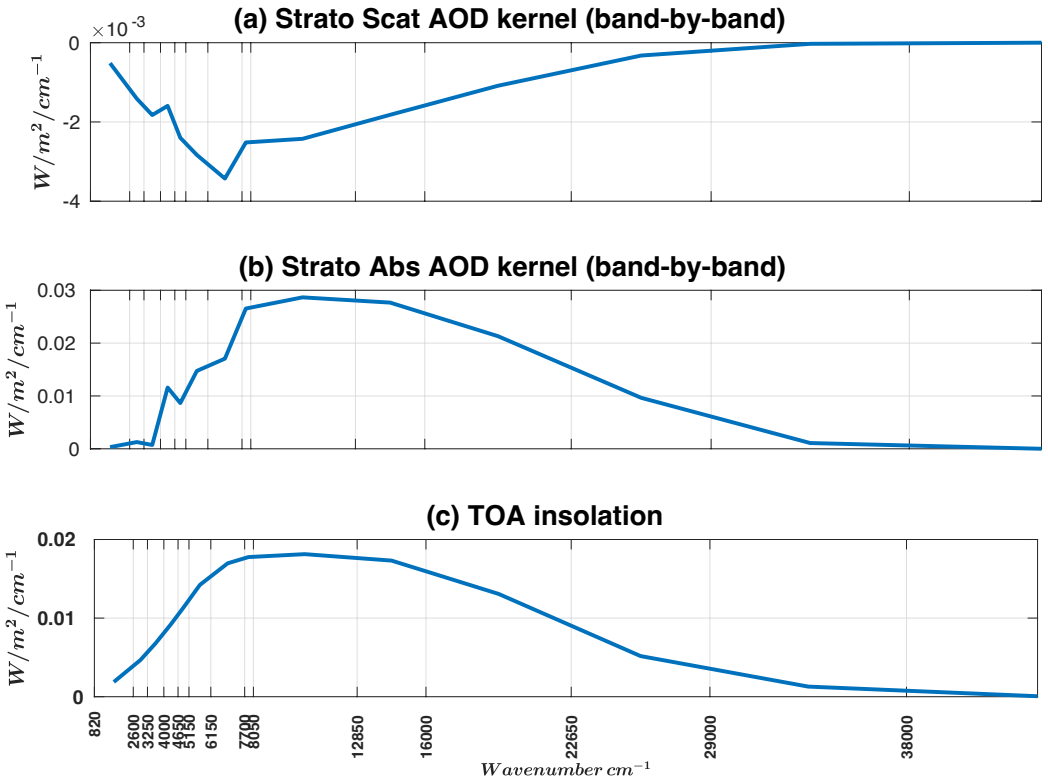

Figure 4.3 Global mean annual mean stratospheric aerosol band-by-band kernels for (a) AOD_{scat} and (b) AOD_{abs}. For demonstration purposes, kernels are normalized by the corresponding bandwidth. The normalized kernel unit is watts per meter squared per unit change in the respective stratospheric AOD per wavenumber. (c) Normalized spectral solar radiation.

Figure 4.3 presents the global mean band-by-band stratospheric AOD_{scat} and AOD_{abs} kernels. For comparison purposes, the spectral kernels are normalized by the bandwidth. The results indicate that the spectral signatures of the band-by-band aerosol kernels are primarily dominated by the strength of incoming solar radiation. The aerosol radiative sensitivity peaks from the near-ultraviolet band (~22650 cm^{-1}) to the near-infrared band (~8080 cm^{-1}), which corresponds to band 23 to 25 (442 nm-1242 nm) in RRTMG as indicated in Table 4.1.

Accurately determining aerosol optical properties in these bands can help constrain the ADRE without needing the aerosol information across the full spectrum. Most aerosol retrieval

products provide optical properties at a few discrete wavelengths ranging from near-ultraviolet to near-infrared. For example, the AErosol RObotic NETwork (AERONET) provides AOD products at 340, 380, 440, 500, 675, 870, and 1020 nm (Giles et al., 2019). By interpolating observed AOD values at the central AOD wavelengths in the RRTMG configuration for relevant bands and assuming spectral dependence of optical properties for the remaining bands, users can calculate stratospheric ADRE more accurately than using broadband kernels. In the following section, we will use the spectral AOD observations to compare the ADRE values computed from the broadband and band-by-band stratospheric aerosol kernels.

4.2.3 OMPS Aerosol Data and Quality Control

To quantify the stratospheric ADRE, we utilize the aerosol extinction coefficient profiles from the OMPS-LP Level 2 daily product. The Ozone Mapping and Profiler Suite (OMPS) measures limb scattering of sunlight at tangent altitudes from ground level up to approximately 100 km with a vertical resolution of 1km (Flynn et al., 2006). The aerosol product from OMPS has been widely used to study the stratospheric ADRE (Damany-Pearce et al., 2022; Bourassa et al., 2023; Schoeberl et al., 2023, 2024a). This study uses aerosol extinction coefficient retrievals along the center slit (aligned with the orbital track) of the OMPS-LP. The retrieved extinction profiles extend up to 40km, and quality control procedures are applied before the analysis following Damany-Pearce et al. (2022). Only data with ResidualFlag = 0, SingleScatteringAngle $\leq 145^{\circ}$, and SwathLevelQualityFlags with bits 0, 1, and 7 = 0 are considered valid. The tropopause definition is consistent with that used in the kernel calculation. We integrate the extinction coefficient throughout the stratosphere to calculate the stratospheric AOD. To facilitate kernel application, we average the AOD data onto the same 2.5° × 2.5° latitude-longitude grid.

For using the broadband aerosol kernels, we choose the 869 nm extinction coefficient from OMPS and scale it to 550 nm, assuming an AE value of 1. This AE value is chosen because it represents the background stratospheric aerosol conditions and the specific conditions of the Hunga aerosols, and has been applied in other similar studies (Schoeberl et al., 2023; Sellitto et al., 2024). The 869 nm wavelength is chosen over other channels closer to 550 nm because OMPS aerosol products have performance issues at shorter wavelengths in the southern hemisphere (Taha et al., 2021).

For the band-by-band kernel application, we utilize extinction coefficients measured at 510 nm, 600 nm, 675 nm, 745 nm, 869 nm, and 997 nm, and interpolate extinction values to 527.1 nm, 693.5 nm, and 944.3 nm using measurements from the nearest wavelengths as required by the aerosol kernels. For the remaining bands, we scale the extinction coefficient from 869 nm to the corresponding central AOD wavelength, assuming an AE of 1. In the following section, we use the OMPS spectral AODs as an example to demonstrate the usage of our kernels.

Our goal is to estimate the changes in stratospheric ADRE (ΔADRE) due to the 2022 Hunga volcanic eruption and the 2020 Australia wildfires using our aerosol kernels. We consider the MERRA-2 stratospheric AOD as the background aerosol states because no eruptive volcanoes are included in MERRA-2 after 2010 (Randal et al., 2016). Therefore, the stratospheric AOD anomaly is calculated by subtracting the background stratospheric AOD values given by MERRA-2 from OMPS stratospheric AOD. For the kernel application, the AOD values in Equations 4.8 and 4.13 are the differences between OMPS and MERRA-2 stratospheric AOD. To validate the performance of our aerosol kernels, we use the same AOD anomalies as input to the RRMTG model to calculate the "truth" values of stratospheric ADRE for comparison.

4.3 Physically Sorted Aerosol Kernels

As shown in the previous section (e.g., Figures 4.1 and 4.2), there are strong spatial and temporal variabilities in the kernel values. It is thus important to understand how the aerosol properties and environmental variables (e.g., surface albedo and clouds) interact with each other to influence the radiative sensitivity. To address this question, we follow a widely used conceptual model of ADRE (Chlek & Coakley Jr, 1974; J. M. Haywood & Shine, 1995) to identify the key factors and their expressions to use in an analytical model to predict the kernel values. We then determine the coefficient values statistically using a multivariable regression method following (Q. Yu & Huang, 2023a, 2023b). Different from the geographically gridded kernels presented in the previous section, the physically sorted kernels developed here are not constrained by space and time, allowing one to more flexibly estimate the stratospheric ADRE.

4.3.1 Physical Model

We follow the formulation of Haywood & Shine (1995), but consider the stratospheric aerosols as a scattering layer and represent the troposphere-surface system as a whole with a reflectance parameter at the tropopause. The all-sky stratospheric ADRE at the TOA can be expressed as follows:

$$\mathrm{ADRE} = -\mathrm{S}\cdot \mathrm{T}_{\mathrm{at}}^{2}\cdot \beta\cdot \omega\cdot \tau\cdot \sec\theta \frac{(1-R_S)^2 - \frac{R_S\cdot(1-\omega)}{\beta}\left[\frac{2-\tau\cdot\sec\theta}{\omega} - \tau\cdot\sec\theta\cdot(2\beta-1)\right]}{1-R_S\cdot\beta\cdot\omega\cdot\tau\cdot\sec\theta} \quad (4.14)$$

The environment-related variables are solar insolation (S), atmospheric transmittance (T_{at}) above the aerosol layer, the solar zenith angle (θ), and tropopause reflectance (R_s). The aerosol-related variables are the aerosol backscattering ratio (β), aerosol single scattering albedo (ω), and aerosol optical depth (τ). The stratospheric ADRE is further expanded as:

$$\mathrm{ADRE} = \tag{4.15}$$

$$-\mathrm{S}\cdot \mathrm{T}_{\mathrm{at}}^{2}\cdot \beta \cdot \omega \cdot \tau \cdot \sec\theta(1+R_s\cdot \tau \cdot \sec\theta \cdot \beta \cdot \omega)\{(1-R_s)^2-\frac{R_s(1-\omega)}{\beta}[\frac{2-\tau\cdot\sec\theta}{\omega}-\tau \cdot \sec\theta\cdot(2\beta-1)]\}$$

The sensitivity of stratospheric ADRE to τ is

$$\frac{\partial ADRE}{\partial \tau} = -\mathrm{S}\cdot \mathrm{T}_{\mathrm{at}}^{2}\cdot \beta \cdot \omega(1-R_s)^2(1+2\beta\cdot\omega\cdot R_s\cdot\tau\cdot\sec\theta) \tag{4.16}$$

$$+\mathrm{S}\cdot \mathrm{T}_{\mathrm{at}}^{2}\cdot \beta \cdot \omega(1+2\beta\cdot\omega\cdot R_s\cdot\tau\cdot\sec\theta)\frac{R_s(1-\omega)}{\beta}\left[\frac{2-\tau\cdot\sec\theta}{\omega}-\tau\cdot\sec\theta(2\beta-1)\right]+\mathrm{S}\cdot \mathrm{T}_{\mathrm{at}}^{2}\cdot \beta \cdot \omega(\tau\cdot\sec\theta+\beta\cdot\omega\cdot R_s\cdot\tau\cdot\sec\theta^2)\left[-\frac{R_s}{\beta}\frac{1-\omega}{\omega}-2\beta+1\right]$$

Neglecting higher-order terms, Equation 4.16 is approximated as

$$\frac{\partial ADRE}{\partial \tau} \tag{4.17}$$

$$= -\mathrm{S}\cdot \mathrm{T}_{\mathrm{at}}^{2}[\beta\cdot\omega+R_s(2\beta\cdot\omega+2-3\omega)-R_s^2\beta\cdot\omega+R_s\cdot\tau\cdot\sec\theta(-2+3\omega-2\omega\beta-\omega^2)+\beta\cdot\omega\cdot\tau\cdot\sec\theta]$$

This equation suggests that stratospheric aerosol kernels are influenced by these terms: R_s, $R_s\tau$, τ, and R_s^2. The combination terms arise from the coupling effects between the stratospheric aerosol layer and the underlying troposphere-surface system. In the following section, we will use these terms as predictors to reproduce the spatiotemporally varying stratospheric aerosol kernels. The goal is to capture the physical processes governing ADRE sensitivity, which should be independent from geographic locations.

4.3.2 Statistical Model

Regression models have been a useful tool in predicting radiative forcing and capturing nonlinear radiative interactions in many studies (Y. Huang et al., 2016; Datseris et al., 2022; Q.

Yu & Huang, 2023a, 2023b). In this work, we built a multi-variable regression model to represent the annual mean global stratospheric aerosol kernels following Q. Yu & Huang (2023b, 2023a). The model is expressed as:

$$\frac{\mathbf{Y(i,j)}-\overline{\mathbf{Y}}}{\overline{\mathbf{Y}}} = \sum_{\mathbf{k=1}}^{\mathbf{n}} \mathbf{A_k} \cdot \frac{\mathbf{X_k(i,j)}-\overline{\mathbf{X_k}}}{\overline{\mathbf{X_k}}} \quad (4.18)$$

Here, X are predictors (e.g., R_s, $R_s\tau$) at latitude i and longitude j. Y is either the broadband aerosol kernels for stratospheric AOD_{scat} or AOD_{abs}. A_k is the regression coefficient and n is the number of predictors. Note that the global field of Y is predicted by one uniform set of A_k values. Both predictors and predictands are normalized by their global mean values, denoted by a bar.

Following the physical model derived above, we select R_s, $R_s\tau$, τ, and R_s^2 as predictors. As TOA reflectance (R) is more easily obtained, we use it as a proxy for the tropopause reflectance. To accurately represent global aerosol kernels using as few predictors as possible, we have tested the performance of all possible combinations of predictors (listed in Appendix C Table C1-C2). Results suggest that the four predictors are sufficient to capture almost all main features of stratospheric aerosol kernels.

The physically sorted broadband aerosol kernels for stratospheric AOD_{scat} is given by

$$\frac{\frac{\partial(ADRE)}{\partial(AOD_{scat})}_S-(-0.076)}{(-0.076)} = -2.264\frac{\mathrm{R}-0.413}{0.413} + 0.753\frac{R^2-0.184}{0.184} + 0.671\frac{\tau-0.002}{0.002} - 0.3186\frac{\mathrm{R}\cdot\tau-0.001}{0.001} \quad (4.19)$$

The physically sorted broadband aerosol kernels for stratospheric AOD_{abs} is given by

$$\frac{\frac{\partial(ADRE)}{\partial(AOD_{abs})}_S - 1.323}{1.323} = -0.313\frac{R-0.413}{0.413} + 0.696\frac{R^2-0.184}{0.184} - 0.175\frac{\tau-0.002}{0.002} + 0.258\frac{\mathrm{R}\cdot\tau-0.001}{0.001} \quad (4.20)$$

The comparison of statistically fitted broadband aerosol kernels for stratospheric AOD_{scat} and AOD_{abs} against benchmark RRTMG calculations is shown in the Appendix C (Figures C8).

Results suggest that more than 94% of the spatial variance in aerosol kernels is captured by the regression model, indicating its effectiveness in predicting the variability of aerosol kernels.

Figure 4.4 displays the impact of environmental variables (TOA insolation S and reflectance R) on the distributions of annual mean global aerosol kernels. Generally speaking, an increase in solar insolation results in a larger magnitude of aerosol kernels, while a more reflective underlying "surface" (due to clouds or Earth's surface) leads to a less cooling or more warming impact on net TOA fluxes. The physically sorted aerosol kernels can well capture their sensitivity to those environmental variables. More importantly, they can estimate stratospheric ADRE sensitivity in idealized conditions where actual observations are lacking.

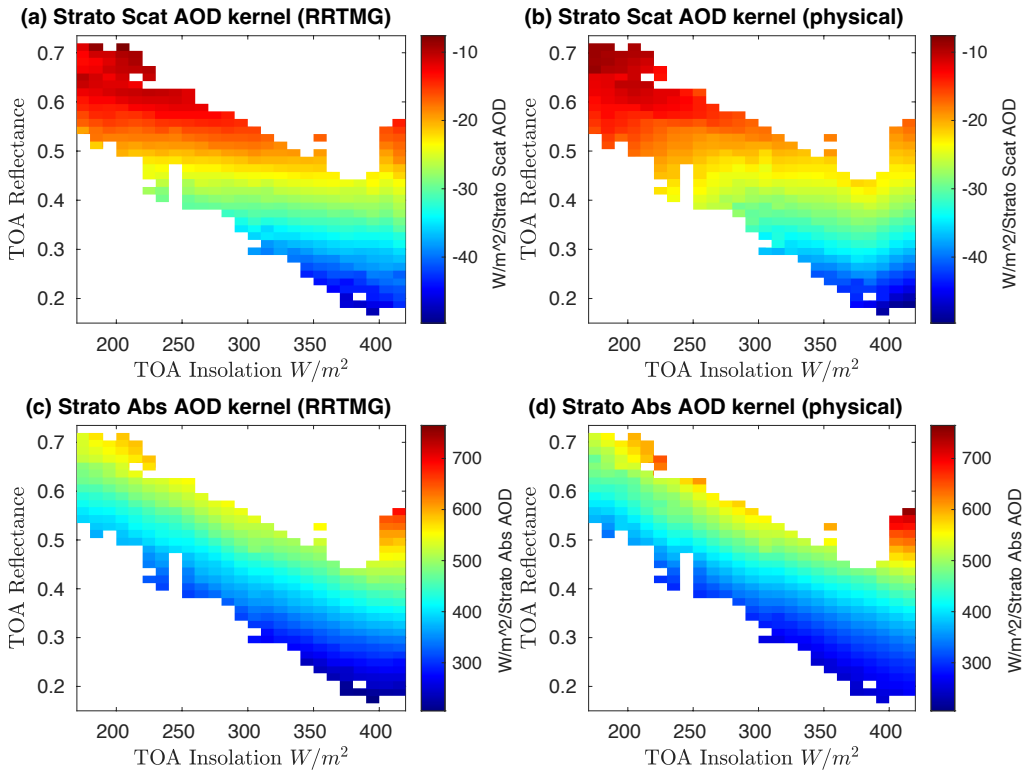

Figure 4.4 Distributions of broadband stratospheric AOD_{scat} and AOD_{abs} kernels as a function of TOA reflectance and TOA insolation. Left column: RRTMG-calculated stratospheric aerosol kernels; Right column: the physically sorted aerosol kernels predicted by the regression model.

4.4 Stratospheric Aerosol Kernel Applications

Multiplying aerosol radiative kernels by changes in stratospheric AOD from specific events (e.g., volcanic eruptions) provides estimates of the corresponding ADRE. In this section, we examine the radiative effects of the volcanic ash plume from the 2022 Hunga eruption and the biomass-burning aerosols from the 2020 Australia wildfires to demonstrate the application of stratospheric aerosol kernels. We compare the results of broadband, band-by-band, and physically sorted kernels.

4.4.1 Aerosol Radiative Kernel Comparisons

Given the kernels here are developed specifically for stratospheric aerosols, it is of interest to compare them with other kernels not designed this way. Besides the simple scaling relations given in the literature (e.g., Hansen et al. 2005; P. Yu et al. 2021), Q. Yu & Huang, (2023b, denoted as YH23 from here on) derived a set of global ADRE sensitivity kernels mainly for tropospheric aerosols and validated against the independent results of Thorsen et al. (2020). Schoeberl et al. (2023, 2024) used the YH23 kernels to estimate the radiative impact of the Hunga eruption. We include the YH23 kernels for comparison in the following.

In Figure 4.5, we compare the zonal mean AOD_{scat} and AOD_{abs} sensitivity in YH23 with the broadband stratospheric aerosol kernels calculated by RRTMG and the statistical regression model. Results show that the aerosol kernels display significant latitudinal differences. For all-sky stratospheric AOD_{scat} kernels, the magnitude peaks in the subtropical regions because the relative brightness of aerosols is reduced above the tropical cloudy regions. The physically sorted kernels closely match the RRTMG results, indicating a good performance of the physical sorting method. Interestingly, the clear-sky, as opposed to the all-sky, AOD_{scat} kernels given by YH23 render more similar magnitudes to the all-sky stratospheric AOD_{scat} kernels developed here, especially in the

mid-latitudes. This is because the stratospheric aerosols are located above tropospheric clouds, which suppress the radiative sensitivity to tropospheric AOD perturbations but do not strongly affect the radiative effect of stratospheric aerosols. Compared to the AOD_{abs} kernels in YH23, the stratospheric AOD_{abs} kernels developed here are much larger due to the enhanced ADRE sensitivity to AOD_{abs} above bright underlying clouds.

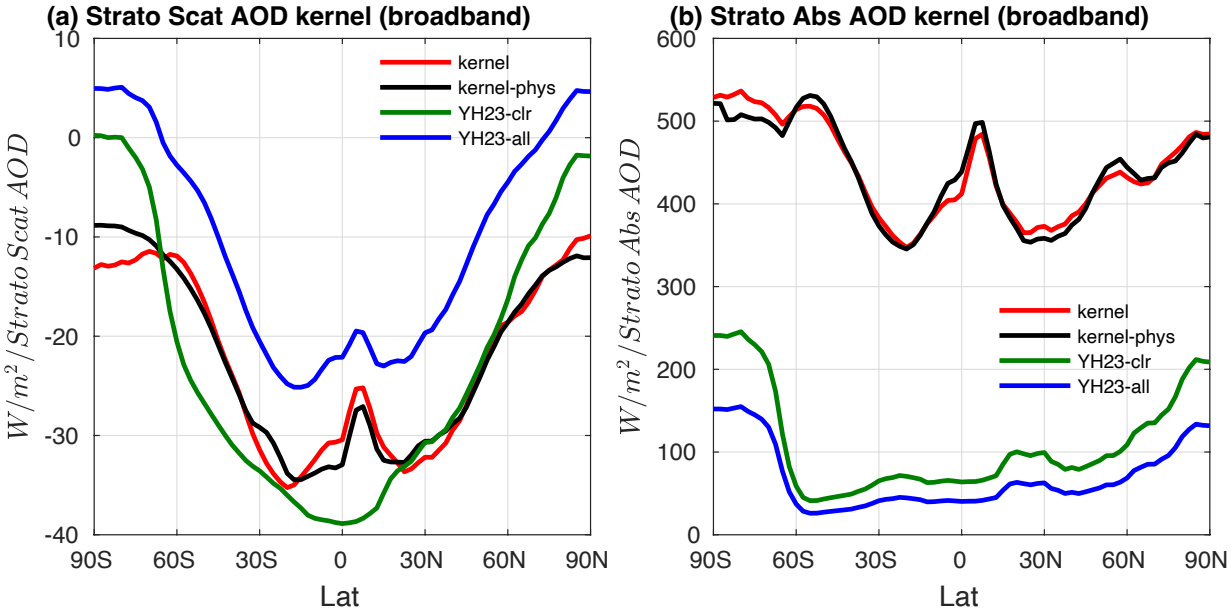

Figure 4.5 Annual mean and zonal mean broadband stratospheric (a) AOD_{scat} and (b) AOD_{abs} radiative kernels. YH23-clr and YH23-all represent the clear-sky and all-sky scattering AOD radiative sensitivity quantified in Q. Yu & Huang (2023b) for tropospheric aerosols. Kernel and Kernel-phys indicate the broadband kernels calculated from RRTMG and emulated by a regression model, respectively.

4.4.2 2022 Hunga Volcanic Eruption

On January 15, 2022, the Hunga Tonga volcano (20.57°S, 175.38°W) erupted violently, releasing sulfur compounds and other aerosols into the atmosphere (Kloss et al., 2022; Taha et al.,

2022; Schoeberl et al., 2023, 2024). To assess the corresponding ADRE, we first calculate the stratospheric AOD anomaly following Section 4.2.3.

Figure 4.6a - 4.6d shows the evolution of the zonal mean stratospheric AOD anomaly relative to the background at different wavelengths throughout 2022. Although the Hunga eruption occurred in late January, the OMPS product showed little AOD signal initially because the extinction retrieval becomes unreliable in the presence of clouds and optically thick aerosol plumes (Taha et al., 2021). Over time, the aerosol plume descented to the lower stratosphere and dispersed horizontally. Within four months after the eruption, the aerosols primarily remained in tropical latitudes with some northward spread. This led to an initial AOD peak in the tropical regions due to the immediate formation and accumulation of aerosols, as reported by other studies (Schoeberl et al., 2023; Taha et al., 2022). As the southern hemisphere approached winter, a meridional circulation developed between the tropics and subtropics to maintain the thermal wind balance, known as the QBO direct, meridional, or secondary circulation (Strahan et al., 2015). This circulation transported stratospheric aerosols into the mid-latitudes. Meanwhile, the polar vortex acted as a barrier, causing the accumulated aerosols in the subtropics to create a second AOD peak during July-September. The double peak features shown here were also reported in other observations and model simulations (Wang et al., 2023; Schoeberl et al., 2024). Gaps in the data are caused by spacecraft anomalies or failures to meet the data screening criteria.

Figure 4.6e also suggests that the zonal average stratospheric AOD anomaly varies significantly with wavelength, indicating that assuming a simple Angstrom exponent cannot fully represent the wavelength dependency of AOD. Therefore, it is important to incorporate the band-by-band kernels with AOD observations to accurately calculate the stratospheric ADRE.

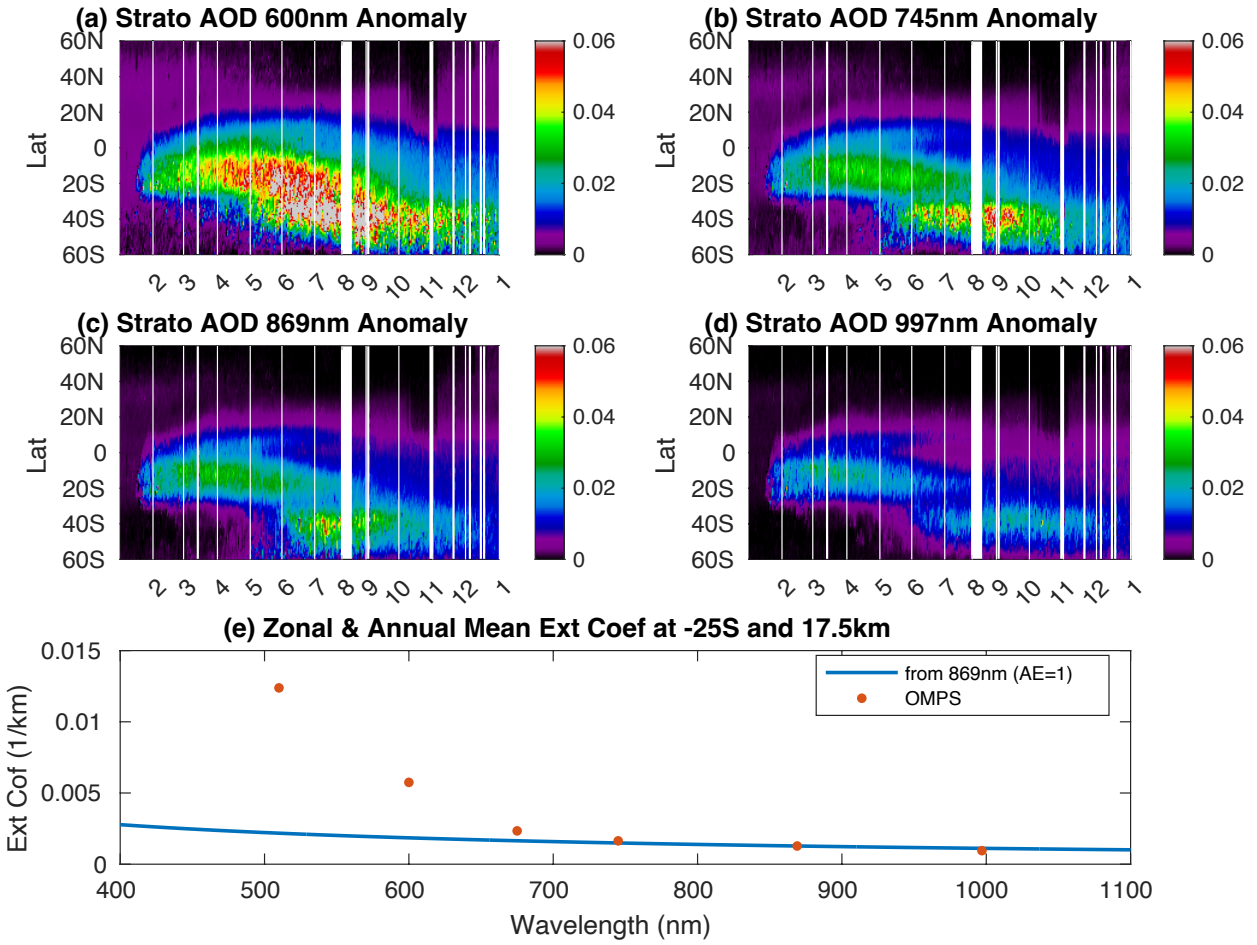

Figure 4.6 Latitude-time plots of the zonal mean stratospheric AOD anomaly at (a) 600 nm, (b) 745 nm, (c) 869 nm, and (d) 997 nm from OMPS-LP in 2022, with the x-axis in (a)-(d) representing corresponding months. (e) Zonal and annual mean aerosol extinction coefficient at -25S and 17.5 km. The red dots represent OMPS observations, while the blue line shows the wavelength dependency assuming an AE of 1.

In the ADRE calculation, we assume the AOD anomaly with SSA = 1 because observations suggest that the absorbing particles in the volcanic ashes are of small amounts and do not significantly impact the radiative properties (Kloss et al., 2022). We also assume the stratospheric AOD anomalies from OMPS at a discrete set of wavelengths represent the observational truth.

Figure 4.7a displays the global mean stratospheric AOD anomaly as calculated in Section 4.2.3 throughout 2022. We have listed the spectral AOD anomaly at RRTMG mid-visible bands (bands 23-25). These values are interpolated from the nearby wavelengths from OMPS. For the broadband AOD anomaly, we calculate the AOD using OMPS 869 nm, assuming an AE of 1. This way, we can estimate the relative errors of the broadband kernel method when there are observation uncertainties in AE. Results indicate distinct features in the spectra AOD, suggesting a peak in global mean AOD values around June.

We further calculated the stratospheric ADRE using both the stratospheric kernels developed here and the kernels from YH23. The YH23 kernels, although based on total column aerosols, have been used in stratospheric ADRE quantifications in Schoeberl et al. (2023, 2024). By including YH23 kernels in the comparison, we show the discrepancies that would be caused by kernels not specifically made for stratospheric aerosols. Figure 4.7b shows the stratospheric ADRE from the Hunga Eruption in 2022. For comparison, the RRTMG-calculated results based on the band-by-band AOD inputs are indicated by the red line. In general, the ADRE peaks with AOD near June, and using the band-by-band aerosol kernels can quantify it most accurately. The performance of broadband and physically sorted stratospheric aerosol kernels is slightly worse than that of the band-by-band kernels, as they fail to capture the wavelength dependency information and the Angstrom exponent assumption may be inadequate. In terms of global mean values, using the YH23 clear-sky kernel overestimates the cooling effect of the Hunga eruption, while using the YH23 all-sky kernel underestimates it.

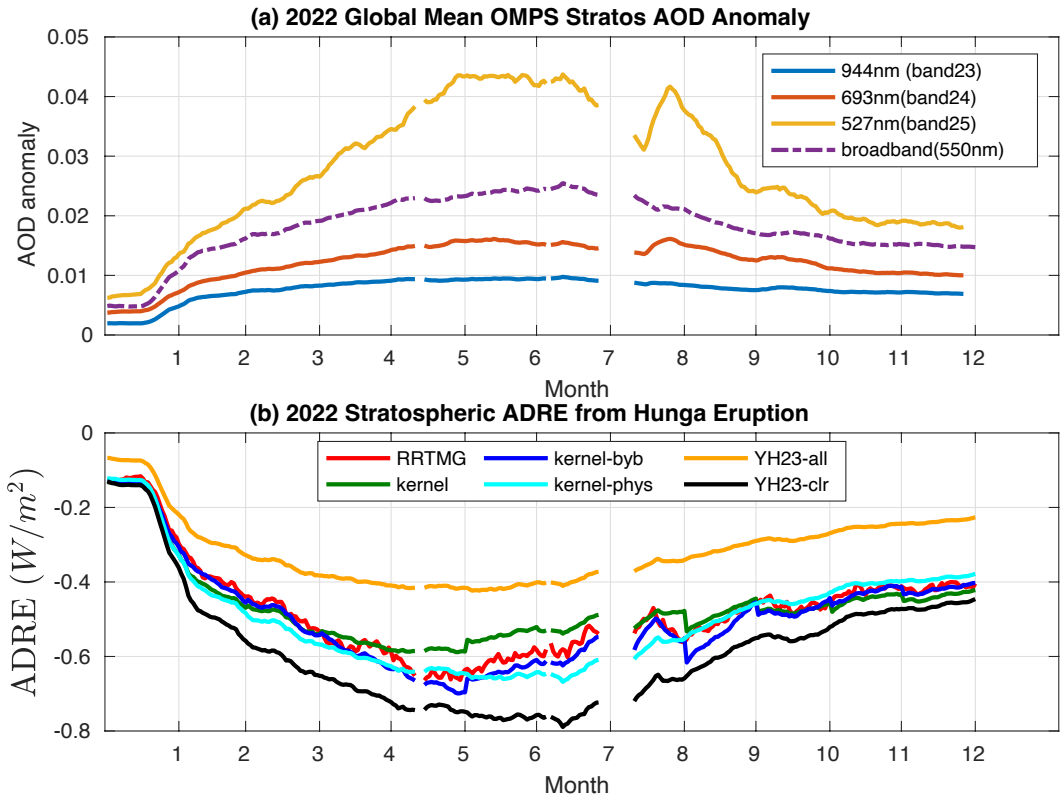

Figure 4.7 Time series of the global mean (a) stratospheric AOD anomaly from OMPS-LP following the Hunga Eruption in 2022 and (b) stratospheric ADRE from Hunga Eruption in 2022. YH23-clr and YH23-all represent the clear-sky and all-sky scattering AOD radiative sensitivity quantified in Q. Yu & Huang (2023b), respectively. Kernel, kernel-phys, and kernel-byb indicate the broadband kernels calculated from RRTMG, broadband kernels from the regression model, and the band-by-band kernels, respectively.

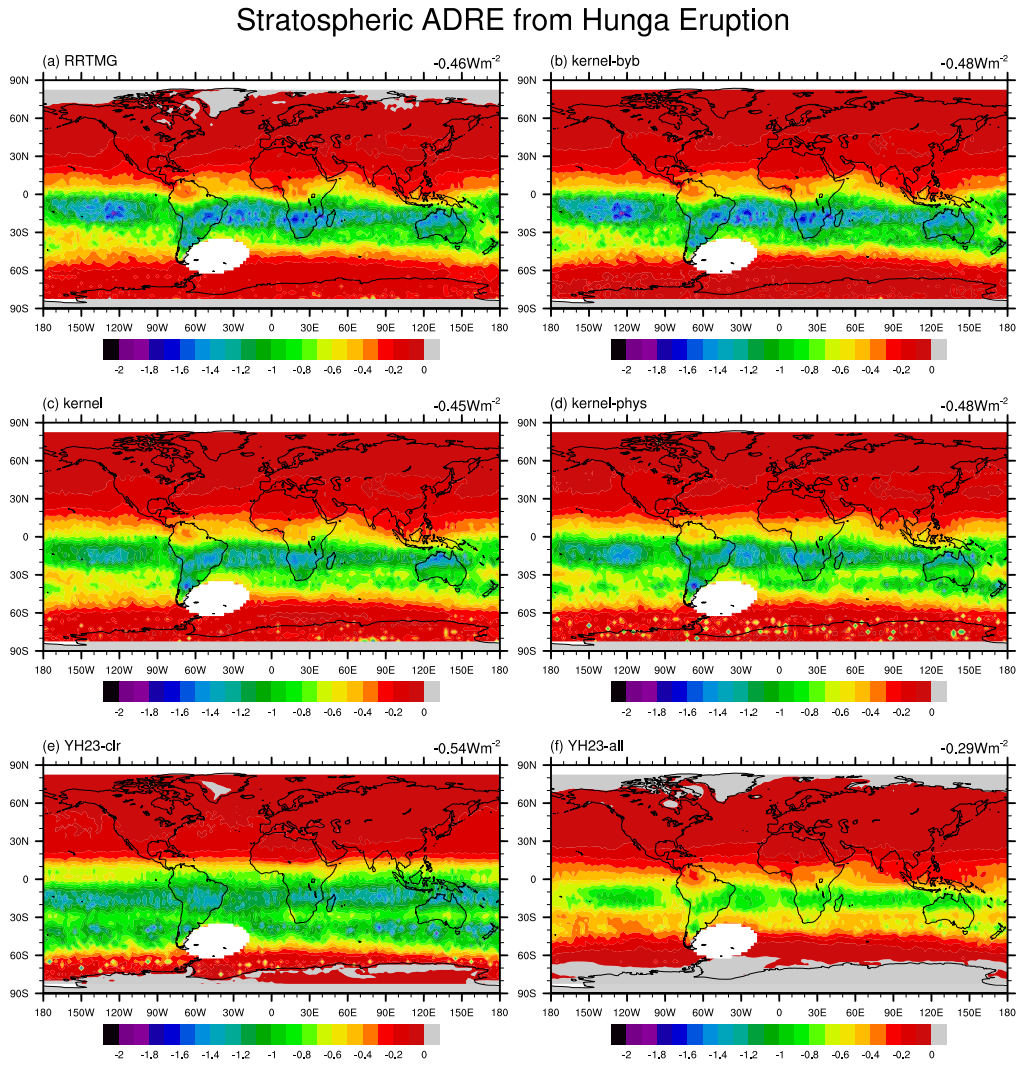

Figure 4.8 Annual mean stratospheric ADRE from the Hunga eruption in 2022, with global mean values indicated in the top right of each subplot. (a) RRTMG benchmark calculations; (b) Band-by-band kernel quantifications; (c) Broadband kernel quantifications; (d) Physically sorted kernel quantifications; (e) YH23 clear-sky kernel quantifications; (f) YH23 all-sky kernel quantifications. Global mean values are shown in the top right of each subplot.

Apart from the time evolution, we also compare the spatial patterns of stratospheric ADRE using different kernel schemes. Figure 4.8 displays the annual mean stratospheric ADRE from the

Hunga eruption calculated from RRTMG as well as the kernels developed in this work. Results show that the volcanic eruption caused a uniform cooling in the southern hemisphere's tropical and subtropical regions due to the dispersion of aerosols described before. In terms of global mean ADRE, the Hunga eruption induced a cooling of -0.46 W/m^2. All stratospheric kernels developed in this work can reproduce the spatial features of ADRE relatively well, with the band-by-band kernels performing the best. Although the YH23 clear-sky scheme can approximately reproduce the global mean stratospheric ADRE values, it fails to capture the spatial patterns, especially over the cloudy regions.

Table 4.2 listed the R^2 and RMSE values comparing the ADRE induced by the Hunga eruption, calculated using different kernel schemes and the RRTMG model. Globally, the band-by-band, broadband, and physically sorted aerosol kernels capture 98.89%, 93.83%, and 94.33% of the variance in RRTMG-calculated ADRE, with RMSEs less than 0.04 W/m² (approximately 8.7% relative to the global mean values). Using YH23 kernels results in RMSEs greater than 0.11 W/m², which is 23.91% relative to the global mean.

Table 4.2 Performance of Stratospheric Kernels Calculated in This Study and Kernels from YH23 in Quantifying the ADRE of the 2022 Hunga Volcanic Eruption and 2020 Australia Wildfire.

	2022 Hunga volcanic eruption			**2020 Australia wildfire**		
	R^2	**RMSE (W/m^2)**	**Relative errors**	**R^2**	**RMSE(W/m^2)**	**Relative errors**

Band-by-band kernels	98.89%	0.02	4.35%	99.02%	0.01	3.57%
Broadband kernels	93.83%	0.04	8.70%	94.75%	0.04	14.29%
Physically sorted kernels	94.33%	0.04	8.70%	83.19%	0.08	28.57%
YH23-clr	95.11%	0.11	23.91%	83.59%	0.37	132.14%
YH23-all	91.88%	0.17	36.96%	51.32%	0.31	110.71%

Note: R^2 represents the coefficient of determination, and RMSE is the Root Mean Squared Error. Relative errors are calculated by dividing the RMSE by the global mean values. Broadband and physically sorted kernels are used under the assumption of AE being 1.

4.4.3 2020 Australia Wildfire

In late December 2019, massive bushfires occurred in southeastern Australia and lifted a considerable amount of smoke into the stratosphere via pyrocumulonimbus clouds. Unlike the volcanic eruption case, we apply both the AOD_{scat} and AOD_{abs} kernels to study the stratospheric ADRE of the black-carbon-containing smoke particles as they are partly absorbing.

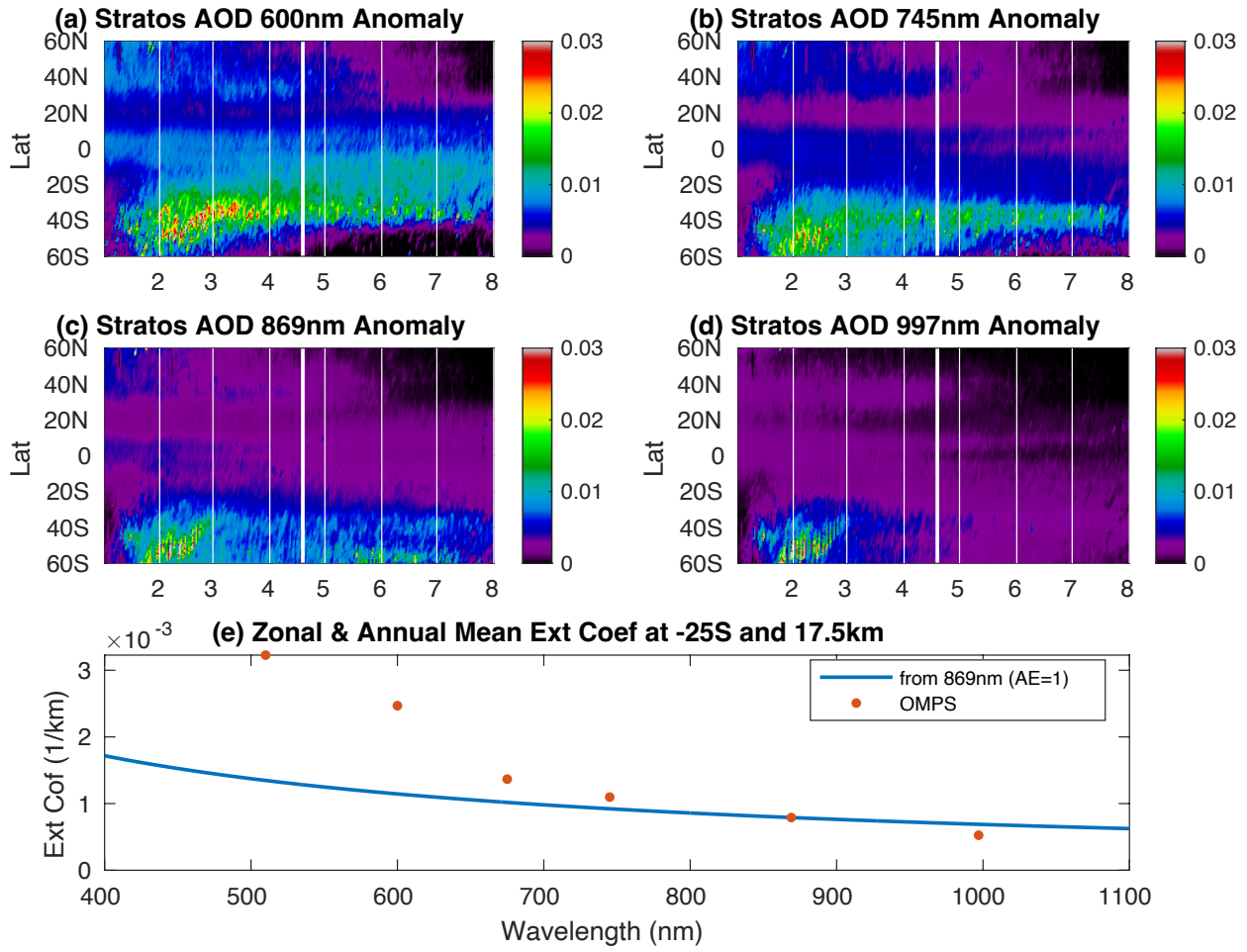

Figure 4.9 Same as Figure 4.6, but for the year 2020.

Figure 4.9 shows the zonal mean stratospheric AOD anomaly at different wavelengths, over 8 months starting in January 2020. After several periods of intense fires in early January 2020, the stratospheric AOD reached a maximum in early February and decayed afterward. The delay in reaching the AOD peaks might be due to the subsequent self-lofting of upper tropospheric aerosols, caused by buoyancy changes from the aerosols absorbing solar radiation (Ohneiser et al., 2020). After being lifted, aerosols spread equatorward and dilute significantly, leading to a decrease in the stratospheric AOD anomaly which lasts around eight months. Same as Figure 4.6e, Figure 4.9e

also suggests that the AOD wavelength dependency relationship is complex, and assuming a certain Angstrom exponent may not be sufficient to represent the band-by-band AOD.

To investigate the performance of kernels in quantifying wildfire-related events, we assume the stratospheric aerosol anomaly consists of aged biomass burning aerosols with a single scattering albedo at 550 nm of 0.86 as suggested by recent studies (Damany-Pearce et al., 2022; Ohneiser et al., 2020). Figure 4.10a shows the global mean stratospheric AOD anomaly in the mid-visible bands in 2020. The interpolated AOD at RRTMG bands shows distinct differences compared to the broadband AOD, especially in February. Broadband AOD is calculated from scaling 869 nm to 550 nm assuming an AE of 1. Stratospheric ADRE is further calculated with known AOD and SSA. Figure 4.10b shows ADRE calculated from the RRTMG as well as kernel methods. Results show that using YH23 kernel schemes significantly underestimates the warming effect of stratospheric aerosols. This is because the stratospheric AOD_{abs} kernels are nearly twice as large as the YH-clearsky AOD_{abs} kernels, whereas the AOD_{scat} kernels show similar magnitudes compared with the YH-clearsky values (Figure 4.5b and Figure C9 in the Appendix C). These results further emphasize the need to use kernels specifically designed for stratospheric aerosols to accurately quantify ADRE. As a comparison, using the stratospheric aerosol kernels captures wildfire-induced ADRE relatively well. The agreements in ADRE calculations indicate that our stratospheric aerosol kernel dataset is applicable for quantifying ADRE regardless of aerosol types (either scattering or absorbing). For the Australia wildfire, the carbonaceous aerosols led to a peak global mean warming of over +0.4 W/m^2 in mid-February 2020.

Figure 4.11 shows the comparison of the spatial distributions of ADRE calculated by different kernel schemes. Similar to the Hunga volcanic eruption case, the band-by-band kernel quantifications align most closely with the RRTMG-calculated results, with the R^2 being 99.02%

(Table 4.2). Both the broadband and the physically sorted kernels slightly overestimate the aerosol warming, especially in the high-latitude regions. The slightly lower performance of broadband and physically sorted kernels in capturing the spatial patterns of ADRE might come from the bias in AOD_{550}, as using a uniform AE value for AOD wavelength conversion across the globe may not be representative. This aligns with other studies indicating that the Angstrom exponent can vary significantly (Malinina et al., 2019), particularly during wildfire events when the inclusion of organics can complicate the particle size distribution interpretation (Bourassa et al., 2019). Overall, the stratospheric kernels can capture more than 83.19% of the variance in the Australia wildfire-induced ADRE, with the RMSEs less than 0.08 W/m^2 (i.e. 28.57% relative to the global mean). Both Figure 4.11 and Table 4.2 suggest that YH23 kernel schemes are not suitable for quantifying the wildfire-dominated stratospheric ADRE because of its significant underestimation of AOD_{abs} kernels.

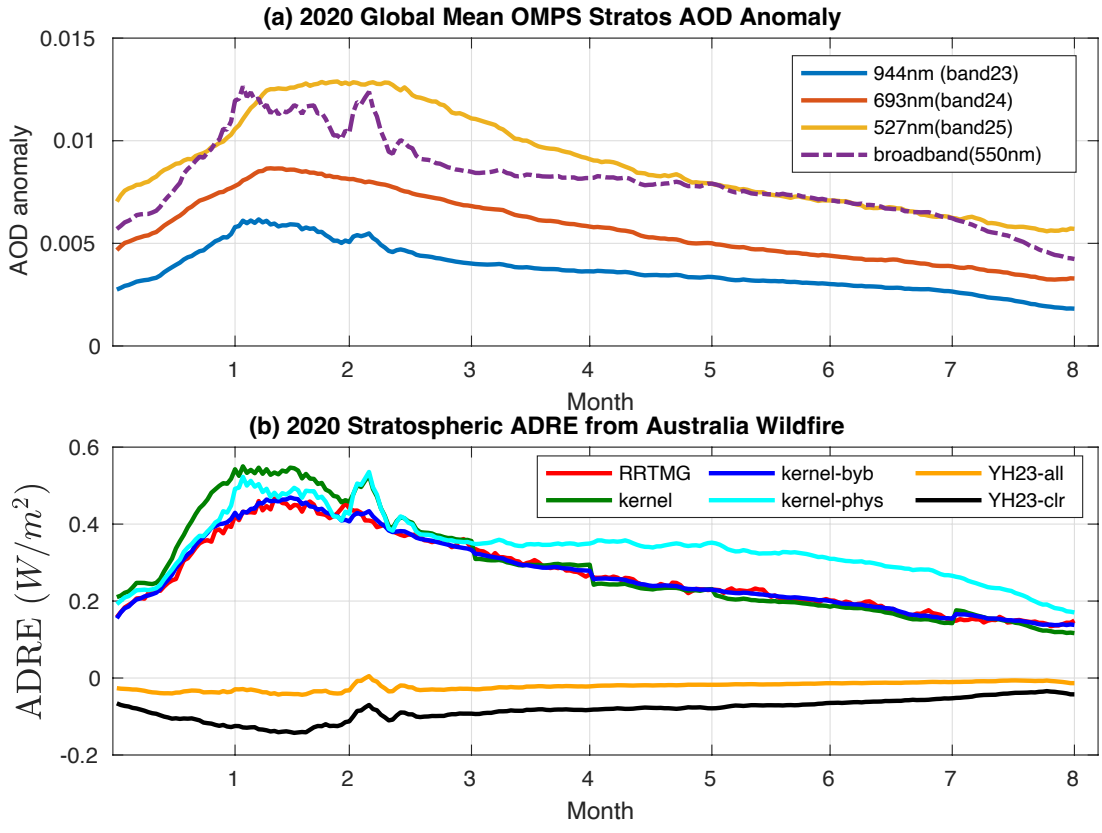

Figure 4.10 Same as Figure 4.7 but for the 2020 Australia wildfire.

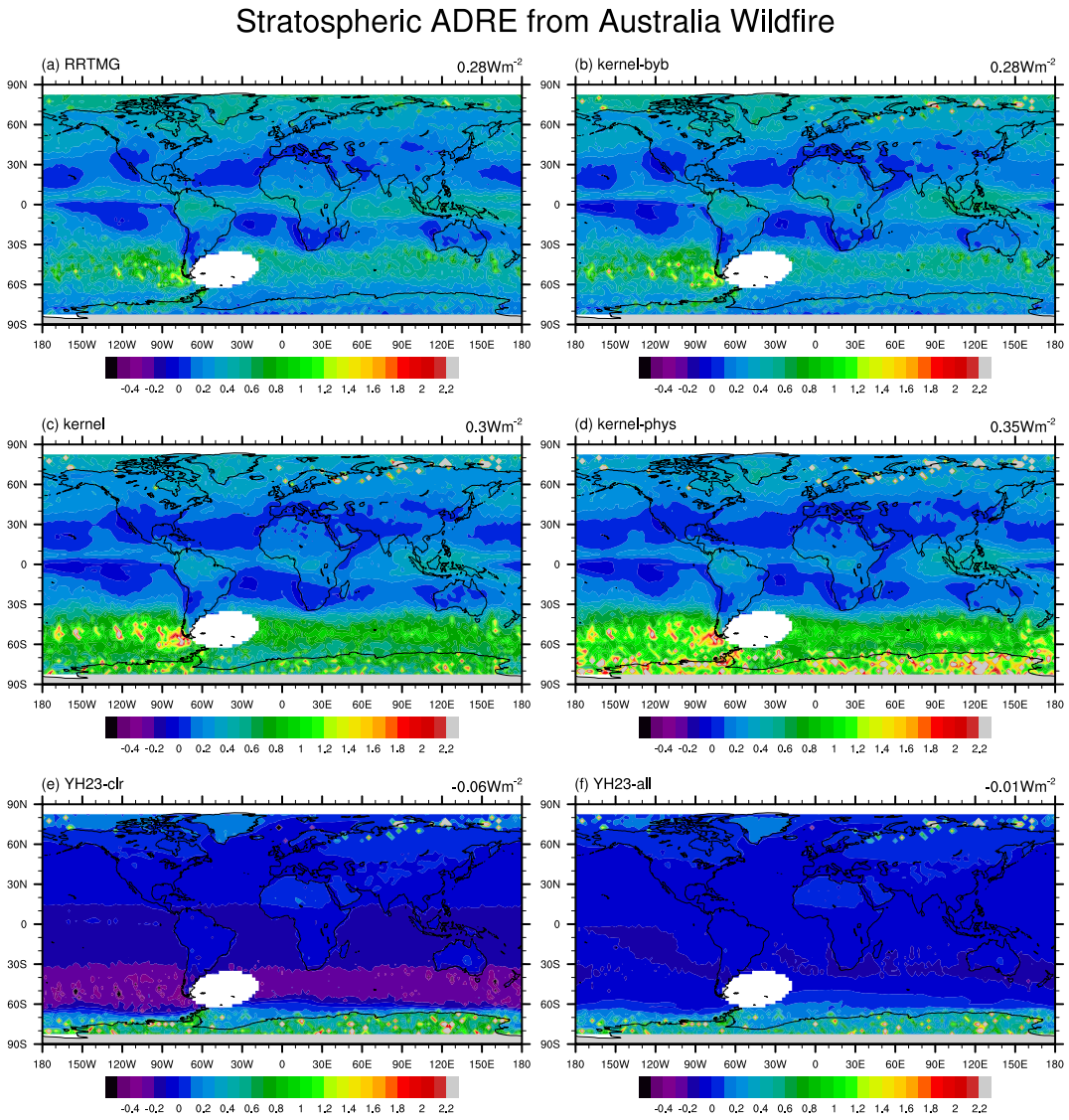

Figure 4.11 Same as Figure 4.8 but for the 2020 Australia wildfire.

4.5 Conclusions

This paper provides, for the first time, a comprehensive set of radiative kernels for stratospheric aerosols. The kernels are derived for the scattering and absorbing aerosol optical depth, respectively, based on partial radiative perturbation (PRP) computations using one year of

3-hourly MERRA-2 data. We analyzed the spatial variability of broadband aerosol kernels, demonstrating that they can be emulated as a joint function of solar insolation, TOA reflectance, and stratospheric aerosol optical depth. The developed aerosol radiative kernels provide a versatile tool for assessing the stratospheric ADRE of different aerosol types.

Stratospheric aerosol kernels exhibit significant spatial, temporal, and spectral variability (Figures 4.1-4.3). Validation tests have been done to evaluate the aerosol height dependency, linear scaling, and linear additivity of the kernels (Figures C4-C6). On a global scale, a 0.1 increase in stratospheric AOD_{scat}^{550} leads to a cooling effect of -2.65 W/m^2 at the TOA, while a similar increase in AOD_{abs}^{550} results in a warming effect of +41.95 W/m^2 (Figure 4.1). The magnitude of stratospheric aerosol kernels is greater than that for tropospheric aerosols (e.g., Thorsen et al., 2020; Q. Yu & Huang, 2023b), particularly for absorbing aerosols. This is due to the higher placement of aerosols, which interact with radiation less attenuated by clouds or tropospheric absorbers. Additionally, underlying clouds enhance the brightness of dark surfaces, thus amplifying the sensitivity of stratospheric ADRE to absorbing aerosols. Band-by-band aerosol kernels were calculated for the 14 bands in RRTMG SW, with spectral signatures indicating peak sensitivity from the near ultraviolet to the near-infrared (bands 23 to 25, 442 nm-1242 nm) (Figure 4.3). Using discrete AOD observations at these wavelengths allows for a more accurate constraint on ADRE.

From the single-layer aerosol analytical model, we identified that broadband aerosol kernels are related to TOA insolation, tropospheric reflectance, and stratospheric aerosol optical depth. We proposed a physically sorted set of aerosol kernels using a multivariate regression model, which can effectively reproduce the RRTMG-calculated broadband kernels (Figure 4.4 &

C8). These physically sorted kernels are independent from geophysical location and can provide first-order estimations of stratospheric ADRE using satellite measurements.

The kernels were applied to calculate the ADRE for two stratospheric aerosol injection events: the 2022 Hunga volcanic eruption and the 2020 Australia wildfire. There is overall good agreement between the RRTMG-calculated results and those obtained using the kernels (Figures 4.7-4.8, Figures 4.10-4.11, and Table 4.2). Band-by-band kernels perform best by constraining the wavelength dependency of AOD. Using band-by-band kernels can reproduce 99% of the ADRE variance with relative errors of less than 4%. Using other stratospheric kernels can capture more than 90% of the variance with relative errors of less than 10% (Table 4.2), despite the uncertainty in AE. The stratospheric ADRE from the 2022 Hunga eruption peaked six months after the event, inducing a global mean cooling of -0.46 W/m^2 (Figures 4.7-4.8). For the 2020 Australia wildfire, the stratospheric ADRE peaks one month after the event and results in a global mean warming of +0.28 W/m^2 from January to August (Figures 4.10-4.11).

To accurately calculate stratospheric ADRE, users are recommended to use the band-by-band kernels when reliable spectral AOD data is available. If such information is unavailable, the broadband aerosol kernels can be used alternatively, although the results should be used with caution as the broadband kernels are calculated based on an assumed Angstrom Exponent of 1. The physically sorted kernels have the advantage of not being restricted to specific geographical locations. With climate change, the aerosol-related and environmental conditions at a location may change. In such cases, physically sorted kernels may have an advantage for the ADRE quantification. Considering that there may be rapid stratospheric temperature adjustments in response to the instantaneous perturbations of the aerosols, the kernels developed in this work can

be extended to include the radiative effects of such adjustments in future work, to provide an estimation of the effective (adjusted) radiative effect of the stratospheric aerosols.

Data Availability Statement

The Modern-Era Retrospective Analysis for Research and Applications, Version 2 (MERRA-2) data used to calculate stratospheric aerosol kernels are provided by NASA Global Modeling and Assimilation Office (Randles et al., 2017). The aerosol mixing ratio, assimilated meteorological fields, radiation and aerosol diagnostics data are available at Global Modeling and Assimilation Office via https://doi.org/10.5067/LTVB4GPCOTK2, https://doi.org/10.5067/WWQSXQ8IVFW8, https://doi.org/10.5067/Q9QMY5PBNV1T and https://doi.org/10.5067/KLICLTZ8EM9D (Gelaro et al., 2017). The dataset of stratospheric aerosol direct radiative effect kernels (monthly mean broadband, band-by-band, and the annual mean physically sorted ones), along with the scripts and data to reproduce the findings in this paper, are available on Mendeley Data at https://data.mendeley.com/datasets/t87tfnk2xd/1

Chapter 5 Accounting for the Effect of Aerosols in GHGSat Methane Retrieval

This Chapter is a reprint of the published article in Atmospheric Measurement Techniques.

Yu, Q., Jervis, D., and Huang, Y.: Accounting for the effect of aerosols in GHGSat methane retrieval, Atmos. Meas. Tech., 17, 3347–3366, https://doi.org/10.5194/amt-17-3347-2024, 2024.

The thesis author is the lead author and principal investigator for this paper.

Accounting for Aerosols Effect in GHGSat Methane Retrieval

Qiurun Yu[1], Dylan Jervis[2], Yi Huang[1]

[1]Department of Atmospheric and Oceanic Sciences, McGill University, Montréal, QC, H3A 0B9, Canada

[2]GHGSat, Inc., Montréal, QC, H2W 1Y5, Canada

Correspondence to: Qiurun Yu (qiurun.yu@mail.mcgill.ca)

Abstract

GHGSat comprises a constellation of satellites with high spatial and spectral resolution that specialize in monitoring methane emissions at 1.65 μm. This study investigates the ability to accurately retrieve both the methane mixing-ratio enhancement ΔX_{CH_4} and the aerosol optical depth (AOD) simultaneously from simulated GHGSat observations that incorporate angle-dependent scattering information. Results indicate that the sign of the ΔX_{CH_4} bias when neglecting aerosols changes from negative to positive as surface albedo increases, which is consistent with previous studies. The bias in ΔX_{CH_4} is most pronounced when AOD is not simultaneously retrieved, ranging from −3.0 % to 6.3 % with an AOD of 0.1, a 60° solar zenith angle, and a surface albedo of 0.2 for the nadir-only retrieval. Using multiple satellite viewing angles during the GHGSat observation sequence with a scattering angle ranging from 100 to 140°, the study shows that the mean bias and standard deviation of ΔX_{CH_4} are within 0.3 % and 2.8 % relative to the background. The correlation between simultaneously retrieved ΔX_{CH_4} and AOD shifts from being positive to negative as surface albedo increases and the aerosol asymmetry factor decreases, signifying a transition of the dominant aerosol effect from aerosol-only scattering to aerosol–surface multiple

scattering. The variety of scattering angle ranges has little impact on the performance of the multi-angle viewing method. This study improves the understanding of the impact of aerosols on the GHGSat ΔX_{CH_4} retrieval and provides guidance for improving future GHGSat-like point-source imagers.

5.1 Introduction

Aerosols can modify photon path lengths via their scattering and absorption effects and have been identified as one of the major sources of errors when retrieving greenhouse gases from spectrally resolved backscattered solar radiation in the shortwave infrared (SWIR) (Aben et al., 2007; Butz et al., 2009; Connor et al., 2016; X. Chen et al., 2017; J. Huang et al., 2021). Accurately assessing greenhouse gas emissions in the presence of aerosols remains a challenge. This is because unaccounted-for aerosols can either enhance or reduce the absorption of light by gases, depending on factors such as the aerosol concentration, aerosol height distribution, viewing geometry, and surface albedo, among others (Butz et al., 2009; Frankenberg et al., 2012; Sanghavi et al., 2020). Houweling et al., (2005) analyzed Scanning Imaging Absorption Spectrometer for Atmospheric Chartography (SCIAMACHY) measurements of total-column CO_2 over the Sahara and found that the unrealistically large CO_2 variability of the total column, 10 % (37 ppm), was caused by mineral dust aerosols. Butz et al. (2009) found that if aerosols are not considered, atmospheric CO_2 retrieval errors larger than 1 % may occur when using SCIAMACHY and Greenhouse gases Observing SATellite (GOSAT)-like observers. These errors are dependent on both the surface albedo and the type of aerosols present. Huang et al. (2020) simulated Airborne Visible/Infrared Imaging Spectrometer Next Generation (AVIRIS-NG) measurements for methane emissions. Their results show an underestimation of CH_4 resulting from aerosols, particularly those with a high single-scattering albedo and a low asymmetry factor (such as water-soluble aerosols). These studies, among many others, underlined the importance of understanding the effect of aerosols on the remote sensing of greenhouse gases.

To account for the atmospheric scattering in the SWIR satellite retrieval of greenhouse gas, a "full-physics" retrieval requires simultaneously solving for the vertical profile of gas concentration, aerosol extinction, and the surface reflectivity through the inversion of the radiance spectrum using a radiative-transfer model (Butz et al., 2012; Jacob et al., 2022). However, this method is time-consuming and is likely to fail if the atmosphere is heavily polluted or if the surface is too dark (Lorente et al., 2021). In contrast to "physics-based" methods, some proxy methods, which are much faster than full-physics retrieval and achieve similar precision and accuracy, have been proposed. To simultaneously retrieve the CO_2 total-column and aerosol properties, the "three-band" retrieval exploits measurements of the absorption bands of O_2 (0.77 μm) and CO_2 (1.61 and 2.06 μm) to retrieve the aerosol amount, height distribution, and size distribution based on a simple aerosol microphysical model (Butz et al., 2009). However, this approach requires additional consideration of the uncertainty of a prior estimate of CO_2 (Butz et al., 2012). According to Parker et al. (2020), methane mixing ratio ($\boldsymbol{X_{CH_4}}$) can be retrieved using both CH_4 (1.65 μm) and the adjacent CO_2 band (1.61 μm) by taking advantage of the $\frac{\boldsymbol{X_{CH_4}}}{\boldsymbol{X_{co_2}}}$ ratio without accounting for atmospheric scattering. However, this "CO_2 proxy" method is subject to bias for sources that co-emit CH_4 and CO_2, such as gas flaring. Depending on the instrument design and its limitations, the approach to accounting for the effect of aerosols on greenhouse gas retrieval varies.

GHGSat, Inc., has developed a nano-satellite system that measures greenhouse gas emissions from individual industrial facilities (Varon et al., 2019). Its satellite achieves a combination of fine spatial resolution and spectral resolution by pointing at targeted methane point sources (Jervis et al., 2021; Jacob et al., 2022). As of the time of writing, GHGSat has launched a constellation of 11 commercial satellites (GHGSat-C1 to GHGSat-C11) which monitor methane emissions from natural-gas industry operations, landfills, hydroelectric reservoirs, and oil sand operations, among others (Calvello et al., 2017; Varon et al., 2019; Jacob et al., 2022; Maasakkers et al., 2022). However, industrial activities such as oil extraction and pre-treatment involve not only gaseous emission but also aerosol production (e.g., water-soluble and black-carbon aerosols). The continued development of the GHGSat satellite requires identifying and minimizing the uncertainty in methane retrieval due to aerosol interference. Newer GHGSat satellites only target the CH_4 band; consequently, the above-mentioned "proxy" methods to account for the aerosol effects do not apply to their instrument. An accurate aerosol retrieval model for GHGSat would not only reduce the uncertainty in their methane retrieval but also provide a new aerosol data product, potentially allowing high spatial-resolution air quality measurements from space.

The angular dependence of aerosol scattering allows space-borne observations of aerosol properties based on multi-angle measurements, which have the potential to mitigate aerosol-induced errors in current greenhouse gas satellite observations. Frankenberg et al. (2012) demonstrated that adding multiple satellite viewing angles to Orbiting Carbon Observatory 2 (OCO-2)-like observations enhances the ability to retrieve aerosol properties. The aerosol information can, in turn, significantly decrease errors in the measurement of CO_2 and CH_4 total columns. However, this multiangle viewing method was applied to area flux mappers which are designed to observe emissions on regional scales. There has been little study of how to retrieve aerosols using point-source imagers like GHGSat. A method to co-retrieve aerosols and methane using GHGSat spectral content could address a gap in current research on point-source imagers, improve the accuracy of their greenhouse gas retrieval, and provide greater details about local aerosol and methane concentrations.

This study has three objectives. First, we assess how aerosols impact the accuracy of GHGSat methane mixingratio enhancement (ΔX_{CH_4}) retrieval when the aerosols are present but not retrieved. This assessment involves simulating GHGSat satellite observations for a wide range of aerosol optical properties and surface albedo values to evaluate the distribution and magnitude of any resulting bias in ΔX_{CH_4} under different aerosol and surface conditions. Second, we simultaneously retrieve the aerosol optical depth (AOD) and ΔX_{CH_4} using a multi-angle viewing method and perform a comparison with the ΔX_{CH_4}-only retrieval obtained under the same conditions. Finally, we investigate how different scattering angles as well as uncertainties in aerosol type, height distributions, and surface albedo affect the performance of the simultaneous retrieval.

This paper is organized into five sections. Section 5.2 provides an overview of the atmospheric models, the GHGSat instrument model, and the simultaneous retrieval methods for aerosols and methane. Section 5.3 evaluates the errors that occur in GHGSat methane retrieval under various aerosol, surface, and satellite zenith angle conditions. Synthetic data are used to conduct retrieval under two scenarios: methane-only nadir retrieval and the simultaneous retrieval of methane and aerosols using the multi-angle viewing method. Section 5.4 investigates the impact of satellite viewing angles as well as the uncertainty in aerosol and surface albedos on simultaneous retrieval. A summary is presented in Sect. 5.5.

5.2 Method

5.2.1 Atmospheric Model

The top-of-the-atmosphere (TOA) radiance detected by the satellite comes from both direct and diffuse reflections. The incoming sunlight is reflected into space by the Earth's surface and atmospheric scatterers such as aerosols. When the solar beam travels through the atmosphere, it can be partly absorbed along its path by atmospheric absorbers, such as methane molecules and aerosols. Additionally, multiple scattering processes occur between the surface and aerosol layers. To assess the radiative impact of aerosols in the GHGSat methane retrieval, a forward model to simulate GHGSat-measured solar radiation is required.

The radiative-transfer forward model used in this study is DIScreet Ordinate Radiative Transfer (DISORT) version 4.0.99 (Stamnes et al., 1988). As one of the most general and versatile plane-parallel radiative-transfer models, DISORT has been widely used for the remote sensing of greenhouse gases, aerosols, and clouds (Tzanis and Varotsos 2008; Wang et al. 2013; Boiyo et al. 2019). It can numerically compute satellite-measured radiance at different wavenumbers using discrete vertical coordinates. For each atmospheric layer, the spectral optical depth and single

scattering albedo for atmospheric molecules are computed by using a rigorous line-by-line radiative-transfer model (LBLRTM) over a 0.1 cm^2 interval (Clough et al., 2005). The mid-latitude summer profile is chosen as the default atmospheric state. The absorption of four main atmospheric absorptive gases (H_2O, CO_2, O_3, CH_4) at 45 layers is considered through line-by-line calculations.

To facilitate the analysis of aerosol-induced errors during the GHGSat CH_4 retrieval, this study focuses on the shortwave near-infrared band (1662–1672 nm). This band covers absorption lines which are mainly caused by CH_4. The surface is assumed to be Lambertian, and we adopt the 16-stream approximation. With the specified viewing geometry and surface albedo, DISORT can calculate the solar radiation that is backscattered into space by the Earth's surface and atmosphere. For a clean atmosphere with a surface albedo of 0.2, the TOA upward radiance simulated by DISORT is shown in Figure 5.1b. The solar zenith angle is 60°, and the satellite field of view is in the nadir position. In Figure 5.1b, strong CH4 absorptions are observed around 1666 nm, consistent with results from other studies like Jervis et al. (2021) and Chan Miller et al. (2023). Given that GHGSat measures methane concentrations by analyzing spectrally decomposed solar backscattered radiation within the methane absorption band (~ 1.65 μm), this alignment supports the adequacy of DISORT-simulated radiance for capturing the methane effect. With the TOA incoming solar radiance known (Figure 5.1a), the TOA reflectance ($\mathrm{Ref}_\lambda^{\mathrm{TOA}}$) can be calculated via

$$\mathrm{Ref}_\lambda^{\mathrm{TOA}} = \frac{\mathrm{radiance}_\lambda^{\mathrm{TOA}\uparrow}}{\mathrm{radiance}_\lambda^{\mathrm{TOA}\downarrow}}, \tag{5.1}$$

Where $\mathrm{radiance}_\lambda^{\mathrm{TOA}\downarrow}$ and $\mathrm{radiance}_\lambda^{\mathrm{TOA}\uparrow}$ are the TOA downward and upward radiance at wavelength λ. The radiance is in units of $Wm^{-2}sr^{-1}m^{-1}$. For GHGsat retrieval considering only gas absorbers, the relative depth of the absorption line directly corresponds to the retrieved methane

enhancement compared to the background. Therefore, Ref_{λ}^{TOA} is directly linked to the retrieved CH_4 enhancement and is shown in Figure 5.1c.

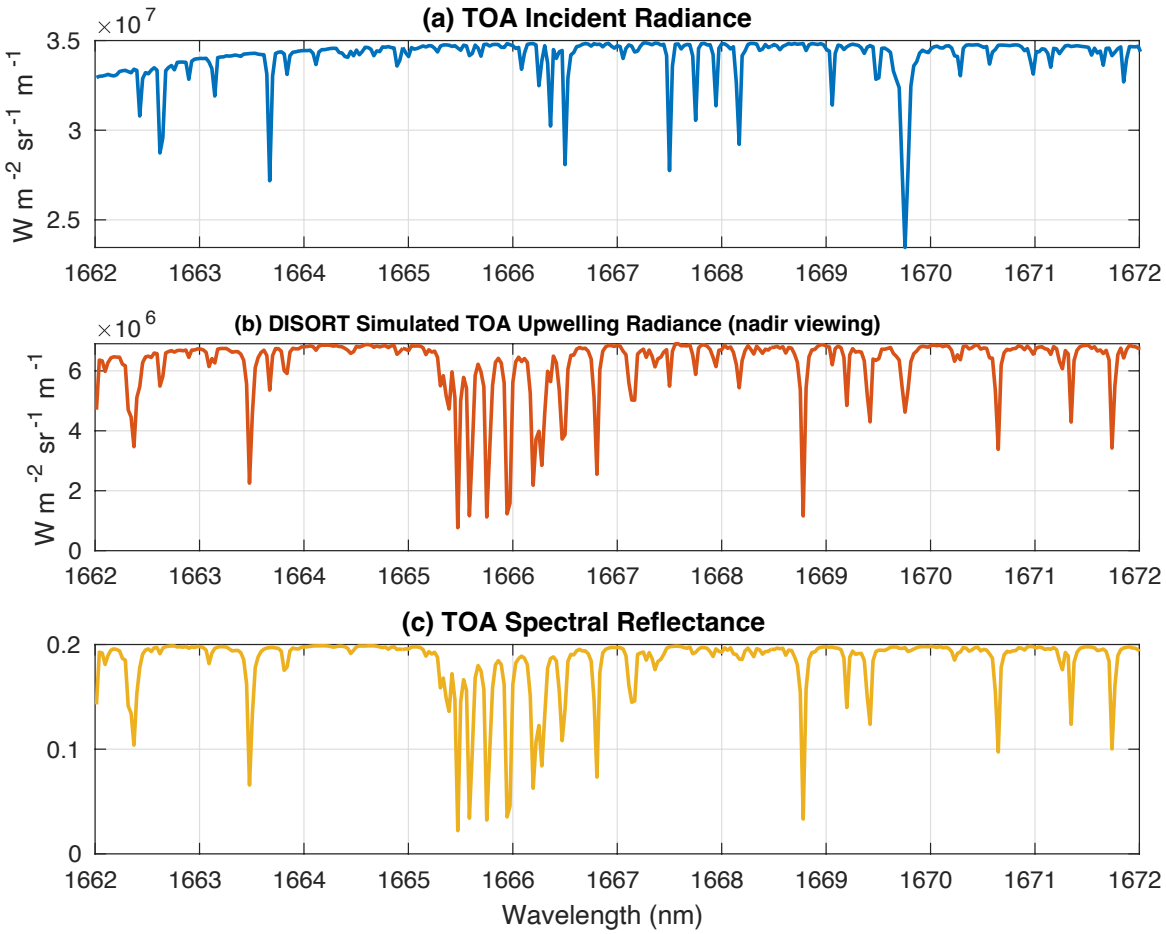

Figure 5.1 (a) TOA incoming solar radiance; (b) Simulated TOA upward radiance (nadir viewing); (c) Spectral reflectance (nadir viewing). Spectra are simulated with a surface albedo of 0.2 and a solar zenith angle of 60°.

5.2.2 Aerosol Settings

Many factors, such as aerosol type, concentration, and height distribution, can impact the radiance measurement. In this study, the aerosol types are predefined in the retrieval. We used climatological aerosol optical-property values from Ayash et al. (2008) to account for the diverse

range of particles found in industrial sites. For aerosols composed of multiple components, the single-scattering albedo (SSA) spans from 0.86 to 0.98, while the asymmetry factor (g) ranges from 0.54 to 0.76. GHGSat mainly focuses on measuring the CH_4 enhancement over methane hotspots, where CH_4 and the co-emitted aerosols are concentrated near the surface. To emulate the aerosol emissions from the industrial plume, one arbitrary aerosol layer is added near the surface between 1000 to 900 hPa. Considering the limitation of the instrument to one spectral band, the simplified treatment of aerosols in the forward model allows for a more direct physical interpretation of the effect of aerosols on methane retrieval. We focus mainly on the AOD retrieval because this variable is highly representative of the aerosol radiation effect (Frankenberg et al., 2012; Q. Yu & Huang, 2023a, 2023b). In this study, the simulated truth of the AOD is 0.1 at the SWIR (~ 0.3 AOD at 550 nm). This threshold is selected in the retrieval because it is used to filter values in other XCH_4 retrieval studies (Lorente et al., 2021).

5.2.3 The Multi-angle Viewing Method

The multi-angle aerosol retrieval method proposed by Frankenberg et al. (2012) uses the radiance difference at various viewing geometries to retrieve aerosol information and takes advantage of the fact that aerosols scatter more light forward than backward. In this study, the satellite azimuth angles are chosen to be 0 and 180° to represent forward-viewing and backward-viewing observations (i.e., straight south- and north-looking), respectively. Table 5.1 summarizes the angles used in the multi-angle viewing simulations. The scattering angle Θ is calculated following (Thompson et al., 2022) as

$$\Theta = 180° - \arccos[\cos\theta_1 \cdot \cos\theta_2 + \sin\theta_1 \cdot \sin\theta_2 \cdot \cos(\varphi_1 - \varphi_2)], \quad (5.2)$$

where θ_1 and θ_2 are the solar and satellite zenith angles, respectively, and φ_1 and φ_2 are the solar and satellite azimuth angles, respectively. Figure 5.2 shows the schematics of the multi-

angle viewing method and its corresponding angles. This study assumes the Henyey-Greenstein Phase Function for aerosols (Toublanc, 1996), which defines the phase function via

$$P_{HG}(\cos\Theta) = \frac{1-g^2}{(1-2g\cdot\cos\Theta+g^2)^{\frac{3}{2}}}, \tag{5.3}$$

where g is the aerosol asymmetry factor. The high g value implies that most of the scattered light is directed forward in the same general direction as the incident light.

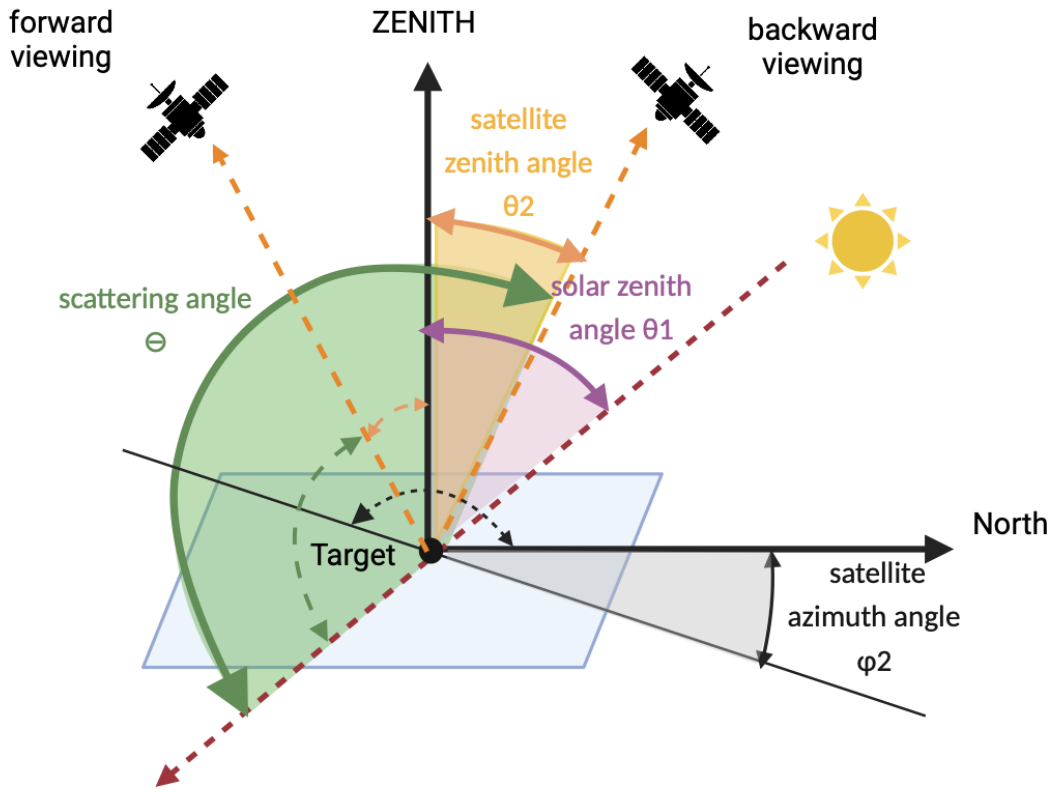

Figure 5.2 Schematic of a given solar and viewing geometry, as well as corresponding scattering angle for forward and backward viewing modes. Solar zenith angle θ_1, satellite zenith angle θ_2, and satellite azimuth angles φ_2 are indicated by the purple, orange, and black double arrow curves. Scattering angle Θ is represented by the green double arrow curves. The viewing

angles are depicted using solid and dashed double-arrow curves for the backward and forward viewing modes, respectively. In this case, the satellite azimuth angles are 0° and 180° for the backward and forward viewing directions (angles relative to the north-facing vector).

Table 5.1 Angles used in the multi-angle satellite viewing simulations for Sects. 5.3.1 and 5.3.2

	Solar zenith angle θ_1	Satellite zenith angle θ_2	Solar azimuth angle φ_1	Satellite azimuth angle φ_2	Scattering angle Θ
Forward viewing	60°	20°	180°	0°	100°
Nadir	60°	0°	180°	0°	120°
Backward viewing	60°	20°	180°	180°	140°

5.2.4 GHGSat Instrument Model

A nominal GHGSat measurement covers a targeted 12 × 15 km^2 area with approximately 25 × 25 m^2 pixel resolution and 0.3 nm spectral resolution (Jervis et al., 2021; Jacob et al., 2022). The instrument adjusts its altitude to ensure that the targeted area remains within its field of view for an extended period, thereby enhancing its signal-to-noise ratio (SNR). During the observation sequences, the GHGSat spectrometer typically takes 200 images of closely overlapping atmospheric absorption spectra. A more detailed description of the design of the GHGSat instrument and its measurement concept is presented in Jervis et al. (2021). To simulate GHGSat measurements, this study focuses on the spectral region between 1662 and 1672 nm and applies a

Gaussian broadening kernel of 0.3 nm full width at half maximum (FWHM). Using the multi-angle viewing method, the satellite observes the target position from different angles, transitioning from a forward view to a view looking directly downward (nadir) and finally to a backward view.

As an example, Figure 5.3 displays the simulated GHGSat radiance corresponding to the solar geometry detailed in Table 1, under the assumption of a single layer of sulfate aerosols near the surface with an SSA of 1 and a g of 0.78. These simulations are based on a surface albedo of 0.2 and an AOD of 0.1 at the SWIR for illustration purposes. Figure 3 indicates that with the addition of a highly reflective aerosol layer, TOA reflectance in the forward viewing direction exceeds that in the nadir or backward viewing direction. This suggests the importance of viewing angles in GHGSat observations when aerosols are present and highlights the potential for retrieving them using multi-angle information. In the following discussions, a positive satellite zenith angle corresponds to an azimuth angle of 0° (forward viewing), while a negative zenith angle corresponds to an azimuth angle of 180° (backward viewing).

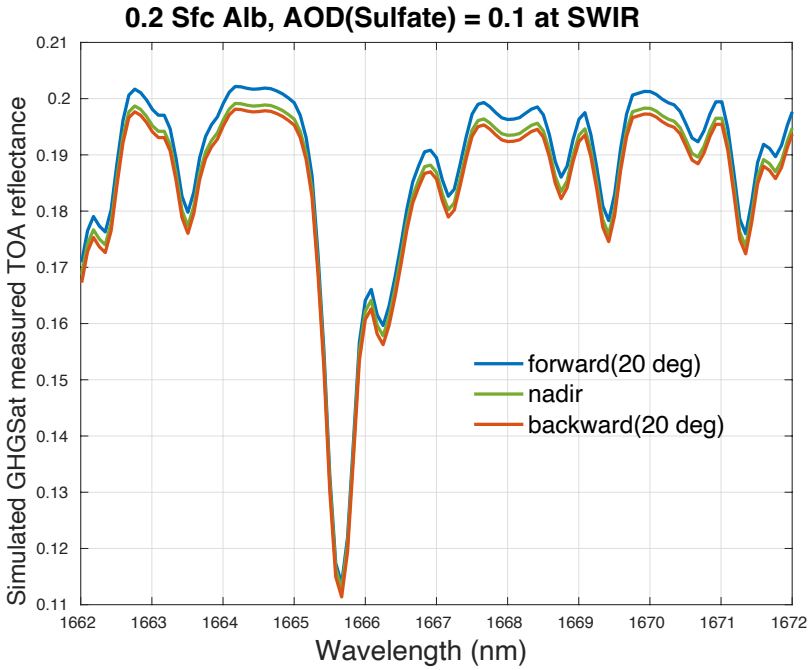

Figure 5.3 Simulated TOA reflectance measured by the GHGSat instrument at a spectral resolution of 0.3 nm FWHM. The instrument observes the surface with an albedo of 0.2 from different viewing positions as defined in Table 1: forward viewing, nadir, and backward viewing. Sulfate aerosols with an AOD of 0.1 at the SWIR are added near the surface.

5.2.5 Retrieval Methods

Figure 5.4 illustrates the steps in the simulated retrieval process in this study. First, we combine the atmospheric-molecule optical properties calculated from the LBLRTM with the aerosol optical properties to run the atmospheric model (DISORT). Then DISORT is further modified according to the GHGSat instrument design to build a complete forward model $\boldsymbol{F}(\boldsymbol{X})$ to simulate the TOA reflectance (Equation 5.1). **X** is the state vector, which includes elements such as the methane mixing ratio XCH_4, the aerosol optical depth (AOD), and the the surface albedo X_{alb}. The goal of the retrieval is to estimate ΔX_{CH_4} and X_{alb} for the ΔX_{CH_4}-only retrievals, and to estimate ΔX_{CH_4}, AOD, and X_{alb} for the simultaneous retrieval using the multi-angle viewing method from the measurement vector $\boldsymbol{y}$:

$$\boldsymbol{y} = \boldsymbol{F}(\boldsymbol{X}) + \boldsymbol{\epsilon_y} \tag{5.4}$$

where $\boldsymbol{\epsilon_y}$ is the measurement error.

Full GHGSat retrieval consists of two steps: a scene-wide retrieval to estimate the background average state vector $\widehat{\boldsymbol{X}}$ and a per-cell retrieval to estimate the local methane plume enhancement. Note that surface albedo is retrieved in both cases. In this study, we focus on the per-cell retrieval assuming known background $\widehat{\boldsymbol{X}}$. In Jervis et al. (2021), a linearized forward model (LFM) is proposed for the GHGSat spatially resolved ΔX_{CH_4}-only retrieval.

$$\boldsymbol{F}^{LFM}(\boldsymbol{X}) = (X_{alb} + b_1 n + b_2 n^2)\left[\boldsymbol{F}(\widehat{\boldsymbol{X}}) + \left(X_{CH_4} - \widehat{X_{CH_4}}\right)\widehat{K_{X_{CH_4}}}\right] \quad (5.5)$$

$$= (X_{alb} + b_1 n + b_2 n^2)\left[\boldsymbol{F}(\widehat{\boldsymbol{X}}) + \Delta X_{CH_4}\widehat{K_{X_{CH_4}}}\right]$$

$\widehat{\boldsymbol{X}}$ is the linearization point, at which the state vector in the observation scene is assumed to be in the background state. $\boldsymbol{K}_{\widehat{\boldsymbol{X}}}$, the Jacobian that corresponds to different state vector elements, is a matrix of partial derivatives that describes how the simulated TOA reflectance changes with respect to the elements of the state vector.

$$\boldsymbol{K} = \frac{\partial \boldsymbol{F}(\boldsymbol{X})}{\partial \boldsymbol{X}} \quad (5.6)$$

To account for the bidirectional distribution of surface albedo and the per-pixel signal changes resulting from satellite motion, the forward model includes a second-order polynomial that is a function of the image frame index n (Jervis et al., 2021). In this study, we employed the LFM model with current GHGSat instruments and estimated ΔX_{CH_4} and X_{alb} by minimizing the difference between the simulated instrument-measured $\boldsymbol{y}$ and $\boldsymbol{F}^{LFM}(\boldsymbol{X})$.

For simultaneous ΔX_{CH_4} and AOD retrieval, we added AOD as an additional variable of interest in the LFM, as depicted below.

$$\boldsymbol{F}^{LFM} = (X_{alb} + b_1 n + b_2 n^2)\left[\boldsymbol{F}(\widehat{\boldsymbol{X}}) + \Delta X_{CH_4}\widehat{K_{X_{CH_4}}} + AOD\widehat{K_{AOD}}\right] \quad (5.7)$$

The applicability of the simultaneous ΔX_{CH_4} and AOD retrieval method mainly comes from two aspects: it enhances the methane gas retrieval accuracy by accounting for the effect of aerosols for GHGSat-like point-source imagers, and it enables the measurement of aerosol plumes using those imagers. By integrating the LBLRTM, DISORT, and the GHGSat instrument model and applying the same inverse model (Equation. 5.5) utilized in current GHGSat operations, our retrieval results can provide a truthful assessment of the simultaneous ΔX_{CH_4} and AOD retrieval

technique on GHGSat-like point-source imagers using the multi-angle viewing method. In the following section, the retrieval method is tested across a wide range of aerosol optical properties, surface albedos, and satellite zenith angle conditions, demonstrating its direct applicability to real measurements.

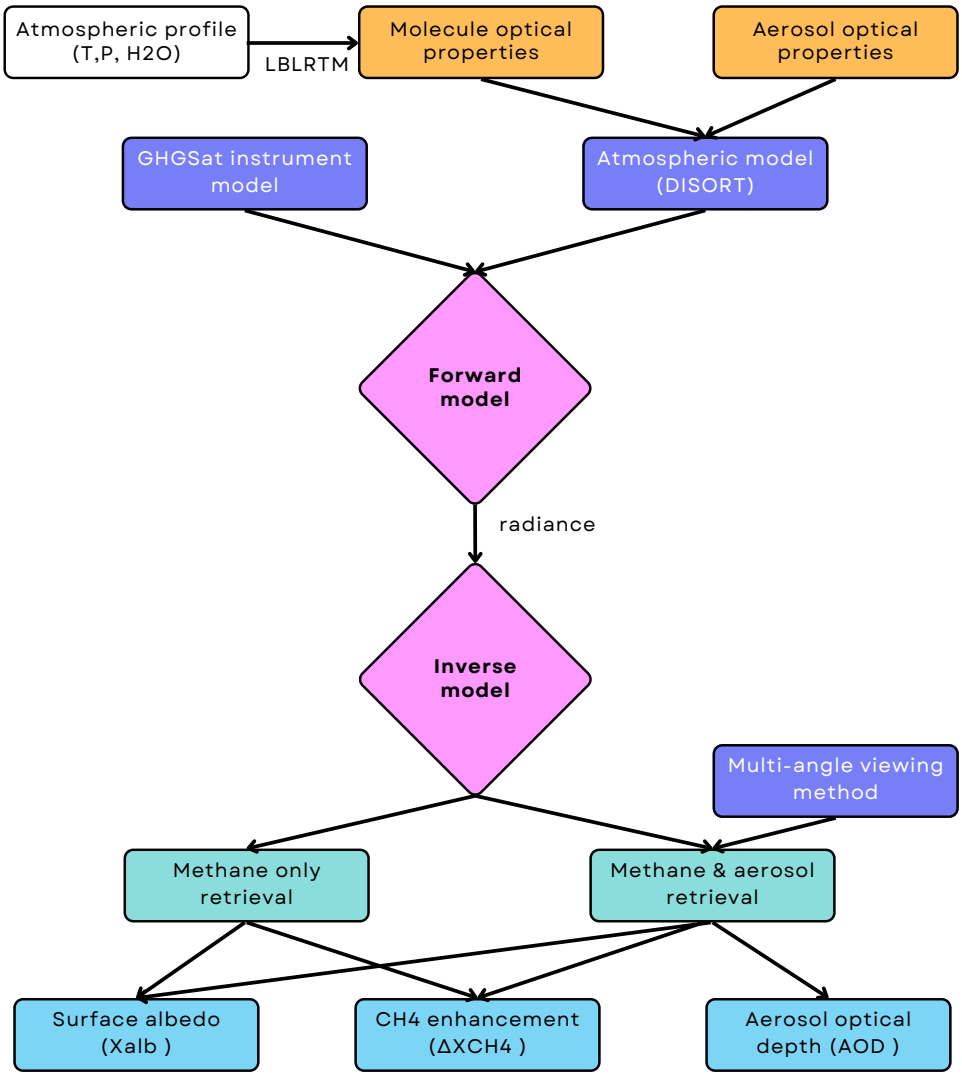

Figure 5.4 Schematic diagram of the retrieval steps.

5.3 Assessment of Two Retrieval Methods

This paper aims to estimate the impact of aerosols on GHGSat methane retrieval, assess the validity of the multiangle viewing method for GHGSat aerosol and methane co-retrieval, and understand the algorithm's sensitivity to different input parameters, including surface albedo, SSA, g, and satellite geometry. To achieve this, retrieval experiments were conducted using synthetic data, and the retrieval errors were estimated.

Figure 5.5 depicts Jacobians with respect to the methane mixing ratio and the AOD with different SSA and g values when the surface albedo is 0.2 and the solar zenith angle is 60°. A negative K_X value indicates that the reflectance at the TOA decreases as the value of the state-vector element X increases. As expected, considering the absorption properties of methane, K_{CH_4} is negative. Similarly, K_{AOD} is also negative in the case of absorbing aerosols (SSA = 0.1). For strongly scattering aerosols (SSA = 0.95) with a high g (0.7) over a dark surface (0.2), K_{AOD} is slightly positive at the forward viewing position and negative at the backward viewing position (Figure 5.5b). When the satellite is at the backward viewing position, the aerosol-only scattering is less pronounced because less light scatters towards space in that direction, resulting in a negative K_{AOD}. In contrast, in the forward viewing position, more light is scattered by aerosols towards space, and this effect prevails over the effect of atmospheric-absorption enhancement due to aerosol–surface multiple scattering, resulting in a slightly positive K_{AOD}. This is particularly noticeable when the asymmetry factor, g, is low (0.1). In this case, the dominant factor is the shortening of the light path caused by aerosol-only scattering, which leads to a positive K_{AOD}, regardless of the viewing angle (Figure 5.5c). For aerosol with a low g (0.1) over a mid-range albedo (0.5), the competition between aerosol-only scattering and aerosol–surface multiple scattering results in a near-zero K_{AOD} (Figure 5.5e).

Figure 5.5 also compares the Jacobians between the satellite forward (scattering angle 100°) and backward (scattering angle 140°) viewing positions. With high SSA and g values, differences in aerosol Jacobian between the two angles increase, providing more information to the simultaneous retrieval. For simulated GHGSat retrieval using the multi-angle viewing technique, the scattering angle increases from 100 to 140° from forward viewing to backward viewing, as depicted in Figure 5.6a. Given a specific asymmetry factor value (g = 0.78), the angular distribution of aerosol scattering energy within this scattering angle range is depicted in Figure 5.6b. This illustrates that the intensity of scattering energy diminishes as the scattering angle increases, leading a decrease in TOA reflectance. The greater the variation in TOA reflectance at various angles, the richer the aerosol information it can provide for simultaneous retrieval.

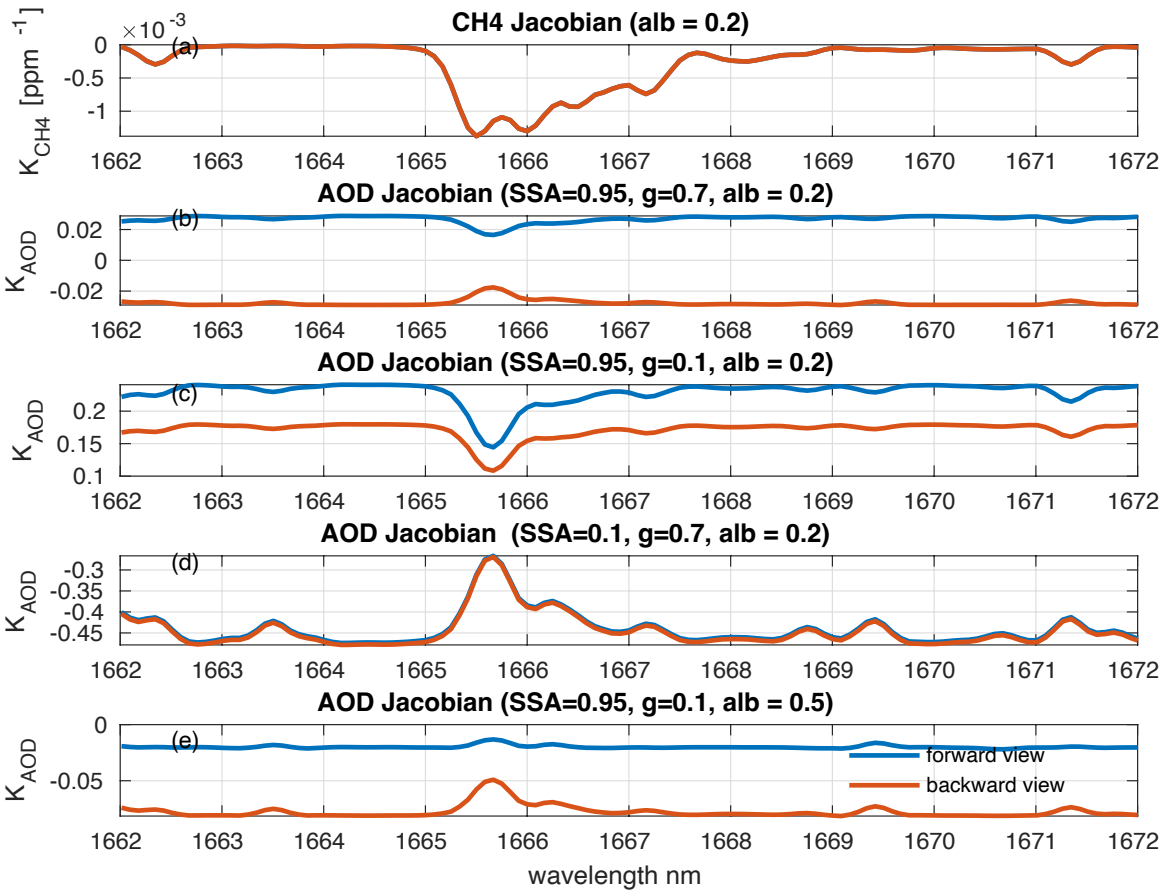

Figure 5.5 Jacobians of TOA reflectance with respect to (a) the methane mixing ratio; (b) the AOD with an SSA of 0.95, a g of 0.7, and a surface albedo of 0.2; (c) the AOD with an SSA of 0.95, a g of 0.1, and a surface albedo of 0.2; (d) the AOD with an SSA of 0.1, a g of 0.7, and a surface albedo of 0.2; and (e) the AOD with a SSA of 0.95, a g of 0.1, and a surface albedo of 0.5. Aerosols are concentrated near the surface, and the forward and backward viewing-angle settings follow Table 5.1.

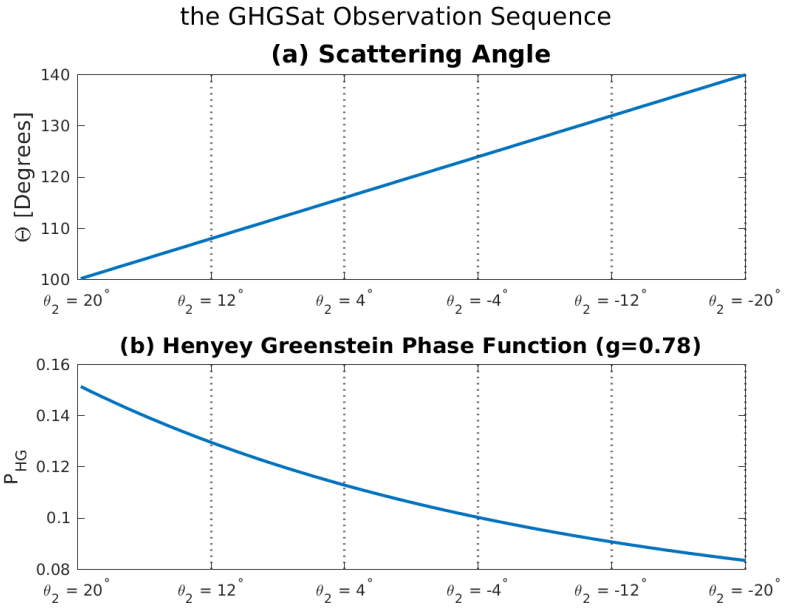

Figure 5.6 (a) Scattering angles Θ and (b) Phase function P_{HG} for g =0.78 as a function of the satellite zenith angle θ_2 during a GHGSat observation sequence when applying the multi-angle viewing method with a maximum satellite zenith angle of 20°.

As instrument measurements are always subject to noise and errors, it is important to include these in the simulated retrieval process to represent real-world conditions. During the simulated retrieval, white noise and 1/f errors with a magnitude of 0.2 % each (calculated as the standard deviation of the individual noise fields) are added to the TOA reflectance. The

background value for the methane mixing ratio is 1.7 ppm. The simulated truths of methane enhancement (ΔX_{CH_4}) and aerosol optical depth (AOD) are 0.1 ppm and 0.1, respectively. We performed 1000 independent retrievals for each aerosol and surface albedo setting, and we quantified the mean bias and standard deviation of the retrieved ΔX_{CH_4} relative to the background to represent the level of accuracy and consistency of the retrieved data.

5.3.1 The Impact of Incorporating the AOD and Employing the Multi-angle Viewing Method

To assess the extent to which incorporating aerosols and applying the multi-angle viewing method can improve the GHGSat methane retrieval, we conducted retrieval under four conditions: when aerosols are present but not retrieved for the (1) nadir-only methane retrieval and (2) the multiangle viewing methane retrieval and when aerosols and methane are co-retrieved (3) in the nadir viewing mode and (4) in the multi-angle viewing mode. The mean bias in the retrieved ΔX_{CH_4} and AOD is shown in Figure 5.7.

Figure 5.7a - 5.7b indicate that the multi-angle viewing method alone has little impact on the methane retrieval accuracy for the methane-only retrieval. For extreme aerosol SSA and g values, the mean bias in ΔX_{CH_4} ranges from 6 % to −25 % when aerosols are neglected in the retrieval. After adding AOD as an additional retrieval variable, the mean bias in ΔX_{CH_4} significantly decreased to 0.32 % (Figure 5.7c). Further applying the multi-angle viewing method with angles specific in Table 1 reduced the mean bias in ΔX_{CH_4} even further to 0.15 % (Figure 5.7d). This suggests that the good performance of aerosol and methane co-retrieval using the multi-angle method largely comes from incorporating AOD as an additional retrieval variable.

As for the AOD retrieval performance, Figure 5.7e - 5.7f suggest that applying the multi-angle viewing method yields better accuracy in the AOD retrieval than the nadir-only method, with the mean bias in AOD being less than 0.02. In theory, the multi-angle viewing method should provide more information than nadir viewing observations, especially for aerosol retrieval. The relatively modest improvement observed with the multi-angle viewing method in our study compared to the substantial enhancement achieved by adding AOD alone may stem from the instrumental limitation of intensity-only measurements within a single spectral band. Nevertheless, our study continues to employ the multi-angle viewing method for simultaneous aerosol and methane retrieval, as it yields the most significant improvement in retrieval accuracy and precision for both ΔX_{CH_4} and AOD.

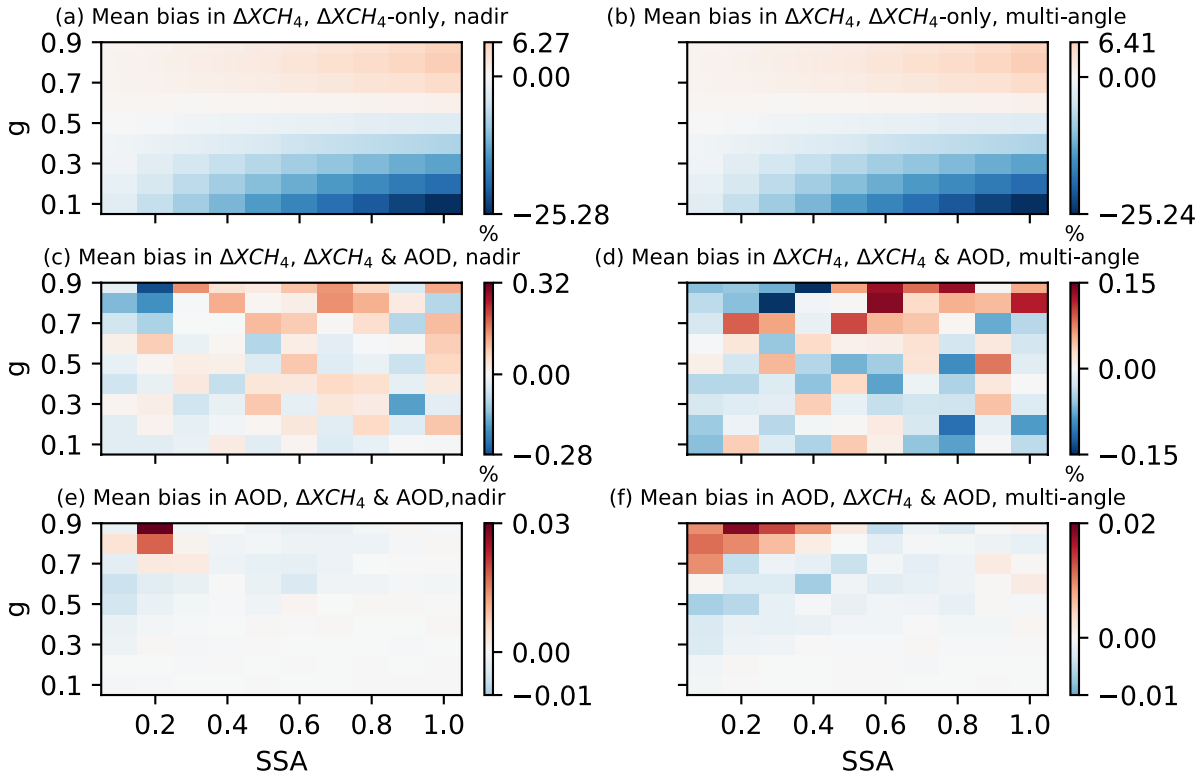

Figure 5.7 (a, c, e) Nadir-only viewing mode. (b, d, f) Multi-angle viewing mode (Table 5.1; the scattering angle ranges from 100–140°). (a, b) Mean bias in retrieved ΔX_{CH_4} values when aerosols are present but not retrieved. (c, d) Mean bias in retrieved ΔX_{CH_4} values when aerosols and methane are simultaneously retrieved. (e, f) Mean bias in retrieved AOD values when aerosols and methane are simultaneously retrieved. Retrieval results are displayed as a function of aerosol SSA and g when the surface albedo is 0.2. The simulated truths of ΔX_{CH_4} and AOD are 0.1 ppm and 0.1, respectively. The mean bias in ΔX_{CH_4} is calculated relative to the background methane mixing ratio.

5.3.2 Comparisons between the ΔX_{CH_4}-only Retrieval and Simultaneous ΔX_{CH_4} and AOD Retrieval

To examine the performance of different retrieval methods, we conduct simulated retrieval with a range of surface albedos and aerosol optical properties. We compare two scenarios in terms of the mean bias and standard deviations of retrieved variables (ΔX_{CH_4}, AOD, and X_{alb}): (1) when aerosols are present but not retrieved in the nadir-viewing mode and (2) when both ΔX_{CH_4} and AOD are retrieved simultaneously using the multi-angle viewing method.

5.3.2.1 Impact of Aerosol SSA and g

As we only retrieve the AOD for aerosol-related parameters, unaccounted-for variables such as the aerosol single scattering albedo (SSA) and asymmetry factor (g) can influence our results. To assess this impact, we fix the background surface albedo at 0.2 and examine how the mean bias and SD vary with different combinations of aerosol SSA and g.

Figure 5.8a – 5.8d display the mean bias of the retrieved ΔX_{CH_4} and X_{alb} values for the ΔX_{CH_4}-only retrieval scenario. The angle setting follows Table 5.1. When retrieving ΔX_{CH_4} without

accounting for aerosols, the ΔX_{CH_4} only method underestimates ΔX_{CH_4} for situations with low aerosol g and overestimates it in cases with high aerosol g. This occurs because aerosols scatter more light back into space when g is low, reducing the absorption of CH_4. Conversely, when aerosol g is high, increased aerosol–surface multiple scatterings lead to greater atmospheric CH_4 absorption. Figure 5.8a also shows that the magnitude of the retrieval bias increases with increasing SSA. For a surface albedo of 0.2, the maximum bias in ΔX_{CH_4} for ΔX_{CH_4}-only retrieval can reach −25 % relative to the background with extremely high SSA and low g values. These results are in agreement with other studies (Huang et al., 2020). Both increasing SSA and decreasing g enhance the radiation scatter back into space, thereby decreasing the atmospheric-methane absorption. For typical optical-property ranges of aerosols (SSA ∈ [0.86, 0.98] and g ∈ [0.54, 0.76]), the mean bias in ΔX_{CH_4} falls between −3.0 % and 6.3 % for ΔX_{CH_4}-only nadir retrieval. Neglecting aerosols also affects the retrieval of X_{alb}. As shown in Figure 5.8d, X_{alb} is underestimated (overestimated) when SSA is small (large).

In contrast, Figure 5.9 suggests that simultaneous retrieval of ΔX_{CH_4} and AOD can significantly improve the accuracy of ΔX_{CH_4} retrieval while also retrieving relatively accurate values for AOD and X_{alb}. Using simultaneous retrieval can reduce the mean bias in ΔX_{CH_4} to within 0.1 % (Table 5.2) for typical optical-property ranges of aerosols. As for the consistency of the simultaneous retrieval, Figure 5.9d indicates that the maximum SD in ΔX_{CH_4} is near to 2.5 %, which is slightly higher than that in the ΔX_{CH_4}-only retrieval (~ 1.6 %). This results from the near-zero AOD Jacobian values (Figure 5.5b). Although aerosols have little effect on the TOA reflectance under these conditions, their inclusion in the simultaneous retrieval inevitably increases the uncertainty in retrieved ΔX_{CH_4}. As for the AOD results, the mean bias falls within 1.7 % for typical aerosol optical-property ranges (Figure 5.9b), with the SD showing a slightly high value,

suggesting that retrieval uncertainties are larger when aerosol SSA and g vary. In general, the multi-angle method performs better for AOD retrieval when aerosols have a high SSA and a high g, which can be explained by the more pronounced AOD Jacobian differences between forward and backward viewing angles, as indicated by Figure 5.5b. In the retrieved surface albedo results (Figure 5. 9c), the mean bias in X_{alb} is less than 2.1 % for typical aerosol optical-property ranges. The mean bias and SD distribution pattern of X_{alb} are similar to those of AOD as a result of the interference of aerosol scattering energy with surface albedo retrieval.

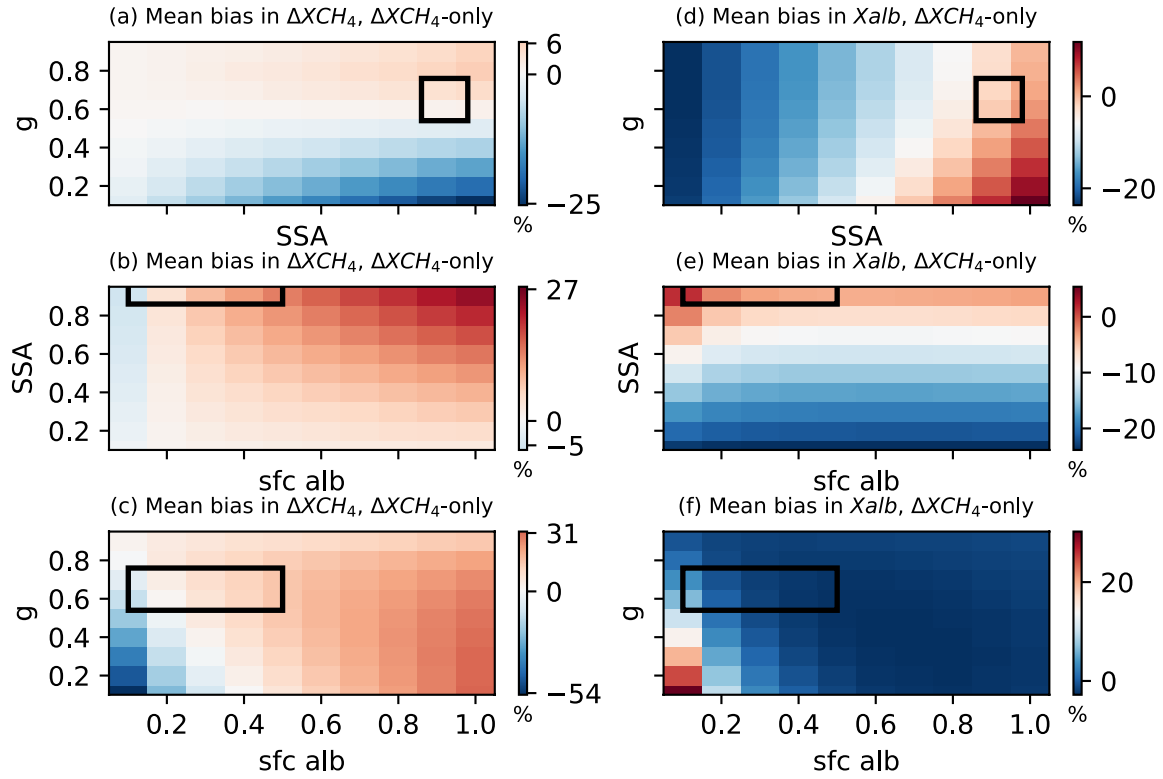

Figure 5.8 Mean bias of retrieved ΔX_{CH_4} (a, b, c) and X_{alb} (d, e, f) values when aerosols are present but not retrieved in the nadir viewing mode. (a, d) Mean bias as a function of aerosol SSA and g when the surface albedo is 0.2. (b, e) Mean bias as a function of surface albedo and aerosol SSA when aerosol g is 0.7. (c, f) Mean bias as a function of surface albedo and aerosol g

when aerosol SSA is 0.95. The black box represents typical values for aerosol optical-property and surface albedo (sfc alb) ranges (SSA ∈ [0.86, 0.98], g ∈ [0.54, 0.76] and sfc alb ∈ [0.1, 0.5]) in the observations. The simulated truths of ΔX_{CH_4} and AOD are 0.1 ppm and 0.1, respectively. The scattering angle ranges from 100–140°.

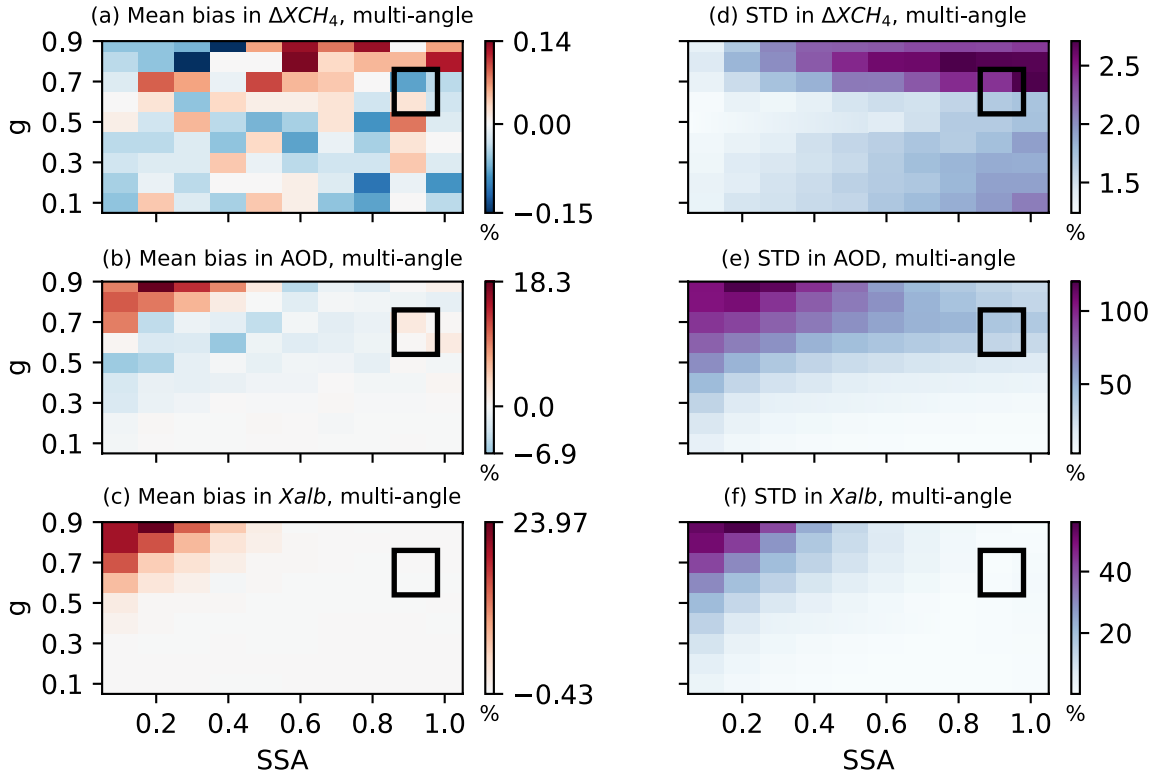

Figure 5.9 Mean bias (a, b, c) and standard deviations (SDs) (d, e, f) of the retrieved ΔX_{CH_4}, AOD, and X_{alb} as a function of aerosol SSA and g. The simulated truths of ΔX_{CH_4}, AOD, and X_{alb} are 0.1 ppm, 0.1, and 0.2, respectively. The scattering angle ranges from 100–140°. The black box represents the typical values for aerosol optical-property ranges (SSA ∈ [0.86, 0.98] and g ∈ [0.54, 0.76]) in the observations.

5.3.2.2 Surface Albedo Impact

Since the interaction between aerosols and the underlying surface can largely determine the retrieval performance, we further explored the accuracy and precision of the retrieved ΔX_{CH_4}, AOD, and X_{alb} for ΔX_{CH_4}-only retrieval and simultaneous retrieval under different surface albedo conditions.

Figure 5.8b - 5.8e display the distribution of mean bias in ΔX_{CH_4} and that in X_{alb} for ΔX_{CH_4}nadir retrieval when aerosol g is fixed at 0.7. As shown in Figure 5.8b, neglecting aerosols results in an overestimation (underestimation) of the retrieved ΔX_{CH_4} with high (low) surface albedo. These results are in agreement with other studies (Butz et al., 2009; Huang et al., 2020), despite the differences in retrieval variables, experiment settings, and instruments. A high surface albedo enhances the surface and aerosol multiple scattering, leading to increased methane absorptions. Conversely, a low surface albedo favours aerosol-only scattering, reducing methane absorptions. As a result, in the case of ΔX_{CH_4}-only retrieval, the bias is most pronounced ($\sim$ 27 %) when both aerosol SSA and surface albedo are extremely high. Therefore, it is advisable to refrain from performing methane retrieval over highly reflective surfaces. For commonly encountered aerosol SSA (0.86–0.98) and surface albedo (0.1–0.5) values, the mean bias in ΔX_{CH_4} for ΔX_{CH_4}-only retrieval ranges from −5.9 % to 13.1 % when g is fixed at 0.7. Similar to Figure 5.8d, Figure 5.8e suggests that the retrieved X_{alb} value increases with an increase in SSA.

When simultaneously retrieving methane and aerosols, Figure 5.10a suggests that the mean bias in ΔX_{CH_4} is significantly reduced to 0.1 % when compared with the ΔX_{CH_4}-only retrieval. The SD of the retrieved methane is slightly higher when high-SSA aerosols are present over low-albedo surfaces. This is explained by the near-zero AOD Jacobian values (Figure 5.5b), as previously

discussed. Moreover, the SDs of the retrieved ΔX_{CH_4} and AOD are a bit higher when SSA is extremely low (0.1). This decrease in retrieval precision results from the positive values in the AOD Jacobian as well as minimal differences in the AOD Jacobian between forward and backward viewing (Figure 5.5d), considering the strongly absorbing characteristics of aerosols. In this scenario, it is challenging to distinguish between aerosols and the surface, thereby affecting the CH_4 and aerosol retrieval. The mean bias in the retrieved AOD and X_{alb} is within 1.7 % and 0.07 %, respectively, for typical values of aerosol SSA and surface albedo ranges (sfc alb ∈ [0.1, 0.5] and SSA ∈ [0.86, 0.98]). In general, the multi-angle viewing technique demonstrates higher accuracy compared with the ΔX_{CH_4}-only retrieval, regardless of surface albedo values, especially when aerosols with stronger scattering abilities are present.

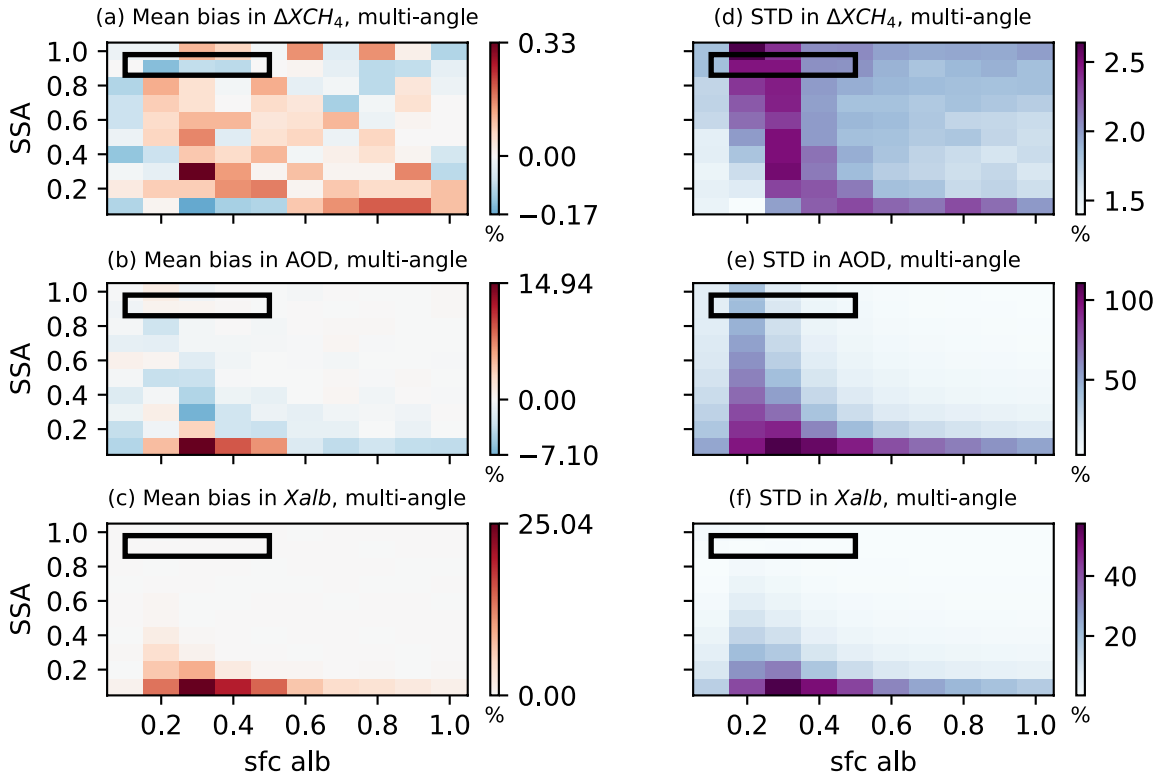

Figure 5.10 Mean bias (a, b, c) and standard deviations (SDs) (d, e, f) of the retrieved ΔX_{CH_4}, AOD, and X_{alb} as a function of surface albedo and aerosol SSA when aerosol g is 0.7. The simulated truths of ΔX_{CH_4} and AOD are 0.1 ppm and 0.1, respectively. The scattering angle ranges from 100–140°. The black box represents the typical values for aerosol optical-property and surface albedo ranges (sfc alb ∈ [0.1, 0.5] and SSA ∈ [0.86, 0.98]) in the observations.

Apart from SSA, it is also interesting to examine how the retrieval bias varies under different combinations of aerosol asymmetry factor and surface albedo. Figure 5.8c – 5.8f present the mean bias in ΔX_{CH_4} and X_{alb} for ΔX_{CH_4}-only retrieval and simultaneous retrieval when aerosol SSA is fixed at 0.95. For ΔX_{CH_4}-only retrieval, ΔX_{CH_4} is underestimated (overestimated) with low (high) surface albedo, especially when g is small. These errors arise because aerosols with low g over dark surfaces tend to scatter more light towards space. However, when the surface is bright, it reflects a larger proportion of the light towards aerosols, and aerosols with low g tend to scatter this light back to the surface again, thereby enhancing methane absorption. The maximum bias in ΔX_{CH_4} for ΔX_{CH_4}-only retrieval is around −50 % when both aerosol g and surface albedo are extremely low. For typical values of g (0.54–0.76) and surface albedo (0.1–0.5), neglecting aerosols results in a mean bias in ΔX_{CH_4} ranging from −20.5 % to 12.2 %.

By employing simultaneous retrieval, the mean bias in ΔX_{CH_4} can be reduced to 0.27 % (Figure 5.11a), demonstrating an enhancement in ΔX_{CH_4} accuracy. An increase in surface albedo enhances surface–aerosol multiple scattering, while a decrease in g enhances aerosol backscattering. This competition effect results in a slope in the distribution of large SD values. Regarding the retrieved AOD and X_{alb}, their mean bias falls within −4.9 % and 0.06 % (Figure 5.11b – 5.11c), respectively, in the presence of strongly scattering aerosols (SSA = 0.95).

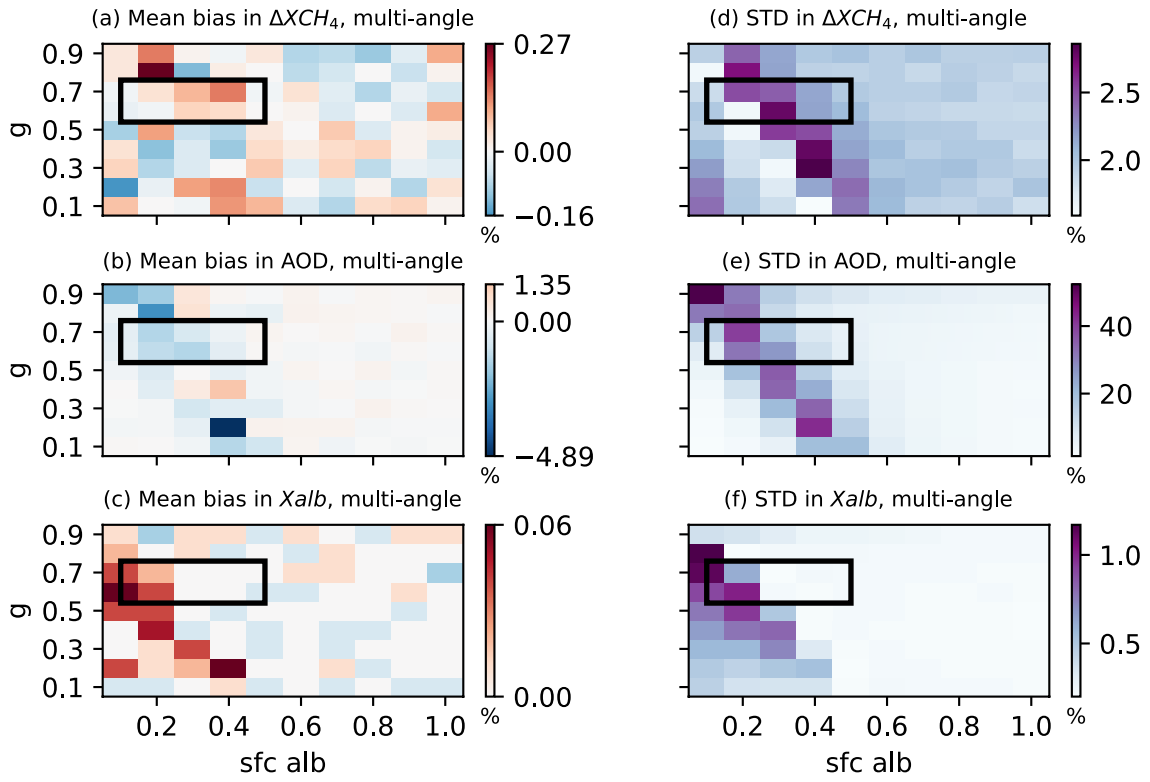

Figure 5.11 Mean bias (a, b, c) and standard deviations (SDs) (d, e, f) of the retrieved ΔX_{CH_4}, AOD, and X_{alb} as a function of surface albedo and aerosol g when aerosol SSA is 0.95. The simulated truths of ΔX_{CH_4} and AOD are 0.1 ppm and 0.1, respectively. The scattering angle ranges from 100–140°. The black box represents the typical values for aerosol optical-property and surface albedo ranges (sfc alb ∈ [0.1, 0.5] and g ∈ [0.54, 0.76]) in the observations.

Overall, in simultaneous ΔX_{CH_4} and AOD retrieval using the multi-angle viewing method, the retrieved ΔX_{CH_4}, AOD, and X_{alb} values generally match very well with the simulated truths across various aerosol optical properties and surface albedo conditions. Table 5.2 summarizes the mean bias and SDs in the retrieved ΔX_{CH_4} , AOD, and X_{alb} for the ΔX_{CH_4}-only retrieval in the nadir viewing mode and for the simultaneous ΔX_{CH_4} and AOD retrieval in the multi-angle viewing mode, considering typical values of aerosol optical properties and surface albedo encountered in

the observations. Using the simultaneous retrieval method, the mean bias and SD in ΔX_{CH_4} fall within the ranges of 0.3 % and 2.8 %, respectively. Similarly, the mean bias in AOD and X_{alb} remains within 3.1 % and 0.1 %, respectively. It should be noted that under certain conditions characterized by near-zero AOD Jacobian values, such as scenarios with high SSA and high g values over a low-albedo surface and high SSA and low g values over a moderately reflective surface, or for positive AOD Jacobian values when SSA is extremely low over surfaces with medium-to-high albedo, we observe a slightly higher SD in simultaneous retrieval. Although the retrieved AOD shows relatively high accuracy, its SD can exceed 10 %, suggesting an uncertainty in AOD retrieval when SSA and g are not constrained.

Table 5.2 Mean bias and SDs in retrieved ΔX_{CH_4}, AOD, and X_{alb} values for the ΔX_{CH_4}-only retrieval in the nadir viewing mode and for the simultaneous ΔX_{CH_4} and AOD retrieval in the multi-angle viewing mode with a 20° maximum satellite zenith angle. The simulated truths of ΔX_{CH_4} and AOD are 0.1 ppm and 0.1, respectively. The mean bias and SD are given CH_4 relative to the background values. Experiment nos. 1 to 3 correspond to Sect. 5.3.2, and experiment no. 4 corresponds to Sect. 5.4.1. "Correlation coef": correlation coefficient.

	Mean bias in ΔX_{CH_4}	SD in ΔX_{CH_4}	Mean bias in AOD	SD in AOD	Mean bias in X_{alb}	SD in X_{alb}	Correlation coef (ΔX_{CH_4} and AOD)
Experiment no. 1: SSA ∈ [0.86, 0.98], g ∈ [0.54, 0.76], sfc alb = 0.2							
ΔX_{CH_4}-only nadir retrieval	−3.0 % to 6.3 %	1.6 %	–	–	−5.7 % to 3.4 %	0.2 %	–
ΔX_{CH_4} and AOD multi-angle retrieval	−0.1 % to 0.1 %	1.6 % to 2.7 %	−1.7 % to 1.7 %	18.2 % to 48.6 %	−0.07 % to 0.04 %	0.3 % to 2.1 %	−85 % to 30 %
Experiment no. 2: sfc alb ∈ [0.1, 0.5], SSA ∈ [0.86, 0.98], g = 0.7							
ΔX_{CH_4}-only nadir retrieval	−5.9 % to 13.1 %	1.5 % to 1.6 %	–	–	−6.7 % to 5.4 %	0.2 %	–
ΔX_{CH_4} and AOD multi-angle retrieval	−0.1 % to 0.1 %	1.7 % to 2.6 %	−3.1 % to 1.1 %	8.0 % to 47.0 %	−0.1 % to 0.04 %	0.2 % to 1.83 %	−81 % to 43 %
Experiment no. 3: sfc alb ∈ [0.1, 0.5], g ∈ [0.54, 0.76], SSA = 0.95							
ΔX_{CH_4}-only nadir retrieval	−20.5 % to 12.2 %	1.5 % to 1.6 %	–	–	−2.3 % to 10.1 %	0.2 %	–
ΔX_{CH_4} and AOD multi-angle retrieval	−0.1 % to 0.3 %	1.6 % to 2.8 %	−3.0 % to 0.7 %	4.7 % to 39.9 %	0 % to 0.1 %	0.2 % to 1.2 %	−83 % to 52 %
Experiment no. 4: sfc alb ∈ [0.1, 0.5], max(sat zenith) ∈ [0°, 20°], SSA = 0.95, g = 0.7							
ΔX_{CH_4}-only multi-angle retrieval	−5.7 % to 12.4 %	1.6 % to 1.7 %	–	–	−2.3 % to 5.1 %	0.2 %	–
ΔX_{CH_4} and AOD multi-angle retrieval	−0.1 % to 0.1 %	1.8 % to 2.2 %	−0.2 % to 0.8 %	6.6 % to 26.8 %	0 %	0.2 % to 0.6 %	−65 % to 42 %

5.4 Simultaneous Retrieval Analysis

5.4.1 The Effect of Satellite Zenith Angle on Simultaneous Retrieval

The discussions above have proved that using the multiangle viewing method for simultaneous ΔX_{CH_4} and AOD retrieval can significantly improve the retrieval accuracy of ΔX_{CH_4} when compared with the ΔX_{CH_4}-only nadir retrieval. It is still worth investigating whether the retrieval results are highly dependent on the chosen satellite zenith angles. In this section, satellite zenith angles ranging from 0 to 80° are tested in both the ΔX_{CH_4}-only retrieval and the simultaneous retrieval. As shown in Table 5.3, the scattering angle range broadens with increasing satellite zenith angle magnitude, which could benefit aerosol retrieval, as it leads to more distinct differences in TOA reflectance across various satellite viewing positions. However, larger satellite zenith angles could also introduce more bias into methane retrieval because of the slanted-path effect.

Considering aerosols with an AOD of 0.1, a SSA of 0.95, and a g of 0.7, the mean bias and SDs for the ΔX_{CH_4}-only retrieval and for the simultaneous retrieval as a function of surface albedo and the maximum magnitude of the satellite zenith angle are shown in Figure 5.12. If aerosols are neglected, the retrieved ΔX_{CH_4} is always overestimated except under the extremely low surface albedo (0.1) condition. The retrieval bias magnitude escalates with growing maximum magnitude of the satellite zenith angle. A larger satellite zenith angle brings a longer light path, which enhances atmospheric absorption and introduces larger retrieval errors. The maximum mean bias in ΔX_{CH_4} for ΔX_{CH_4}-only retrieval can exceed 80 % when the satellite zenith angle exceeds 70°. For typical ranges of the GHGSat satellite zenith angle (10–20°) and the surface albedo (0.1–0.5), the mean bias in ΔX_{CH_4} for ΔX_{CH_4}-only retrieval is −5.7 % to 12.4 %.

For simultaneous ΔX_{CH_4} and AOD retrieval, the mean bias in ΔX_{CH_4} remains below 0.1 %, and it varies little with the chosen satellite zenith angle. This suggests that the multiangle viewing method is effective for GHGSat-like satellites, regardless of their observation swath. The better retrieval performance of simultaneous retrieval in the multi-angle viewing mode largely results from adding AOD as an additional predictor instead of applying the multi-angle method, considering that the GHGSat satellite is an intensity-only instrument targeting one specific band.

The magnitude of the SD in ΔX_{CH_4} from the simultaneous retrieval experiences a slight increase and then decreases as the satellite zenith angle magnitude increases. This happens because, with the increase in the satellite's zenith angle, more energy scatters back into space, while a longer light path leads to greater atmospheric absorption. At a specific point, the aerosol Jacobian approaches zero, which introduces relatively high uncertainty into the simultaneous retrieval process.

Table 5.3 Satellite zenith angle ranges tested for ΔX_{CH_4}-only retrieval and simultaneous ΔX_{CH_4} and AOD retrieval using the multi-angle viewing method. The solar zenith angle is 60°.

Satellite zenith angle range	0°	-10° ~ 10°	-20° ~ 20°	-30° ~ 30°	-40° ~ 40°	-50° ~ 50°	-60° ~ 60°	-70° ~ 70°	-80° ~ 80°
Scattering angle range	120°	110° ~ 130°	100° ~ 140°	90° ~ 150°	80° ~ 160°	70° ~ 170°	60° ~ 180°	50° ~ 180°	40° ~ 180°

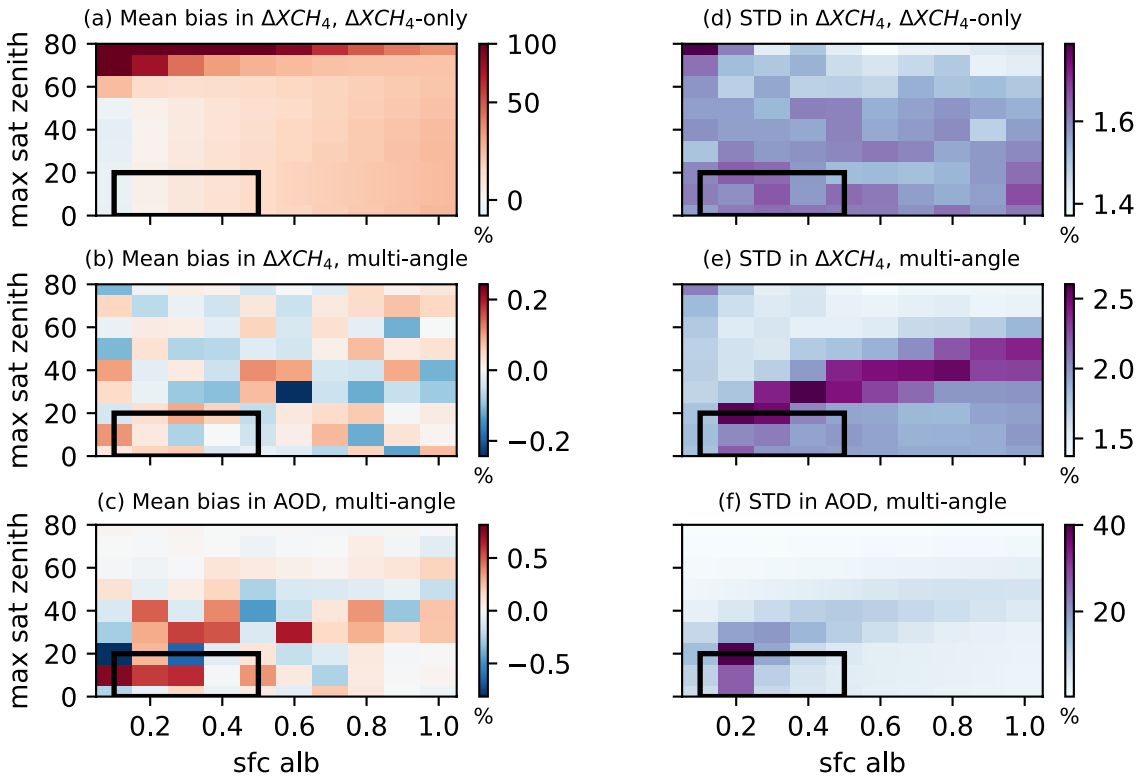

Figure 5.12 (a) Mean bias and (d) standard deviations (SD) of retrieved ΔX_{CH_4} values when aerosols are present but not retrieved. (b) Mean bias and (e) SD of retrieved ΔX_{CH_4} values for simultaneous ΔX_{CH_4} and AOD retrieval. (c) Mean bias and (f) SD of retrieved X_{AOD} values for simultaneous ΔX_{CH_4} and AOD retrieval. The retrieval results are displayed as a function of surface albedo and maximum magnitude of satellite zenith angle when aerosol SSA is 0.95, g is 0.7, and the solar zenith angle is 60°. The satellite is in the multi-angle viewing mode. The black box represents the typical values for the GHGSat satellite zenith angle range and the surface albedo range (max(sat zenith) $\theta_2 \in [0°, 20°]$ and sfc alb $\in [0.1, 0.5]$).

5.4.2 Relationship between the Retrieved ΔX_{CH_4} and AOD from Simultaneous Retrieval

Figure 5.13 illustrates the correlation coefficients between the retrieved ΔX_{CH_4} and AOD for various combinations of SSA, g, surface albedo, and satellite zenith values. The simultaneous retrieval is conducted under four specific conditions using the multi-angle viewing method: (1) when the surface albedo is 0.2, (2) when the g is 0.7, (3) when the SSA is 0.95, and (4) when the SSA is 0.95 and g is 0.7. For conditions (1) to (3), the angle setting follows Table 5.1, while for condition (4), the angle settings are based on Table 5.3. Figure 5.13a suggests that ΔX_{CH_4} and AOD are negatively correlated for high g values and negatively correlated for low g values when the surface is dark. A high g results in more concentrated forward scattering towards the ground, causing more atmospheric absorption via aerosol–surface multiple scattering. To maintain the relative depth of the CH4 absorption spectra, less ΔX_{CH_4} needs to be retrieved to balance the effect of the increasing AOD. In Figure 5.13b, ΔX_{CH_4} and AOD are positively correlated for low-albedo surfaces and negatively correlated for mid- and high-albedo surfaces when g is 0.7. With a dark surface, increasing the aerosol causes a greater amount of light to be scattered back into space, leaving less light to interact with CH4. Consequently, a larger ΔX_{CH_4} is retrieved to counterbalance the impact of the increasing AOD. Figure 5.13c shows that the correlation between ΔX_{CH_4} and AOD changes from positive to negative with increasing g and surface albedo when SSA is 0.95. This pattern occurs because of the shift in the dominant aerosol-involved physical processes from the aerosol-only scattering effect to the aerosol–surface multiple scattering effect. Figure 5.13d shows that for aerosols with an SSA of 0.95 and a g of 0.7, ΔX_{CH_4} and AOD are positively (negatively) correlated at low (high) albedo. With increasing satellite zenith angle, the magnitude of the correlation coefficient first increases and then decreases, suggesting that it is still beneficial

to apply large scattering angle ranges in the multi-angle viewing method to better distinguish aerosols and methane.

When considering a surface with an albedo of 0.2, a SSA from 0.86 to 0.98, and a g from 0.54 to 0.76, the correlation coefficient between the retrieved ΔX_{CH_4} and AOD falls within the range of −85 % to 30 %. Similarly, when the SSA is maintained between 0.86 and 0.98, the surface albedo varies from 0.1 to 0.5, and g is fixed at 0.7, the correlation coefficient ranges from −81 % to 43 %. Lastly, for cases where g ranges from 0.54 to 0.76, the surface albedo spans from 0.1 to 0.5, and SSA is set at 0.95, the correlation coefficient varies from −83 % to 52 %. In general, the pattern in Figure 5.13 is similar to the ΔX_{CH_4} SD pattern in Figures 5.9–5.12, which confirms that the high correlation of ΔX_{CH_4} with AOD results in a larger SD in ΔX_{CH_4}.

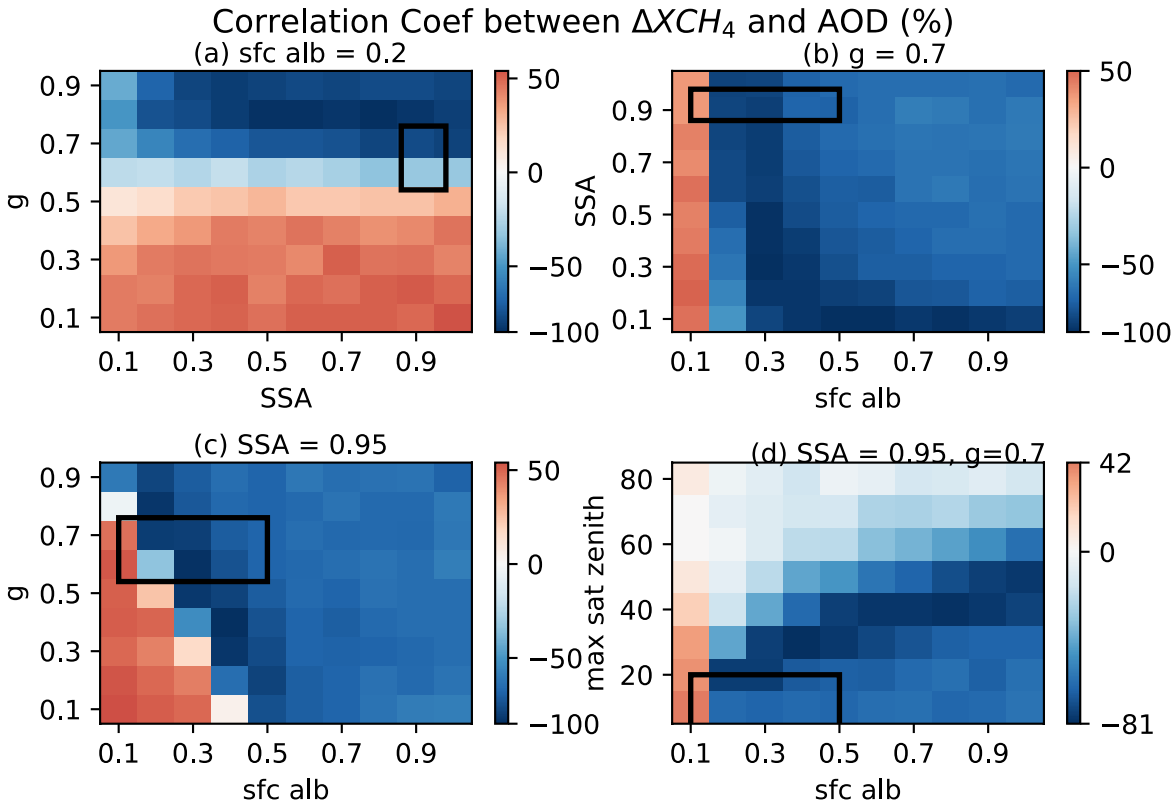

Figure 5.13 Correlation coefficient (%) between the simultaneously retrieved methane enhancement (ΔX_{CH_4}) and aerosol optical depth (AOD) for varying aerosol types and surface albedo values. (a) Surface albedo is fixed at 0.2. (b) Aerosol g is fixed at 0.7. (c) Aerosol SSA is fixed at 0.95. For panels (a) to (c), the maximum magnitude of the satellite zenith angle is 20°. (d) Aerosol SSA is fixed at 0.95 and g is fixed at 0.7. The black box represents the typical values of the ranges for aerosol optical properties, surface albedo, and solar zenith angle in the GHGSat observations.

5.4.3 Impact of Aerosol and Surface Albedo Uncertainties on Simultaneous Retrieval

Although aerosol types could be inferred from emission plumes by considering the combustion type and its location, the uncertainty that arises from inaccurate representation of aerosol types and distributions could impact the performance of our simultaneous retrieval. Additionally, assumptions regarding the Lambertian surface and satellite viewing geometry could potentially introduce uncertainties in surface albedo retrieval. To access such uncertainty, we employ certain aerosol SSA and g, height distributions, and surface albedo in retrieval, while for the simulated GHGSat radiance, we incorporate more complex representations of aerosol type and distributions, and surface albedo. The differences between retrieval with fixed (inaccurate) parameters and retrieval with real (accurate) parameters enable us to quantify the uncertainty resulting from the inaccurate representation of these parameters.

5.4.3.1 Aerosol Type Uncertainties

Figure 5.14 presents the differences in the mean bias and standard deviations of retrieved variables between retrieval assuming SSA = 0.95 and g = 0.7 for aerosols and retrieval assuming the correct SSA and g (ranging from 0 to 1). These differences could suggest that there is

uncertainty in simultaneous retrieval when assuming inaccurate aerosol types. Figure 5.14a -5.14d show that the uncertainties in the mean bias and SD of ΔX_{CH_4} related to aerosol types range from −5.8 % to 2.7 % and from −0.2 to 0.9 %, respectively, for typical aerosol optical-property values. The uncertainties in the mean bias and SD of AOD fall within −40.2 % to 16.1 % and within −9.6 % to 20 %, respectively. Similarly, the uncertainties in the mean bias and SD of X_{alb} range from −5.6 % to 5.4 % and from −1.5 % to 0.39 %, respectively. These findings suggest that even with incorrect SSA and g assumptions in the retrieval, the maximum uncertainty induced in the accuracy of the retrieved ΔX_{CH_4} is within 5.8 %.

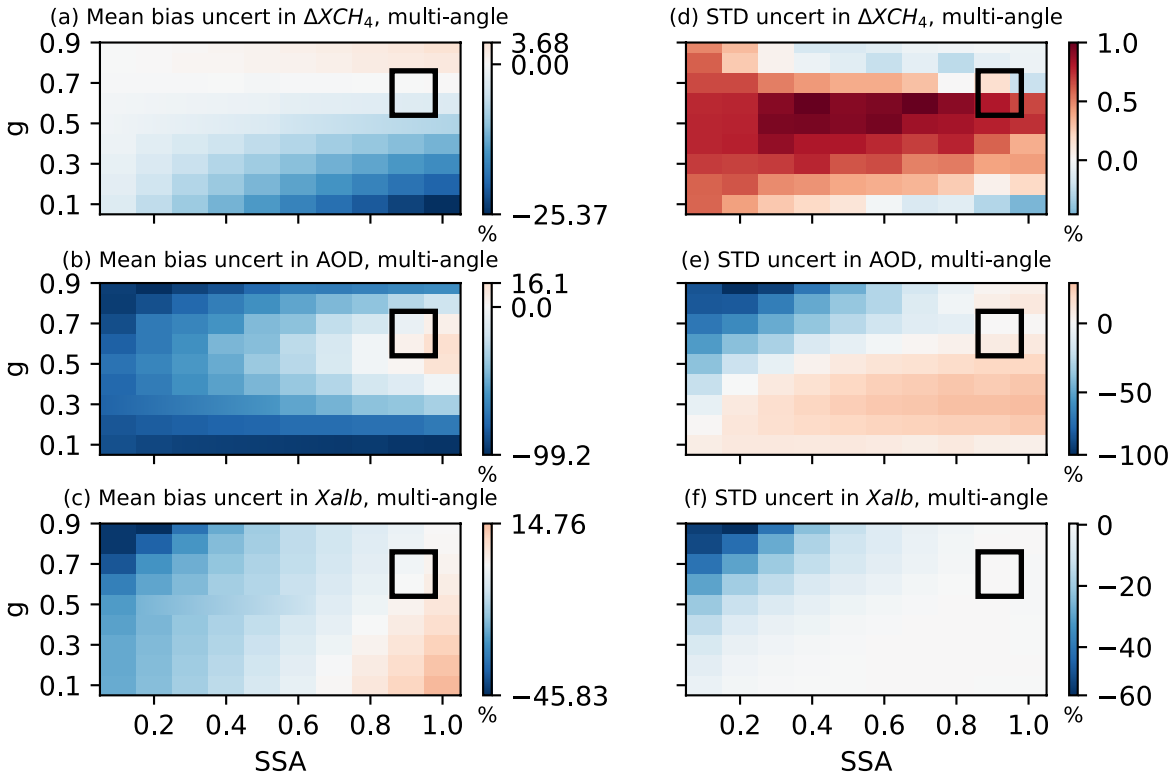

Figure 5.14 Uncertainties induced by aerosol type in the mean bias (a, b, c) and standard deviations (SD) (d, e, f) of the retrieved ΔX_{CH_4}, AOD, and X_{alb}, assuming aerosols with an SSA of 0.95 and a g of 0.7 in the retrieval. The simulated truths of ΔX_{CH_4}, AOD, and X_{alb} are 0.1 ppm,

0.1, and 0.2, respectively. The scattering angle ranges from 100–140°. The black box represents the typical values for aerosol optical-property ranges (SSA ∈ [0.86, 0.98] and g ∈ [0.54, 0.76]) in the observations.

5.4.3.2 Aerosol Height Distribution Uncertainties

While aerosols primarily reside near the surface at the industrial site, they could also ascend to higher altitudes under favourable atmospheric conditions. Therefore, we examined the uncertainty brought by aerosol height assumptions. We compared the difference between the retrieval when we assume aerosols are near the surface and the retrieval when aerosols are elevated to 5 km. In the latter case, AOD linearly decreases with height, but we still use the near-surface Jacobian calculations in retrieval. Figure 5.15 shows the uncertainties in simultaneous retrieval when assuming an incomplete aerosol height.

Similar to the uncertainty results related to aerosol types, Figure 5.15a and d show that the uncertainty induced by aerosol height in the mean bias and SD of ΔX_{CH_4} ranges from 2.3 % to 6.4 % and from −0.1 % to 0.1 %, respectively, for typical values of aerosol optical properties. The mean bias uncertainties for AOD and X_{alb} fall within the ranges of 2.3 % to 41.5 % and −0.8 % to 1.4 %, respectively. The SD uncertainties for ΔX_{CH_4}, AOD, and X_{alb} are generally small, indicating minimal sensitivity of the retrieval precision to the aerosol height distributions.

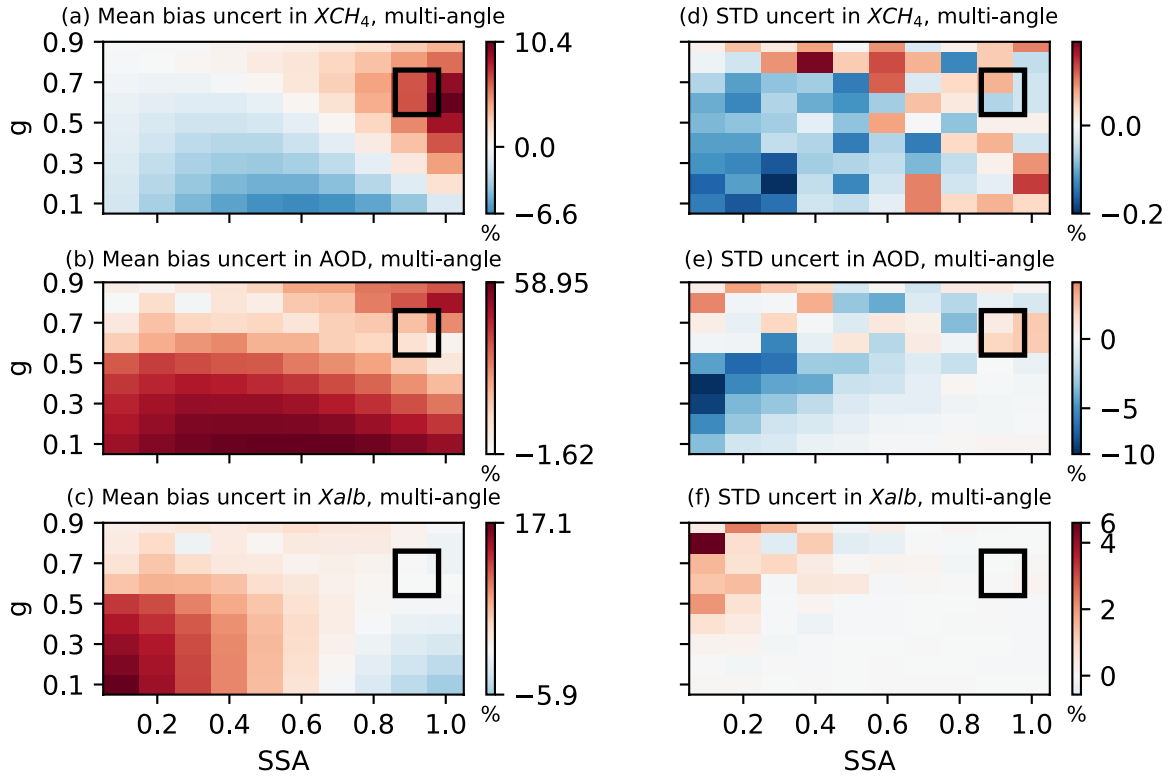

Figure 5.15 Uncertainties induced by aerosol height distributions in the mean bias (a, b, c) and standard deviations (SDs) (d, e, f) of retrieved ΔX_{CH_4}, AOD, and X_{alb}, assuming near-surface aerosols in the retrieval. The simulated truths of ΔX_{CH_4}, AOD, and X_{alb} are 0.1 ppm, 0.1, and 0.2, respectively. The scattering angle ranges from 100–140°. The black box represents the typical values for aerosol optical-property ranges (SSA ∈ [0.86, 0.98] and g ∈ [0.54, 0.76]) in the observations.

5.4.3.3 Surface Albedo Uncertainties

Although a second-order polynomial was applied in the retrieval to account for the bidirectional distribution of surface albedo, the imperfect representation of surface albedo, particularly in regions with heterogeneous landscapes, could introduce uncertainty into the simultaneous retrieval. To quantify such uncertainty, we compared the differences between the

retrieval when we assume the surface albedo is 0.2 and the retrieval with the correct surface albedo values. Figure 5.16 shows the uncertainties in simultaneous retrieval when assuming imperfect surface albedo.

Figure 5.16a and d show that the uncertainty in the mean bias and SD of ΔX_{CH_4} resulting from surface albedo variations ranges from −15.1 % to 4 % and from −0.1 % to 0.7 %, respectively, for typical aerosol SSA and surface albedo ranges (sfc alb ∈ [0.1, 0.5] and SSA ∈ [0.86, 0.98]). The mean bias uncertainties for AOD and X_{alb} fall within the ranges of −12.7 % to 37.6 % and −5.9 % to 3.5 %, respectively, while the SD uncertainties for AOD and X_{alb} range from −1.1 % to 31.9 % and from −0.31 % to 2.25 %, respectively.

In summary, the uncertainties in the mean bias and SD of ΔX_{CH_4} induced by inaccurate aerosol types, height distributions, and surface albedo are less than 15.1 % and 0.9 %, respectively. These uncertainties are obtained when assuming near-surface aerosols with fixed SSA (0.95) and g (0.7) and a surface albedo of 0.2 in the retrieval, while simulated radiance, aerosol SSA, g, height distribution, and surface albedo vary across typical observation ranges.

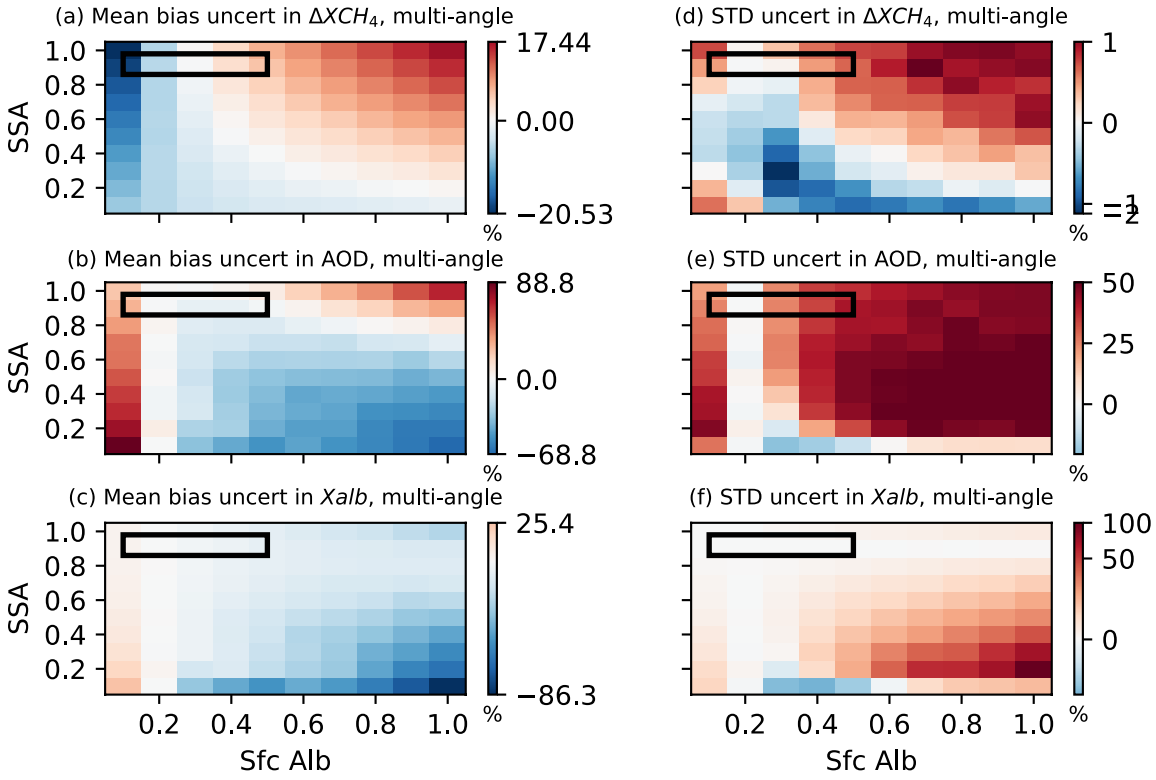

Figure 5.16 Uncertainties induced by surface albedo in the mean bias (a, b, c) and standard deviations (SD) (d, e, f) of retrieved ΔX_{CH_4}, AOD, and X_{alb}, assuming a surface albedo of 0.2 in the retrieval. The simulated truths of ΔX_{CH_4} and AOD are 0.1 ppm and 0.1, respectively. The scattering angle ranges from 100–140°. The black box represents the typical values for aerosol optical-property and surface albedo ranges (sfc alb ∈ [0.1, 0.5] and SSA ∈ [0.86, 0.98]) in the observations.

5.5 Conclusions

This study investigates the impacts of aerosols on GHGSat methane retrieval in the shortwave near-infrared band by exploiting dynamic aerosol scattering behaviour during the GHGSat "multi-angle" observation sequence. Specifically, this research assesses how reliably aerosols can be simultaneously retrieved with methane using the multi-angle viewing method

under different aerosol optical-property, surface albedo, and satellite zenith angle conditions. Observing system simulation experiments (OSSEs) are conducted to simulate GHGSat observations and perform retrieval in the presence of white noise and 1/f errors. These experiments involve a comparative assessment of retrieval accuracy and precision under two conditions: (1) when aerosols are present but not retrieved in the satellite nadir viewing mode and (2) when both methane mixing-ratio enhancement (ΔX_{CH_4}) and aerosol optical depth (AOD) are retrieved simultaneously in the multi-angle viewing mode.

The general behaviour observed in the ΔX_{CH_4}-only retrieval experiment is that ΔX_{CH_4} is underestimated for low-albedo surfaces and overestimated for high-albedo surfaces when aerosols are not taken into account. The estimated errors in ΔX_{CH_4} for non-aerosol retrieval become more significant as the aerosol single-scattering albedo (SSA) increases and the asymmetry factor (g) decreases. For nadir viewing simulations where AOD is set at 0.1 and the solar zenith angle at 60°, the mean bias in the retrieved ΔX_{CH_4} is most significant when scattering aerosols over bright surfaces are neglected. For a surface with an albedo of 0.2, the bias in ΔX_{CH_4} varies from −3.0 % to 6.3 % for typical aerosol optical properties (SSA ∈ [0.86, 0.98] and g ∈ [0.54, 0.76]) (Figure 5.9a); for a satellite zenith angle ranging from 0–20° and a surface albedo varying between 0.1 and 0.5, the mean bias in ΔX_{CH_4} for ΔX_{CH_4}-only retrieval spans from −5.7 % to 12.4 % (Figure 5.12a), assuming an AOD of 0.1, SSA of 0.95, and a g value of 0.7.

Using the multi-angle viewing method for simultaneous ΔX_{CH_4} and AOD retrieval, we find that the bias in retrieved ΔX_{CH_4} is significantly reduced at the modest cost of slightly worse ΔX_{CH_4} precision. Through simultaneous retrieval, the mean bias in ΔX_{CH_4} can be reduced to as low as 0.3 % for the typical ranges of aerosol optical properties, surface albedos, and satellite zenith angles

(Table 5.2). The standard deviation (SD) of ΔX_{CH_4} in simultaneous retrieval experiences a slight increase when aerosols have a minimum impact on the TOA radiance, as indicated by near-zero AOD Jacobian values. Nevertheless, this SD remains within 2.8 %. The uncertainties in the mean bias and SD of ΔX_{CH_4} induced by inaccuracies in aerosol types, height distributions, and the surface albedo are less than 15.1 % and 0.9 %, respectively (Figures. 5.14 – 5.16). The multi-angle viewing method also performs relatively well in AOD retrieval, as characterized by a mean bias of less than 3.1 % (Table 5.2). The performance assessment shows that retrieving aerosols and methane simultaneously using the multi-angle viewing method is a viable approach for operational application to GHGSat.

The correlation coefficient between simultaneously retrieved AOD and ΔX_{CH_4} switches from positive to negative with increasing surface albedo and decreasing aerosol g (Figures 5.13a–5.13c). This transition occurs because the dominant influence of aerosols on the radiance shifts from the aerosol-only scattering effect to the aerosol–surface multiple scattering effect, which suggests that the ability to differentiate between aerosols and methane is highly dependent on the aerosols and surface conditions present.

This study also explored whether the success of the AOD and ΔX_{CH_4} co-retrieval with multi-angle viewing technique is largely determined by the range of scattering angles present in the GHGSat observation sequence. After conducting retrieval over a range of satellite zenith angle values (0 to 80°), results suggest that a broader scattering angle range, such as a larger satellite zenith angle, has little impact on the improvement in AOD and ΔX_{CH_4} co-retrieval accuracy and precision. Therefore, the multi-angle viewing method is relatively insensitive to the satellite angle setting for the GHGSat-like instrument when AOD is incorporated into the retrieval. Finally, future

work on the GHGSat retrieval algorithm and a real retrieval test will investigate the feasibility of adding an aerosol retrieval capability to current and future instruments.

Data Availability

The atmospheric model, synthetic data used by the assessment can be obtained from the Mendeley Data https://data.mendeley.com/datasets/jxcmc63p2h/1.

Chapter 6 Conclusions and Future Work

6.1 Conclusions

This thesis comprehensively explores the interactions between aerosols and radiation, examining their impact on the radiative budget, climate variability, atmospheric modeling, and trace-gas monitoring. Improvement in understanding the ADRE were achieved through: 1) Analyzing the spatial-temporal variations of global ADRE throughout the 21st century; 2) Investigating the discrepancy of ADRE across CMIP6 models to understand inter-model differences; 3) Developing radiative kernels specifically for stratospheric ADRE; 4) Simulating the simultaneous aerosol and methane retrieval for GHGSat to improve the accuracy of their methane measurement.

In Chapter 2, we developed a multivariate regression model to simulate global clear-sky and all-sky ADREs, isolating the effects of aerosol-related and environmental factors on their spatial distributions and trends. Additionally, we utilized this model to analyze how these factors contribute to poleward energy transport driven by ADRE. Our findings indicate that while factors such as scattering AOD, absorbing AOD, surface albedo, and solar zenith angle predominantly influence clear-sky ADRE, AOD alone explains just over half of the spatial variance. This highlights the significant impact of environmental conditions in determining ADRE. For all-sky conditions, the model suggests that the cloud shortwave radiative effect, combined with the aforementioned predictors, adequately represents the all-sky ADRE.

The regression model also quantifies how ADRE responds to changes in key variables. Globally, for each unit increase in SAOD, the ADRE decreases by 29.4 W/m² under clear-sky conditions and 15.7 W/m² under all-sky conditions. Conversely, each unit increase in AAOD raises

the ADRE by 83.5 W/m² under clear-sky and 52.7 W/m² under all-sky conditions. Additionally, a 0.1 increase in surface albedo results in a uniform 1.0 W/m² increase in both $ADRE_{clr}$ and $ADRE_{all}$.

The analysis also highlights significant hemispheric differences in scattering AOD, which primarily drive the northward cross-equator energy transport in both clear-sky and all-sky scenarios. Despite a generally weak global trend in ADRE over the decades, regional trends can vary substantially. For example, in India, ADRE cooling has intensified (-1.8 W m^{-2}/decade for all-sky conditions), whereas in Northeastern America, Europe, and East Asia, it has diminished. Changes in the environmental variables also have a significant impact on the regional ADRE trend. For example, the decreasing surface albedo in the Arctic enhanced ADRE cooling, while changes in cloud radiative effects at midlatitudes in the Southern Hemisphere counteract the impact of scattering AOD trends, diminishing local ADRE trends.

In Chapter 3, we applied the regression model from Chapter 2 to analyze the variability among CMIP6 models regarding the ADRE. We found that the ADRE discrepancies across models account for approximately 38% of the multi-model mean value, highlighting significant uncertainties in ADRE simulations. To delve into the causes of these anomalies, we dissected the ADRE variations into components attributable to differences in state variables and radiative sensitivities. The regression model successfully captured 86 ± 3% of the inter-model ADRE anomaly. Differences in state variables, such as SAOD, explained 67 ± 16%, while variations in radiative sensitivity, such as how ADRE responds to changes in SAOD, accounted for 17 ± 21%.

In assessing specific state variables, the anomaly in SAOD was identified as a major contributor to the global distributions in ADRE anomalies. Other factors, such as anomalies in cloud properties and surface albedo, showed significant regional effects. The influence of differences in radiative sensitivity also varied geographically; over oceans, aerosol-only scattering

effects were predominant, whereas in desert regions and East Asia, interactions between aerosols and the surface were more critical.

The key drivers of ADRE inter-model discrepancy differed among the models. For example, the CNRM-ESM2 model's ADRE anomaly stemmed primarily from an underestimation of SAOD, whereas the GFDL model's ADRE anomaly mainly resulted from an overestimation of AAOD. In models like HadGEM3, MPI-ESM, and MRI-ESM2, the sensitivity of ADRE to aerosol-only scattering effects was the principal contributor. Our results suggest that better constraints on key state variables (AOD, surface albedo, and CRE), along with refined ADRE sensitivities to aerosol-related processes (e.g., aerosol-only scattering and aerosol-surface interaction), could reduce uncertainties in ADRE modeling.

In Chapter 4, we developed a set of radiative kernels tailored for stratospheric aerosols, accounting for their spatial, temporal, and spectral variations. These kernels, which include both broadband and band-specific versions, serve as effective tools for analyzing the stratospheric ADRE across various aerosol types. We found that the impact of stratospheric aerosol kernels on radiation is more pronounced than that of tropospheric aerosols, especially for absorbing aerosols. Globally, a unit increase in SAOD results in a cooling effect of -26.5 W/m^2 at the TOA, whereas a similar increase in AAOD leads to a warming effect of +419.5 W/m^2. This difference is attributed to the higher altitude of these aerosols, which allows them to interact with less attenuated radiation and enhances their interaction with underlying clouds, thus increasing the brightness of darker surfaces below and amplifying stratospheric ADRE sensitivity to absorbing aerosols.

Based on our ADRE regression analysis framework, we developed a physically sorted set of aerosol kernels using TOA insolation, TOA reflectance, and stratospheric AOD as predictors.

These kernels, which are geographically independent, can provide initial estimates of stratospheric ADRE using satellite data.

We tested the performance of our kernels by applying them to evaluate the stratospheric ADRE resulting from the 2022 Hunga volcanic eruption and the 2020 Australia wildfire. The kernel estimation can capture over 90% of the ADRE variance with relative errors within 10%, in these assessments, confirming that our radiative kernels effectively capture the characteristics of stratospheric ADRE.

In Chapter 5, we conducted a detailed study on the effects of aerosol-radiation interactions on methane retrieval accuracy for GHGSat under varying conditions of aerosol optical properties, surface albedo, and satellite zenith angles. Our analysis showed that disregarding aerosols leads to an underestimation of methane enhancement (ΔX_{CH_4}) over low-albedo surfaces and an overestimation over high-albedo surfaces. The error in ΔX_{CH_4} become more pronounced with increasing aerosol SSA and decreasing asymmetry factor (g). Specifically, for a surface albedo of 0.2, the bias in ΔX_{CH_4} ranges from -3.0% to 6.3% for typical aerosol properties (SSA $\in$ [0.86, 0.98] and g $\in$ [0.54, 0.76]).

To mitigate the influence of aerosols, we implemented simultaneous retrievals of ΔX_{CH_4} and AOD using a multi-angle viewing technique. This approach significantly reduced the mean bias in ΔX_{CH_4} to as low as 0.3%, while keeping the standard deviation within 2.8%. The uncertainty in these measurements, influenced by variations in aerosol types, their vertical distribution, and surface albedo, remained below 15.1% for mean bias and 0.9% for standard deviation. Additionally, we observed that the correlation between ΔX_{CH_4} and AOD shifted from positive to negative as surface albedo increased and the aerosol g decreased, indicating a shift from

predominant aerosol-only scattering to complex aerosol-surface multiple scattering interactions. These findings validate the effectiveness of the multi-angle viewing strategy in enhancing the accuracy of GHGSat methane retrievals by accounting for aerosol-radiation interactions, paving the way for improvements in future point-source imagers similar to GHGSat.

6.2 Future Work

Despite significant advancements in aerosol observation and modeling in recent years, many critical questions about aerosol-radiation-climate interactions remain unresolved. Key challenges include improving the representation of aerosols, from their microphysical characteristics to their observable impacts on weather and climate systems, deepening our understanding of how aerosols influence climate systems—such as their interactions with monsoon climates and boundary layers—and reducing discrepancies between models and observations to refine estimates of aerosol radiative forcing. Addressing these challenges requires enhancements in observational techniques, analytical understanding, and modeling approaches.

Rapid Adjustments to Aerosol-Radiation Interactions

The effective radiative forcing (ERF) for aerosol-radiation interactions allows shorter-timescale atmospheric elements to adjust to equilibrium while fixing sea surface temperatures. This ERF can be separated into the instantaneous ADRE and subsequent rapid adjustments, involving both the stratosphere and troposphere. These adjustments may amplify or mitigate the initial ADRE through changes in atmospheric temperature, cloud dynamics, and land surface modifications. The complexity of these adjustments varies with the type, amount, and location of aerosols relative to clouds, underscoring the need for a nuanced understanding of aerosol impacts under varying conditions.

For stratospheric aerosols, although many studies convert the global mean ERF directly from the stratospheric AOD, the scaling factor varies a lot among studies. For example, Marshall et al. (2020) reported a scaling factor of -17.0 ± 0.2 W/m^2 per unit of volcanic stratospheric AOD using the HadGEM3-GA4 climate model, compared to the IPCC AR5's factor of -26 W/m^2 per unit volcanic stratospheric AOD (Intergovernmental Panel on Climate Change, 2014). Using the GISS model based on the Pinatubo eruption, Hansen (2005) suggested a factor of -22 W/m^2. While the adjustment for volcanic aerosols is relatively straightforward (slightly mitigates the instantaneous ADRE sign), the adjustment for stratospheric absorbing aerosols can be more significant. Yu et al. (2023) estimated a scaling factor of $-37\ Wm^{-2}$ per unit stratospheric wildfire smoke AOD anomaly, averaged over the period from 2014 to 2022, highlighting that stratospheric aerosols offset about 20% of the CO_2-induced ERF increase during that time. These findings reveal that the relationship between stratospheric AOD and ERF is complex and not accurately captured by a single global mean conversion factor. Future research should focus on how ERF adjustments for stratospheric aerosols vary with aerosol distribution, solar radiation, and the timing and location of emissions. Such studies will enhance our understanding of the global radiation budget, provide insights for stratospheric geoengineering strategies, and aid climate projections, especially in scenarios with increased wildfire activity.

For tropospheric aerosols, the magnitude and mechanisms behind the spatial variability of ERF remain unclear, especially for absorbing aerosols (Bellouin et al., 2020; C. J. Smith et al., 2018; Williams et al., 2022). This uncertainty arises from the 'critical surface albedo' at which the instantaneous ADRE for absorbing aerosols shifts from negative to positive (Koch & Del Genio, 2010; J. Li et al., 2022; Williams et al., 2022). Subsequent adjustments depend on environmental conditions such as the co-location of aerosols with different cloud types (Quaas et al., 2024; Stjern

et al., 2017). For instance, the semi-direct effect can exhibit opposite signs depending on the position of BC relative to the altitude of the cloud layer (Koch & Del Genio, 2010). Localized aerosol heating (or cooling) can dynamically influence atmospheric circulation, affecting regional precipitation and clouds, which leads to markedly different responses in ERF (Bellouin et al., 2020; C. J. Smith et al., 2018; Stjern et al., 2017; Williams et al., 2022). For example, Williams et al. (2022) found that ERF is positive in response to midlatitude anthropogenic absorbing aerosols and negative in the tropical Western Pacific. Future research should focus on (1) deepening the analytical understanding of ERF mechanisms, (2) quantifying ERF variations across models to reduce discrepancies, and (3) using observations to refine model estimates of ERF for tropospheric aerosols.

Appendix A

A Chapter 2 Supplementary Information

A1 Introduction

Figure A1 shows the comparison of the regression method used in this study with the radiative kernel method for a single site. The site is Beijing (40N, 115.625E) and the study time is 00:00 UTC on May 1, 2019. First, we use RRTMG to calculate the ADRE when SAOD (AAOD) and surface albedo are perturbed from 0 to 1 respectively. Apart from these variables, other variables all take realistic values (e.g., atmospheric and aerosols profile). The star in the upper panel shows the ADRE value with the actual SAOD and AAOD. The benchmark RRTMG calculations in the upper panel clearly show the nonlinear change of the ADRE with surface albedo and SAOD (AAOD). To reproduce the ADRE, we use the regression model $\frac{\frac{\mathrm{ADRE_i^{clr}}}{TISR}+9.86\times10^{-3}}{-9.86\times10^{-3}} = \mathrm{A_1}\frac{\mathrm{SAOD_i}-0.13}{0.13} + \mathrm{A_2}\frac{\cos\theta_\mathrm{i}-0.25}{0.25} + \mathrm{A_3}\frac{(\mathrm{SAOD\cdot alb})_\mathrm{i}-0.02}{0.02} + \mathrm{A_4}\frac{(\mathrm{AAOD\cdot alb})_\mathrm{i}-1.1\times10^{-3}}{1.1\times10^{-3}}$ and the results are shown in the middle panel. Note that the sensitivity values $\mathrm{A_1}$- $\mathrm{A_4}$ are trained according to the ADRE on this site. The R^2 value for using the regression model is larger than 98%, indicating the regression model can well reproduce this nonlinear ADRE feature. As a comparison, we also calculated the SAOD, AAOD and surface kernel values by imposing small perturbations to the base-state values (the location of stars). Appling kernel values to $\mathrm{ADRE_i^{clr}} = \mathrm{ADRE_0^{clr}} + \frac{\partial \mathrm{ADRE_0}}{\partial \mathrm{SAOD_0}}(\mathrm{SAOD_i} - \mathrm{SAOD_0}) + \frac{\partial \mathrm{ADRE_0}}{\partial \mathrm{AAOD_0}}(\mathit{A}\mathrm{AOD_i} - \mathrm{AAOD_0}) + \frac{\partial \mathrm{ADRE_0}}{\partial \mathrm{alb_0}}(\mathrm{alb_i} - \mathrm{alb_0})$, we can get the results in the lower panel, which have R^2 values less than 62%. These results suggest the ADRE variations can be well captured by the combination of predictors chosen in our study, while the kernel method may be less representative of the nonlinear ADRE behaviors.

Figure A2 illustrates the performance of the regression model when using predictors that are either 100% correlated or uncorrelated. The location under examination is Beijing (40N, 115.625E) and the data was collected at 00:00 UTC on May 1, 2019. In the scenario where SAOD and AAOD are perfectly correlated (depicted in the right column), as SAOD increases from 0 to 1, AAOD also increases by the same relative proportion. In contrast, when SAOD and AAOD are uncorrelated, AAOD remains constant as SAOD increases from 0 to 1. The star in the upper panel represents the ADRE value using the actual SAOD and AAOD. The R-squared values are 98.53% and 99.72% for the perfectly correlated and uncorrelated SAOD and AAOD scenarios, respectively. This figure demonstrates that the performance of the regression model is not influenced by the degree of correlation among the predictors.

Figure A3 shows the all-sky ADRE sensitivities to the SAOD, surface albedo, AAOD and CRE/TISR calculated using the partial least square regression method. This figure is similar to Fig. 4, indicating the regression results are not sensitive to the regression techniques.

Figure A4 shows the distributions of the climatological mean aerosol optical depth of five aerosol species included in the MERRA-2 data, which aids the interpretation of the global AOD and ADRE distribution.

Figure A5 compares the global ADRE sensitivities to AOD and surface albedo between the regression model and Thorsen et al. (2020). The upper panel is for clear-sky conditions and the lower panel is for all-sky conditions.

To facilitate the AOD kernel comparison, we assume single scattering albedo (SSA) is fixed for all grids, so that

$$\frac{\partial \mathrm{ADRE}}{\partial \mathrm{AOD}} = \frac{\partial \mathrm{ADRE}}{\partial \mathrm{SAOD}}\frac{\partial \mathrm{SAOD}}{\partial \mathrm{AOD}} + \frac{\partial \mathrm{ADRE}}{\partial \mathrm{AAOD}}\frac{\partial \mathrm{AAOD}}{\partial \mathrm{AOD}} = \frac{\partial \mathrm{ADRE}}{\partial \mathrm{SAOD}}(\mathrm{SSA}) + \frac{\partial \mathrm{ADRE}}{\partial \mathrm{AAOD}}(1 - \mathrm{SSA})$$

where $\frac{\partial \mathrm{ADRE}}{\partial \mathrm{SAOD}}$ and $\frac{\partial \mathrm{ADRE}}{\partial \mathrm{AAOD}}$ are calculated by regression models and SSA is the climatological value. The results show our ADRE sensitivities are quite consist with the sensitivities calculated from radiative transfer model. The R-squared (R^2) values are larger than 80% regardless of sky types. These comparisons give confidence that our regression model can well separate the aerosol effect and surface albedo effect.

Figure A6 is the validation of the predicted ADRE trends against the MERRA2 ADRE trends.

Figure A7 and A8 display the trends in the global mean ADRE and key predictors.

Figure A9 The distribution for the trends of scattering aerosol optical depth, surface albedo, absorbing aerosol optical depth and cloud shortwave radiative effect normalized by insolation.

Tables A1 to A3 summarize the predictors tested in this work and the performance of regression models using different combinations of them.

A2 List of Figures and Tables

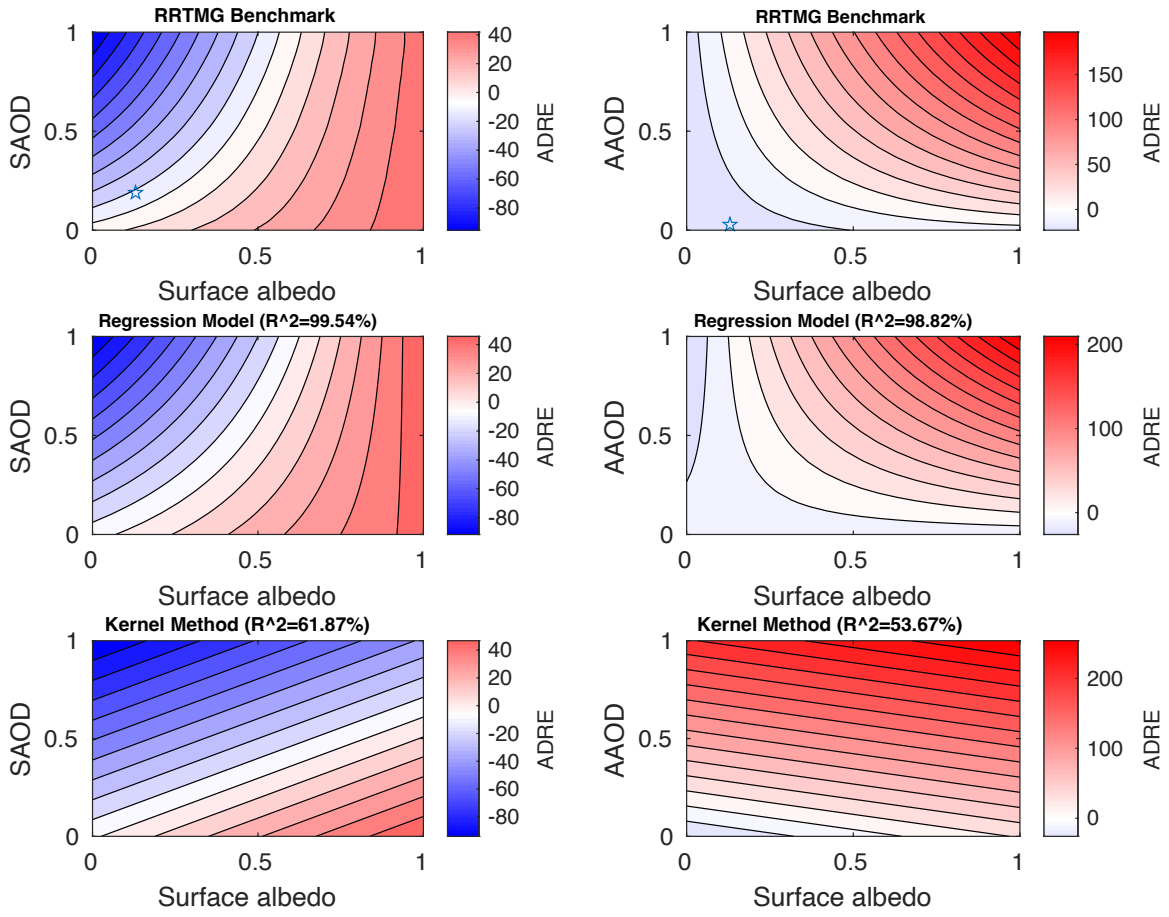

Figure A. 1 The comparison of the regression model built in this study with the radiative kernel method for a single site.

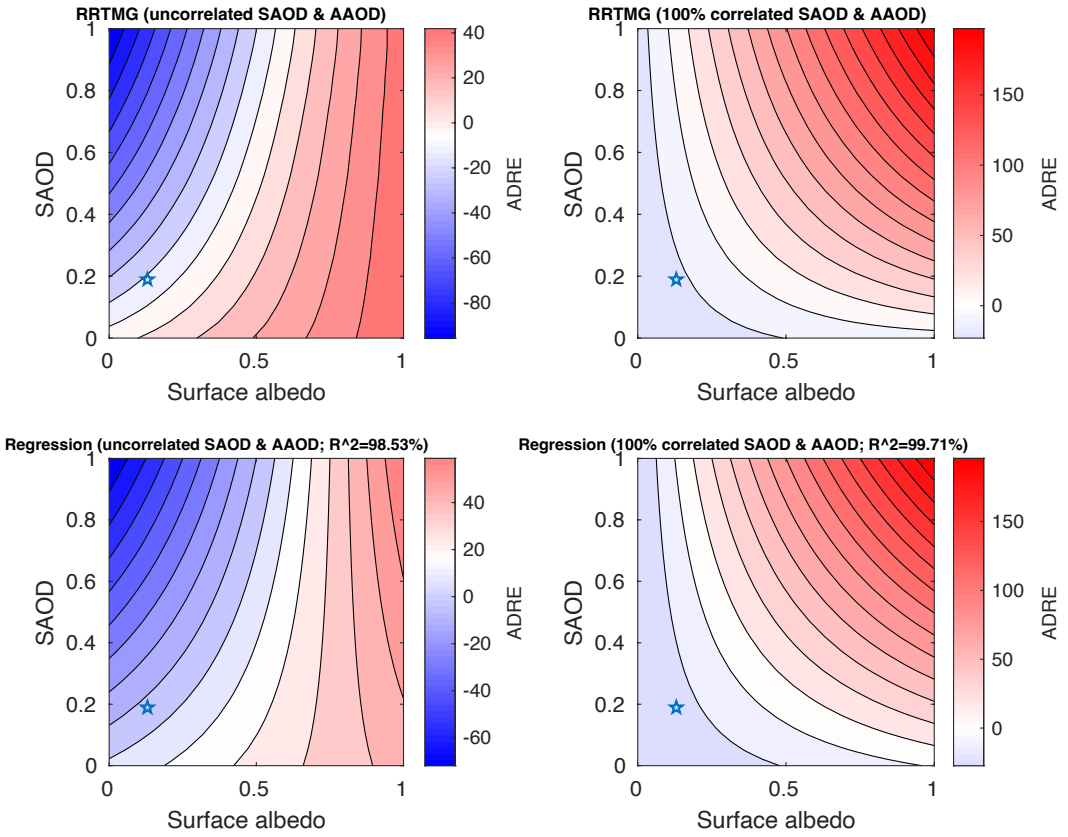

Figure A. 2 Performance of the regression model when using predictors that are either perfectly correlated or uncorrelated. Left column: uncorrelated scenario (AAOD remains constant as SAOD increases from 0 to 1); Right column: perfectly correlated scenario (as SAOD increases from 0 to 1, AAOD increases by the same relative proportion); Upper panel: RRMTG benchmark results; Lower panel: regression model results.

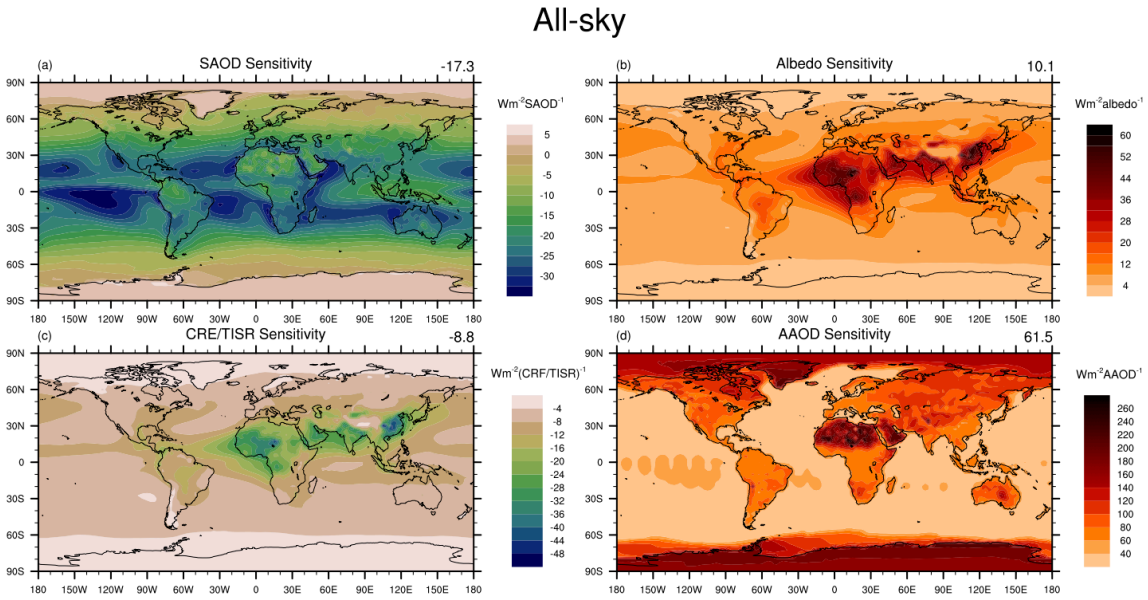

Figure A. 3 The sensitivities of the $ADRE_{all}$ to (a) scattering aerosol optical depth, (b) surface albedo, (c) cloud shortwave radiative effect normalized by insolation, and (d) absorbing aerosol optical depth calculated by using the partial least square regression method. The global mean values are indicated in the top-right corner of each subplot.

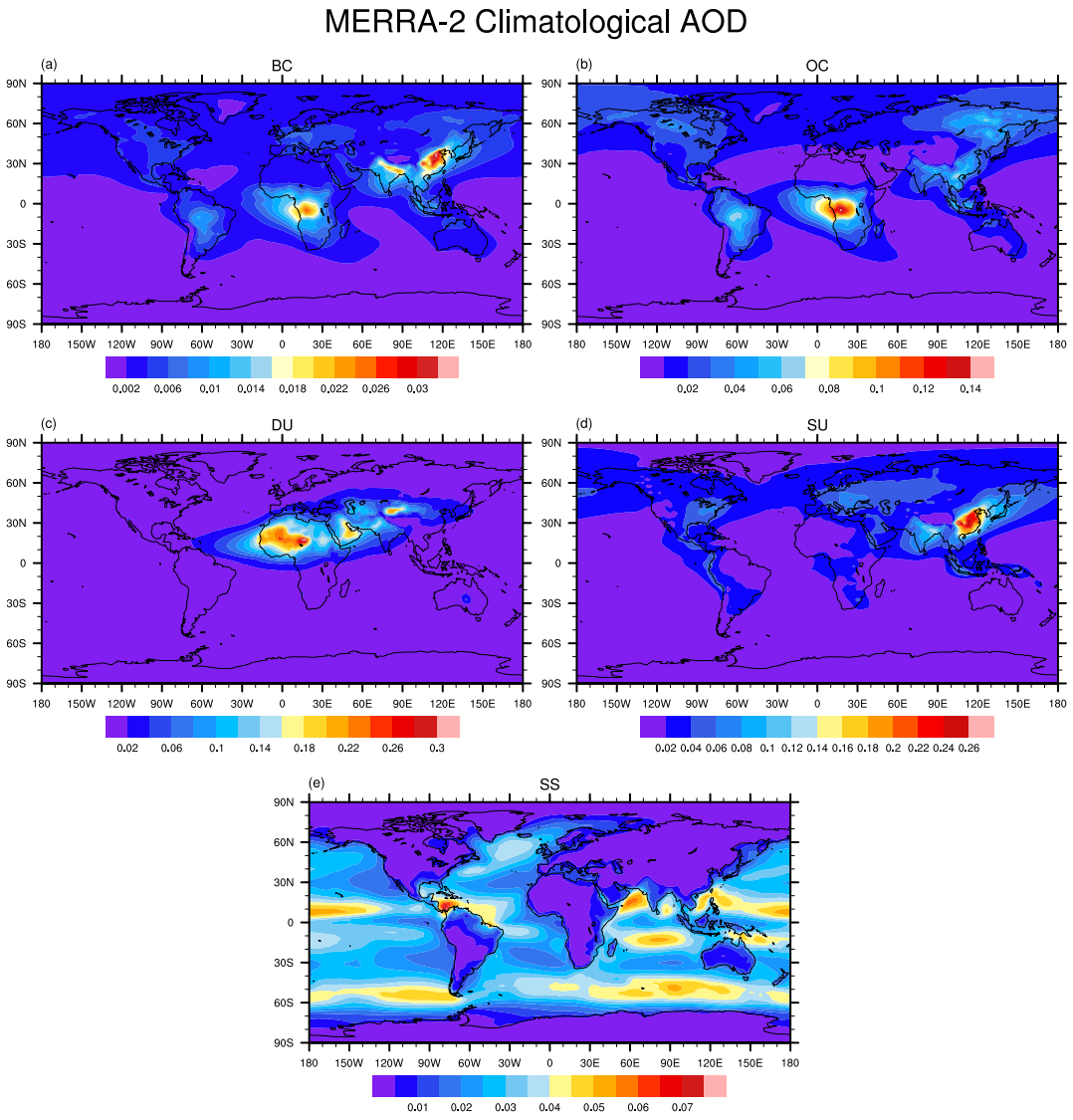

Figure A. 4 The climatological mean aerosol optical depth for (a) black carbon, (b) organic carbon, (c) dust, (d) sulfate and (e) sea salt

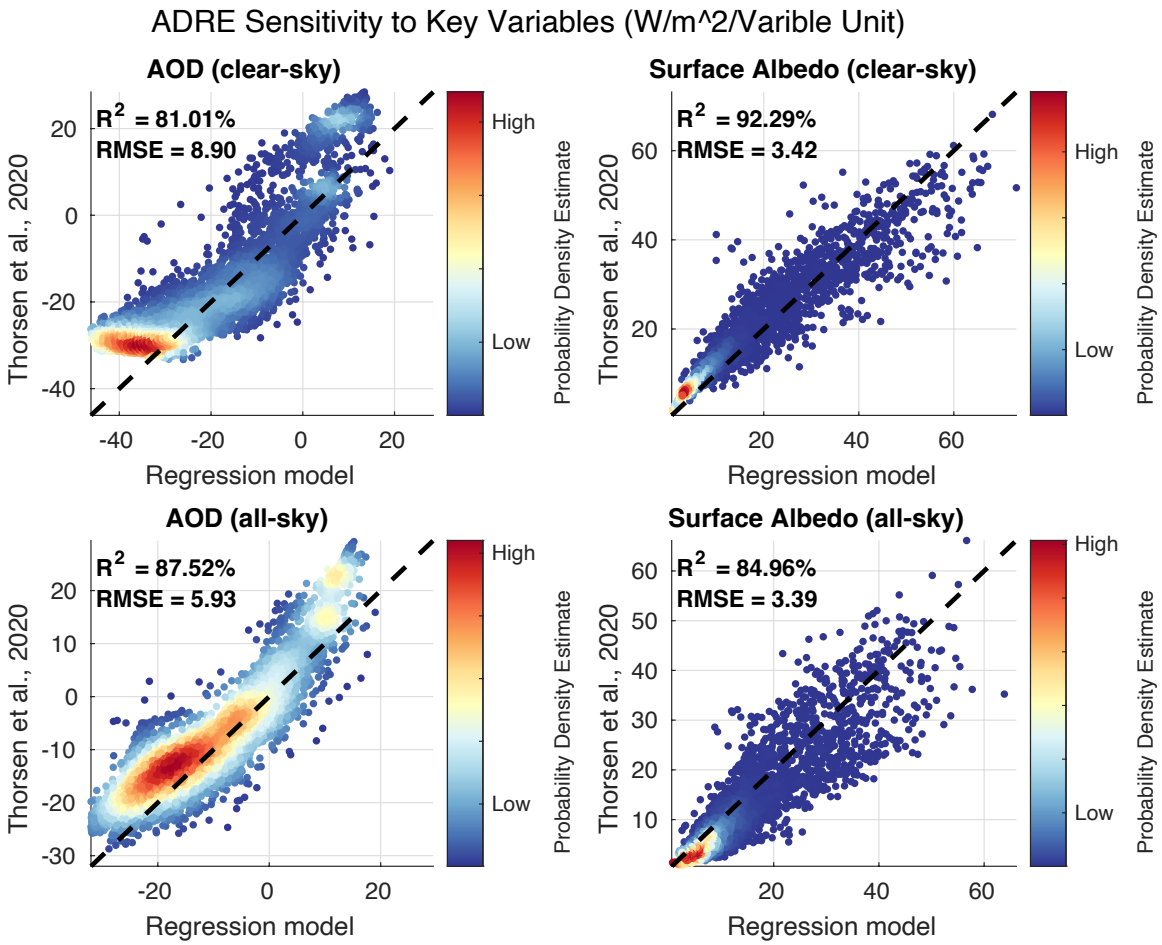

Figure A. 5 Comparisons of the global ADRE sensitivities to AOD and surface albedo between the regression model and Thorsen et al. (2020). The upper panel is for clear-sky conditions and the lower panel is for all-sky conditions.

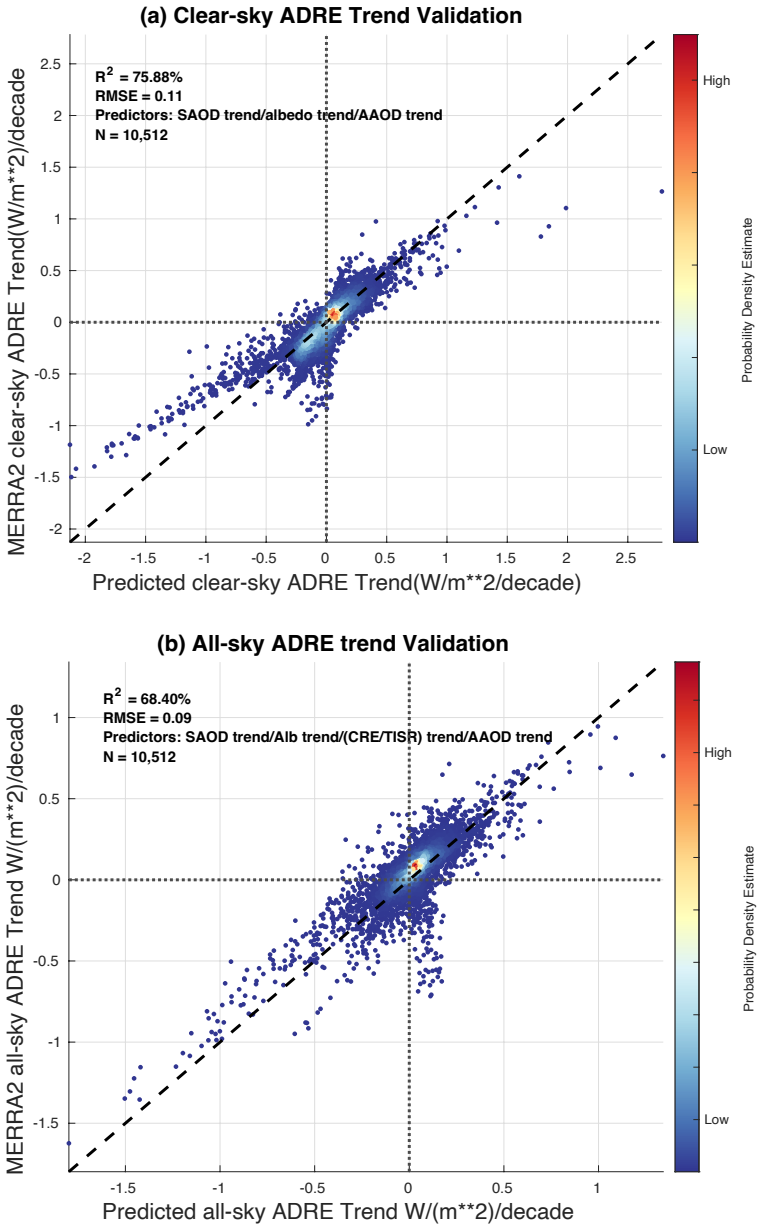

Figure A. 6 Comparison of the predicted 2000 – 2021 ADRE trend against the MERRA-2 ADRE trend in (a) clear-sky, (b) all-sky conditions. The color coding indicates probability density.

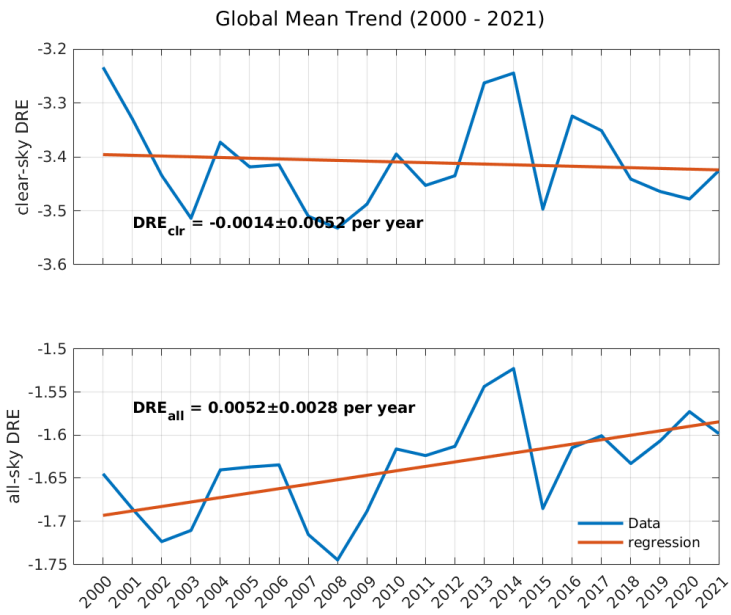

Figure A. 7 The trends of global mean $ADRE_{clr}$ and $ADRE_{all}$.

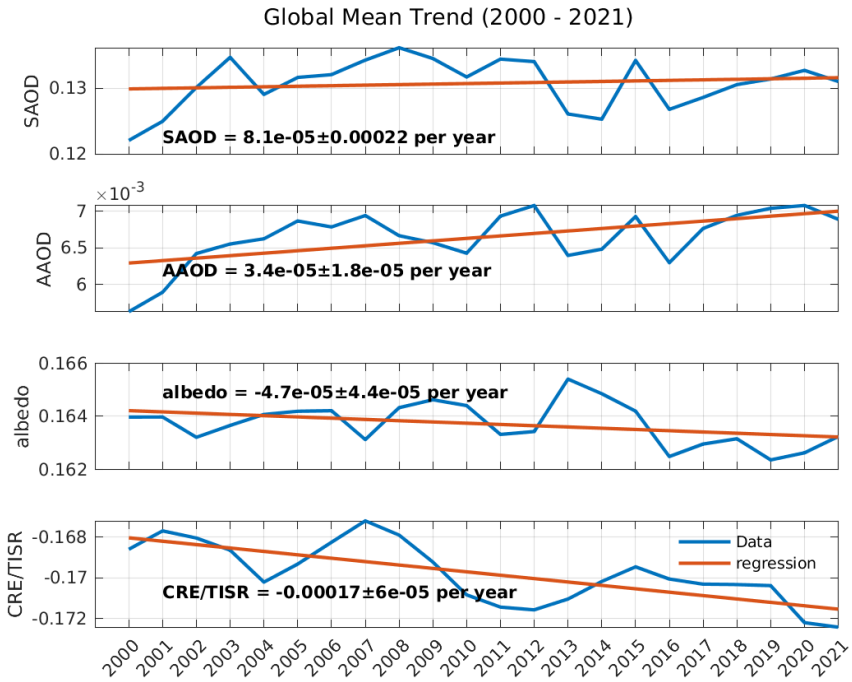

Figure A. 8 The trends of global mean scattering aerosol optical depth, absorbing aerosol optical depth, surface albedo, and cloud shortwave radiative effect normalized by insolation.

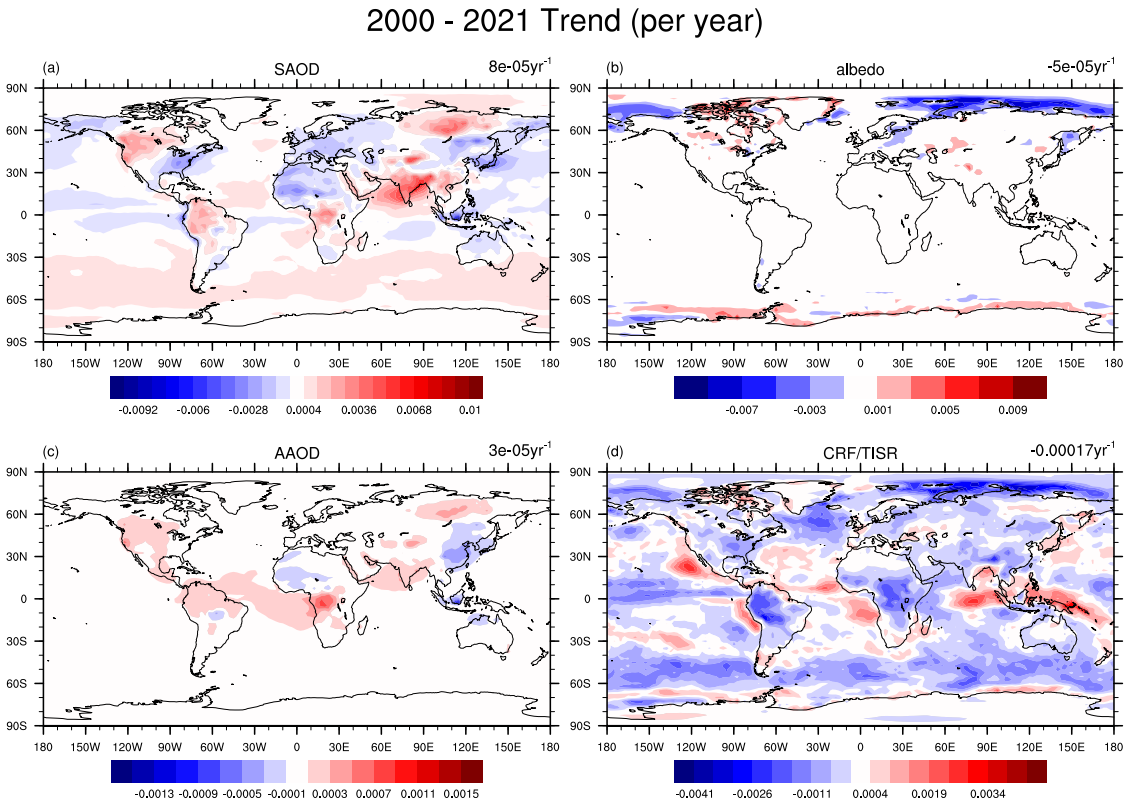

Figure A. 9 The trends of scattering aerosol optical depth, surface albedo, absorbing aerosol optical depth and cloud shortwave radiative effect normalized by insolation.

Table A. 1 Name of predictors and their performances in predicting ADRE. R^2 is the coefficient of determination.

Predictor	**1**	**2**	**3**	**4**	**5**	**6**	**7**	**8**	**9**	**10**
	SAOD	AAOD	AOD	cosθ	alb	SAOD · alb	AAOD · alb	AOD · alb	log(AOD)	SSA
Predictor	**11**	**12**	**13**	**14**	**15**	**16**	**17**	**18**	**19**	

	O_3	Column Water Vapor	Asymmetry factor	$\frac{CRF}{TISR}$	$SAOD \cdot \frac{CRF}{TISR}$	$AAOD \cdot \frac{CRF}{TISR}$	$AOD \cdot \frac{CRF}{TISR}$	Cloud Fraction	Cloud optical depth	

Table A. 2 Combination of predictors and their performances in predicting global clear-sky ADRE. R^2 is the coefficient of determination.

predictor	**1**	**2**	**3**	**4**	**5**	**6**	**7**	**8**	**9**	**10**	**11**	**12**	**13**	**R^2**	**Comment**
	√													56.42%	
		√												46.14%	
			√											56.06%	
				√										37.99%	
					√									55.65%	
						√								39.93%	
							√							40.38%	
								√						39.97%	
									√					62.48%	
										√				40.01%	
											√			48.69%	
												√		39.05%	
													√	39.24%	
			√		√					√				71.94%	

					√				√	√				69.96%	
			√	√	√									83.63%	
	√			√	√									93.90%	
			√	√	√					√				83.99%	
	√	√		√	√									83.92%	
	√			√		√								92.02%	
			√	√				√						91.13%	
	√			**√**		**√**	**√**							**92.96%**	Chosen scheme
	√	√		√		√	√							92.95%	
	√			√		√	√			√				93.00%	
	√			√		√	√				√			92.96%	
	√			√		√	√					√		93.21%	
	√			√		√	√						√	92.99%	

Table A. 3 Same as Table A2, but for all-sky conditions.

Predictor	**1**	**2**	**3**	**4**	**5**	**6**	**7**	**8**	**13**	**14**	**15**	**16**	**17**	**18**	**19**	**R^2**	**Comment**
	√															53.80%	
		√														47.92%	
			√													53.48%	

				√											50.57%	
					√										52.07%	
						√									50.07%	
							√								53.62%	
								√							50.47%	
									√						42.98%	
										√					46.35%	
											√				48.03%	
												√			49%	
													√		48.01%	
														√	45.32%	
															√	43.79%
			√	√	√									√		72.31%
			√	√	√										√	70.87%
			√	√	√					√						76.99%
			√	√		√					√					92.51%
	√			√			√				√					90.88%
	√			**√**			**√**	**√**			**√**					**93.13 %**	**Chosen scheme**
	√			√			√	√			√	√				93.23%	
	√			√			√	√	√		√					93.42%	

	√			√			√	√			√	√		√		93.69%	
	√			√			√	√			√	√			√	93.20%	

Appendix B

B Chapter 3 Supplementary Information

B1 Text B1

The full decomposition of the inter-model differences in the Aerosol Direct Radiative Effects (ΔADRE) are as follows:

For the j[th] GCM, the truth ADRE is

$$\mathrm{ADRE_j} = \mathrm{rsut_j} - \mathrm{rsutaf_j} \tag{B1}$$

Where rsut is TOA outgoing shortwave radiation, and rsutaf is TOA outgoing aerosol-free shortwave radiation.

$\mathrm{ADRE_j}$ can be predicted using

$$\frac{\frac{\mathrm{ADRE_j^p}}{\mathrm{TISR}} - \frac{\overline{\mathrm{ADRE_j}}}{\mathrm{TISR}}}{\frac{\overline{\mathrm{ADRE_j}}}{\mathrm{TISR}}} = \sum_{i=1}^{4} \beta_{i,j} \frac{X_{i,j} - \overline{X_{I,J}}}{\overline{X_{I,J}}} \tag{B2}$$

or

$$\mathrm{ADRE_j^p} = \left(\sum_{i=1}^{4} \frac{\beta_{I,j}}{\overline{X_{I,j}}} X_{I,j} + 1 - \sum_{i=1}^{4} \beta_{I,j}\right) \cdot \frac{\overline{\mathrm{ADRE_j}}}{\mathrm{TISR}} \cdot \mathrm{TISR} \tag{B3}$$

The i[th] predictor ($X_{I,j}$) includes $\mathrm{SAOD_j}$; $\mathrm{SAOD_j} \cdot \mathrm{ALB_j}$; $\mathrm{AAOD_j} \cdot \mathrm{ALB_j}$; $\mathrm{SAOD_j} \cdot \frac{\mathrm{CRE}}{\mathrm{TISR_j}}$ for all grid points over the global. SAOD and AAOD are the scattering and absorptive aerosol optical depth, respectively. ALB is the broad-band shortwave surface albedo, and CRE is the shortwave cloud radiative effect. TISR is the Top of the Atmosphere (TOA) incoming solar radiation. $B_{I,j}$ are

the regression coefficient, and their values are listed in Table B1. The overbar denotes global mean values.

For the CMIP6 multi-model mean ADRE (ADRE_0), the predicted ADRE is

$$\frac{\frac{\mathrm{ADRE}_0^{\mathrm{p}}}{\mathrm{TISR}}-\frac{\overline{\mathrm{ADRE}_0}}{\mathrm{TISR}}}{\frac{\overline{\mathrm{ADRE}_0}}{\mathrm{TISR}}}=\sum_{\mathrm{i}=1}^{4}\beta_{\mathrm{i},0}\frac{\mathrm{X}_{\mathrm{i},0}-\overline{\mathrm{X}_{\mathrm{i},0}}}{\overline{\mathrm{X}_{\mathrm{i},0}}} \tag{B4}$$

or

$$\mathrm{ADRE}_0^{\mathrm{p}}=\left(\sum_{\mathrm{i}=1}^{4}\frac{\beta_{\mathrm{I},0}}{\overline{\mathrm{X}_{\mathrm{I},0}}}\mathrm{X}_{\mathrm{I},0}+1-\sum_{\mathrm{i}=1}^{4}\beta_{\mathrm{I},0}\right)\cdot\frac{\overline{\mathrm{ADRE}_0}}{\mathrm{TISR}}\cdot\mathrm{TISR} \tag{B5}$$

The predicted ADRE anomalies with respect to the multi-model mean ADRE is

$$\Delta\mathrm{ADRE}_{\mathrm{j}}^{\mathrm{p}}=\mathrm{ADRE}_{\mathrm{j}}^{\mathrm{p}}-\mathrm{ADRE}_0^{\mathrm{p}} \tag{B6}$$

The full expansion of $\Delta\mathrm{ADRE}_{\mathrm{j}}^{\mathrm{p}}$ is

$$\Delta\mathrm{ADRE}_{\mathrm{j}}^{\mathrm{p}}= \tag{B7}$$

$$\left\{\frac{\partial\mathrm{ADRE}_0^{\mathrm{p}}}{\partial\mathrm{SAOD}_0}+\left[\Delta\beta_{1,\mathrm{j}}+\Delta\beta_{2,\mathrm{j}}\mathrm{ALB}_0+\Delta\beta_{4,\mathrm{j}}\left(\frac{\mathrm{CRE}}{\mathrm{TISR}}\right)_0\right]\cdot\frac{\overline{\mathrm{ADRE}_0}}{\mathrm{TISR}}\cdot\mathrm{TISR}\right\}\cdot\Delta\mathrm{SAOD}_{\mathrm{j}} \quad \text{(term 1)}$$

$$+\left[\frac{\partial\mathrm{ADRE}_0^{\mathrm{p}}}{\partial\mathrm{AAOD}_0}+\left(\Delta\beta_{3,\mathrm{j}}\mathrm{ALB}_0\right)\cdot\frac{\overline{\mathrm{ADRE}_0}}{\mathrm{TISR}}\cdot\mathrm{TISR}\right]\cdot\Delta\mathrm{AAOD}_{\mathrm{j}} \quad \text{(term 2)}$$

$$+\left[\frac{\partial\mathrm{ADRE}_0^{\mathrm{p}}}{\partial\mathrm{alb}_0}+\left(\Delta\beta_{2,\mathrm{j}}\mathrm{SAOD}_0+\Delta\beta_{3,\mathrm{j}}\cdot\mathrm{AAOD}_0\right)\cdot\frac{\overline{\mathrm{ADRE}_0}}{\mathrm{TISR}}\cdot\mathrm{TISR}\right]\cdot\Delta\mathrm{ALB}_{\mathrm{j}} \quad \text{(term 3)}$$

$$+\left[\frac{\partial\mathrm{ADRE}_0^{\mathrm{p}}}{\partial\left(\frac{\mathrm{CRE}}{\mathrm{TISR}}\right)_0}+\Delta\beta_{4,\mathrm{j}}\mathrm{SAOD}_0\cdot\frac{\overline{\mathrm{ADRE}_0}}{\mathrm{TISR}}\cdot\mathrm{TISR}\right]\cdot\Delta\left(\frac{\mathrm{CRE}}{\mathrm{TISR}}\right)_{\mathrm{j}} \quad \text{(term 4)}$$

$$+\Sigma(\Delta\mathrm{X})^{\mathrm{n}} \quad \text{(term 5)}$$

$$+\Delta\beta_{1,\mathrm{j}}\cdot\frac{\overline{\mathrm{ADRE}_0}}{\mathrm{TISR}}\cdot\mathrm{TISR}\cdot\mathrm{SAOD}_0 \quad \text{(term 6)}$$

$$+\Delta\beta_{2,\mathrm{j}}\cdot\frac{\overline{\mathrm{ADRE}_0}}{\mathrm{TISR}}\cdot\mathrm{TISR}\cdot\left(\mathrm{SAOD}_0\cdot\mathrm{ALB}_0\right) \quad \text{(term 7)}$$

$$+\Delta\beta_{3,\mathrm{j}}\cdot\frac{\overline{\mathrm{ADRE}_0}}{\mathrm{TISR}}\cdot\mathrm{TISR}\cdot\left(\mathrm{AAOD}_0\cdot\mathrm{ALB}_0\right) \quad \text{(term 8)}$$

$$+\Delta\beta_{4,j} \cdot \frac{\overline{\mathrm{ADRE}_0}}{\mathrm{TISR}} \cdot \mathrm{TISR} \cdot \left[\mathrm{SAOD}_0 \cdot \left(\frac{\mathrm{CRE}}{\mathrm{TISR}}\right)_0\right] \quad \text{(term 9)}$$

$$+ \text{regr-clos} \quad \text{(term 10)}$$

In Equation. (B7), $\Delta X_{I,j}$ is the anomaly of the ith predictor in the jth model with respect to the multi-model mean. $\Delta\beta_{I,j}$, which measures the anomaly in the ADRE sensitivity to the ith predictor in the jth model, is denoted as

$$\Delta\beta_{i,j} = \frac{\beta_{i,j}}{\overline{X_{1,j}}} - \frac{\beta_{i,0}}{\overline{X_{1,0}}} \quad \text{(B8)}$$

Terms 1-5 are composed of the aerosol and environment state variable anomalies $\Delta X_{I,j}$. We denote the sum of terms 1-5 as

$$\Delta_X \mathrm{ADRE}_j^p = \sum_{k=1}^{5} \mathrm{term}_k \quad \text{(B9)}$$

Terms 6-10 are composed of the ADRE sensitivity differences to aerosol-related radiative processes $\Delta\beta_{I,j}$. We denote the sum of terms 6-10 as

$$\Delta_\beta \mathrm{ADRE}_j^p = \sum_{k=6}^{10} \mathrm{term}_k \quad \text{(B10)}$$

Therefore,

$$\Delta\mathrm{ADRE}_j^p = \Delta_X \mathrm{ADRE}_j^p + \Delta_\beta \mathrm{ADRE}_j^p \quad \text{(B11)}$$

In the expressions of terms 1-5 in $\Delta_X \mathrm{ADRE}_j^p$, the partial differential factor, e.g., $\frac{\partial \mathrm{ADRE}_0^p}{\partial \mathrm{SAOD}_0}$, measures the ADRE sensitivity to the corresponding state variable according to the multi-model mean regression model (Equation. B7); their respective expressions are:

$$\frac{\partial \mathrm{ADRE}_0^p}{\partial \mathrm{SAOD}_0} = \left[\frac{\beta_{1,0}}{\overline{X_{1,0}}} + \frac{\beta_{2,0}}{\overline{X_{2,0}}} \mathrm{ALB}_0 + \frac{\beta_{4,0}}{\overline{X_{4,0}}} \left(\frac{\mathrm{CRE}}{\mathrm{TISR}}\right)_0\right] \cdot \frac{\overline{\mathrm{ADRE}_0}}{\mathrm{TISR}} \cdot \mathrm{TISR} \quad \text{(B12)}$$

$$\frac{\partial \mathrm{ADRE}_0^p}{\partial \mathrm{AAOD}_0} = \left(\frac{\beta_{3,0}}{\overline{X_{3,0}}} \mathrm{ALB}_0\right) \cdot \frac{\overline{\mathrm{ADRE}_0}}{\mathrm{TISR}} \cdot \mathrm{TISR} \quad \text{(B13)}$$

$$\frac{\partial \mathrm{ADRE}_0^{\mathrm{p}}}{\partial \mathrm{ALB}_0} = \left(\frac{\beta_{2,0}}{\overline{X_{2,0}}}\mathrm{SAOD}_0 + \frac{\beta_{3,0}}{\overline{X_{3,0}}}\mathrm{AAOD}_0\right) \cdot \frac{\overline{\mathrm{ADRE}_0}}{\mathrm{TISR}} \cdot \mathrm{TISR}$$

(B14)

$$\frac{\partial \mathrm{ADRE}_0^{\mathrm{p}}}{\partial\left(\frac{\mathrm{CRE}}{\mathrm{TISR}}\right)_0} = \left(\frac{\beta_{4,0}}{\overline{X_{4,0}}}\mathrm{SAOD}_0\right) \cdot \frac{\overline{\mathrm{ADRE}_0}}{\mathrm{TISR}} \cdot \mathrm{TISR} \quad \text{(B15)}$$

The spatial distribution the values of $\frac{\partial \mathrm{ADRE}_0^{\mathrm{p}}}{\partial \mathrm{SAOD}_0}$, $\frac{\partial \mathrm{ADRE}_0^{\mathrm{p}}}{\partial \mathrm{AAOD}_0}$, and $\frac{\partial \mathrm{ADRE}_0^{\mathrm{p}}}{\partial \mathrm{ALB}_0}$, which measure the ADRE sensitivity to these state variables, are shown and validated to the quantification of Thorsen et al. (2020) in Figure B4 and B5. These results evidence that the regression model, despite its simplicity, very well captures the radiative sensitivity to these state variables.

Term 5, $\Sigma(\Delta X)^{\mathrm{n}}$, denotes the contribution from the higher-order ΔX terms:

$$\Sigma(\Delta X)^{\mathrm{n}} = \frac{\partial^2 \mathrm{ADRE}_0^{\mathrm{p}}}{\partial \mathrm{SAOD}_0\, \partial \mathrm{ALB}_0}\Delta\mathrm{SAOD}_{\mathrm{j}}\Delta\mathrm{ALB}_{\mathrm{j}} + \frac{\partial^2 \mathrm{ADRE}_0^{\mathrm{p}}}{\partial \mathrm{AAOD}_0\, \partial \mathrm{ALB}_0}\Delta\mathrm{AAOD}_{\mathrm{j}}\Delta\mathrm{ALB}_{\mathrm{j}} +$$

$$\frac{\partial^2 \mathrm{ADRE}_0^{\mathrm{p}}}{\partial \mathrm{SAOD}_0\, \partial\left(\frac{\mathrm{CRE}}{\mathrm{TISR}}\right)_0}\Delta\mathrm{SAOD}_{\mathrm{j}}\Delta\left(\frac{\mathrm{CRE}}{\mathrm{TISR}}\right)_{\mathrm{j}} + (\Delta\beta_{2,\mathrm{j}}\Delta\mathrm{SAOD}_{\mathrm{j}}\Delta\mathrm{ALB}_{\mathrm{j}} + \Delta\beta_{3,\mathrm{j}}\Delta\mathrm{AAOD}_{\mathrm{j}}\Delta\mathrm{ALB}_{\mathrm{j}} +$$

$$\Delta\beta_{4,\mathrm{j}}\Delta\left(\frac{\mathrm{CRE}}{\mathrm{TISR}}\right)_{\mathrm{j}}\Delta\mathrm{SAOD}_{\mathrm{j}})] \cdot \frac{\overline{\mathrm{ADRE}_0}}{\mathrm{TISR}} \cdot \mathrm{TISR} \quad \text{(B16)}$$

This term has a considerably smaller magnitude than the first order terms 1-4 in Equation. (B7).

Terms 1-4 can be further separated into two contributions: one with the ADRE sensitivity quantified by the multi-model mean regression model, i.e., assuming universal sensitivities to these state variables governed by the same radiative transfer physics:

$$\Delta_{\mathrm{X}}\mathrm{ADRE}_{\mathrm{j}}^{\mathrm{p,universal}} = \quad \text{(B17)}$$

$$\frac{\partial \mathrm{ADRE}_0^{\mathrm{p}}}{\partial \mathrm{SAOD}_0} \cdot \Delta\mathrm{SAOD}_{\mathrm{j}} + \frac{\partial \mathrm{ADRE}_0^{\mathrm{p}}}{\partial \mathrm{AAOD}_0} \cdot \Delta\mathrm{AAOD}_{\mathrm{j}} + \frac{\partial \mathrm{ADRE}_0^{\mathrm{p}}}{\partial \mathrm{alb}_0} \cdot \Delta\mathrm{ALB}_{\mathrm{j}} + \frac{\partial \mathrm{ADRE}_0^{\mathrm{p}}}{\partial\left(\frac{\mathrm{CRE}}{\mathrm{TISR}}\right)_0} \cdot \Delta\left(\frac{\mathrm{CRE}}{\mathrm{TISR}}\right)_{\mathrm{j}}$$

$$+ \frac{\partial^2 \mathrm{ADRE}_0^{\mathrm{p}}}{\partial \mathrm{SAOD}_0\, \partial \mathrm{ALB}_0}\Delta\mathrm{SAOD}_{\mathrm{j}}\Delta\mathrm{ALB}_{\mathrm{j}} + \frac{\partial^2 \mathrm{ADRE}_0^{\mathrm{p}}}{\partial \mathrm{AAOD}_0\, \partial \mathrm{ALB}_0}\Delta\mathrm{AAOD}_{\mathrm{j}}\Delta\mathrm{ALB}_{\mathrm{j}}$$

$$+\frac{\partial^2 \mathrm{ADRE}_0^{\mathrm{p}}}{\partial \mathrm{SAOD}_0\, \partial\left(\frac{\mathrm{CRE}}{\mathrm{TISR}}\right)_0} \Delta\mathrm{SAOD_j} \Delta\left(\frac{\mathrm{CRE}}{\mathrm{TISR}}\right)_{\mathrm{j}}$$

and the other one addressing differences in ADRE sensitivity to selected predictors in individual GCMs:

$$\Delta_{\mathrm{X}}\mathrm{ADRE}_{\mathrm{j}}^{\mathrm{p,individual}} = \tag{B18}$$

$$\left\{\left[\Delta\beta_{1,\mathrm{j}} + \Delta\beta_{2,\mathrm{j}}\mathrm{ALB}_0 + \Delta\beta_{4,\mathrm{j}}\left(\frac{\mathrm{CRE}}{\mathrm{TISR}}\right)_0\right] \cdot \frac{\overline{\mathrm{ADRE}_0}}{\mathrm{TISR}} \cdot \mathrm{TISR}\right\} \cdot \Delta\mathrm{SAOD_j} + \left[\frac{\partial \mathrm{ADRE}_0^{\mathrm{p}}}{\partial \mathrm{AAOD}_0} + \right.$$

$$\left.\left(\Delta\beta_{3,\mathrm{j}}\mathrm{ALB}_0\right) \cdot \frac{\overline{\mathrm{ADRE}_0}}{\mathrm{TISR}} \cdot \mathrm{TISR}\right] \cdot \Delta\mathrm{AAOD_j} + \left[\left(\Delta\beta_{2,\mathrm{j}}\mathrm{SAOD}_0 + \Delta\beta_{3,\mathrm{j}} \cdot \mathrm{AAOD}_0\right) \cdot \frac{\overline{\mathrm{ADRE}_0}}{\mathrm{TISR}} \cdot \mathrm{TISR}\right] \cdot$$

$$\Delta\mathrm{ALB_j} + \left[\Delta\beta_{4,\mathrm{j}}\mathrm{SAOD}_0 \cdot \frac{\overline{\mathrm{ADRE}_0}}{\mathrm{TISR}} \cdot \mathrm{TISR}\right] \cdot \Delta\left(\frac{\mathrm{CRE}}{\mathrm{TISR}}\right)_{\mathrm{j}} + \left(\Delta\beta_{2,\mathrm{j}}\Delta\mathrm{SAOD_j}\Delta\mathrm{ALB_j} + \right.$$

$$\left.\Delta\beta_{3,\mathrm{j}}\Delta\mathrm{AAOD_j}\Delta\mathrm{ALB_j} + \Delta\beta_{4,\mathrm{j}}\Delta\left(\frac{\mathrm{CRE}}{\mathrm{TISR}}\right)_{\mathrm{j}}\Delta\mathrm{SAOD_j}\right)] \cdot \frac{\overline{\mathrm{ADRE}_0}}{\mathrm{TISR}} \cdot \mathrm{TISR}$$

We find that $\Delta_{\mathrm{X}}\mathrm{ADRE}_{\mathrm{j}}^{\mathrm{p,universal}}$ terms dominate the $\Delta_{\mathrm{X}}\mathrm{ADRE}_{\mathrm{j}}^{\mathrm{p,individual}}$ terms, as shown in Figure B6.

Terms 6-9 in Equation. (B7) measure the ADRE anomalies caused by the regression coefficient differences in each model: $\Delta\beta_{\mathrm{I,j}}$. As explained by Yu & Huang (2023), the expressions involving SAOD, SAOD · ALB, AAOD · ALB, and $\mathrm{SAOD} \cdot \frac{\mathrm{CRE}}{\mathrm{TISR}}$ in the regression equation represent the aerosol-only scattering, scattering aerosol and surface interaction, absorptive aerosol and surface interaction, and cloud masking effect, respectively. Therefore, the $\Delta\beta_{\mathrm{I,j}}$ terms associated with these expressions can be considered to be caused by different ADRE sensitivity to those radiative transfer processes in each GCM. This may be due to either structural differences in the radiation model used in a GCM or different state variables other than selected predictors in the GCM because the ADRE sensitivity varies with state variables.

Lastly, the regression closure term is:

$$\text{regr-clos} = \frac{\overline{\text{ADRE}_0}}{\text{TISR}} \cdot \text{TISR} \cdot \left(\sum_{i=1}^{4} \beta_{i,0} - \sum_{i=1}^{4} \beta_{i,j}\right) \quad \text{(B19)}$$

This term occurs because of the imperfect global mean value closure of the regression model, which results from representing the nonlinear radiative transfer processes with linear representations. However, its magnitude is relatively small, and it does not impact the inhomogeneous distribution of the ADRE anomalies, because it is only a function of the TISR and thus latitude.

Therefore, the radiative sensitivity effect, which consists of the different treatments of the above processes across models, is denoted as the sum of terms 6-10 following:

$$\Delta_\beta \text{ADRE}_j^p = \Delta\beta_{1,j} \cdot \frac{\overline{\text{ADRE}_0}}{\text{TISR}} \cdot \text{TISR} \cdot \text{SAOD}_0 + \Delta\beta_{2,j} \cdot \frac{\overline{\text{ADRE}_0}}{\text{TISR}} \cdot \text{TISR} \cdot (\text{SAOD}_0 \cdot \text{ALB}_0) +$$

$$\Delta\beta_{3,j} \cdot \frac{\overline{\text{ADRE}_0}}{\text{TISR}} \cdot \text{TISR} \cdot (\text{AAOD}_0 \cdot \text{ALB}_0) + \Delta\beta_{4,j} \cdot \frac{\overline{\text{ADRE}_0}}{\text{TISR}} \cdot \text{TISR} \cdot \left[\text{SAOD}_0 \cdot \left(\frac{\text{CRE}}{\text{TISR}}\right)_0\right] + \text{regr-clos} \quad \text{(B20)}$$

To illustrate the decomposition as detailed above, the spatial distributions of all the decomposed components of the ADRE of one GCM, the GFDL-ESM4 model, are shown in Figure. B7 as an example.

B2 Text B2

The average of global mean values for the SAOD, AAOD, ALB, CRE, and ADRE from the 5-model subset are as 0.13 ± 0.02, 0.006 ± 0.003, 0.16 ± 0.01, -48.61 ± 2.58 W/m^2, and -1.89 ± 0.49 W/m^2, respectively. The standard deviation of ADRE is around 26% of its absolute value, indicating a significant inter-model difference. The regression coefficients for predictor SAOD, SAOD·ALB, AAOD·ALB, and $\frac{\text{CRE}}{\text{TISR}}$·SAOD are 2.17 ± 0.34 W/m^2, -0.24 ± 0.26 W/m^2, -0.29 ± 0.14 W/m^2, -0.81 ± 0.26 W/m^2, respectively. Variations in the regression coefficients suggest

that the ADRE sensitivity to predictors differs considerably among models. For the individual model, the regression coefficients are listed in Table B1.

Figure B1 displays the 2001-2014 global mean values of 31 CMIP6 models that archive predictors (SAOD, AOD, and ALB). The red star indicates the selected 5 models in our study. The multi-model global mean values of SAOD, AAOD, and ALB for the 31 models are 0.14 ± 0.06, 0.006 ± 0.004, 0.15 ± 0.03, respectively. For the selected 5 models, the average values are 0.13 ± 0.04, 0.006 ± 0.003, 0.16 ± 0.02, respectively. Results suggest that the selected 5 models are representative in terms of global mean values.

Figure B2-B3 compare the spatial distribution of the multi-model mean and standard deviations of predictors (SAOD, AOD, and ALB) between all models available and the 5-model subset. Results indicate that the selected models are representative in terms of spatial distributions. However, the standard deviation (STD) values for the selected 5 models are relatively smaller than those for 31 models, especially in North Africa and polar regions. This suggests that there may be larger STD in ADRE among GCMs than those that are selected in our study.

Figure B4 shows the spatial distribution of the ADRE sensitivities using the CMIP6 multi-model mean data with the regression model (subplots (a)-(c)). The regression-based ADRE sensitivities are compared with the kernel data (Thorsen et al., 2020) derived from radiative transfer calculations (subplots (d)-(f)). It is important to note that the ADRE sensitivities obtained from the regression model are based on the CMIP6 historical experiments for the 2000-2014 period, while the kernel data is derived from the MERRA2 reanalysis for the year 2007. Despite the differences in datasets and study periods, the relatively good agreement in the ADRE sensitivities obtained from the two methods indicates the robustness of the regression method.

Figure B5 shows the point-by-point comparisons between the ADRE sensitivities obtained from the regression method and the kernel data. The R^2 for the ADRE sensitivity to SAOD, AADO, and ALB is 70%, 95%, and 77%, respectively, which also suggests the relatively good performance of the regression method.

Figure B6 compares the standard deviations of contributions from input difference terms when the ADRE sensitivity is the same across models (Equation B17) and when it changes (Equation B18). Results suggest that the input difference terms when assuming the same ADRE sensitivity across different models are the major contributor to the total input difference terms.

Figure B7 shows all the decomposed components of the ADRE anomalies for the GFDL-ESM4 model. This is used as an example to illustrate our decomposition method.

Figure B8-B9 show the regional mean values for the decomposition terms among different models for East Asia and the Arctic, respectively.

Figure B10 shows the distinct compensating effects between different contributors for both the input difference terms and the radiative sensitivity terms.

Table B1 listed the R^2 and RSME of the predicted ADRE for each CMIP6 model and the multi-model mean data using the regression method by comparing with the model outputs. On average, the regression method can explain over 90% of the variance in ADRE.

Table B2 listed the radiative schemes used in the selected CMIP6 models. This shows that all models adopt some form of the two-stream approximation for RT computation. The delta-Eddington method is used in the CNRM-ESM2-1, MPI-ESM-1-2-HAM, and MRI-ESM2-0 models (Stevens et al., 2013; Voldoire et al., 2013; Yukimoto et al., 2019). For the GFDL-ESM4 model, the delta-Eddington method is used to solve for the reflection and transmission, while the adding method is used to combine the layers (Freidenreich & Ramaswamy, 1999). For the

HadGEM3-GC31-LL model, the delta-Eddington approximation with δ-rescaling of τ, ω and, g are used (Edwards & Slingo, 1996). Apart from the differences in RT schemes, the differences in aerosol schemes could potentially lead to ADRE sensitivity differences.

B3 List of Figures and Tables

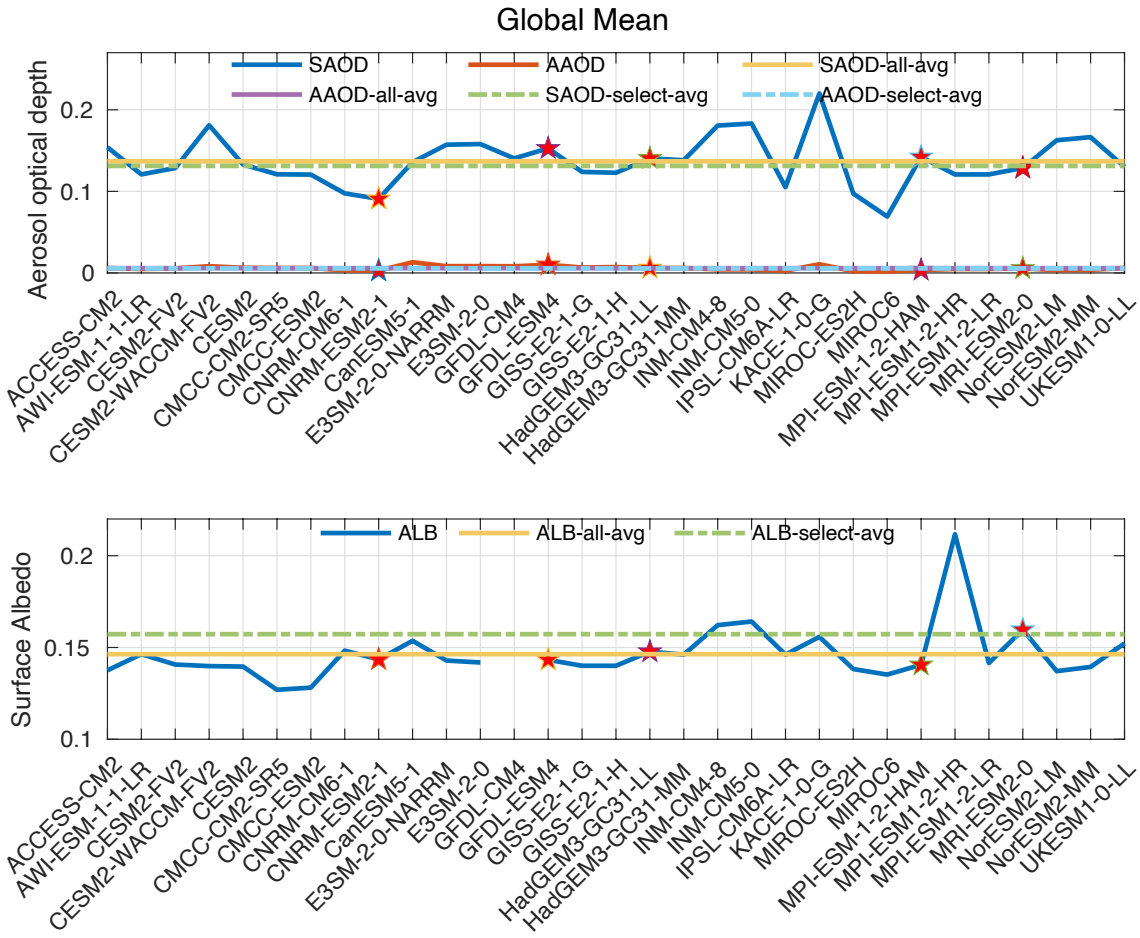

Figure B. 1 The global mean values of SAOD, AAOD, and ALB for 31 CMIP6 models. The solid horizontal lines are multi-model mean results for all models, while the dashed horizontal lines are multi-model mean results for selected 5 models. The corresponding values for selected models are marked by red stars.

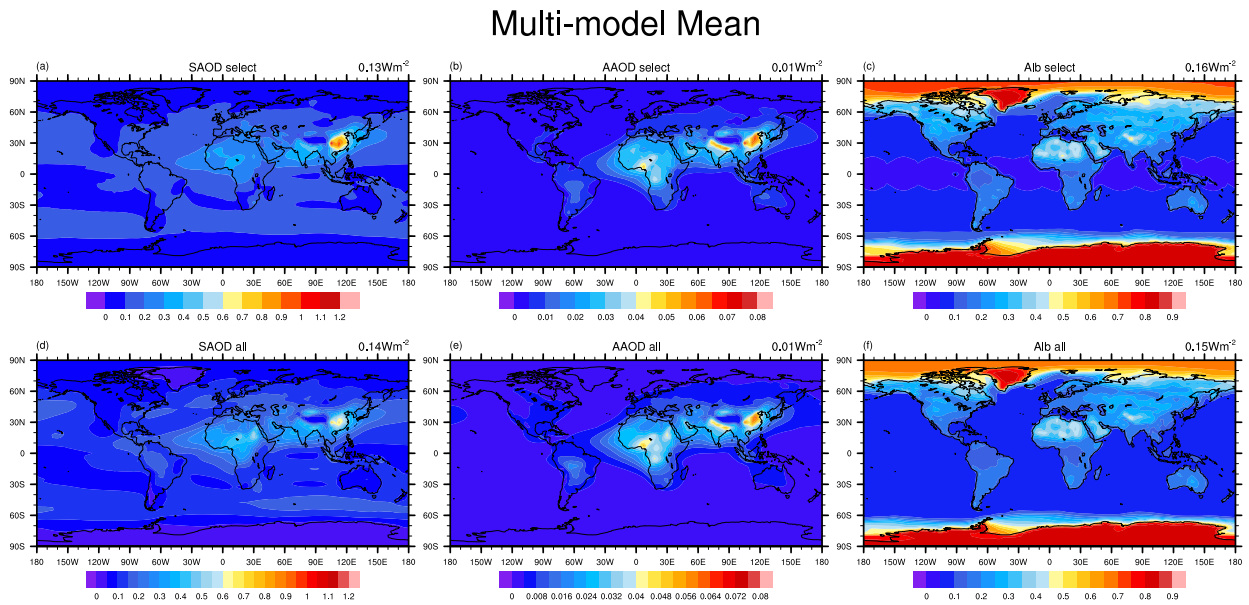

Figure B. 2 The spatial distribution of the multi-model mean SAOD, AAOD, and ALB. The upper panel is for the selected five CMIP6 models, and the lower panel is for 31 CMIP6 models. Global mean values are indicated in the top-right corner of each subplot.

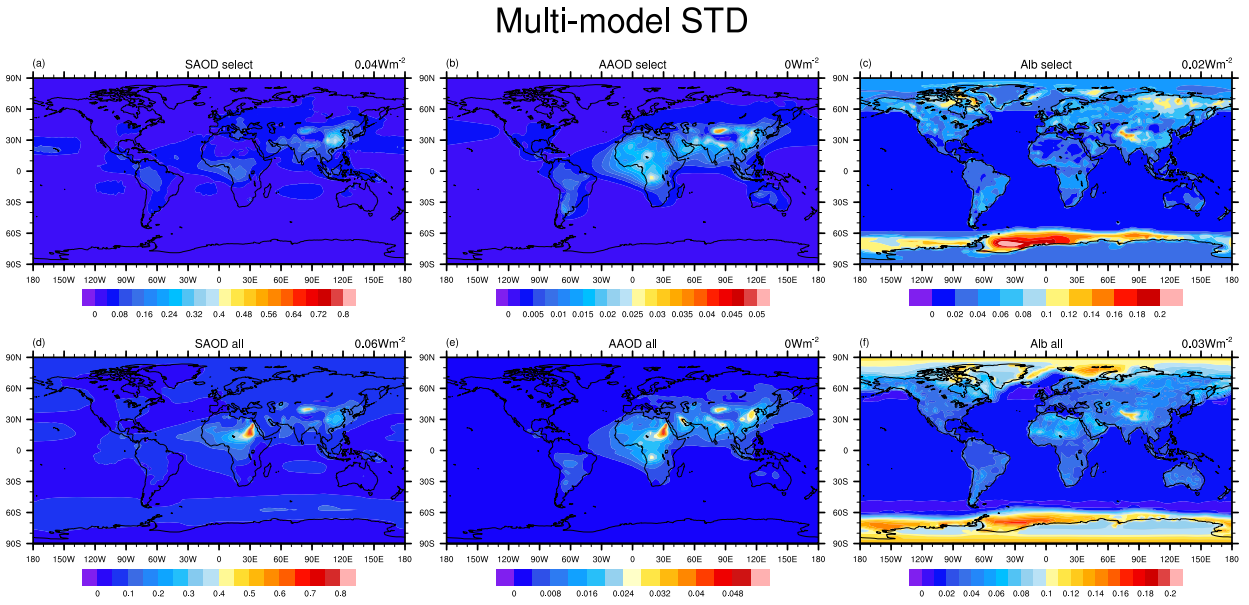

Figure B. 3 The same as Figure B2, but for the standard deviation.

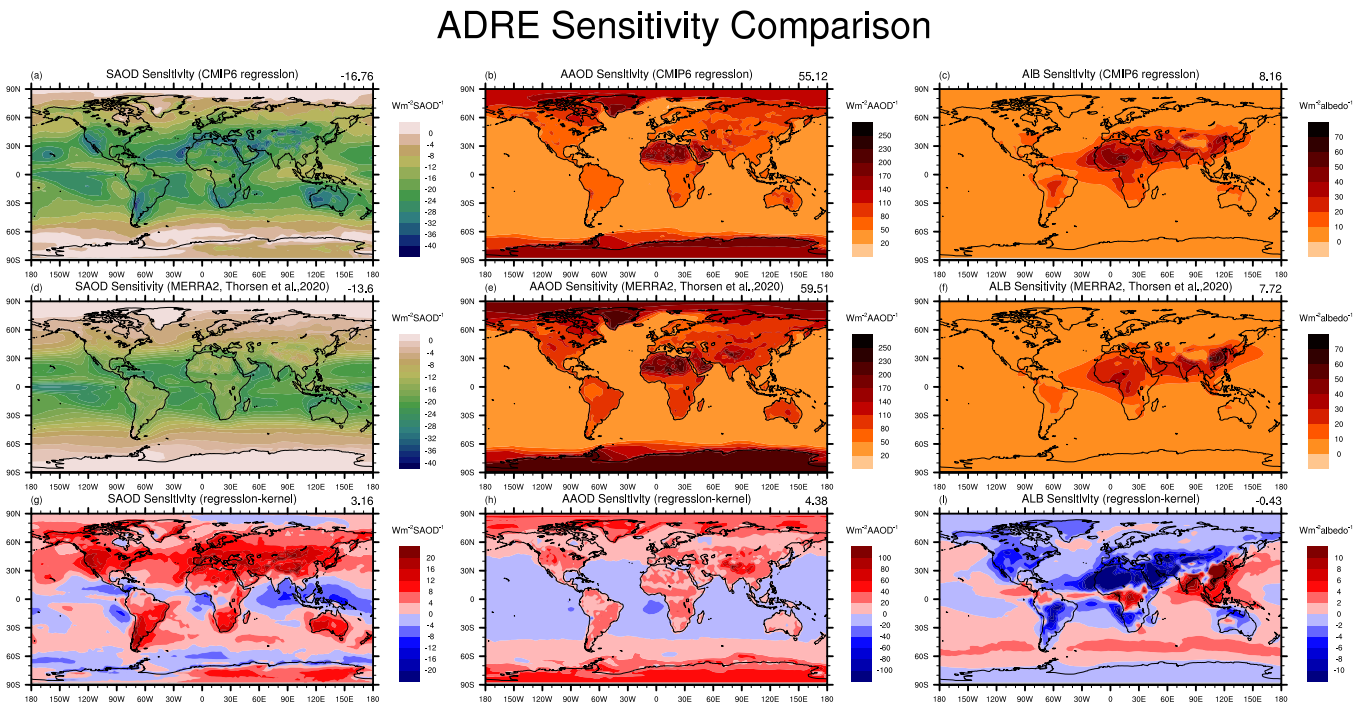

Figure B. 4 Spatial distributions of the ADRE sensitivity to SAOD, AAOD, and ALB (a) based on the multi-model mean regression model (Equation. B4); (b) from the aerosol kernels computed from a reanalysis dataset MERRA2 (Thorsen et al., 2020); (c) Their differences.

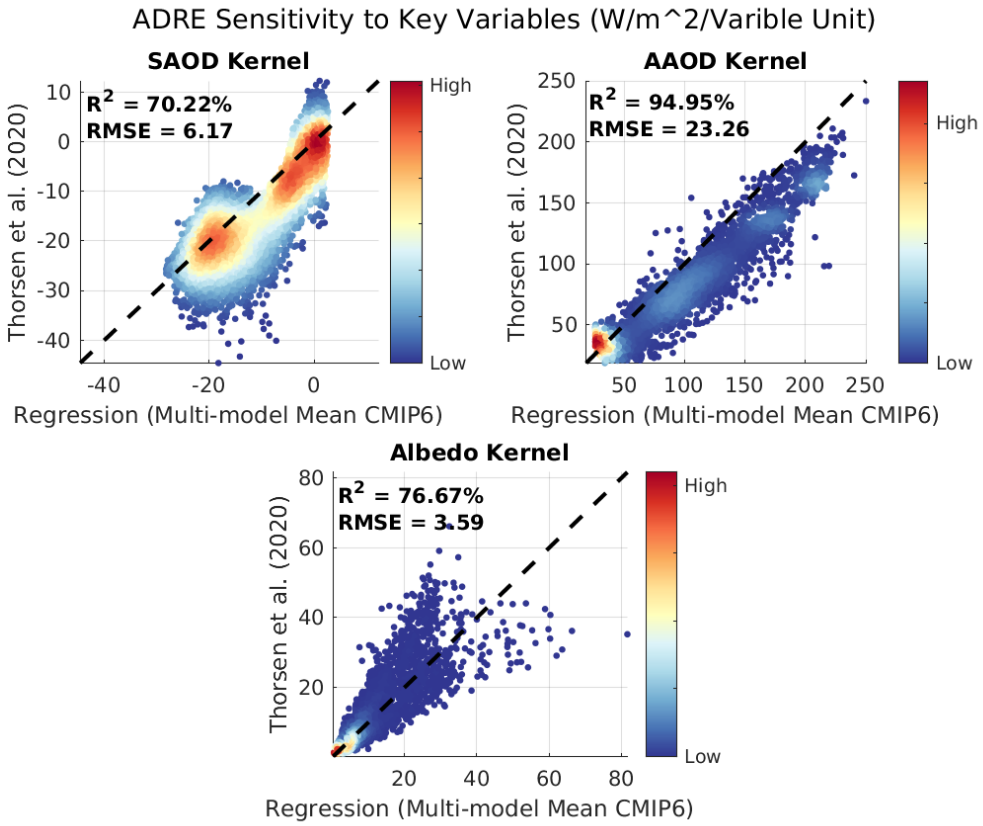

Figure B. 5 Comparison between the sensitivity of ADRE calculated by regression model and the kernel data from Thorsen et al. (2020)

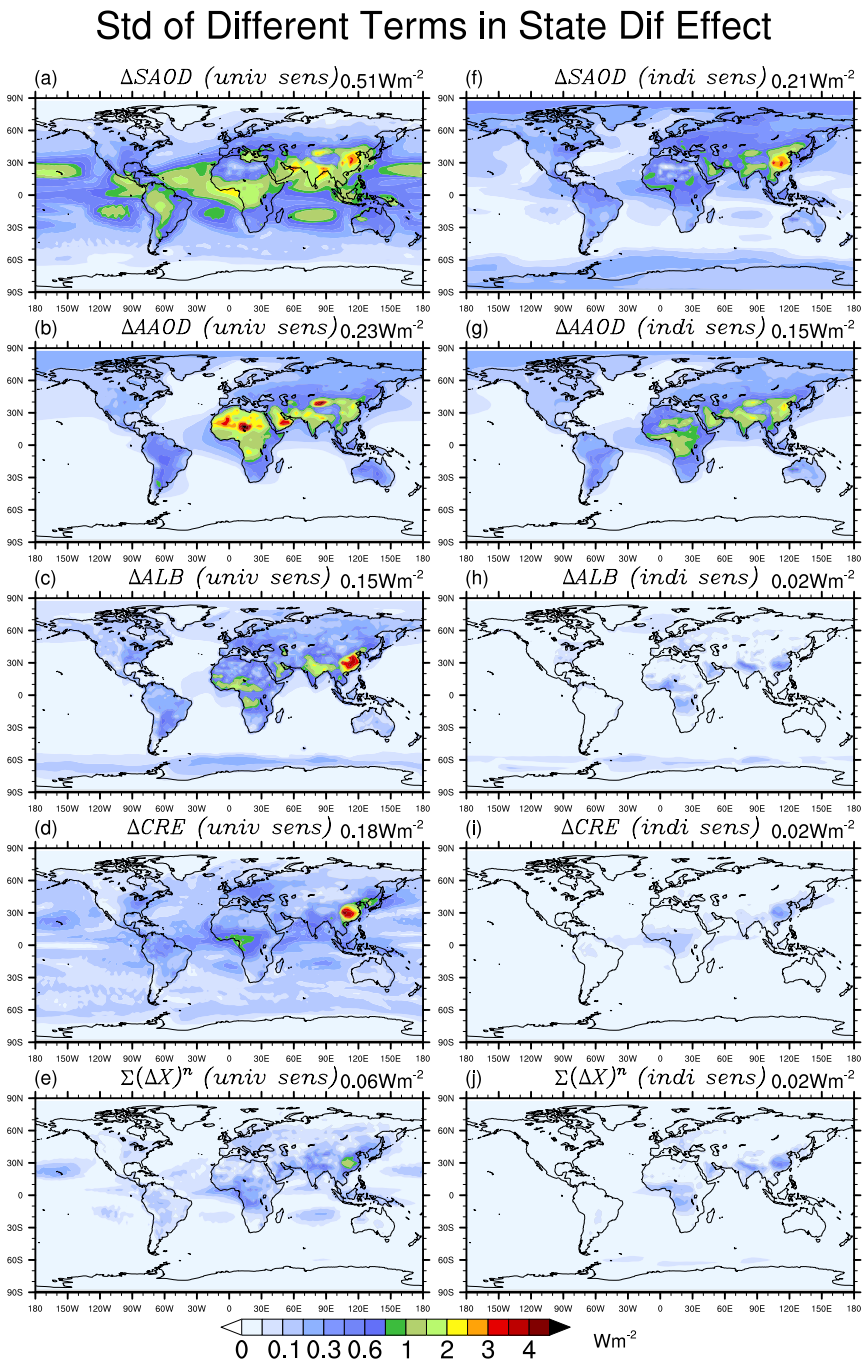

Figure B. 6 Standard deviations of the ADRE anomaly components caused by differences in state variables, (a-e) quantified with the universal ADRE sensitivity (Equation. (B17)) and (f-j) due to the anomalous ADRE sensitivity in individual models (Equation. (B18)).

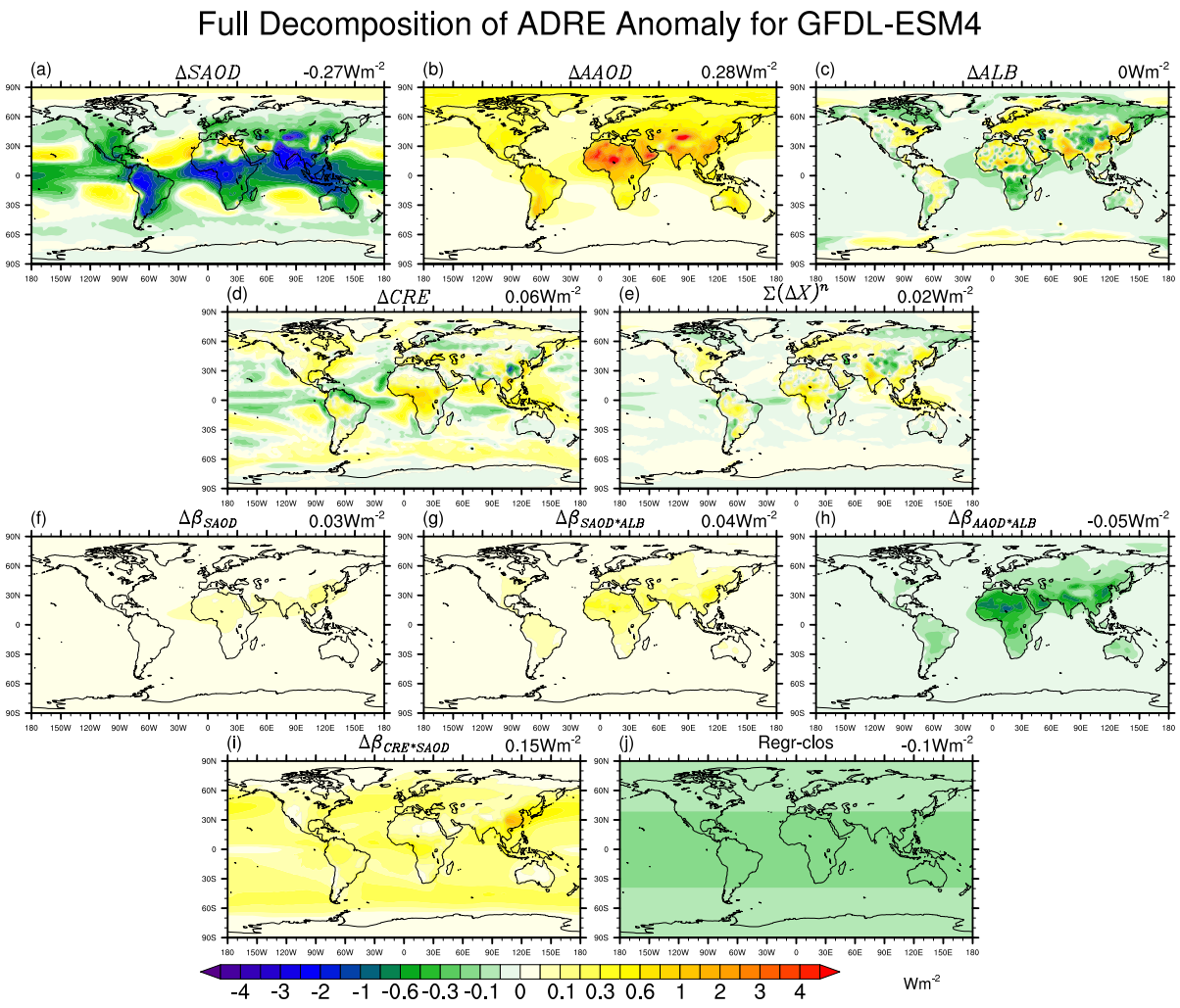

Figure B. 7 Contributions to the ADRE anomalies in the GFDL-ESM4 model from (a-e) state variable anomalies and (f-j) from ADRE sensitivity differences.

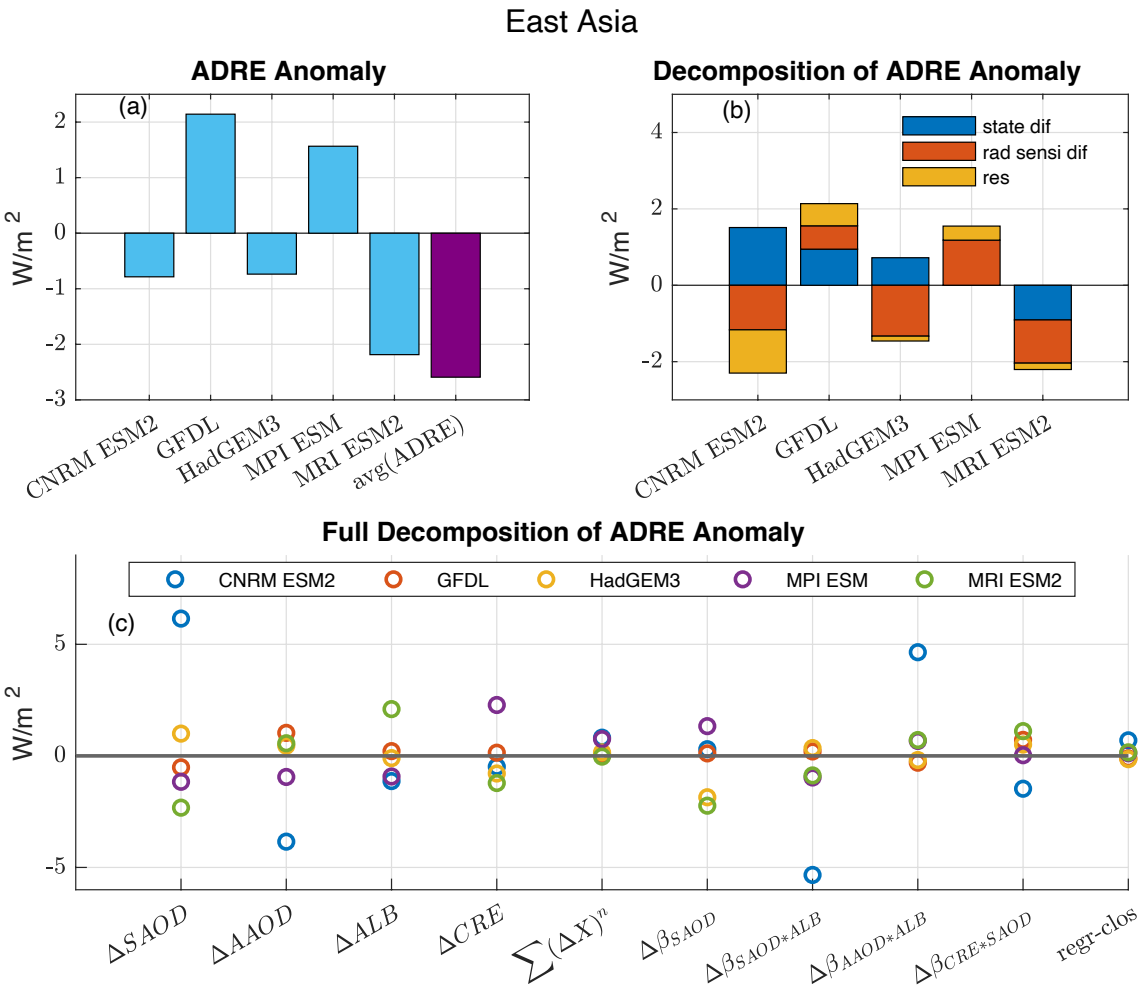

Figure B. 8 Similar to Figure 3.2, but for the regional mean ADRE anomalies in the CMIP6 GCMs for East Asia. (a) ADRE inter-model anomalies; (b) decomposition terms of ADRE inter-model anomalies; (c) all contributions.

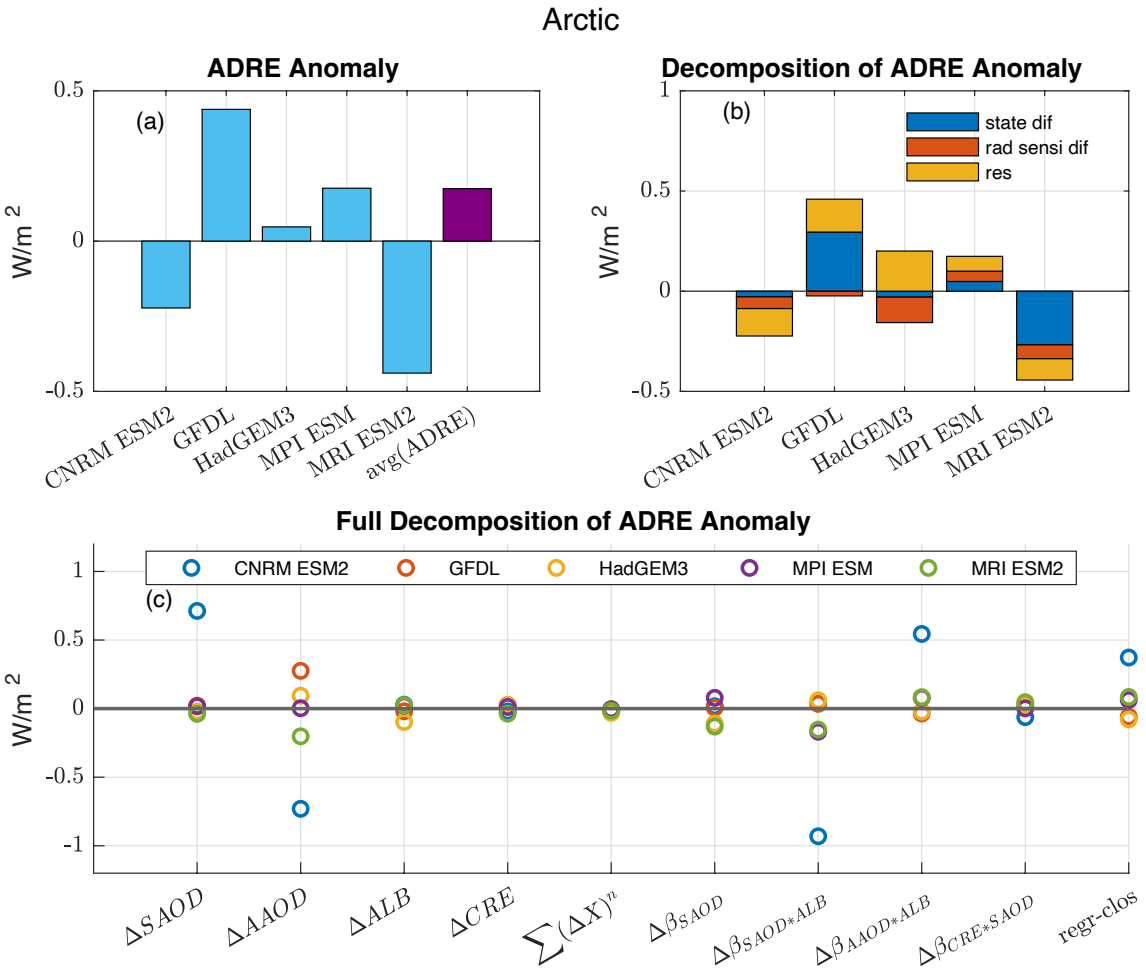

Figure B. 9 Same as Figure B8, but for the Arctic.

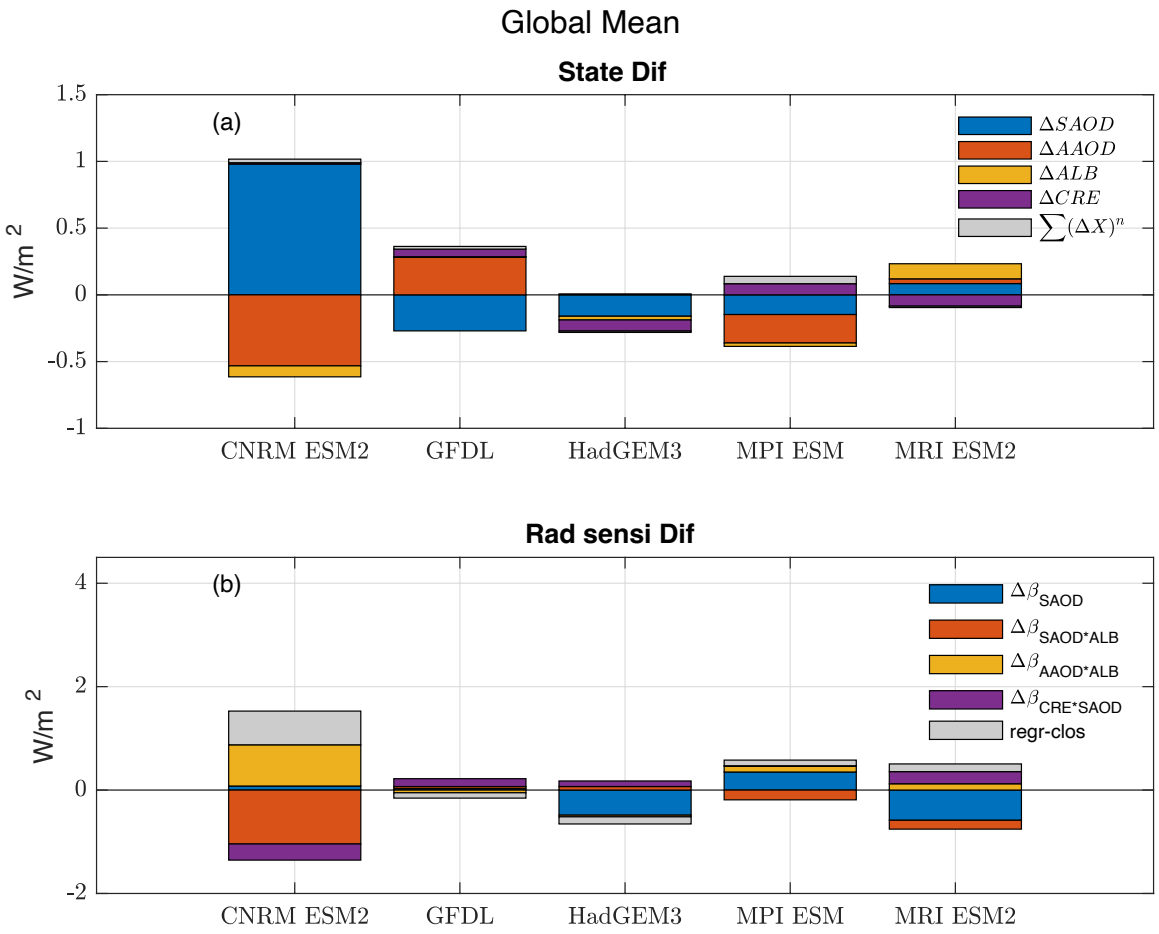

Figure B. 10 The global mean component contributions to ADRE anomalies by (a) state variables ($\Delta X_{I,j}$ terms) and (b) radiative sensitivity difference ($\Delta\beta_{I,j}$ terms).

Table B. 1 For each CMIP6 model and the multi-model mean, the regression coefficient β_I, and the R^2 and the RSME compared to the truth values provided by the model outputs.

	R^2	**RMSE (Wm^{-2})**	**β_{SAOD}**	**$\beta_{SAOD\cdot ALB}$**	**$\beta_{AAOD\cdot ALB}$**	**$\beta_{SAOD\cdot CRE}$**

CNRM-ESM2-1	95%	0.28	1.97	0.20	-0.47	-0.52
GFDL-ESM4	94%	0.41	2.67	-0.52	-0.41	-1.08
HadGEM3-GC31-LL	93%	0.50	1.78	-0.30	-0.16	-0.56
MPI-ESM-1-2-HAM	92%	0.39	2.23	-0.28	-0.20	-0.95
MRI-ESM2-0	95%	0.35	2.17	-0.29	-0.32	-0.71
Multi-model mean	95%	0.32	2.06	-0.37	-0.24	-0.71

Table B. 2 Name, radiation scheme, short-wave spectral resolution, spatial resolution, aerosol scheme, and references for selected models.

	Radiation scheme	**Spectral resolution**	**Spatial resolution**	**Aerosol scheme**
CNRM-ESM2-1	2-stream, δ-Ed (Dqu et al., n.d.)	6 SW bands (Voldoire et al., 2013)	Arpege 6.3 (T127; Gaussian Reduced with 24572 grid points in total distributed over 128 latitude circles); 91 levels; top level 78.4 km)	TACTIC_v2
GFDL-ESM4	δ-Ed+adding (Freidenreich & Ramaswamy, 1999)	18 SW bands	GFDL-AM4.1 (Cubed-sphere (c96) - 1 degree nominal horizontal resolution; 360 x 180 longitude/latitude; 49 levels; top level 1 Pa)	interactive

HadGEM3-GC31-LL	SW: 2-stream δ-Ed + δ-scaling; LW: 2-stream PIFM + δ-scaling (Edwards & Slingo, 1996; Mulcahy et al., 2020)	6 SW bands	MetUM-HadGEM3-GA7.1 (N96; 192 x 144 longitude/latitude; 85 levels; top level 85 km)	UKCA-GLOMAP-mode
MPI-ESM-1-2-HAM	2-stream δ-Ed (Stevens et al., 2013)	14 SW bands	ECHAM6.3 (spectral T63; 192 x 96 longitude/latitude; 47 levels; top level 0.01 hPa)	HAM2.3
MRI-ESM2-0	2-stream δ-Ed (Yukimoto et al., 2019)	22 SW bands	MRI-AGCM3.5 (TL159; 320 x 160 longitude/latitude; 80 levels; top level 0.01 hPa)	MASINGAR mk2r4 (TL95; 192 x 96 longitude/latitude; 80 levels; top level 0.01 hPa)
Abbreviations: adding = adding method, δ-Ed = delta Eddington, δ -scaling = delta scaling, PIFM = Practical Improved Flux Method				

Appendix C

C Chapter 4 Supplementary Information

C1 List of Figures and Tables

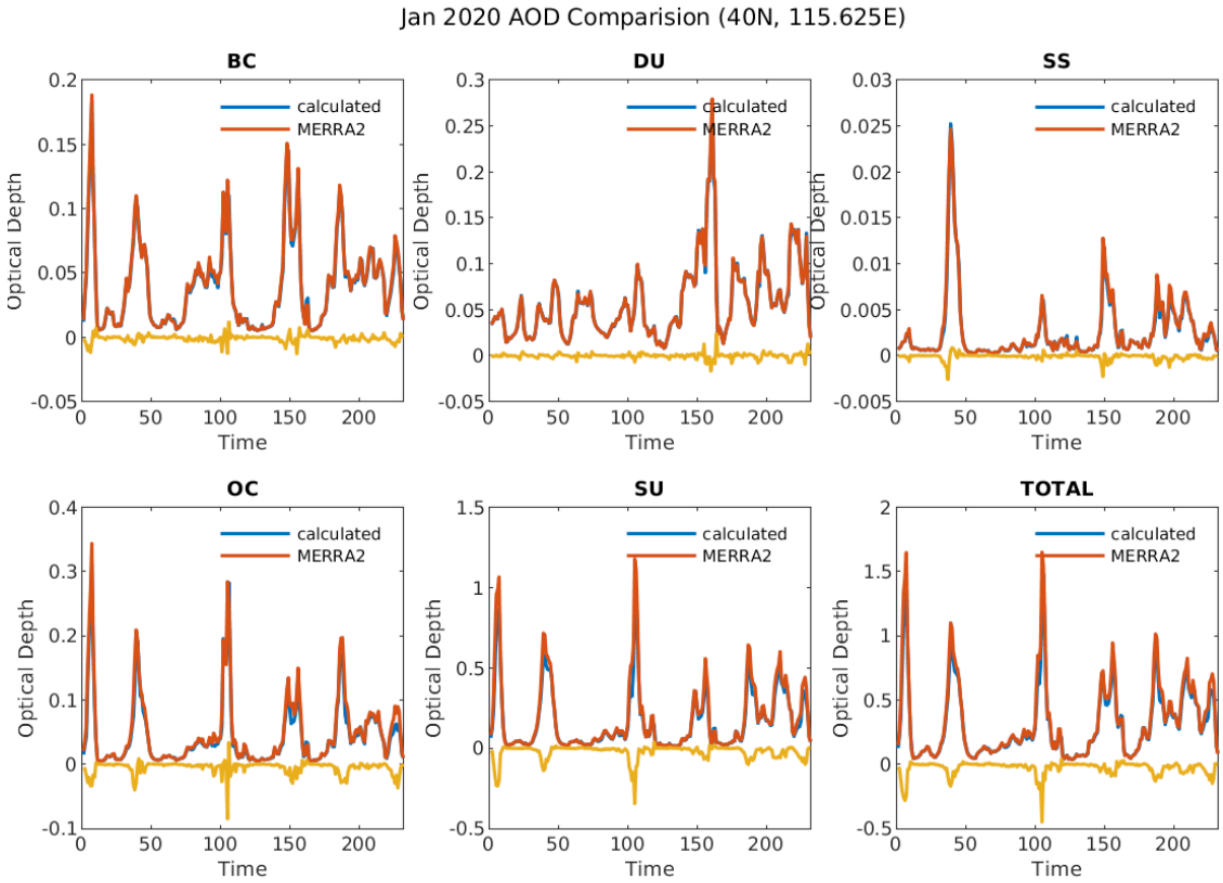

Figure C. 1 Validation of total column aerosol optical depth (AOD) reconstructed from MERRA-2 aerosol mixing ratio data for black carbon (BC), dust (DU), sea salt (SS), organic carbon (OC), and sulfate (SU) aerosols. The validation is conducted for Beijing, China, in January 2020.

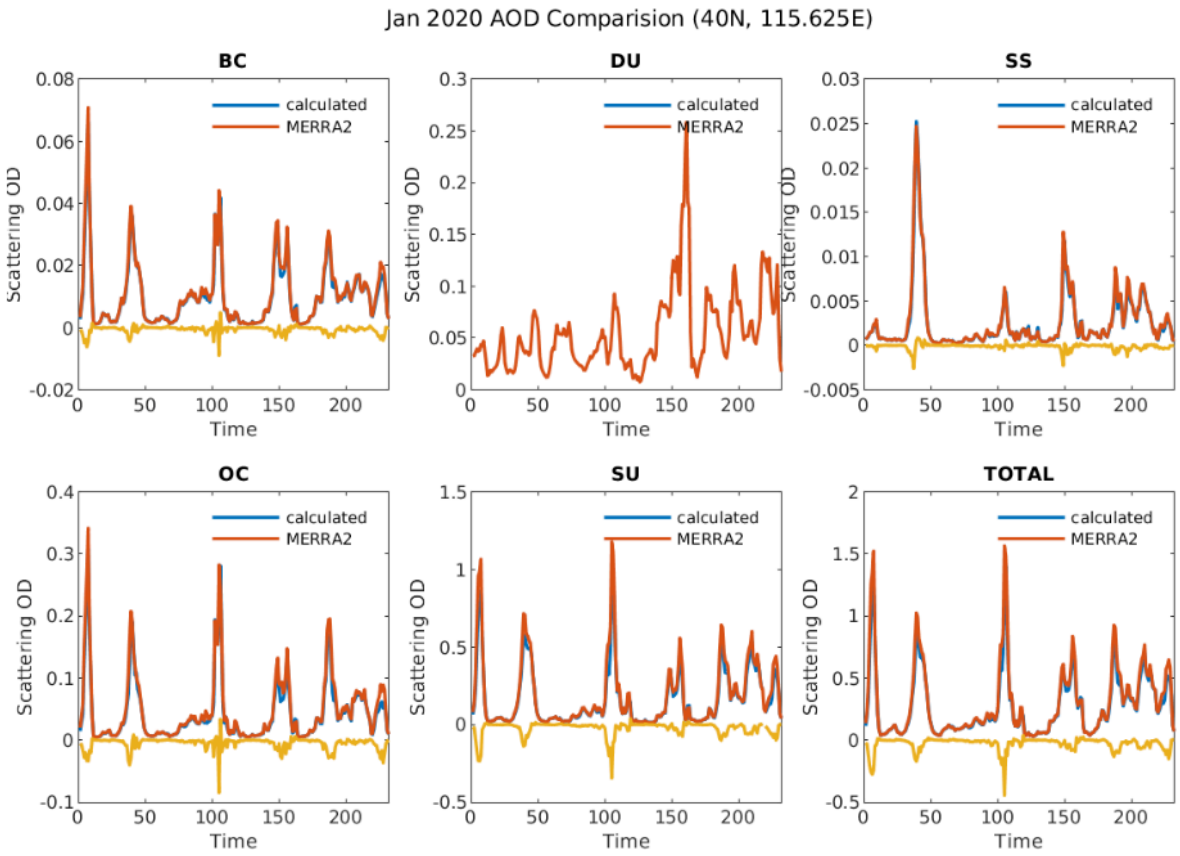

Figure C. 2 The same as Figure C1 but for total column scattering aerosol optical depth.

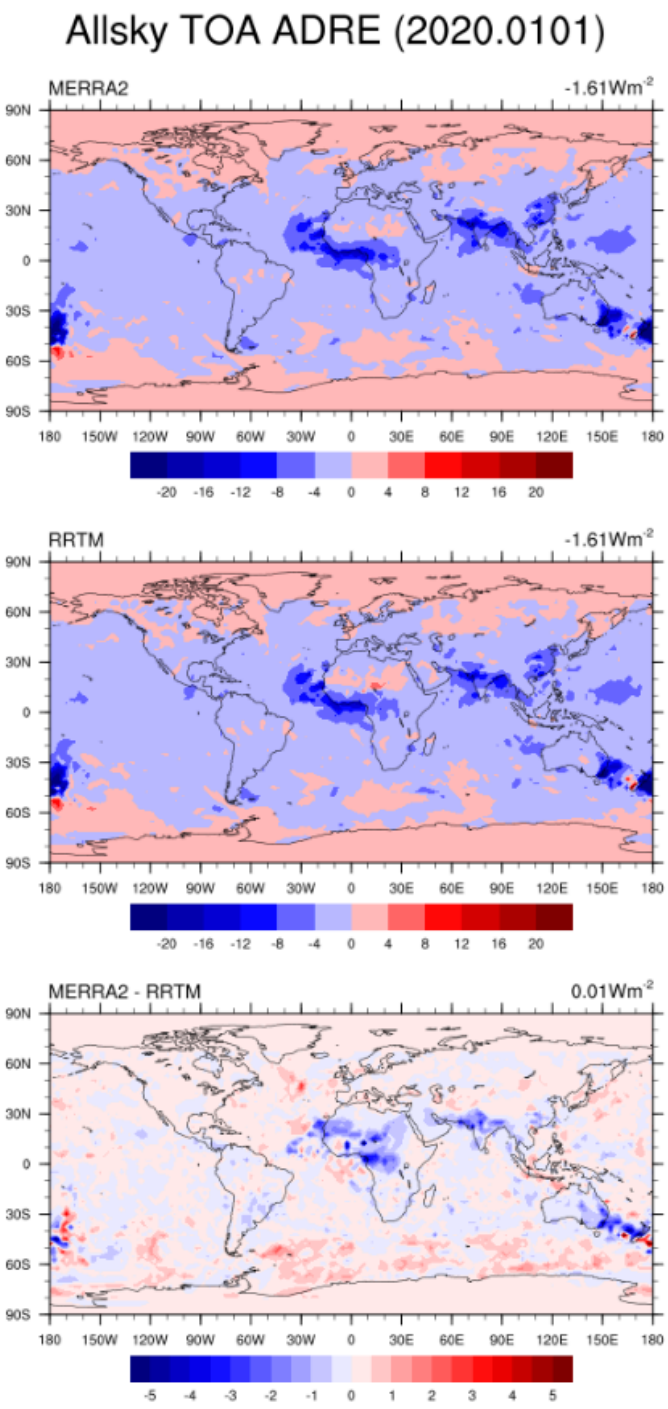

Figure C. 3 Validation of all-sky total column ADRE calculations using RRMTG for January 1st, 2020. Upper: ADRE from MERRA2; Middle: RRTMG-calculated ADRE; Bottom: Bias.

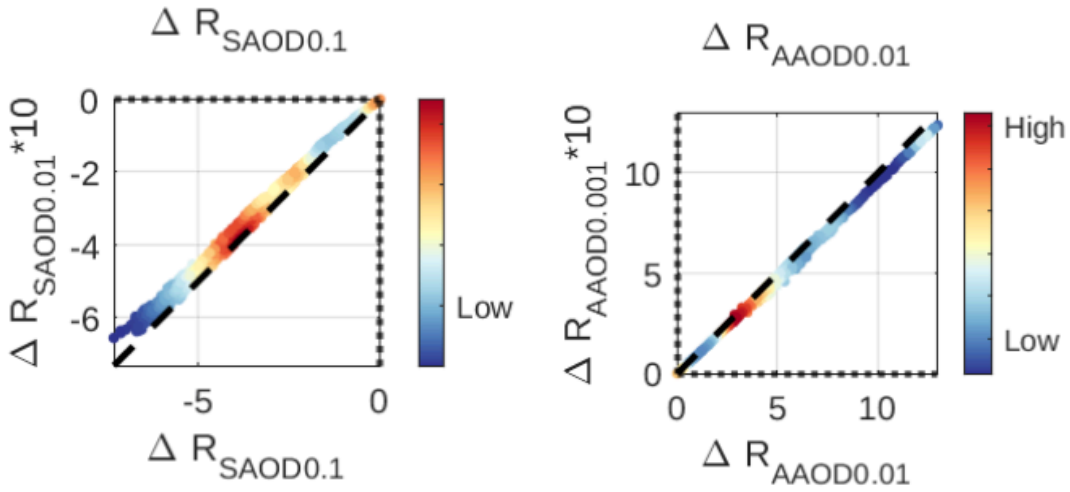

Figure C. 4 Linear scaling test for broadband Top-Of-Atmosphere (TOA) flux changes (ΔR) in response to perturbations in stratospheric scattering and absorbing AOD. Aerosols are placed at the 1st layer above tropopause. The scattering AOD perturbations are 0.1 and 0.01, while the absorbing AOD perturbations are 0.01 and 0.001, respectively.

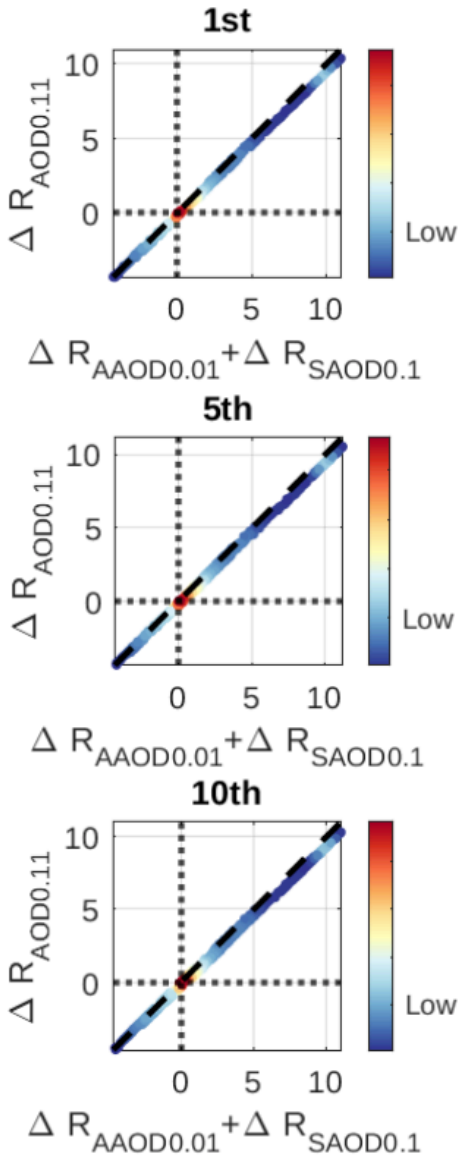

Figure C. 5 Linear additivity test for broadband TOA flux changes (ΔR) in response to perturbations in both stratospheric scattering and absorbing AOD. Aerosols are positioned at the 1st, 5th, and 10th layer above the tropopause, respectively. The perturbations are set to 0.1 for scattering AOD and 0.01 for absorbing AOD. The summed ΔR for scattering and absorbing AOD perturbations shows good agreement with the results from total AOD perturbations.

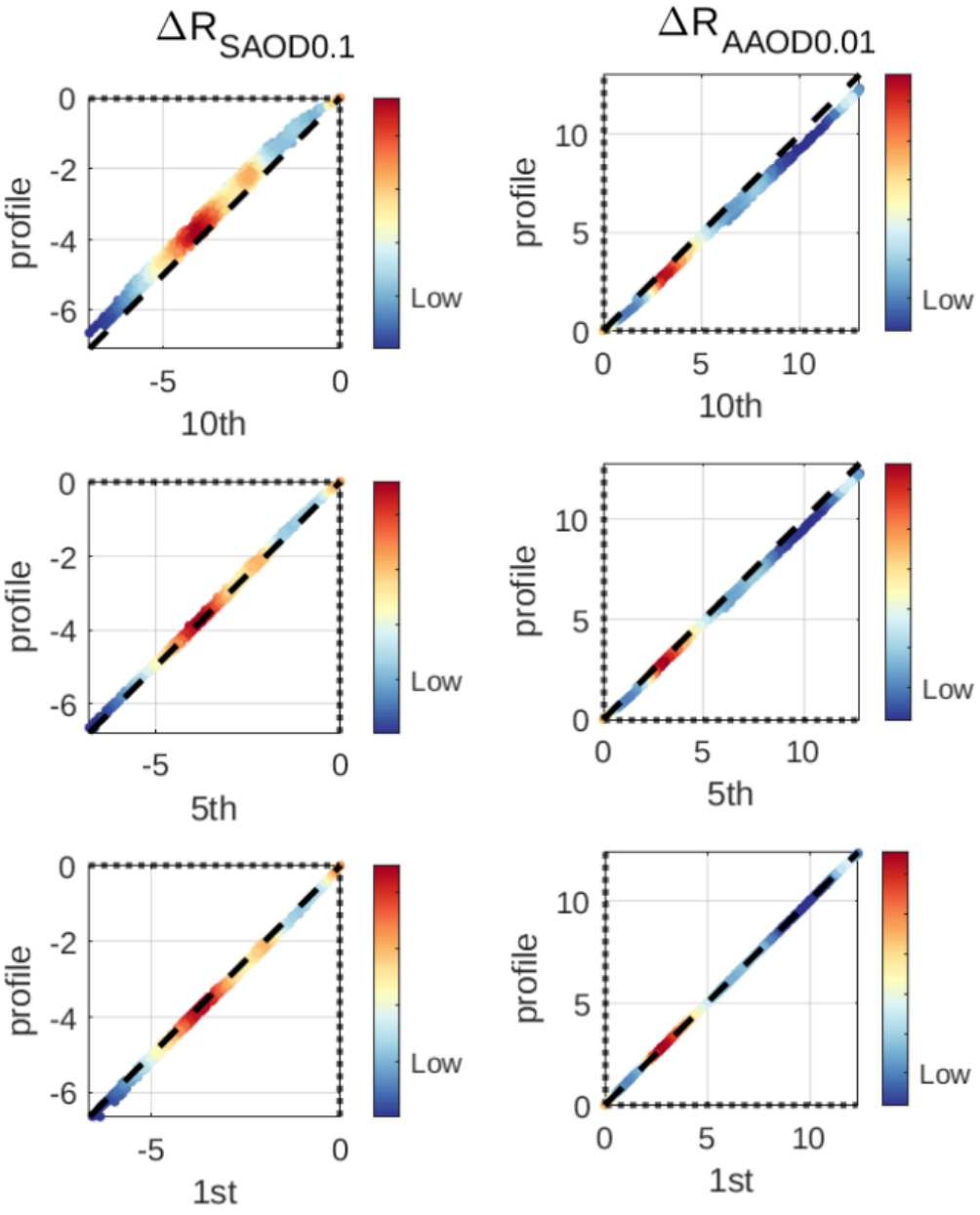

Figure C. 6 Height dependency test for broadband TOA flux changes (ΔR) in response to aerosol perturbation layer height. The ADRE results from perturbing AOD at a single random layer (e.g., 1st, 5th, 10th above the tropopause) are similar to those obtained from perturbing the entire stratospheric aerosol profiles.

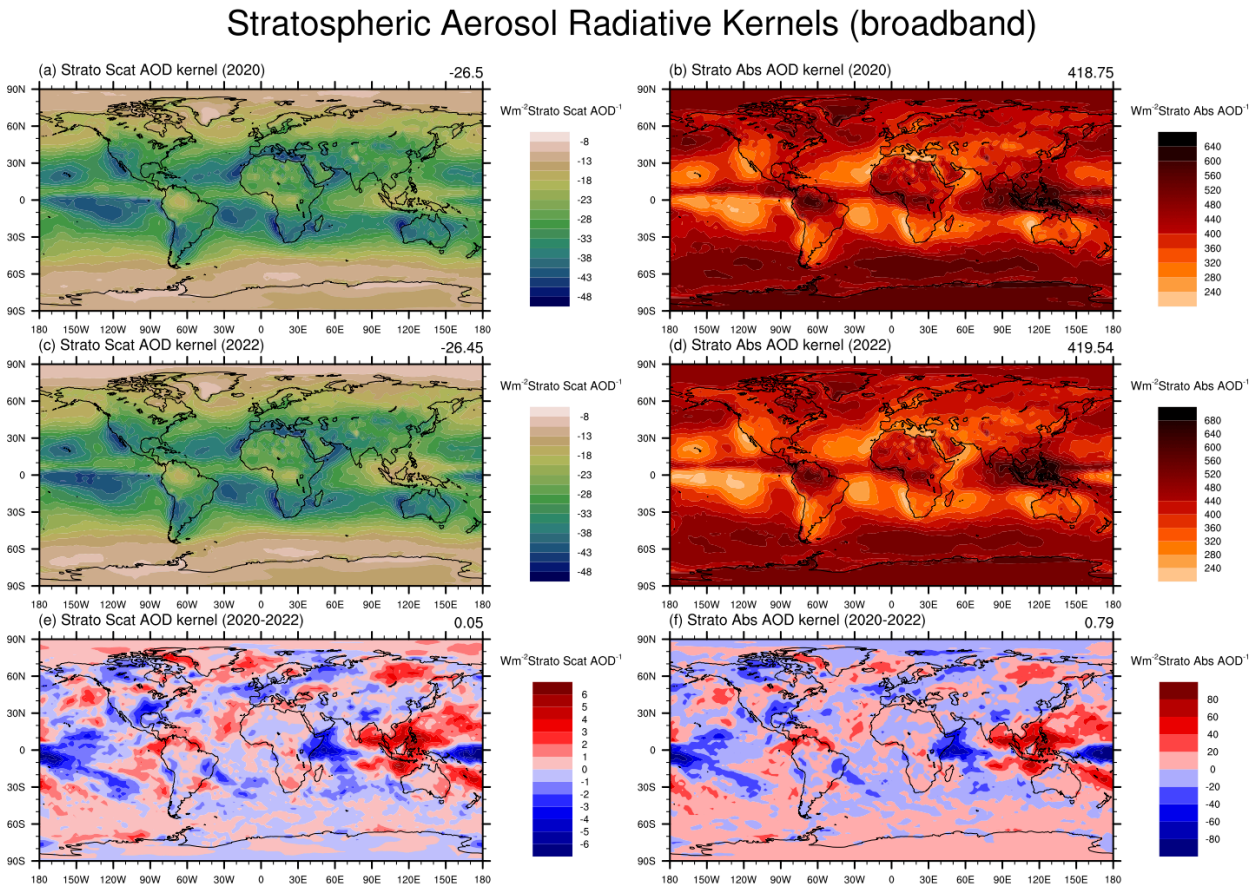

Figure C. 7 Comparisons between the annual mean stratospheric AOD_{scat} and AOD_{abs} kernels for the years 2020 and 2022. First row: 2020; Middle row: 2022; Bottom row: differences (2020-2022).

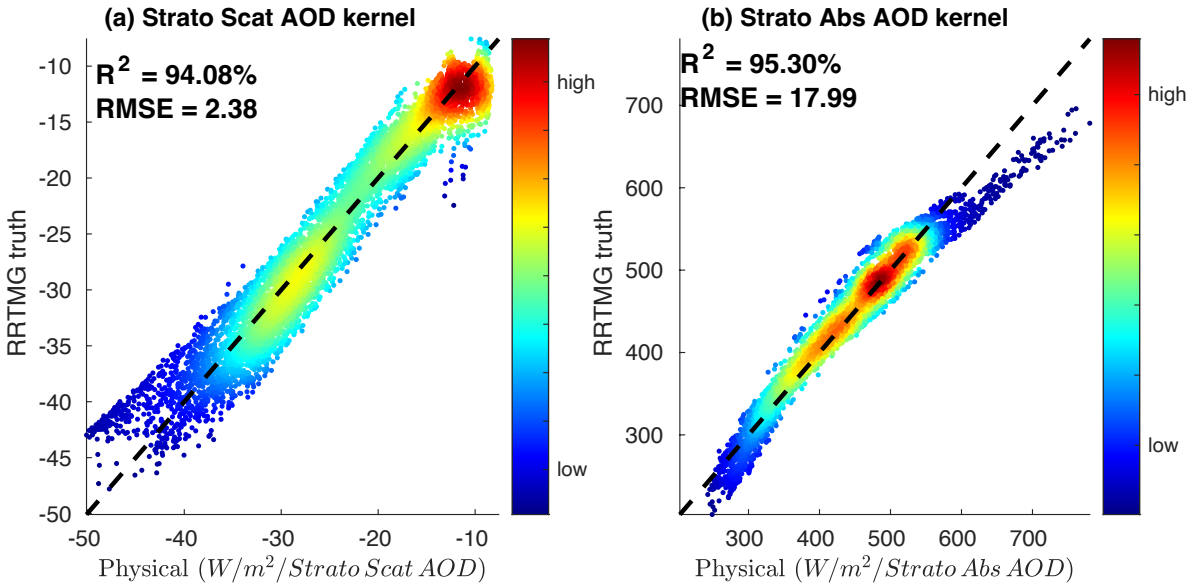

Figure C. 8 Validations of the physically sorted broadband aerosol kernels for stratospheric AOD_{scat} and AOD_{abs} against benchmark RRTMG calculations.

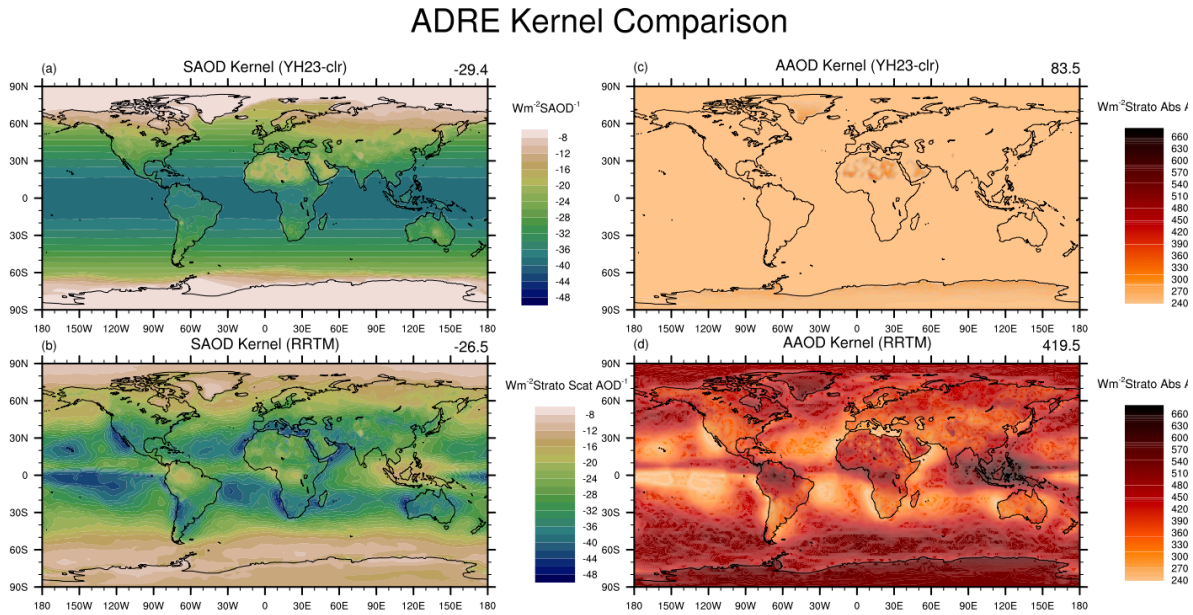

Figure C. 9 Comparisons between the stratospheric ADRE kernels developed in this work and the YH23 clear-sky kernels for total column aerosols. Left column: kernels for AOD_{scat}; Right column: kernels for AOD_{abs}.

Table C. 1 Evaluation of predictor performance for SAOD kernels normalized by insolation ($\frac{1}{S}\frac{\partial ADRE}{\partial SAOD}$). R is the TOA reflectance and τ is the stratospheric aerosol optical depth. R^2 represents the coefficient of determination, and RMSE is the Root Mean Squared Error.

1 predictor	R_s	R_s^2	τ	R_s τ	-	-
R^2	86.04%	84.21%	69.82%	73.18%	-	-
RMSE	3.40	3.63	4.75	4.51	-	-
2 predictors	(R_s τ& (R_s^2)	(R_s τ& (τ	(R_sτ& (R_s)	(R_s^2) & (τ	(R_s) & (τ	(R_s^2) & (R_s)
R^2	92.50%	83.87%	92.50%	91.72%	93.91%	87.30%
RMSE	2.27	3.55	2.27	2.44	2.02	3.15
3 predictors	(R_s^2) & (R_s) & (τ)	(R_s^2) & (R_s) & (R_s τ)	(R_s^2) & (τ) & (R_s τ)			
R^2	94.01%	93.55%	92.50%	-	-	-
RMSE	rmse=2.99	rmse=3.06	rmse=3.26	-	-	-
4 predictors	(τ) & R_s^2 & (R_s) & (R_s τ)	-	-	-	-	-
R^2	94.08%	-	-	-	-	-
RMSE	2.38	-	-	-	-	-

Table C. 2 Evaluations of predictor performances for AAOD kernels normalized by insolation ($\frac{1}{S}\frac{\partial ADRE}{\partial AAOD}$). R is the TOA reflectance and τ is the stratospheric aerosol optical depth.

1 predictor	R_s	R_s^2	τ	R_s τ	-	-
R^2	74.03%	87.49%	1.97%	50.86%	-	-
RMSE	45.45	29.54	83.21	52.46	-	-
2 predictors	(R_s τ) & (R_s^2)	(R_s τ) & (τ)	(R_sτ) & (R_s)	(R_s^2) & (τ)	(R_s) & (τ)	(R_s^2) & (R_s)
R^2	90.43%	86.32%	82.59%	88.64%	76.37%	89.89%
RMSE	23.96	27.55	32.37	26.59	39.53	25.57
3 predictors	(R_s^2) & (R_s) & (τ)	(R_s^2) & (R_s) & (R_s τ)	(R_s^2) & (τ) & (R_s τ)			
R^2	90.43%	86.32%	82.59%	-	-	-
RMSE	23.96	27.55	32.37	-	-	-
4 predictors	(τ) & R_s^2 & (R_s) & (R_s τ)	-	-	-	-	-
R^2	95.30%	-	-	-	-	-
RMSE	17.99	-	-	-	-	-

Bibliography

Aben, I., Hasekamp, O., & Hartmann, W. (2007). Uncertainties in the space-based measurements of CO2 columns due to scattering in the Earth's atmosphere. *Journal of Quantitative Spectroscopy and Radiative Transfer*, *104*(3), 450–459. https://doi.org/10.1016/j.jqsrt.2006.09.013

Adebiyi, A. A., & Zuidema, P. (2018). Low Cloud Cover Sensitivity to Biomass-Burning Aerosols and Meteorology over the Southeast Atlantic. *Journal of Climate*, *31*(11), 4329–4346. https://doi.org/10.1175/JCLI-D-17-0406.1

Aller, J. Y., Kuznetsova, M. R., Jahns, C. J., & Kemp, P. F. (2005). The sea surface microlayer as a source of viral and bacterial enrichment in marine aerosols. *Journal of Aerosol Science*, *36*(5–6), 801–812.

Andersson, S. M., Martinsson, B. G., Vernier, J.-P., Friberg, J., Brenninkmeijer, C. A. M., Hermann, M., van Velthoven, P. F. J., & Zahn, A. (2015). Significant radiative impact of volcanic aerosol in the lowermost stratosphere. *Nature Communications*, *6*(1), 7692. https://doi.org/10.1038/ncomms8692

Andreae, M. O., & Rosenfeld, D. (2008). Aerosol–cloud–precipitation interactions. Part 1. The nature and sources of cloud-active aerosols. *Earth-Science Reviews*, *89*(1–2), 13–41. https://doi.org/10.1016/j.earscirev.2008.03.001

Ångström, A. (1929). On the atmospheric transmission of sun radiation and on dust in the air. *Geografiska Annaler*, *11*(2), 156–166.

Ayash, T., Gong, S. L., Jia, C. Q., Huang, P., Zhao, T. L., & Lavoue, D. (2008). Global modeling of multicomponent aerosol species: Aerosol optical parameters. *Journal of Geophysical Research: Atmospheres*, *113*(D12). https://doi.org/10.1029/2007JD008968

Balmes, K. A., & Fu, Q. (2021). All-Sky Aerosol Direct Radiative Effects at the ARM SGP Site. *Journal of Geophysical Research: Atmospheres*, *126*(17), e2021JD034933. https://doi.org/10.1029/2021JD034933

Bellouin, N., Quaas, J., Gryspeerdt, E., Kinne, S., Stier, P., Watson-Parris, D., Boucher, O., Carslaw, K. S., Christensen, M., Daniau, A. -L., Dufresne, J. -L., Feingold, G., Fiedler, S., Forster, P., Gettelman, A., Haywood, J. M., Lohmann, U., Malavelle, F., Mauritsen, T., … Stevens, B. (2020). Bounding Global Aerosol Radiative Forcing of Climate Change. *Reviews of Geophysics*, *58*(1). https://doi.org/10.1029/2019RG000660

Boers, R., Brandsma, T., & Siebesma, A. P. (2017). Impact of aerosols and clouds on decadal trends in all-sky solar radiation over the Netherlands (1966–2015). *Atmospheric Chemistry and Physics*, *17*(13), 8081–8100. https://doi.org/10.5194/acp-17-8081-2017

Boiyo, R., Kumar, K. R., Zhao, T., & Guo, J. (2019). A 10-Year Record of Aerosol Optical Properties and Radiative Forcing Over Three Environmentally Distinct AERONET Sites in Kenya, East Africa. *Journal of Geophysical Research: Atmospheres*, *124*(3), 1596–1617. Scopus. https://doi.org/10.1029/2018JD029461

Bond, T. C., Doherty, S. J., Fahey, D. W., Forster, P. M., Berntsen, T., DeAngelo, B. J., Flanner, M. G., Ghan, S., Kärcher, B., Koch, D., Kinne, S., Kondo, Y., Quinn, P. K., Sarofim, M. C., Schultz, M. G., Schulz, M., Venkataraman, C., Zhang, H., Zhang, S., … Zender, C. S. (2013). Bounding the role of black carbon in the climate system: A scientific assessment.

Journal of Geophysical Research: Atmospheres, *118*(11), 5380–5552. https://doi.org/10.1002/jgrd.50171

Boucher, O., & Boucher, O. (2015). Atmospheric aerosols (pp. 9-24). Springer Netherlands.

Bourassa, A. E., Rieger, L. A., Degenstein, D. A., Cole, J. N., Langille, J., Blanchet, J.-P., & Blanchard, Y. (2020). Monitoring High Altitude Aerosol Injections and Climate Impacts from a New Canadian Instrument Suite Concept (HAWC). *AGU Fall Meeting Abstracts*, *2020*, GC037-0007.

Bourassa, A. E., Rieger, L. A., Zawada, D. J., Khaykin, S., Thomason, L. W., & Degenstein, D. A. (2019). Satellite Limb Observations of Unprecedented Forest Fire Aerosol in the Stratosphere. *Journal of Geophysical Research: Atmospheres*, *124*(16), 9510–9519. https://doi.org/10.1029/2019JD030607

Bourassa, A. E., Zawada, D. J., Rieger, L. A., Warnock, T. W., Toohey, M., & Degenstein, D. A. (2023). Tomographic Retrievals of Hunga Tonga-Hunga Ha'apai Volcanic Aerosol. *Geophysical Research Letters*, *50*(3), e2022GL101978. https://doi.org/10.1029/2022GL101978

Buchard, V., Randles, C. A., Silva, A. M. da, Darmenov, A., Colarco, P. R., Govindaraju, R., Ferrare, R., Hair, J., Beyersdorf, A. J., Ziemba, L. D., & Yu, H. (2017). The MERRA-2 Aerosol Reanalysis, 1980 Onward. Part II: Evaluation and Case Studies. *Journal of Climate*, *30*(17), 6851–6872. https://doi.org/10.1175/JCLI-D-16-0613.1

Butz, A., Galli, A., Hasekamp, O., Landgraf, J., Tol, P., & Aben, I. (2012). TROPOMI aboard Sentinel-5 Precursor: Prospective performance of CH4 retrievals for aerosol and cirrus loaded atmospheres. *Remote Sensing of Environment*, *120*, 267–276. https://doi.org/10.1016/j.rse.2011.05.030

Butz, A., Hasekamp, O. P., Frankenberg, C., & Aben, I. (2009). Retrievals of atmospheric CO_2 from simulated space-borne measurements of backscattered near-infrared sunlight: Accounting for aerosol effects. *Applied Optics*, *48*(18), 3322. https://doi.org/10.1364/AO.48.003322

Calvello, M., Caggiano, R., Esposito, F., Lettino, A., Sabia, S., Summa, V., & Pavese, G. (2017). IMAA (Integrated Measurements of Aerosol in Agri valley) campaign: Multi-instrumental observations at the largest European oil/gas pre-treatment plant area. *Atmospheric Environment*, *169*, 297–306. https://doi.org/10.1016/j.atmosenv.2017.09.026

Chan Miller, C., Roche, S., Wilzewski, J. S., Liu, X., Chance, K., Souri, A. H., Conway, E., Luo, B., Samra, J., Hawthorne, J., Sun, K., Staebell, C., Chulakadabba, A., Sargent, M., Benmergui, J. S., Franklin, J. E., Daube, B. C., Li, Y., Laughner, J. L., … Wofsy, S. C. (2023). *Methane retrieval from MethaneAIR using the CO $_2$ Proxy Approach: A demonstration for the upcoming MethaneSAT mission* [Preprint]. Gases/Remote Sensing/Data Processing and Information Retrieval. https://doi.org/10.5194/egusphere-2023-1962

Chand, D., Wood, R., Anderson, T. L., Satheesh, S. K., & Charlson, R. J. (2009). Satellite-derived direct radiative effect of aerosols dependent on cloud cover. *Nature Geoscience*, *2*(3), 181–184.

Charlson, R. J., Langner, J., Rodhe, H., Leovy, C. B., & Warren, S. G. (1991). Perturbation of the northern hemisphere radiative balance by backscattering from anthropogenic sulfate aerosols*. *Tellus A*, *43*(4), 152–163. https://doi.org/10.1034/j.1600-0870.1991.00013.x

Charlson, R. J., Lovelock, J. E., Andreae, M. O., & Warren, S. G. (1987). Oceanic phytoplankton, atmospheric sulphur, cloud albedo and climate. *Nature*, *326*(6114), 655–661. https://doi.org/10.1038/326655a0

Charlson, R. J., Schwartz, S. E., Hales, J. M., Cess, R. D., Coakley, J. A., Hansen, J. E., & Hofmann, D. J. (1992). Climate Forcing by Anthropogenic Aerosols. *Science*, *255*(5043), 423–430. https://doi.org/10.1126/science.255.5043.423

Chauvigné, A., Waquet, F., Auriol, F., Blarel, L., Delegove, C., Dubovik, O., Flamant, C., Gaetani, M., Goloub, P., Loisil, R., Mallet, M., Nicolas, J.-M., Parol, F., Peers, F., Torres, B., & Formenti, P. (2021). Aerosol above-cloud direct radiative effect and properties in the Namibian region during the AErosol, RadiatiOn, and CLOuds in southern Africa (AEROCLO-sA) field campaign – Multi-Viewing, Multi-Channel, Multi-Polarization (3MI) airborne simulator and sun photometer measurements. *Atmospheric Chemistry and Physics*, *21*(10), 8233–8253. https://doi.org/10.5194/acp-21-8233-2021

Chen, A., Zhao, C., & Fan, T. (2022). Spatio-temporal distribution of aerosol direct radiative forcing over mid-latitude regions in north hemisphere estimated from satellite observations. *Atmospheric Research*, *266*, 105938. https://doi.org/10.1016/j.atmosres.2021.105938

Chen, X., Yang, D., Cai, Z., Liu, Y., & Spurr, R. (2017). Aerosol Retrieval Sensitivity and Error Analysis for the Cloud and Aerosol Polarimetric Imager on Board TanSat: The Effect of Multi-Angle Measurement. *Remote Sensing*, *9*(2), 183. https://doi.org/10.3390/rs9020183

Chen, Z., Bhartia, P. K., Torres, O., Jaross, G., Loughman, R., DeLand, M., Colarco, P., Damadeo, R., & Taha, G. (2020). Evaluation of the OMPS/LP stratospheric aerosol extinction product using SAGE III/ISS observations. *Atmospheric Measurement Techniques*, *13*(6), 3471–3485. https://doi.org/10.5194/amt-13-3471-2020

Cherian, R., & Quaas, J. (2020). Trends in AOD, Clouds, and Cloud Radiative Effects in Satellite Data and CMIP5 and CMIP6 Model Simulations Over Aerosol Source Regions. *Geophysical Research Letters*, *47*(9), e2020GL087132. https://doi.org/10.1029/2020GL087132

Chin, M., Chu, A., Levy, R., Remer, L., Kaufman, Y., Holben, B., Eck, T., Ginoux, P., & Gao, Q. (2004). Aerosol distribution in the Northern Hemisphere during ACE-Asia: Results from global model, satellite observations, and Sun photometer measurements. *Journal of Geophysical Research: Atmospheres*, *109*(D23).

Chin, M., Ginoux, P., Kinne, S., Torres, O., Holben, B. N., Duncan, B. N., Martin, R. V., Logan, J. A., Higurashi, A., & Nakajima, T. (2002). Tropospheric Aerosol Optical Thickness from the GOCART Model and Comparisons with Satellite and Sun Photometer Measurements. *JOURNAL OF THE ATMOSPHERIC SCIENCES*, *59*, 23.

Chlek, P., & Coakley Jr, J. A. (1974). Aerosols and climate. *Science*, *183*(4120), 75–77.

Choomanee, P., Bualert, S., Thongyen, T., Rungratanaubon, T., Rattanapotanan, T., & Szymanski, W. W. (2024). Beyond common urban air quality assessment: Relationship between PM2.5 and black carbon during haze and non-haze periods in Bangkok. *Atmospheric Pollution Research*, *15*(2), 101992. https://doi.org/10.1016/j.apr.2023.101992

Christensen, M. W., Gettelman, A., Cermak, J., Dagan, G., Diamond, M., Douglas, A., Feingold, G., Glassmeier, F., Goren, T., Grosvenor, D. P., Gryspeerdt, E., Kahn, R., Li, Z., Ma, P.-L., Malavelle, F., McCoy, I. L., McCoy, D. T., McFarquhar, G., Mülmenstädt, J., … Yuan, T. (2022). Opportunistic experiments to constrain aerosol effective radiative forcing. *Atmospheric Chemistry and Physics*, *22*(1), 641–674. https://doi.org/10.5194/acp-22-641-2022

Christian, K., Wang, J., Ge, C., Peterson, D., Hyer, E., Yorks, J., & McGill, M. (2019). Radiative Forcing and Stratospheric Warming of Pyrocumulonimbus Smoke Aerosols: First Modeling Results With Multisensor (EPIC, CALIPSO, and CATS) Views from Space. *Geophysical Research Letters*, *46*(16), 10061–10071. https://doi.org/10.1029/2019GL082360

Chylik, J., Chechin, D., Dupuy, R., Kulla, B. S., Lüpkes, C., Mertes, S., ... & Neggers, R. A. (2023). Aerosol impacts on the entrainment efficiency of Arctic mixed-phase convection in a simulated air mass over open water. *Atmospheric Chemistry and Physics*, *23*(8), 4903-4929.

Cinquini, L., Crichton, D., Mattmann, C., Harney, J., Shipman, G., Wang, F., Ananthakrishnan, R., Miller, N., Denvil, S., Morgan, M., Pobre, Z., Bell, G. M., Doutriaux, C., Drach, R., Williams, D., Kershaw, P., Pascoe, S., Gonzalez, E., Fiore, S., & Schweitzer, R. (2014). The Earth System Grid Federation: An open infrastructure for access to distributed geospatial data. *Future Generation Computer Systems*, *36*, 400–417. https://doi.org/10.1016/j.future.2013.07.002

Clough, S. A., Shephard, M. W., Mlawer, E. J., Delamere, J. S., Iacono, M. J., Cady-Pereira, K., Boukabara, S., & Brown, P. D. (2005). Atmospheric radiative transfer modeling: A summary of the AER codes. *Journal of Quantitative Spectroscopy and Radiative Transfer*, *91*, 233–244. https://doi.org/10.1016/j.jqsrt.2004.05.058

Connor, B., Bösch, H., McDuffie, J., Taylor, T., Fu, D., Frankenberg, C., O'Dell, C., Payne, V. H., Gunson, M., Pollock, R., Hobbs, J., Oyafuso, F., & Jiang, Y. (2016). Quantification of uncertainties in OCO-2 measurements of XCO₂:simulations and linear error analysis. *Atmospheric Measurement Techniques*, *9*(10), 5227–5238. https://doi.org/10.5194/amt-9-5227-2016

Damany-Pearce, L., Johnson, B., Wells, A., Osborne, M., Allan, J., Belcher, C., Jones, A., & Haywood, J. (2022). Australian wildfires cause the largest stratospheric warming since Pinatubo and extends the lifetime of the Antarctic ozone hole. *Scientific Reports*, *12*(1), 12665. https://doi.org/10.1038/s41598-022-15794-3

Datseris, G., Blanco, J., Hadas, O., Bony, S., Caballero, R., Kaspi, Y., & Stevens, B. (2022). Minimal Recipes for Global Cloudiness. *Geophysical Research Letters*, *49*(20), e2022GL099678. https://doi.org/10.1029/2022GL099678

Diao, C., Xu, Y., & Xie, S.-P. (2021). Anthropogenic aerosol effects on tropospheric circulation and sea surface temperature (1980–2020): Separating the role of zonally asymmetric forcings. *Atmospheric Chemistry and Physics*, *21*(24), 18499–18518. https://doi.org/10.5194/acp-21-18499-2021

Diner, D. J., Beckert, J. C., Reilly, T. H., Bruegge, C. J., Conel, J. E., Kahn, R. A., Martonchik, J. V., Ackerman, T. P., Davies, R., & Gerstl, S. A. (1998). Multi-angle Imaging SpectroRadiometer (MISR) instrument description and experiment overview. *IEEE Transactions on Geoscience and Remote Sensing*, *36*(4), 1072–1087. Draine, B. T., & Flatau, P. J. (1994). Discrete-dipole approximation for scattering calculations. *Josa a*, *11*(4), 1491-1499.

Duce, R. A. (1995). Sources, distributions, and fluxes of mineral aerosols and their relationship to climate. *Aerosol Forcing of Climate*, *6*, 43–72.

Dunne, J. P., Horowitz, L. W., Adcroft, A. J., Ginoux, P., Held, I. M., John, J. G., Krasting, J. P., Malyshev, S., Naik, V., Paulot, F., Shevliakova, E., Stock, C. A., Zadeh, N., Balaji, V., Blanton, C., Dunne, K. A., Dupuis, C., Durachta, J., Dussin, R., … Zhao, M. (2020). The GFDL Earth System Model Version 4.1 (GFDL-ESM 4.1): Overall Coupled Model

Description and Simulation Characteristics. *Journal of Advances in Modeling Earth Systems*, *12*(11), e2019MS002015. https://doi.org/10.1029/2019MS002015

Edwards, J. M., & Slingo, A. (1996). Studies with a flexible new radiation code. I: Choosing a configuration for a large-scale model. *Quarterly Journal of the Royal Meteorological Society*, *122*(531), 689–719. https://doi.org/10.1002/qj.49712253107

Flynn, L. E., Seftor, C. J., Larsen, J. C., & Xu, P. (2006). The ozone mapping and profiler suite. In *Earth Science Satellite Remote Sensing: Vol. 1: Science and Instruments* (pp. 279–296). Springer.

Frankenberg, C., Hasekamp, O., O'Dell, C., Sanghavi, S., Butz, A., & Worden, J. (2012). Aerosol information content analysis of multi-angle high spectral resolution measurements and its benefit for high accuracy greenhouse gas retrievals. *Atmospheric Measurement Techniques*, *5*(7), 1809–1821. https://doi.org/10.5194/amt-5-1809-2012

Freidenreich, S. M., & Ramaswamy, V. (1999). A new multiple-band solar radiative parameterization for general circulation models. *Journal of Geophysical Research: Atmospheres*, *104*(D24), 31389–31409. https://doi.org/10.1029/1999JD900456

Friberg, J., Martinsson, B. G., & Sporre, M. K. (2023). Short- and long-term stratospheric impact of smoke from the 2019–2020 Australian wildfires. *Atmospheric Chemistry and Physics*, *23*(19), 12557–12570. https://doi.org/10.5194/acp-23-12557-2023

Frierson, D. M. W., & Hwang, Y.-T. (2012). Extratropical Influence on ITCZ Shifts in Slab Ocean Simulations of Global Warming. *Journal of Climate*, *25*(2), 720–733. https://doi.org/10.1175/JCLI-D-11-00116.1

Fromm, M., Lindsey, D. T., Servranckx, R., Yue, G., Trickl, T., Sica, R., Doucet, P., & Godin-Beekmann, S. (2010). The untold story of pyrocumulonimbus. *Bulletin of the American Meteorological Society*, *91*(9), 1193–1210.

Fromm, M., Servranckx, R., Stocks, B. J., & Peterson, D. A. (2022). Understanding the critical elements of the pyrocumulonimbus storm sparked by high-intensity wildland fire. *Communications Earth & Environment*, *3*(1), 1–7. https://doi.org/10.1038/s43247-022-00566-8

Gao, J., Huang, Y., Peng, Y., & Wright, J. S. (2023). Aerosol Effects on Clear-Sky Shortwave Heating in the Asian Monsoon Tropopause Layer. *Journal of Geophysical Research: Atmospheres*, *128*(4), e2022JD036956. https://doi.org/10.1029/2022JD036956

Gelaro, R., McCarty, W., Suárez, M. J., Todling, R., Molod, A., Takacs, L., Randles, C. A., Darmenov, A., Bosilovich, M. G., Reichle, R., Wargan, K., Coy, L., Cullather, R., Draper, C., Akella, S., Buchard, V., Conaty, A., Silva, A. M. da, Gu, W., … Zhao, B. (2017). The Modern-Era Retrospective Analysis for Research and Applications, Version 2 (MERRA-2). *Journal of Climate*, *30*(14), 5419–5454. https://doi.org/10.1175/JCLI-D-16-0758.1

Gharibzadeh, M., Bidokhti, A. A., & Alam, K. (2021). The interaction of ozone and aerosol in a semi-arid region in the Middle East: Ozone formation and radiative forcing implications. *Atmospheric Environment*, *245*, 118015.

Giles, D. M., Sinyuk, A., Sorokin, M. G., Schafer, J. S., Smirnov, A., Slutsker, I., Eck, T. F., Holben, B. N., Lewis, J. R., Campbell, J. R., Welton, E. J., Korkin, S. V., & Lyapustin, A. I. (2019). Advancements in the Aerosol Robotic Network (AERONET) Version 3 database – automated near-real-time quality control algorithm with improved cloud screening for

Sun photometer aerosol optical depth (AOD) measurements. *Atmospheric Measurement Techniques*, *12*(1), 169–209. https://doi.org/10.5194/amt-12-169-2019

Goto, D., Seiki, T., Suzuki, K., Yashiro, H., & Takemura, T. (2024). Impacts of a double-moment bulk cloud microphysics scheme (NDW6-G23) on aerosol fields in NICAM.19 with a global 14 km grid resolution. *Geoscientific Model Development*, *17*(2), 651–684. https://doi.org/10.5194/gmd-17-651-2024

Grinsted, A., Moore, J. C., & Jevrejeva, S. (2007). Observational evidence for volcanic impact on sea level and the global water cycle. *Proceedings of the National Academy of Sciences*, *104*(50), 19730–19734. https://doi.org/10.1073/pnas.0705825104

Grythe, H., Ström, J., Krejci, R., Quinn, P., & Stohl, A. (2014). A review of sea-spray aerosol source functions using a large global set of sea salt aerosol concentration measurements. *Atmospheric Chemistry and Physics*, *14*(3), 1277–1297.

Gueymard, C. A., & Yang, D. (2020). Worldwide validation of CAMS and MERRA-2 reanalysis aerosol optical depth products using 15 years of AERONET observations. *Atmospheric Environment*, *225*, 117216. https://doi.org/10.1016/j.atmosenv.2019.117216

Günther, M., Schmidt, H., Timmreck, C., & Toohey, M. (2022). Climate Feedback to Stratospheric Aerosol Forcing: The Key Role of the Pattern Effect. *Journal of Climate*, *35*(24), 7903–7917. https://doi.org/10.1175/JCLI-D-22-0306.1

Günther, M., Schmidt, H., Timmreck, C., & Toohey, M. (2024). Why does stratospheric aerosol forcing strongly cool the warm pool? *Atmospheric Chemistry and Physics*, *24*(12), 7203–7225. https://doi.org/10.5194/acp-24-7203-2024

Guo, H., Ming, Y., Fan, S., Zhou, L., Harris, L., & Zhao, M. (2021). Two-Moment Bulk Cloud Microphysics With Prognostic Precipitation in GFDL's Atmosphere Model AM4.0:

Configuration and Performance. *Journal of Advances in Modeling Earth Systems*, *13*(6), e2020MS002453. https://doi.org/10.1029/2020MS002453

Gutjahr, O., Putrasahan, D., Lohmann, K., Jungclaus, J. H., von Storch, J.-S., Brüggemann, N., Haak, H., & Stössel, A. (2019). Max Planck Institute Earth System Model (MPI-ESM1.2) for the High-Resolution Model Intercomparison Project (HighResMIP). *Geoscientific Model Development*, *12*(7), 3241–3281. https://doi.org/10.5194/gmd-12-3241-2019

Halthore, R. N., Crisp, D., Schwartz, S. E., Anderson, G. P., Berk, A., Bonnel, B., Boucher, O., Chang, F.-L., Chou, M.-D., Clothiaux, E. E., Dubuisson, P., Fomin, B., Fouquart, Y., Freidenreich, S., Gautier, C., Kato, S., Laszlo, I., Li, Z., Mather, J. H., … Wiscombe, W. (2005). Intercomparison of shortwave radiative transfer codes and measurements. *Journal of Geophysical Research: Atmospheres*, *110*(D11). https://doi.org/10.1029/2004JD005293

Hansen, J., Sato, M., Ruedy, R., Nazarenko, L., Lacis, A., Schmidt, G. A., Russell, G., Aleinov, I., Bauer, M., Bauer, S., Bell, N., Cairns, B., Canuto, V., Chandler, M., Cheng, Y., Del Genio, A., Faluvegi, G., Fleming, E., Friend, A., … Zhang, S. (2005). Efficacy of climate forcings. *Journal of Geophysical Research: Atmospheres*, *110*(D18). https://doi.org/10.1029/2005JD005776

Hartmann, D. L. (2015). *Global physical climatology* (Vol. 103). Newnes.

Haywood, J., & Boucher, O. (2000). Estimates of the direct and indirect radiative forcing due to tropospheric aerosols: A review. *Reviews of Geophysics*, *38*(4), 513–543. https://doi.org/10.1029/1999RG000078

Haywood, J. M., & Shine, K. P. (1995). The effect of anthropogenic sulfate and soot aerosol on the clear sky planetary radiation budget. *Geophysical Research Letters*, *22*(5), 603–606. https://doi.org/10.1029/95GL00075

Heald, C. L., Ridley, D. A., Kroll, J. H., Barrett, S. R. H., Cady-Pereira, K. E., Alvarado, M. J., & Holmes, C. D. (2014). Contrasting the direct radiative effect and direct radiative forcing of aerosols. *Atmospheric Chemistry and Physics*, *14*(11), 5513–5527. https://doi.org/10.5194/acp-14-5513-2014

Hinds, W. C., & Zhu, Y. (2022). *Aerosol technology: Properties, behavior, and measurement of airborne particles*. John Wiley & Sons.

Houweling, S., Hartmann, W., Aben, I., Schrijver, H., & Skidmore, J. (2005). Evidence of systematic errors in SCIAMACHY-observed CO2 due to aerosols. *Atmos. Chem. Phys.*, 11.

Huang, H., & Huang, Y. (2023). Diagnosing the Radiation Biases in Global Climate Models Using Radiative Kernels. *Geophysical Research Letters*, *50*(13), e2023GL103723. https://doi.org/10.1029/2023GL103723

Huang, J., Arnott, W. P., Barnard, J. C., & Holmes, H. A. (2021). Theoretical Uncertainty Analysis of Satellite Retrieved Aerosol Optical Depth Associated with Surface Albedo and Aerosol Optical Properties. *Remote Sensing*, *13*(3), Article 3. https://doi.org/10.3390/rs13030344

Huang, Y., Natraj, V., Zeng, Z.-C., Kopparla, P., & Yung, Y. L. (2020). Quantifying the impact of aerosol scattering on the retrieval of methane from airborne remote sensing measurements. *Atmospheric Measurement Techniques*, *13*(12), 6755–6769. https://doi.org/10.5194/amt-13-6755-2020

Huang, Y., Tan, X., & Xia, Y. (2016). Inhomogeneous radiative forcing of homogeneous greenhouse gases: Inhomogeneous Forcing of Homogeneous Gas. *Journal of Geophysical Research: Atmospheres*, *121*(6), 2780–2789. https://doi.org/10.1002/2015JD024569

Huang, Y., & Zhang, M. (2014). The implication of radiative forcing and feedback for meridional energy transport: RADIATIVE FORCING AND ENERGY TRANSPORT. *Geophysical Research Letters*, *41*(5), 1665–1672. https://doi.org/10.1002/2013GL059079

Intergovernmental Panel on Climate Change (Ed.). (2014). Clouds and Aerosols. In *Climate Change 2013 – The Physical Science Basis* (1st ed., pp. 571–658). Cambridge University Press. https://doi.org/10.1017/CBO9781107415324.016

Jacob, D. J., Turner, A. J., Maasakkers, J. D., Sheng, J., Sun, K., Liu, X., Chance, K., Aben, I., McKeever, J., & Frankenberg, C. (2016). Satellite observations of atmospheric methane and their value for quantifying methane emissions. *Atmospheric Chemistry and Physics*, *16*(22), 14371–14396. https://doi.org/10.5194/acp-16-14371-2016

Jacob, D. J., Varon, D. J., Cusworth, D. H., Dennison, P. E., Frankenberg, C., Gautam, R., Guanter, L., Kelley, J., McKeever, J., Ott, L. E., Poulter, B., Qu, Z., Thorpe, A. K., Worden, J. R., & Duren, R. M. (2022). *Quantifying methane emissions from the global scale down to point sources using satellite observations of atmospheric methane* [Preprint]. Gases/Remote Sensing/Troposphere/Chemistry (chemical composition and reactions). https://doi.org/10.5194/acp-2022-246

Jacobson, M. Z. (2001). Strong radiative heating due to the mixing state of black carbon in atmospheric aerosols. *Nature*, *409*(6821), 695–697. https://doi.org/10.1038/35055518

Jahani, B., Andersen, H., Calbó, J., González, J.-A., & Cermak, J. (2022). Longwave radiative effect of the cloud–aerosol transition zone based on CERES observations. *Atmospheric Chemistry and Physics*, *22*(2), 1483–1494. https://doi.org/10.5194/acp-22-1483-2022

Jervis, D., McKeever, J., Durak, B. O. A., Sloan, J. J., Gains, D., Varon, D. J., Ramier, A., Strupler, M., & Tarrant, E. (2021). The GHGSat-D imaging spectrometer. *Atmospheric Measurement Techniques*, *14*(3), 2127–2140. https://doi.org/10.5194/amt-14-2127-2021

Jimenez, J. L., Canagaratna, M. R., Donahue, N. M., Prevot, A. S. H., Zhang, Q., Kroll, J. H., DeCarlo, P. F., Allan, J. D., Coe, H., Ng, N. L., Aiken, A. C., Docherty, K. S., Ulbrich, I. M., Grieshop, A. P., Robinson, A. L., Duplissy, J., Smith, J. D., Wilson, K. R., Lanz, V. A., … Worsnop, D. R. (2009). Evolution of Organic Aerosols in the Atmosphere. *Science*, *326*(5959), 1525–1529. https://doi.org/10.1126/science.1180353

Johnson, B. T., Shine, K. P., & Forster, P. M. (2004). The semi-direct aerosol effect: Impact of absorbing aerosols on marine stratocumulus. *Quarterly Journal of the Royal Meteorological Society*, *130*(599), 1407–1422. https://doi.org/10.1256/qj.03.61

Kanakidou, M., Seinfeld, J. H., Pandis, S. N., Barnes, I., Dentener, F. J., Facchini, M. C., Dingenen, R. V., Ervens, B., Nenes, A., Nielsen, C. J., Swietlicki, E., Putaud, J. P., Balkanski, Y., Fuzzi, S., Horth, J., Moortgat, G. K., Winterhalter, R., Myhre, C. E. L., Tsigaridis, K., … Wilson, J. (2005). Organic aerosol and global climate modelling: A review. *Atmos. Chem. Phys.*

Kinne, S. (2019). The MACv2 aerosol climatology. *Tellus B: Chemical and Physical Meteorology*, *71*(1), 1–21. https://doi.org/10.1080/16000889.2019.1623639

Kloss, C., Sellitto, P., Renard, J.-B., Baron, A., Bègue, N., Legras, B., Berthet, G., Briaud, E., Carboni, E., Duchamp, C., Duflot, V., Jacquet, P., Marquestaut, N., Metzger, J.-M., Payen, G., Ranaivombola, M., Roberts, T., Siddans, R., & Jégou, F. (2022). Aerosol Characterization of the Stratospheric Plume From the Volcanic Eruption at Hunga Tonga

15 January 2022. *Geophysical Research Letters*, *49*(16), e2022GL099394. https://doi.org/10.1029/2022GL099394

Koch, D., Bond, T. C., Streets, D., Unger, N., & van der Werf, G. R. (2007). Global impacts of aerosols from particular source regions and sectors. *Journal of Geophysical Research: Atmospheres*, *112*(D2). https://doi.org/10.1029/2005JD007024

Koch, D., & Del Genio, A. D. (2010). Black carbon semi-direct effects on cloud cover: Review and synthesis. *Atmospheric Chemistry and Physics*, *10*(16), 7685–7696. https://doi.org/10.5194/acp-10-7685-2010

Koffi, B., Schulz, M., Bréon, F.-M., Dentener, F., Steensen, B. M., Griesfeller, J., Winker, D., Balkanski, Y., Bauer, S. E., Bellouin, N., Berntsen, T., Bian, H., Chin, M., Diehl, T., Easter, R., Ghan, S., Hauglustaine, D. A., Iversen, T., Kirkevåg, A., … Zhang, K. (2016). Evaluation of the aerosol vertical distribution in global aerosol models through comparison against CALIOP measurements: AeroCom phase II results. *Journal of Geophysical Research: Atmospheres*, *121*(12), 7254–7283. https://doi.org/10.1002/2015JD024639

Koren, I., Remer, L. A., Kaufman, Y. J., Rudich, Y., & Martins, J. V. (2007). On the twilight zone between clouds and aerosols. *Geophysical Research Letters*, *34*(8). https://doi.org/10.1029/2007GL029253

Korras-Carraca, M.-B., Gkikas, A., Matsoukas, C., & Hatzianastassiou, N. (2021). Global Clear-Sky Aerosol Speciated Direct Radiative Effects over 40 Years (1980–2019). *Atmosphere*, *12*(10), 1254. https://doi.org/10.3390/atmos12101254

Krasting, J. P., John, J. G., Blanton, C., McHugh, C., Nikonov, S., Radhakrishnan, A., Rand, K., Zadeh, N. T., Balaji, V., Durachta, J., Dupuis, C., Menzel, R., Robinson, T., Underwood, S., Vahlenkamp, H., Dunne, K. A., Gauthier, P. P., Ginoux, P., Griffies, S. M., … Zhao,

M. (2018). *NOAA-GFDL GFDL-ESM4 model output prepared for CMIP6 CMIP historical*. Earth System Grid Federation. https://doi.org/10.22033/ESGF/CMIP6.8597

Kremser, S., Thomason, L. W., von Hobe, M., Hermann, M., Deshler, T., Timmreck, C., Toohey, M., Stenke, A., Schwarz, J. P., Weigel, R., Fueglistaler, S., Prata, F. J., Vernier, J.-P., Schlager, H., Barnes, J. E., Antuña-Marrero, J.-C., Fairlie, D., Palm, M., Mahieu, E., … Meland, B. (2016). Stratospheric aerosol—Observations, processes, and impact on climate. *Reviews of Geophysics*, *54*(2), 278–335. https://doi.org/10.1002/2015RG000511

Kristiansen, N. I., Stohl, A., Oliviè, D. J. L., Croft, B., Søvde, O. A., Klein, H., Christoudias, T., Kunkel, D., Leadbetter, S. J., & Lee, Y. H. (2016). Evaluation of observed and modelled aerosol lifetimes using radioactive tracers of opportunity and an ensemble of 19 global models. *Atmospheric Chemistry and Physics*, *16*(5), 3525–3561.

Lapere, R., Thomas, J. L., Marelle, L., Ekman, A. M. L., Frey, M. M., Lund, M. T., Makkonen, R., Ranjithkumar, A., Salter, M. E., Samset, B. H., Schulz, M., Sogacheva, L., Yang, X., & Zieger, P. (2023). The Representation of Sea Salt Aerosols and Their Role in Polar Climate Within CMIP6. *Journal of Geophysical Research: Atmospheres*, *128*(6), e2022JD038235. https://doi.org/10.1029/2022JD038235

Lau, K. M., Kim, M. K., & Kim, K. M. (2006). Asian summer monsoon anomalies induced by aerosol direct forcing: the role of the Tibetan Plateau. *Climate dynamics*, 26, 855-864.

Lei, Y., Zhang, F., Miao, L., Yu, Q.-R., Duan, M., Fraedrich, K., & Yu, Z. (2020). Potential impacts of future reduced aerosols on internal dynamics characteristics of precipitation based on model simulations over southern China. *Physica A: Statistical Mechanics and Its Applications*, *545*, 123808.

Lejeune, Q., Davin, E. L., Guillod, B. P., & Seneviratne, S. I. (2015). Influence of Amazonian deforestation on the future evolution of regional surface fluxes, circulation, surface temperature and precipitation. *Climate Dynamics*, *44*(9), 2769–2786. https://doi.org/10.1007/s00382-014-2203-8

Lenoble, J., Tanre, D., Deschamps, P. Y., & Herman, M. (1982). A simple method to compute the change in earth-atmosphere radiative balance due to a stratospheric aerosol layer. *Journal of Atmospheric Sciences*, *39*(11), 2565–2576.

Lewis, E. R., & Schwartz, S. E. (2004). *Sea salt aerosol production: Mechanisms, methods, measurements, and models* (Vol. 152). American geophysical union.

Li, J., Carlson, B. E., Yung, Y. L., Lv, D., Hansen, J., Penner, J. E., Liao, H., Ramaswamy, V., Kahn, R. A., Zhang, P., Dubovik, O., Ding, A., Lacis, A. A., Zhang, L., & Dong, Y. (2022). Scattering and absorbing aerosols in the climate system. *Nature Reviews Earth & Environment*, *3*(6), Article 6. https://doi.org/10.1038/s43017-022-00296-7

Li, J., Min, Q., Peng, Y., Sun, Z., & Zhao, J.-Q. (2015). Accounting for dust aerosol size distribution in radiative transfer. *Journal of Geophysical Research: Atmospheres*, *120*(13), 6537–6550. https://doi.org/10.1002/2015JD023078

Li, Z., Lau, W. K.-M., Ramanathan, V., Wu, G., Ding, Y., Manoj, M. G., Liu, J., Qian, Y., Li, J., Zhou, T., Fan, J., Rosenfeld, D., Ming, Y., Wang, Y., Huang, J., Wang, B., Xu, X., Lee, S.-S., Cribb, M., … Brasseur, G. P. (2016). Aerosol and monsoon climate interactions over Asia. *Reviews of Geophysics*, *54*(4), 866–929. https://doi.org/10.1002/2015RG000500

Liu, C., Li, J., Yin, Y., Zhu, B., & Feng, Q. (2017). Optical properties of black carbon aggregates with non-absorptive coating. *Journal of Quantitative Spectroscopy and Radiative Transfer*, *187*, 443–452. https://doi.org/10.1016/j.jqsrt.2016.10.023

Liu, C.-C., Portmann, R. W., Liu, S., Rosenlof, K. H., Peng, Y., & Yu, P. (2022). Significant Effective Radiative Forcing of Stratospheric Wildfire Smoke. *Geophysical Research Letters*, *49*(17), e2022GL100175. https://doi.org/10.1029/2022GL100175

Liu, X., Penner, J. E., & Herzog, M. (2005). Global modeling of aerosol dynamics: Model description, evaluation, and interactions between sulfate and nonsulfate aerosols. *Journal of Geophysical Research: Atmospheres*, *110*(D18). https://doi.org/10.1029/2004JD005674

Loeb, N. G., Su, W., Bellouin, N., & Ming, Y. (2021). Changes in Clear-Sky Shortwave Aerosol Direct Radiative Effects Since 2002. *Journal of Geophysical Research: Atmospheres*, *126*(5). https://doi.org/10.1029/2020JD034090

Loeb, N. G., Wang, H., Rose, F. G., Kato, S., Smith, W. L., & Sun-Mack, S. (2019). Decomposing Shortwave Top-of-Atmosphere and Surface Radiative Flux Variations in Terms of Surface and Atmospheric Contributions. *Journal of Climate*, *32*(16), 5003–5019. https://doi.org/10.1175/JCLI-D-18-0826.1

Lorente, A., Borsdorff, T., Butz, A., Hasekamp, O., Schneider, A., Wu, L., Hase, F., Kivi, R., Wunch, D., & Pollard, D. F. (2021). Methane retrieved from TROPOMI: improvement of the data product and validation of the first 2 years of measurements. *Atmospheric Measurement Techniques*, *14*(1), 665–684.

Maasakkers, J. D., Varon, D. J., Elfarsdóttir, A., McKeever, J., Jervis, D., Mahapatra, G., Pandey, S., Lorente, A., Borsdorff, T., Foorthuis, L. R., Schuit, B. J., Tol, P., van Kempen, T. A., van Hees, R., & Aben, I. (2022). Using satellites to uncover large methane emissions from landfills. *Science Advances*, *8*(32), eabn9683. https://doi.org/10.1126/sciadv.abn9683

MacMartin, D. G., Kravitz, B., Tilmes, S., Richter, J. H., Mills, M. J., Lamarque, J.-F., Tribbia, J. J., & Vitt, F. (2017). The Climate Response to Stratospheric Aerosol Geoengineering Can

Be Tailored Using Multiple Injection Locations. *Journal of Geophysical Research: Atmospheres*, *122*(23), 12,574-12,590. https://doi.org/10.1002/2017JD026868

Mahowald, N., Albani, S., Kok, J. F., Engelstaeder, S., Scanza, R., Ward, D. S., & Flanner, M. G. (2014). The size distribution of desert dust aerosols and its impact on the Earth system. *Aeolian Research*, *15*, 53–71. https://doi.org/10.1016/j.aeolia.2013.09.002

Malinina, E., Rozanov, A., Rieger, L., Bourassa, A., Bovensmann, H., Burrows, J. P., & Degenstein, D. (2019). Stratospheric aerosol characteristics from space-borne observations: Extinction coefficient and Ångström exponent. *Atmospheric Measurement Techniques*, *12*(7), 3485–3502. https://doi.org/10.5194/amt-12-3485-2019

Marshall, L. R., Smith, C. J., Forster, P. M., Aubry, T. J., Andrews, T., & Schmidt, A. (2020). Large Variations in Volcanic Aerosol Forcing Efficiency Due to Eruption Source Parameters and Rapid Adjustments. *Geophysical Research Letters*, *47*(19), e2020GL090241. https://doi.org/10.1029/2020GL090241

Martinsson, B. G., Friberg, J., Sandvik, O. S., Hermann, M., van Velthoven, P. F. J., & Zahn, A. (2019). Formation and composition of the UTLS aerosol. *Npj Climate and Atmospheric Science*, *2*(1), 1–6. https://doi.org/10.1038/s41612-019-0097-1

McComiskey, A., Schwartz, S. E., Schmid, B., Guan, H., Lewis, E. R., Ricchiazzi, P., & Ogren, J. A. (2008). Direct aerosol forcing: Calculation from observables and sensitivities to inputs. *Journal of Geophysical Research*, *113*(D9), D09202. https://doi.org/10.1029/2007JD009170

McConnell, J. R., Edwards, R., Kok, G. L., Flanner, M. G., Zender, C. S., Saltzman, E. S., Banta, J. R., Pasteris, D. R., Carter, M. M., & Kahl, J. D. W. (2007). 20th-Century Industrial Black

Carbon Emissions Altered Arctic Climate Forcing. *Science*, *317*(5843), 1381–1384. https://doi.org/10.1126/science.1144856

Merlis, T. M. (2015). Direct weakening of tropical circulations from masked CO2 radiative forcing. *Proceedings of the National Academy of Sciences*, *112*(43), 13167–13171. https://doi.org/10.1073/pnas.1508268112

Mishchenko, M. I., Travis, L. D., & Mackowski, D. W. (1996). T-matrix computations of light scattering by nonspherical particles: A review. *Journal of Quantitative Spectroscopy and Radiative Transfer*, *55*(5), 535-575.

Mishchenko, M. I. (2009). Electromagnetic scattering by nonspherical particles: A tutorial review. *Journal of Quantitative Spectroscopy and Radiative Transfer*, *110*(11), 808–832.

Mlawer, E. J., Iacono, M. J., Pincus, R., Barker, H. W., Oreopoulos, L., & Mitchell, D. L. (2016). Contributions of the ARM Program to Radiative Transfer Modeling for Climate and Weather Applications. *Meteorological Monographs*, *57*(1), 15.1-15.19. https://doi.org/10.1175/AMSMONOGRAPHS-D-15-0041.1

Mlawer, E. J., Taubman, S. J., Brown, P. D., Iacono, M. J., & Clough, S. A. (1997). Radiative transfer for inhomogeneous atmospheres: RRTM, a validated correlated-k model for the longwave. *Journal of Geophysical Research: Atmospheres*, *102*(D14), 16663–16682. https://doi.org/10.1029/97JD00237

Molina, M. J., Tso, T.-L., Molina, L. T., & Wang, F. C.-Y. (1987). Antarctic stratospheric chemistry of chlorine nitrate, hydrogen chloride, and ice: Release of active chlorine. *Science*, *238*(4831), 1253–1257.

Murphy, D. M., Anderson, J. R., Quinn, P. K., McInnes, L. M., Brechtel, F. J., Kreidenweis, S. M., Middlebrook, A. M., Pósfai, M., Thomson, D. S., & Buseck, P. R. (1998). Influence of sea-

salt on aerosol radiative properties in the Southern Ocean marine boundary layer. *Nature*, *392*(6671), 62–65.

Myhre, G., Samset, B. H., Mohr, C. W., Alterskjær, K., Balkanski, Y., Bellouin, N., Chin, M., Haywood, J., Hodnebrog, Ø., Kinne, S., Lin, G., Lund, M. T., Penner, J. E., Schulz, M., Schutgens, N., Skeie, R. B., Stier, P., Takemura, T., & Zhang, K. (2020). Cloudy-sky contributions to the direct aerosol effect. *Atmospheric Chemistry and Physics*, *20*(14), 8855–8865. https://doi.org/10.5194/acp-20-8855-2020

Myhre, G., Samset, B. H., Schulz, M., Balkanski, Y., Bauer, S., Berntsen, T. K., Bian, H., Bellouin, N., Chin, M., Diehl, T., Easter, R. C., Feichter, J., Ghan, S. J., Hauglustaine, D., Iversen, T., Kinne, S., Kirkevåg, A., Lamarque, J.-F., Lin, G., … Zhou, C. (2013). Radiative forcing of the direct aerosol effect from AeroCom Phase II simulations. *Atmospheric Chemistry and Physics*, *13*(4), 1853–1877. https://doi.org/10.5194/acp-13-1853-2013

Neubauer, D., Ferrachat, S., Siegenthaler-Le Drian, C., Stoll, J., Folini, D. S., Tegen, I., Wieners, K.-H., Mauritsen, T., Stemmler, I., Barthel, S., Bey, I., Daskalakis, N., Heinold, B., Kokkola, H., Partridge, D., Rast, S., Schmidt, H., Schutgens, N., Stanelle, T., … Lohmann, U. (2019). *HAMMOZ-Consortium MPI-ESM1.2-HAM model output prepared for CMIP6 AerChemMIP*. Earth System Grid Federation. https://doi.org/10.22033/ESGF/CMIP6.1621

Ohneiser, K., Ansmann, A., Baars, H., Seifert, P., Barja, B., Jimenez, C., Radenz, M., Teisseire, A., Floutsi, A., Haarig, M., Foth, A., Chudnovsky, A., Engelmann, R., Zamorano, F., Bühl, J., & Wandinger, U. (2020). Smoke of extreme Australian bushfires observed in the stratosphere over Punta Arenas, Chile, in January 2020: Optical thickness, lidar ratios, and

depolarization ratios at 355 and 532 nm. *Atmospheric Chemistry and Physics*, *20*(13), 8003–8015. https://doi.org/10.5194/acp-20-8003-2020

Ohneiser, K., Ansmann, A., Witthuhn, J., Deneke, H., Chudnovsky, A., Walter, G., & Senf, F. (2023). Self-lofting of wildfire smoke in the troposphere and stratosphere: Simulations and space lidar observations. *Atmospheric Chemistry and Physics*, *23*(4), 2901–2925. https://doi.org/10.5194/acp-23-2901-2023

Parker, R. J., Webb, A., Boesch, H., Somkuti, P., Barrio Guillo, R., Di Noia, A., Kalaitzi, N., Anand, J. S., Bergamaschi, P., Chevallier, F., Palmer, P. I., Feng, L., Deutscher, N. M., Feist, D. G., Griffith, D. W. T., Hase, F., Kivi, R., Morino, I., Notholt, J., … Wunch, D. (2020). A decade of GOSAT Proxy satellite CH₄ observations. *Earth System Science Data*, *12*(4), 3383–3412. https://doi.org/10.5194/essd-12-3383-2020

Peters, K., Quaas, J., & Bellouin, N. (2011). Effects of absorbing aerosols in cloudy skies: A satellite study over the Atlantic Ocean. *Atmospheric Chemistry and Physics*, *11*(4), 1393–1404. https://doi.org/10.5194/acp-11-1393-2011

Pistone, K., Eisenman, I., & Ramanathan, V. (2014). Observational determination of albedo decrease caused by vanishing Arctic sea ice. *Proceedings of the National Academy of Sciences*, *111*(9), 3322–3326. https://doi.org/10.1073/pnas.1318201111

Pörtner, H. O., Roberts, D. C., Adams, H., Adler, C., Aldunce, P., Ali, E., Begum, R. A., Betts, R., Kerr, R. B., & Biesbroek, R. (2022). *Climate change 2022: Impacts, adaptation and vulnerability*.

Pósfai, M., & Buseck, P. R. (2010). Nature and Climate Effects of Individual Tropospheric Aerosol Particles. *Annual Review of Earth and Planetary Sciences*, *38*(1), 17–43. https://doi.org/10.1146/annurev.earth.031208.100032

Quaas, J., Andrews, T., Bellouin, N., Block, K., Boucher, O., Ceppi, P., Dagan, G., Doktorowski, S., Eichholz, H. M., Forster, P., Goren, T., Gryspeerdt, E., Hodnebrog, Ø., Jia, H., Kramer, R., Lange, C., Maycock, A. C., Mülmenstädt, J., Myhre, G., … Wall, C. J. (2024). *Adjustments to climate perturbations -mechanisms, implications, observational constraints*. https://doi.org/10.22541/essoar.172132456.65321288/v1

Quaas, J., Boucher, O., Bellouin, N., & Kinne, S. (2008). Satellite-based estimate of the direct and indirect aerosol climate forcing: SATELLITE-ESTIMATE OF AEROSOL FORCINGS. *Journal of Geophysical Research: Atmospheres*, *113*(D5), n/a-n/a. https://doi.org/10.1029/2007JD008962

Raes, F., Dingenen, R. V., Vignati, E., Wilson, J., Putaud, J.-P., Seinfeld, J. H., & Adams, P. (2000). Formation and cycling of aerosols in the global troposphere. *Atmospheric Environment*.

Ramanathan, V., & Carmichael, G. (2008). Global and regional climate changes due to black carbon. *Nature Geoscience*, *1*(4), 221–227. https://doi.org/10.1038/ngeo156

Randles, C. A., Kinne, S., Myhre, G., Schulz, M., Stier, P., Fischer, J., Doppler, L., Highwood, E., Ryder, C., Harris, B., Huttunen, J., Ma, Y., Pinker, R. T., Mayer, B., Neubauer, D., Hitzenberger, R., Oreopoulos, L., Lee, D., Pitari, G., … Lu, P. (2013). Intercomparison of shortwave radiative transfer schemes in global aerosol modeling: Results from the AeroCom Radiative Transfer Experiment. *Atmospheric Chemistry and Physics*, *13*(5), 2347–2379. https://doi.org/10.5194/acp-13-2347-2013

Randles, C. A., Silva, A. M. da, Buchard, V., Colarco, P. R., Darmenov, A., Govindaraju, R., Smirnov, A., Holben, B., Ferrare, R., Hair, J., Shinozuka, Y., & Flynn, C. J. (2017). The MERRA-2 Aerosol Reanalysis, 1980 Onward. Part I: System Description and Data

Assimilation Evaluation. *Journal of Climate*, *30*(17), 6823–6850. https://doi.org/10.1175/JCLI-D-16-0609.1

Rauber, M., Salazar, G., Yttri, K. E., & Szidat, S. (2023). An optimised organic carbon / elemental carbon (OC / EC) fraction separation method for radiocarbon source apportionment applied to low-loaded Arctic aerosol filters. *Atmospheric Measurement Techniques*, *16*(3), 825–844. https://doi.org/10.5194/amt-16-825-2023

Reddy, M. S., Boucher, O., Balkanski, Y., & Schulz, M. (2005). Aerosol optical depths and direct radiative perturbations by species and source type. *Geophysical Research Letters*, *32*(12). https://doi.org/10.1029/2004GL021743

Redemann, J., Wood, R., Zuidema, P., Doherty, S. J., Luna, B., LeBlanc, S. E., Diamond, M. S., Shinozuka, Y., Chang, I. Y., & Ueyama, R. (2021). An overview of the ORACLES (ObseRvations of Aerosols above CLouds and their intEractionS) project: Aerosol–cloud–radiation interactions in the southeast Atlantic basin. *Atmospheric Chemistry and Physics*, *21*(3), 1507–1563.

Regayre, L. A., Johnson, J. S., Yoshioka, M., Pringle, K. J., Sexton, D. M. H., Booth, B. B. B., Lee, L. A., Bellouin, N., & Carslaw, K. S. (2018). Aerosol and physical atmosphere model parameters are both important sources of uncertainty in aerosol ERF. *Atmospheric Chemistry and Physics*, *18*(13), 9975–10006. https://doi.org/10.5194/acp-18-9975-2018

Ridley, J., Menary, M., Kuhlbrodt, T., Andrews, M., & Andrews, T. (2019). *MOHC HadGEM3-GC31-LL model output prepared for CMIP6 CMIP historical*. Earth System Grid Federation. https://doi.org/10.22033/ESGF/CMIP6.6109

Robock, A. (2000). Volcanic eruptions and climate. *Reviews of Geophysics*, *38*(2), 191–219.

Sanghavi, S., Nelson, R., Frankenberg, C., & Gunson, M. (2020). Aerosols in OCO-2/GOSAT retrievals of XCO2: An information content and error analysis. *Remote Sensing of Environment*, *251*, 112053. https://doi.org/10.1016/j.rse.2020.112053

Schepanski, K. (2018). Transport of mineral dust and its impact on climate. *Geosciences*, *8*(5), 151.

Schmale, J., Zieger, P., & Ekman, A. M. L. (2021). Aerosols in current and future Arctic climate. *Nature Climate Change*, *11*(2), 95–105. https://doi.org/10.1038/s41558-020-00969-5

Schmidt, A., Carslaw, K. S., Mann, G. W., Rap, A., Pringle, K. J., Spracklen, D. V., Wilson, M., & Forster, P. M. (2012). Importance of tropospheric volcanic aerosol for indirect radiative forcing of climate. *Atmospheric Chemistry and Physics*, *12*(16), 7321–7339. https://doi.org/10.5194/acp-12-7321-2012

Schoeberl, M. R., Wang, Y., Taha, G., Zawada, D. J., Ueyama, R., & Dessler, A. (2024a). Evolution of the Climate Forcing During the Two Years After the Hunga Tonga-Hunga Ha'apai Eruption. *Journal of Geophysical Research: Atmospheres*, *129*(14), e2024JD041296. https://doi.org/10.1029/2024JD041296

Schoeberl, M. R., Wang, Y., Taha, G., Zawada, D. J., Ueyama, R., & Dessler, A. E. (2024b). *Evolution of the Climate Forcing During the Two Years after the Hunga Tonga-Hunga Ha'apai Eruption*. https://doi.org/10.22541/essoar.171288896.63010190/v1

Schoeberl, M. R., Wang, Y., Ueyama, R., Dessler, A., Taha, G., & Yu, W. (2023). The Estimated Climate Impact of the Hunga Tonga-Hunga Ha'apai Eruption Plume. *Geophysical Research Letters*, *50*(18), e2023GL104634. https://doi.org/10.1029/2023GL104634

Schuster, G. L., Dubovik, O., & Holben, B. N. (2006). Angstrom exponent and bimodal aerosol size distributions. *Journal of Geophysical Research: Atmospheres*, *111*(D7). https://doi.org/10.1029/2005JD006328

Seferian, R. (2018). *CNRM-CERFACS CNRM-ESM2-1 model output prepared for CMIP6 CMIP historical*. Earth System Grid Federation. https://doi.org/10.22033/ESGF/CMIP6.4068

Séférian, R., Nabat, P., Michou, M., Saint-Martin, D., Voldoire, A., Colin, J., Decharme, B., Delire, C., Berthet, S., Chevallier, M., Sénési, S., Franchisteguy, L., Vial, J., Mallet, M., Joetzjer, E., Geoffroy, O., Guérémy, J.-F., Moine, M.-P., Msadek, R., … Madec, G. (2019). Evaluation of CNRM Earth System Model, CNRM-ESM2-1: Role of Earth System Processes in Present-Day and Future Climate. *Journal of Advances in Modeling Earth Systems*, *11*(12), 4182–4227. https://doi.org/10.1029/2019MS001791

Seidel, F. C., & Popp, C. (2012). Critical surface albedo and its implications to aerosol remote sensing. *Atmospheric Measurement Techniques*, *5*(7), 1653–1665. https://doi.org/10.5194/amt-5-1653-2012

Seinfeld, J. H., & Pandis, S. N. (2016). *Atmospheric chemistry and physics: From air pollution to climate change*. John Wiley & Sons.

Sellar, A. A., Walton, J., Jones, C. G., Wood, R., Abraham, N. L., Andrejczuk, M., Andrews, M. B., Andrews, T., Archibald, A. T., de Mora, L., Dyson, H., Elkington, M., Ellis, R., Florek, P., Good, P., Gohar, L., Haddad, S., Hardiman, S. C., Hogan, E., … Griffiths, P. T. (2020). Implementation of U.K. Earth System Models for CMIP6. *Journal of Advances in Modeling Earth Systems*, *12*(4), e2019MS001946. https://doi.org/10.1029/2019MS001946

Sellitto, P., Belhadji, R., Kloss, C., & Legras, B. (2022). Radiative impacts of the Australian bushfires 2019–2020 – Part 1: Large-scale radiative forcing. *Atmospheric Chemistry and Physics*, *22*(14), 9299–9311. https://doi.org/10.5194/acp-22-9299-2022

Sellitto, P., Belhadji, R., Legras, B., Podglajen, A., & Duchamp, C. (2024). *The optical properties of stratospheric aerosol layer perturbation of the Hunga volcano eruption of January 15th, 2022*. https://doi.org/10.5194/egusphere-2024-1433

Sfîcă, L., Beck, C., Nita, A.-I., Voiculescu, M., Birsan, M.-V., & Philipp, A. (2021). Cloud cover changes driven by atmospheric circulation in Europe during the last decades. *International Journal of Climatology*, *41*(S1), E2211–E2230. https://doi.org/10.1002/joc.6841

Siegel, A. F. (2016). Chapter 12 - Multiple Regression: Predicting One Variable From Several Others. In A. F. Siegel (Ed.), *Practical Business Statistics (Seventh Edition)* (pp. 355–418). Academic Press. https://doi.org/10.1016/B978-0-12-804250-2.00012-2

Smith, C. J., Kramer, R. J., Myhre, G., Forster, P. M., Soden, B. J., Andrews, T., Boucher, O., Faluvegi, G., Fläschner, D., Hodnebrog, Ø., Kasoar, M., Kharin, V., Kirkevåg, A., Lamarque, J.-F., Mülmenstädt, J., Olivié, D., Richardson, T., Samset, B. H., Shindell, D., … Watson-Parris, D. (2018). Understanding Rapid Adjustments to Diverse Forcing Agents. *Geophysical Research Letters*, *45*(21), 12,023-12,031. https://doi.org/10.1029/2018GL079826

Smith, D. M., Booth, B. B. B., Dunstone, N. J., Eade, R., Hermanson, L., Jones, G. S., Scaife, A. A., Sheen, K. L., & Thompson, V. (2016). Role of volcanic and anthropogenic aerosols in the recent global surface warming slowdown. *Nature Climate Change*, *6*(10), 936–940. https://doi.org/10.1038/nclimate3058

Sokolik, I., Andronova, A., & Johnson, T. C. (1993). Complex refractive index of atmospheric dust aerosols. *Atmospheric Environment. Part A. General Topics*, *27*(16), 2495-2502.

Solomon, S., Daniel, J. S., Neely, R. R., Vernier, J.-P., Dutton, E. G., & Thomason, L. W. (2011). The Persistently Variable "Background" Stratospheric Aerosol Layer and Global Climate Change. *Science*, *333*(6044), 866–870. https://doi.org/10.1126/science.1206027

Stamnes, K., Tsay, S.-C., Wiscombe, W., & Jayaweera, K. (1988). Numerically stable algorithm for discrete-ordinate-method radiative transfer in multiple scattering and emitting layered media. *Applied Optics*, *27*(12), 2502–2509. https://doi.org/10.1364/AO.27.002502

Stephens, G. L., O'Brien, D., Webster, P. J., Pilewski, P., Kato, S., & Li, J. (2015). The albedo of Earth. *Reviews of Geophysics*, *53*(1), 141–163. https://doi.org/10.1002/2014RG000449

Stevens, B., Giorgetta, M., Esch, M., Mauritsen, T., Crueger, T., Rast, S., Salzmann, M., Schmidt, H., Bader, J., Block, K., Brokopf, R., Fast, I., Kinne, S., Kornblueh, L., Lohmann, U., Pincus, R., Reichler, T., & Roeckner, E. (2013). Atmospheric component of the MPI-M Earth System Model: ECHAM6. *Journal of Advances in Modeling Earth Systems*, *5*(2), 146–172. https://doi.org/10.1002/jame.20015

Stier, P., Schutgens, N. a. J., Bellouin, N., Bian, H., Boucher, O., Chin, M., Ghan, S., Huneeus, N., Kinne, S., Lin, G., Ma, X., Myhre, G., Penner, J. E., Randles, C. A., Samset, B., Schulz, M., Takemura, T., Yu, F., Yu, H., & Zhou, C. (2013). Host model uncertainties in aerosol radiative forcing estimates: Results from the AeroCom Prescribed intercomparison study. *Atmospheric Chemistry and Physics*, *13*(6), 3245–3270. https://doi.org/10.5194/acp-13-3245-2013

Stjern, C. W., Samset, B. H., Myhre, G., Forster, P. M., Hodnebrog, Ø., Andrews, T., Boucher, O., Faluvegi, G., Iversen, T., Kasoar, M., Kharin, V., Kirkevåg, A., Lamarque, J.-F., Olivié,

D., Richardson, T., Shawki, D., Shindell, D., Smith, C. J., Takemura, T., & Voulgarakis, A. (2017). Rapid Adjustments Cause Weak Surface Temperature Response to Increased Black Carbon Concentrations. *Journal of Geophysical Research: Atmospheres*, *122*(21), 11,462-11,481. https://doi.org/10.1002/2017JD027326

Stocker, T. (Ed.). (2014). *Climate change 2013: the physical science basis: Working Group I contribution to the Fifth assessment report of the Intergovernmental Panel on Climate Change*. Cambridge university press.

Storelvmo, T. (2017). Aerosol Effects on Climate via Mixed-Phase and Ice Clouds. *Annual Review of Earth and Planetary Sciences*, *45*(Volume 45, 2017), 199–222. https://doi.org/10.1146/annurev-earth-060115-012240

Strahan, S. E., Oman, L. D., Douglass, A. R., & Coy, L. (2015). Modulation of Antarctic vortex composition by the quasi-biennial oscillation. *Geophysical Research Letters*, *42*(10), 4216–4223. https://doi.org/10.1002/2015GL063759

Streets, D. G., Wu, Y., & Chin, M. (2006). Two-decadal aerosol trends as a likely explanation of the global dimming/brightening transition. *Geophysical Research Letters*, *33*(15). https://doi.org/10.1029/2006GL026471

Su, T., Li, Z., Zheng, Y., Wu, T., Wu, H., & Guo, J. (2022). Aerosol-boundary layer interaction modulated entrainment process. *NPJ Climate and Atmospheric Science*, *5*(1), 64.

Su, W., Liang, L., Myhre, G., Thorsen, T. J., Loeb, N. G., Schuster, G. L., Ginoux, P., Paulot, F., Neubauer, D., Checa-Garcia, R., Matsui, H., Tsigaridis, K., Skeie, R. B., Takemura, T., Bauer, S. E., & Schulz, M. (2021). Understanding Top-of-Atmosphere Flux Bias in the AeroCom Phase III Models: A Clear-Sky Perspective. *Journal of Advances in Modeling Earth Systems*, *13*(9), e2021MS002584. https://doi.org/10.1029/2021MS002584

Su, W., Loeb, N. G., Schuster, G. L., Chin, M., & Rose, F. G. (2013). Global all-sky shortwave direct radiative forcing of anthropogenic aerosols from combined satellite observations and GOCART simulations. *Journal of Geophysical Research: Atmospheres*, *118*(2), 655–669. https://doi.org/10.1029/2012JD018294

Taha, G., Loughman, R., Colarco, P. R., Zhu, T., Thomason, L. W., & Jaross, G. (2022). Tracking the 2022 Hunga Tonga-Hunga Ha'apai Aerosol Cloud in the Upper and Middle Stratosphere Using Space-Based Observations. *Geophysical Research Letters*, *49*(19), e2022GL100091. https://doi.org/10.1029/2022GL100091

Taha, G., Loughman, R., Zhu, T., Thomason, L., Kar, J., Rieger, L., & Bourassa, A. (2021). OMPS LP Version 2.0 multi-wavelength aerosol extinction coefficient retrieval algorithm. *Atmospheric Measurement Techniques*, *14*(2), 1015–1036. https://doi.org/10.5194/amt-14-1015-2021

Takemura, T., Nakajima, T., Dubovik, O., Holben, B. N., & Kinne, S. (2002). Single-scattering albedo and radiative forcing of various aerosol species with a global three-dimensional model. *Journal of Climate*, *15*(4), 333–352.

Tegen, I., & Lacis, A. A. (1996). Modeling of particle size distribution and its influence on the radiative properties of mineral dust aerosol. *Journal of Geophysical Research: Atmospheres*, *101*(D14), 19237–19244. https://doi.org/10.1029/95JD03610

Thompson, S. N., van Diedenhoven, B., Colarco, P. R., Castellanos, P., Lian, E., & Martins, J. V. (2022). Analysis of Scattering Angle Sampling by Multi-Angle Imaging Polarimeters for Different Orbit Geometries. *Frontiers in Remote Sensing*, *3*. https://www.frontiersin.org/articles/10.3389/frsen.2022.836262

Thorsen, T. J., Ferrare, R. A., Kato, S., & Winker, D. M. (2020). Aerosol Direct Radiative Effect Sensitivity Analysis. *Journal of Climate*, *33*(14), 6119–6139. https://doi.org/10.1175/JCLI-D-19-0669.1

Thorsen, T. J., Winker, D. M., & Ferrare, R. A. (2021). Uncertainty in Observational Estimates of the Aerosol Direct Radiative Effect and Forcing. *Journal of Climate*, *34*(1), 195–214. https://doi.org/10.1175/JCLI-D-19-1009.1

Tomasi, C., & Lupi, A. (2017). Primary and secondary sources of atmospheric aerosol. *Atmospheric Aerosols: Life Cycles and Effects on Air Quality and Climate*, 1–86.

Toublanc, D. (1996). Henyey–Greenstein and Mie phase functions in Monte Carlo radiative transfer computations. *Applied Optics*, *35*(18), 3270–3274. https://doi.org/10.1364/AO.35.003270

Twomey, S. (1977). The influence of pollution on the shortwave albedo of clouds. *Journal of the Atmospheric Sciences*, *34*(7), 1149–1152.

Tzanis, C., & Varotsos, C. A. (2008). Tropospheric aerosol forcing of climate: A case study for the greater area of Greece. *International Journal of Remote Sensing*, *29*(9), 2507–2517. Scopus. https://doi.org/10.1080/01431160701767575

Varon, D. J., McKeever, J., Jervis, D., Maasakkers, J. D., Pandey, S., Houweling, S., Aben, I., Scarpelli, T., & Jacob, D. J. (2019). Satellite Discovery of Anomalously Large Methane Point Sources From Oil/Gas Production. *Geophysical Research Letters*, *46*(22), 13507–13516. https://doi.org/10.1029/2019GL083798

Visioni, D., MacMartin, D. G., Kravitz, B., Lee, W., Simpson, I. R., & Richter, J. H. (2020). Reduced Poleward Transport Due to Stratospheric Heating Under Stratospheric Aerosols

Geoengineering. *Geophysical Research Letters*, *47*(17), e2020GL089470. https://doi.org/10.1029/2020GL089470

Voldoire, A., Sanchez-Gomez, E., Salas y Mélia, D., Decharme, B., Cassou, C., Sénési, S., Valcke, S., Beau, I., Alias, A., Chevallier, M., Déqué, M., Deshayes, J., Douville, H., Fernandez, E., Madec, G., Maisonnave, E., Moine, M.-P., Planton, S., Saint-Martin, D., … Chauvin, F. (2013). The CNRM-CM5.1 global climate model: Description and basic evaluation. *Climate Dynamics*, *40*(9), 2091–2121. https://doi.org/10.1007/s00382-011-1259-y

Volkamer, R., Jimenez, J. L., San Martini, F., Dzepina, K., Zhang, Q., Salcedo, D., Molina, L. T., Worsnop, D. R., & Molina, M. J. (2006). Secondary organic aerosol formation from anthropogenic air pollution: Rapid and higher than expected. *Geophysical Research Letters*, *33*(17). https://doi.org/10.1029/2006GL026899

Wang, C. (2013). Impact of anthropogenic absorbing aerosols on clouds and precipitation: A review of recent progresses. *Atmospheric Research*, *122*, 237–249. https://doi.org/10.1016/j.atmosres.2012.11.005

Wang, C., Yang, P., Platnick, S., Heidinger, A. K., Baum, B. A., Greenwald, T., Zhang, Z., & Holz, R. E. (2013). Retrieval of Ice Cloud Properties from AIRS and MODIS Observations Based on a Fast High-Spectral-Resolution Radiative Transfer Model. *Journal of Applied Meteorology and Climatology*, *52*(3), 710–726. https://doi.org/10.1175/JAMC-D-12-020.1

Wang, H., Xie, S.-P., & Liu, Q. (2016). Comparison of Climate Response to Anthropogenic Aerosol versus Greenhouse Gas Forcing: Distinct Patterns. *Journal of Climate*, *29*(14), 5175–5188. https://doi.org/10.1175/JCLI-D-16-0106.1

Wang, H., Xie, S.-P., Tokinaga, H., Liu, Q., & Kosaka, Y. (2016). Detecting cross-equatorial wind change as a fingerprint of climate response to anthropogenic aerosol forcing. *Geophysical Research Letters*, *43*(7), 3444–3450. https://doi.org/10.1002/2016GL068521

Wang, X., Randel, W., Zhu, Y., Tilmes, S., Starr, J., Yu, W., Garcia, R., Toon, O. B., Park, M., Kinnison, D., Zhang, J., Bourassa, A., Rieger, L., Warnock, T., & Li, J. (2023). Stratospheric Climate Anomalies and Ozone Loss Caused by the Hunga Tonga-Hunga Ha'apai Volcanic Eruption. *Journal of Geophysical Research: Atmospheres*, *128*(22), e2023JD039480. https://doi.org/10.1029/2023JD039480

Weisenstein, D. K., Keith, D. W., & Dykema, J. A. (2015). Solar geoengineering using solid aerosol in the stratosphere. *Atmospheric Chemistry and Physics*, *15*(20), 11835–11859. https://doi.org/10.5194/acp-15-11835-2015

Wild, M. (2009). Global dimming and brightening: A review. *Journal of Geophysical Research: Atmospheres*, *114*(D10). https://doi.org/10.1029/2008JD011470

Williams, A. I. L., Stier, P., Dagan, G., & Watson-Parris, D. (2022). Strong control of effective radiative forcing by the spatial pattern of absorbing aerosol. *Nature Climate Change*, *12*(8), 735–742. https://doi.org/10.1038/s41558-022-01415-4

Willis, M. D., Leaitch, W. R., & Abbatt, J. P. D. (2018). Processes Controlling the Composition and Abundance of Arctic Aerosol. *Reviews of Geophysics*, *56*(4), 621–671. https://doi.org/10.1029/2018RG000602

Winker, D. M., Vaughan, M. A., Omar, A., Hu, Y., Powell, K. A., Liu, Z., Hunt, W. H., & Young, S. A. (2009). Overview of the CALIPSO mission and CALIOP data processing algorithms. *Journal of Atmospheric and Oceanic Technology*, *26*(11), 2310–2323.

Wiscombe, W. J., & Grams, G. W. (1976). The backscattered fraction in two-stream approximations. *Journal of the Atmospheric Sciences*, *33*(12), 2440-2451.

Wu, C.-H., Lee, S.-Y., Tsai, I.-C., Shiu, C.-J., & Chen, Y.-Y. (2023). Volcanic contribution to the 1990s North Pacific climate shift in winter. *Scientific Reports*, *13*(1), 5672. https://doi.org/10.1038/s41598-023-32956-z

Wu, X., Balmes, K. A., & Fu, Q. (2021). Aerosol Direct Radiative Effects at the ARM SGP and TWP Sites: Clear Skies. *Journal of Geophysical Research: Atmospheres*, *126*(5), e2020JD033663. https://doi.org/10.1029/2020JD033663

Yang, C. K., Chiu, J. C., Marshak, A., Feingold, G., Várnai, T., Wen, G., Yamaguchi, T., & Jan van Leeuwen, P. (2022). Near-Cloud Aerosol Retrieval Using Machine Learning Techniques, and Implied Direct Radiative Effects. *Geophysical Research Letters*, *49*(20), e2022GL098274. https://doi.org/10.1029/2022GL098274

Yang, J., Sakhvidi, M. J. Z., de Hoogh, K., Vienneau, D., Siemiatyck, J., Zins, M., Goldberg, M., Chen, J., Lequy, E., & Jacquemin, B. (2021). Long-term exposure to black carbon and mortality: A 28-year follow-up of the GAZEL cohort. *Environment International*, *157*, 106805. https://doi.org/10.1016/j.envint.2021.106805

Yau, M. K., & Rogers, R. R. (1996). *A short course in cloud physics*. Elsevier.

Yoon, J., Chang, D. Y., Lelieveld, J., Pozzer, A., Kim, J., & Yum, S. S. (2019). Empirical evidence of a positive climate forcing of aerosols at elevated albedo. *Atmospheric Research*, *229*, 269–279. https://doi.org/10.1016/j.atmosres.2019.07.001

Yoshimori, M., & Broccoli, A. J. (2008). Equilibrium response of an atmosphere–mixed layer ocean model to different radiative forcing agents: Global and zonal mean response. *Journal of Climate*, *21*(17), 4399–4423.

Yu, H., Kaufman, Y. J., Chin, M., Feingold, G., Remer, L. A., Anderson, T. L., Balkanski, Y., Bellouin, N., Boucher, O., Christopher, S., DeCola, P., Kahn, R., Koch, D., Loeb, N., Reddy, M. S., Schulz, M., Takemura, T., & Zhou, M. (2006). A review of measurement-based assessments of the aerosol direct radiative effect and forcing. *Atmospheric Chemistry and Physics*, *6*(3), 613–666. https://doi.org/10.5194/acp-6-613-2006

Yu, P., Portmann, R. W., Peng, Y., Liu, C.-C., Zhu, Y., Asher, E., Bai, Z., Lu, Y., Bian, J., Mills, M., Schmidt, A., Rosenlof, K. H., & Toon, O. B. (2023). Radiative Forcing From the 2014–2022 Volcanic and Wildfire Injections. *Geophysical Research Letters*, *50*(13), e2023GL103791. https://doi.org/10.1029/2023GL103791

Yu, P., Toon, O. B., Bardeen, C. G., Zhu, Y., Rosenlof, K. H., Portmann, R. W., Thornberry, T. D., Gao, R.-S., Davis, S. M., & Wolf, E. T. (2019). Black carbon lofts wildfire smoke high into the stratosphere to form a persistent plume. *Science*, *365*(6453), 587–590.

Yu, Q., & Huang, Y. (2023a). A Dissection of the Inter-Model Spread of the Aerosol Direct Radiative Effect in CMIP6 Models. *Geophysical Research Letters*, *50*(21), e2023GL105112. https://doi.org/10.1029/2023GL105112

Yu, Q., & Huang, Y. (2023b). Distributions and Trends of the Aerosol Direct Radiative Effect in the 21st Century: Aerosol and Environmental Contributions. *Journal of Geophysical Research: Atmospheres*, *128*(4). https://doi.org/10.1029/2022JD037716

Yu, Q., Jervis, D., & Huang, Y. (2024). Accounting for the effect of aerosols in GHGSat methane retrieval. *Atmospheric Measurement Techniques*, *17*(11), 3347–3366. https://doi.org/10.5194/amt-17-3347-2024

Yu, Q.-R., Zhang, F., Li, J., & Zhang, J. (2019). Analysis of sea-salt aerosol size distributions in radiative transfer. *Journal of Aerosol Science*, *129*, 71–86. https://doi.org/10.1016/j.jaerosci.2018.11.014

Yukimoto, S., Kawai, H., Koshiro, T., Oshima, N., Yoshida, K., Urakawa, S., Tsujino, H., Deushi, M., Tanaka, T., Hosaka, M., Yabu, S., Yoshimura, H., Shindo, E., Mizuta, R., Obata, A., Adachi, Y., & Ishii, M. (2019). The Meteorological Research Institute Earth System Model Version 2.0, MRI-ESM2.0: Description and Basic Evaluation of the Physical Component. *Journal of the Meteorological Society of Japan. Ser. II*, *97*(5), 931–965. https://doi.org/10.2151/jmsj.2019-051

Zanchettin, D., Timmreck, C., Khodri, M., Schmidt, A., Toohey, M., Abe, M., Bekki, S., Cole, J., Fang, S.-W., Feng, W., Hegerl, G., Johnson, B., Lebas, N., LeGrande, A. N., Mann, G. W., Marshall, L., Rieger, L., Robock, A., Rubinetti, S., … Weierbach, H. (2022). Effects of forcing differences and initial conditions on inter-model agreement in the VolMIP volc-pinatubo-full experiment. *Geoscientific Model Development*, *15*(5), 2265–2292. https://doi.org/10.5194/gmd-15-2265-2022

Zhang, L., Li, J., Jiang, Z., Dong, Y., Ying, T., & Zhang, Z. (2022). Clear-Sky Direct Aerosol Radiative Forcing Uncertainty Associated with Aerosol Optical Properties Based on CMIP6 models. *Journal of Climate*, *35*(10), 3007–3019. https://doi.org/10.1175/JCLI-D-21-0479.1

Zhang, R., Khalizov, A. F., Pagels, J., Zhang, D., Xue, H., & McMurry, P. H. (2008). Variability in morphology, hygroscopicity, and optical properties of soot aerosols during atmospheric processing. *Proceedings of the National Academy of Sciences*, *105*(30), 10291–10296.

Zhao, L., Wang, Y., Zhao, C., Dong, X., & Yung, Y. L. (2022). Compensating Errors in Cloud Radiative and Physical Properties over the Southern Ocean in the CMIP6 Climate Models. *Advances in Atmospheric Sciences*, *39*(12), 2156–2171. https://doi.org/10.1007/s00376-022-2036-z

Zhong, X., Liu, S. C., Liu, R., Wang, X., Mo, J., & Li, Y. (2021). Observed trends in clouds and precipitation (1983–2009): Implications for their cause(s). *Atmospheric Chemistry and Physics*, *21*(6), 4899–4913. https://doi.org/10.5194/acp-21-4899-2021